Technical Design Report
on the Super-FRS

This document has been worked within the NuSTAR collaboration Super-FRS working group.
Team members:

H. Geissel,
M. Winkler,
H. Weick,
K.-H. Behr,
G. Münzenberg,
H. Simon,
K. Sümmerer,
B. Achenbach,
D. Acker,
D. Ackermann,
T. Aumann,
J. Äystö,
R. Baer,
M. Berz,
D. Boutin,
C. Brandau,
A. Brünle,
P. Dendooven,
G. Fehrenbacher,
E. Floch,
M. Gleim,
W. Hüller,
H. Iwase,
A. Kalimov,
C. Karagiannis,
M. Kauschke,
A. Kelic,
B. Kindler,
G. Klappich,
E. Kozlova,
A. Krämer,
A. Kratz,
T. Kubo,
N. Kurz,
K. Kusaka,
H. Leibrock,
J. Lettry,
S. Litvinov,
Y. Litvinov,
B. Lommel,
S. Manikonda,
A. Marbs,
G. Moritz,
C. Mühle,
C. Nociforo,
J. A. Nolen,
H. Penttilä,
W. Plass,
Z. Podolyak,
A. Prochazka,
I. Pschorn,
T. Radon,
H. Ramakers,
H. Reich-Sprenger,
J. Saren,
G. Savard,
C. Scheidenberger,
P. Schnizer,
M. Schwickert,
B.M. Sherrill,
B. Sitar,
A. Stafinak,
R. Stieglitz,
M. Svedentsov,
N.A. Tahir,
An. Tauschwitz,
O. Tarasov,
M. Tomut,
P. Vobly,
H. Welker,
R. Wilfinger,
Ch. Will,
J.S. Winfield,
Y. Xiang,
M. Yavor,
A. Yoshida,
A.F. Zeller.

Project leader of the Super FRS:
H. Geissel, GSI, KP II, phone/fax +49-6159-71-2740/2902, email: H.Geissel@gsi.de,
Deputy M. Winkler, GSI, KP II, phone/fax +49-6159-71-2468/2902, email: M.Winkler@gsi.de

Preface

In 2001, GSI, together with a large international science community, presented a Conceptual Design Report for a major new international Facility for Antiproton and Ion Research (FAIR) at Darmstadt/Germany. Following an in-depth evaluation of the German Wissenschaftsrat conditional approval for construction of FAIR was given in 2003. The approval was contingent upon the condition of international participation and contribution of 25% of total construction cost by the international partners.
In 2006, the International Steering Committee for FAIR (ISC), comprising the FAIR partner states Austria, China, Finland, France, Germany, Great Britain, Greece, India, Italy, Romania, Russia, Slowenia, Spain and Sweden agreed to the scientific case and accelerator infrastructure as outlined in the FAIR Baseline Technical Report (FBTR). This central document provided the technical description, cost, schedule, organizational and management structure and assessment of risk for the FAIR project.

On October 17, 2007, the ISC decided on the realization of the FAIR Start Version without delay according to secure funds. Based on the proposals of the Scientific and Technical Issue Working Group together with the experiment collaborations the scope of the project first phase, FAIR Start Version, was worked out and defined. Already in the Startversion FAIR a unique unprecedented infrastructure for Nuclear- Atomic-, Astrophysics and high density plasma physics will be available that opens new fields in research.

In parallel to the preparatory activities for FAIR research and development for the accelerators and experimental facilities has advanced considerably. A series of Technical Design Reports (TDR), summarizing the actual system design, the status of R&D of key components, and technical aspects of realization for the FAIR accelerators have been composed, based on the ISC resolution and Technical Advisory Committee recommendations.

This TDR describes the actual status of the Super-Fragmentseperator – Super-FRS.

The numbering of chapters follows the systematics of the FAIR work breakdown structure, which was used in FBTR also and in associated documents as the costbook. For the ease of reference we decided to follow this earlier convention rather than to use a consecutive numbering.

The TDR is complemented by the FAIR Costbook on accelerators and associated man power – FAIR Start Version and Phase B, Version 5.0 (June 2008), providing information on project costs based on FY 2005 prices. Furthermore, relevant legal documents between the FAIR partners are compiled in the FAIR Baseline Administrative Report.

Darmstadt, December 2008

Table of Contents

2.4 Super-FRS 1
2.4.1 System Design 3
2.4.1.1 The Role in the FAIR Project 3
2.4.1.2 General Description 4
2.4.2 Magnets 21
2.4.2.1 Dipoles 22
2.4.2.2 Quadrupole Magnets 42
2.4.2.3 Multipoles 52
2.4.2.4 Steerers 57
2.4.2.5 Multipole configuration 60
2.4.2.6 Current Leads 64
2.4.2.7 Quench detection 65
2.4.2.8 Parameters for the Magnets of the Super-FRS 68
2.4.3 Power Converters 69
2.4.3.1 General Aspects of Power Converters 69
2.4.3.2 Dipole Power Converters 75
2.4.3.3 Quadrupole Power Converters 75
2.4.3.4 Multipole Power Converters 75
2.4.3.5 Steerer Power Converters 75
2.4.3.6 Power Distribution 76
2.4.3.7 Parameters for Power Converters 79
2.4.4 RF-Systems 81
2.4.5 Injection/Extraction 83
2.4.6 Beam Diagnostics 85
2.4.6.1 Diagnostics Target Area and Beam Catchers 87
2.4.6.2 Diagnostics for Slowly Extracted Beams 91
2.4.6.3 Diagnostics for Fast Extraction 92
2.4.6.4 Luminosity Monitor (SEETRAM) 93
2.4.6.5 In-Flight Fragment Identification (Bρ, ΔE, ToF) 95
2.4.6.6 Data Acquisition 97
2.4.7 Vacuum 99
2.4.7.1 General Layout 99
2.4.7.2 Maintenance and Handling of Highly-Radioactive Components 100
2.4.7.3 Maintenance and Handling in Low-Radiation Areas 101
2.4.7.4 Vacuum System 101
2.4.7.5 Technical Drawings 107
2.4.8 Particles Sources 117
2.4.9 Electron Cooling 119
2.4.10 Stochastic Cooling 121
2.4.11 Experimental Devices 123
2.4.11.1 Beam Catcher 123
2.4.11.2 Degrader Systems and Ion-Catcher 138
2.4.11.3 Production Targets 143
2.4.12 Local Cryogenics 155
2.4.12.1 Cryogenics for Dipole Stages 155
2.4.12.2 Cryogenics for Multiplets/Quadrupoles 157
2.4.12.3 Cryogenics Distribution for SC Magnets in the Super-FRS 161
2.4.13 Accelerator Controls 167

2.4.13.1 General System architecture 167
2.4.13.2 Hardware for Equipment Interfacing 168
2.4.13.3 Timing System 169
2.4.13.4 Networking 170
2.4.13.5 Computer Systems, FAIR Control Center 171
2.4.13.6 Front-End Software Architecture 171
2.4.13.7 Controls Middleware 172
2.4.13.8 Services and Application Software Architecture 172
2.4.13.9 Accelerator Settings and Management 172
2.4.13.10 Industrial Controls 173
2.4.14 Survey and Alignment 175
2.4.14.1 General Considerations 175
2.4.14.2 Work packages: description of basic principles 177
2.4.14.3 Machine characteristics: impact on alignment procedures 183
2.4.14.4 Closing words 186
2.4.15 NUSTAR DAQ 187
2.4.15.1 Time and trigger distribution systems 189
2.4.15.2 Data collection and storage 190
2.4.15.3 Slow control and monitoring 190
2.4.16 Cryogenics 193
2.4.16.1 Introduction 193
2.4.16.2 The Refrigerator 194
2.4.16.3 The Helium Distribution System 198
2.4.17 Magnet testing 205
2.4.17.1 Introduction 205
2.4.17.2 Conventional Magnets 206
2.4.17.3 Superconducting Magnets 208
2.4.17.4 Reference Magnets 224
2.4.18 Safety 225
2.4.18.1 Interlock system 225
2.4.18.2 Radiation environment (radiation protection) 225
2.4.19 Super-FRS Collaboration 237

2.4 Super-FRS

This Technical Design Report covers the design for the accelerator system Super-Fragmentseparator (PSP-code 2.4).

2.4.1 System Design

The present report gives the status of the Super-FRS project which has been continuously optimised and adapted to the constraints of its technical realization, the discussions and collaborations with industry and leading institutes worldwide. Ion-optical parameters, such as dimensions of magnets and drift lengths, have been modified to accommodate the specific target equipment and beam catchers required for the full operating domain of the FAIR accelerator facilities. The experimental areas of the Low- and High-Energy Branches have been reconsidered in more detail and are designed to enable the planning and construction of the corresponding buildings which will be installed in the first phase of FAIR.

2.4.1.1 The Role in the FAIR Project

The Super-FRS will be the most powerful in-flight separator for exotic nuclei up to relativistic energies. Rare isotopes of all elements up to uranium can be produced and spatially separated within some hundred nanoseconds, thus very short-lived nuclei can be studied efficiently. The Super-FRS is a large-acceptance superconducting fragment separator with three branches serving different experimental areas including a new storage-ring complex. The new rare-isotope facility is based on the experience and successful experimental program with the present FRS [1].

The Super-FRS magnetic system will consist of three branches connecting different experimental areas, see Figure 2.4-1. Reaction studies under complete kinematics, similar to the present ALADIN-LAND [2] setup, will be performed at the High-Energy Branch. Unique studies will be performed in the Ring Branch consisting mainly of a collector ring CR, the NESR, RESR and an electron nucleon collider (eA). Precision experiments with a brilliant electron-cooled exotic beam including reaction studies with the atoms of an internal target will be done in the NESR. A novelty will be electron scattering from exotic nuclei in the eA-collider section. The Low-Energy Branch of the Super-FRS is mainly dedicated to precision experiments with energy-bunched beams stopped in a gas cell. This branch is complementary to the ISOL (Isotope Separator On-Line) facilities since all elements and short-lived isotopes can be studied.

The layout of the Super-FRS consists of magnets with $B\rho_{max}$ of 20 Tm. The increased maximum magnetic rigidity compared with the FRS is determined by the goal to circumvent atomic charge-changing collisions up to the heaviest projectile fragments. Although the CR is restricted to 13 Tm and the energy buncher to 7 Tm it is cost effective to apply the same type of magnetic elements throughout the separator which allows in addition the use of an additional degrader at the final achromatic focal plane, an option which is successfully applied at the present FRS.

Table 2.4-1: Parameters of the Super-FRS compared with the existing FRS

Facility	Max. Magnetic Rigidity $B\rho_{max}$ / [Tm]	Momentum Acceptance $\Delta p/p$	Angular Acceptance ϕ_x / [mrad]	ϕ_y / [mrad]	Momentum Resolution
FRS	18	±1 %	±7.5	±7.5	1500 ($\varepsilon=20\pi$ mm mrad)
Super-FRS	20	±2.5 %	±40	±20	1500 ($\varepsilon=40\pi$ mm mrad)

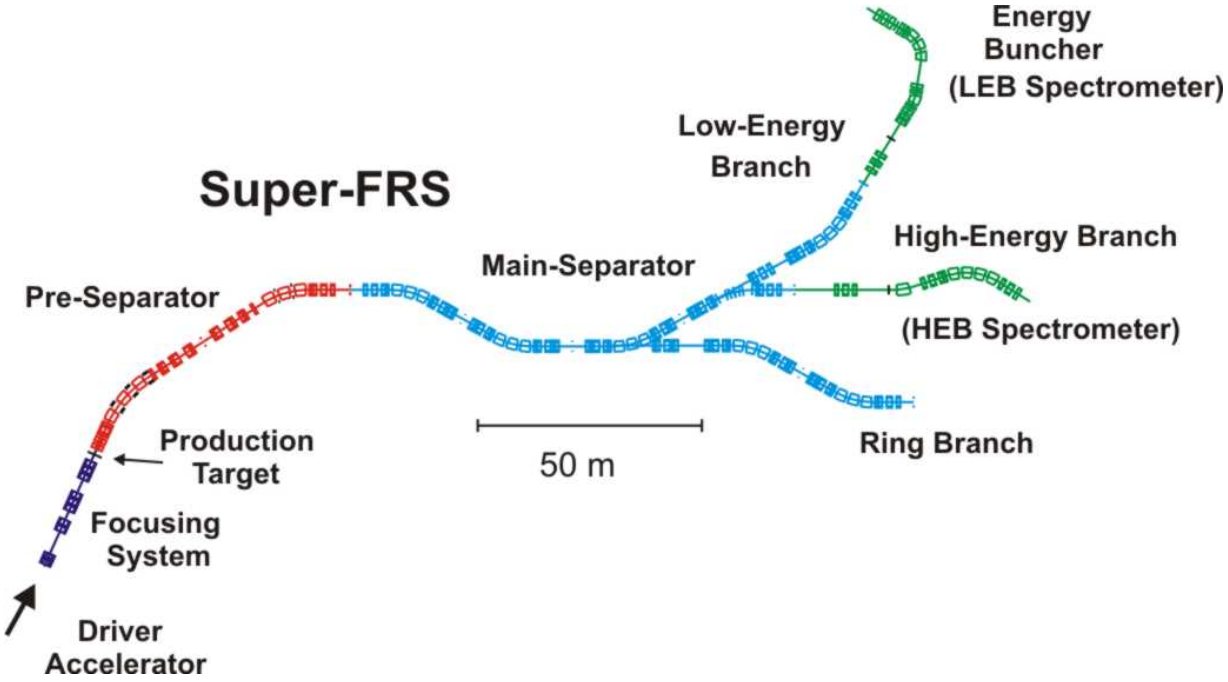

Figure 2.4-1: Layout of the proposed superconducting fragment separator Super-FRS for the production, separation, and investigation of exotic nuclei. Spatially separated rare-isotope beams are delivered to the experimental areas via three different branches. The ion-optical layout of the focusing system in front of the production target and of the energy-buncher system (LEB-spectrometer) has been significantly modified to match the experimental conditions. A high-resolution magnetic spectrometer (HEB-Spectrometer) has been designed for the high-energy experimental area (R^3B project).

2.4.1.2 General Description

The Super-FRS has to separate efficiently in-flight rare isotopes produced via projectile fragmentation of all primary beams up to ^{238}U and via fission of ^{238}U beams. The latter reaction is a prolific source of very neutron-rich nuclei of medium mass. However, due to the relatively large amount of kinetic energy released in the fission reaction, the products populate a large phase space and thus are one reason for the need of a much larger acceptance for the Super-FRS compared with the FRS, see Table 2.4-1. **The gain in transmission for uranium fission products at the Super-FRS is more than one order of magnitude compared to the FRS [3]**. Moreover, the Super-FRS will also provide similar gain factors for projectile fragments because of: 1) the required multiple energy-degrader stages for mono-isotopic spatial separation (Bρ-ΔE-Bρ method), 2) the required enlargement of the primary beam spot at the power target for fast extraction, 3) the large momentum spread ($\sigma_p/p \sim \pm 1\%$) of the incident fast extracted beam, 4) the option to produce the nuclides in secondary reactions at intermediate focal planes of the ion-optical system. Typical examples for the separation of projectile fragments with two degrader stages are illustrated in Figure 2.4-2.

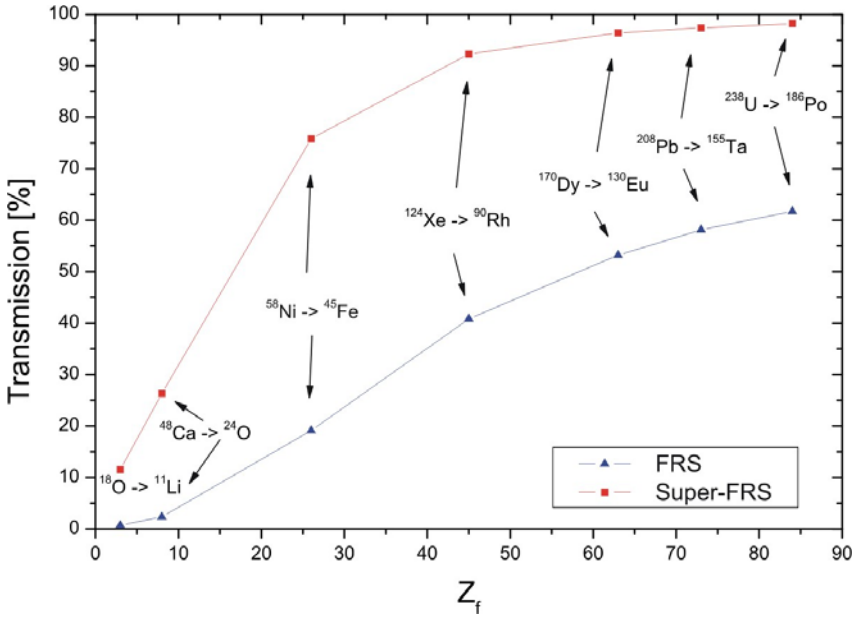

Figure 2.4-2: Transmission of the Super-FRS (at the MF4 focal plane) compared with the present FRS (at the S4 focal plane) for **projectile fragmentation reactions**. The fragment energy after the production target was 700 MeV/u and two Al degraders with a thickness of d/R = 0.5, 0.6 (in units of the atomic range of the fragment). The primary beams used for the reactions are indicated in the figure as well. The derived gain factors for the Super-FRS range from 1.5 (for the heaviest Z) to 16 (for the lighter Z).

Besides the fragment intensities, the selectivity and sensitivity are crucial parameters that strongly influence the success of an experiment with very rare nuclei. A prerequisite for a clean isotopic separation is that the fragments have to be fully ionized to avoid cross contamination from different ionic charge states. Multiple separation stages are necessary to efficiently reduce the background from such contaminants. Based on the experience of successful spatial isotopic separation with the existing FRS at GSI, the Super-FRS also uses the Bρ-ΔE-Bρ method, where a two-fold magnetic rigidity analysis is applied in front of and behind a specially shaped energy degrader. The strong enhancement of the primary beam intensity expected with the SIS100/300 synchrotron requires additional measures to achieve the required separation quality. A solution is at least one additional degrader stage which provides an effective pre-selection before the fragment beam impinges onto the main degrader. A straight forward consequence is that the Super-FRS consists of a two-stage magnetic system, the Pre- and the Main-Separator, each equipped with a degrader, having 6 intermediate focal planes.
The condition mentioned above for fully stripped fragments requires a high-energy operating domain. On the other hand, the thicknesses of the production target and degraders have to be optimized to prevent substantial losses due to secondary nuclear reactions. The selection of the maximum magnetic rigidity of 20 Tm results from these physical criteria, the optimization of the performance, costs of the magnetic elements and their dynamic range.

2.4.1.2.1 Ion-Optical Layout

The ion-optical layout of the Super-FRS (High-Energy-Branch) and its imaging conditions are presented in Figure 2.4-3. The envelopes and the dispersion line are plotted for primary-beam emittances of 40 π mm mrad, and Δp/p of ±2.5 %, respectively. The target spot size is assumed to be ±1 mm and ±2 mm in the x- and y-direction, respectively. The magnet system consists of the Pre-Separator and the Main-Separator, each equipped with an energy-degrader stage. The Pre- and Main-Separator are both achromatic systems, hence the complete system is also achromatic. This means the image size at the final focal plane is independent of the momentum spread of the fragments at the entrance of the system and thus guarantees the best spatial isotopic separation.

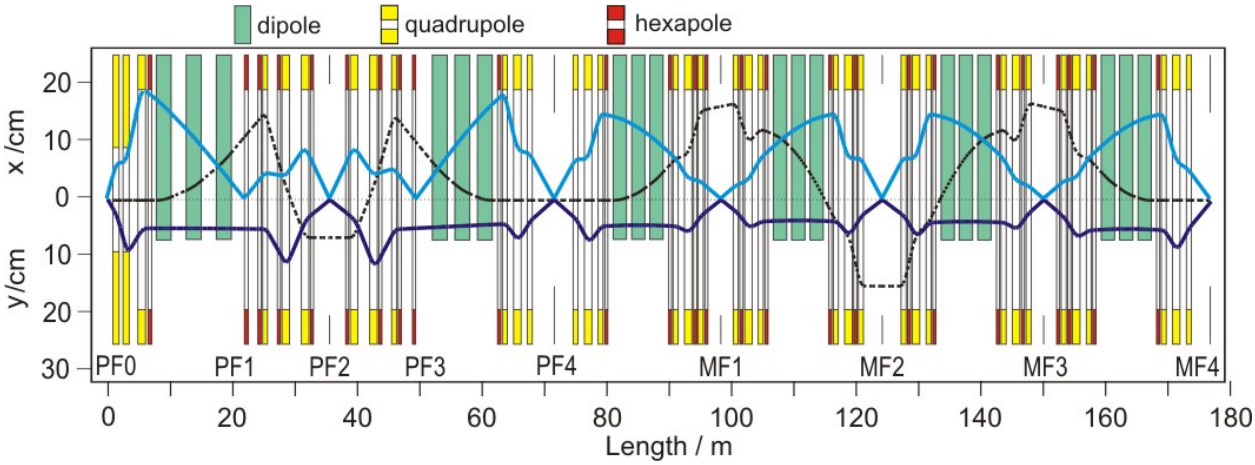

Figure 2.4-3: Ion-optical elements, beam envelopes (full lines) and the dispersion line for 2.5 % momentum deviation (dashed line) are shown in the lattice of the Super-FRS. Here, the High-Energy-Branch (HEB) is presented. The envelopes result from an emittance of 40 π mm mrad in x and y direction. The different focal planes of the Pre-Separator (P) and the Main-Separator (M) are indicated by (P, M) F1–F4. Quadrupole triplets are placed in front of and behind the dipole magnets to achieve the desired ion-optical conditions at the focal planes and to properly illuminate the dipole magnets to achieve the required optical resolving power. Hexapole magnets and octupole correction coils which are superimposed to the quadrupole magnets are applied to correct image aberrations, especially at the degrader positions and the achromatic focal planes. The lengths of hexapole magnets and new dimensions of drift-lengths are the main changes compared to the previous design.

Ion optics from SIS to the production target

The ion-optical momentum resolution determines the separation power of the Super-FRS for the spatially separated fragment beams. Therefore, a small and constant beam spot at the target position is essential, typically 1 and 2 mm in x- and y-direction, respectively. Only an excellent achromatic focus corrected for higher-order aberration can fulfil this necessary condition at the entrance of the Super-FRS. The achromatic condition is especially indispensable for the fast extracted projectile beam which is characterized by the large momentum spread of ±1 % (1σ value), which even exceeds for some fragments the spread due to the nuclear creation process. This has two consequences:

- The magnetic system from the accelerator to the production target has to be an achromatic system (corrected with higher-order multipole fields if necessary).
- A special focusing system subsequent to the achromate will be applied to reach the required spot size at the position of production target indicated by PF0.

The achromatic beam transport is described in section 2.3 of this report. A layout of a split-lens optics for low (10 Tm) and high (100 Tm) magnetic rigidities is presented in Figure 2.4-4. The focusing system must handle the beam from SIS100/300 or from SIS18 directly. The quadrupole lenses in the multiplet are split into several parts corresponding to the operating domain. This configuration has the advantage to apply the super-ferric magnet type as suggested for the Super-FRS. The magnetic system is characterized by a length of 28 m. Operations experience for this type of magnet exists in several laboratories.

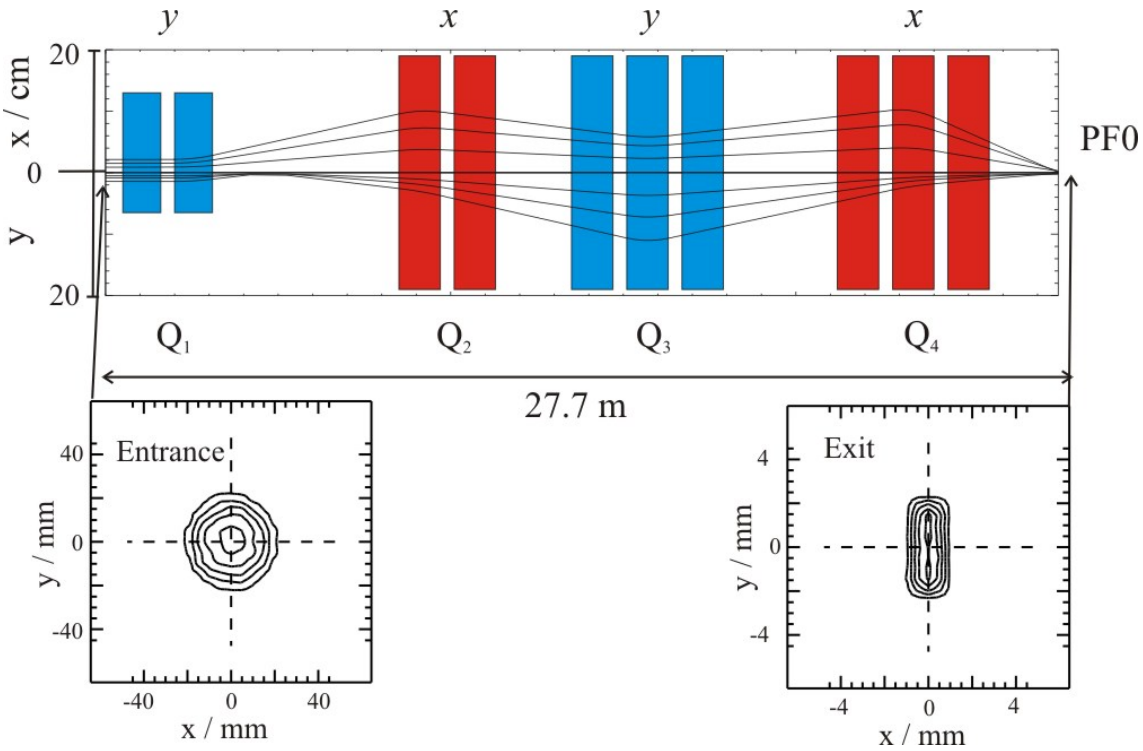

Figure 2.4-4: Ion-optical layout of the split-quadrupole fine-focusing system to be positioned directly in front of the production target. The operating range is determined by the option that projectile beams from SIS18 or SIS100/300 are applied for experiments at the Super-FRS. Q1 is of the SIS100 type, whereas Q2-Q4 have the same type as developed for the Super-FRS. The calculation has been performed at 27 Tm.

Pre-Separator

In order to access the exotic nuclei created via projectile fission and fragmentation a high-energy separator with substantially increased acceptance, compared to the FRS, is required. The design of the Super-FRS has been based upon this criterion [3]. In Table 2.4-1 the main parameters of the FRS and the Super-FRS are compared. The phase-space acceptance of the Super-FRS has been substantially increased by means of larger apertures and fields in the magnets. Besides the technical layout of the production target, the separation and dump of the primary beam are major technical challenges to be solved in the Pre-Separator [4]. The projectile beam emerging from the production target has to be separated from the selected fragments and dumped in a special catcher system; see dedicated section in this report. One major requirement is that the high-intensity primary beam should not impinge on the first degrader, in order to maintain the high-quality separation power of the two achromatic degrader stages. Keeping in mind that the intensity and such the energy deposition of the primary beam is about two orders of magnitude larger than the fragments, the conditions and properties for the material and the high radiation field require special considerations implemented in the optical layout.

The dipole magnets have been divided into three 11-degree parts. The space in between these different dipole magnets (2.4 m) accommodates position-sensitive detectors and primary beam catchers, i.e. the primary beam will not be dumped inside any magnet but only in localized external beam catchers. An extra dispersive focus is required directly behind the first dipole magnet system, i.e. in total the Pre-Separator has 3 dispersive focal planes to form an overall achromatic system.

The division of the dipole magnets into three parts gives also advantages for the technical production which reduces the costs of the magnets. The 6 beam catchers positioned on both sides of the optical axis will stop the primary beam completely. In the target and in these beam catchers the primary beam will be slowed down by atomic interaction and will be partially converted into heavy projectile fragments and light particles, such as protons and neutrons which will even penetrate through the 1 m thick material used for the beam catchers. Therefore, one has in principle to consider if the superconducting magnets right after an interaction zone (target, beam catcher) can survive the high radiation field and how much temperature rise is acceptable to avoid quenching of a superconducting magnet. From detailed Monte Carlo simulations using the PHITS code [5] we can conclude that in principle all superconducting magnets stay below the quench limit. However, due to high radiation load the cryogenic power exceeds the practical limits. Taken this into account and to have a long term save and reliable operation, the first quadrupole and dipole magnets including the hexapole magnet directly behind the focal plane PF1 are produced as normal conducting systems with radiation-hard insulation.

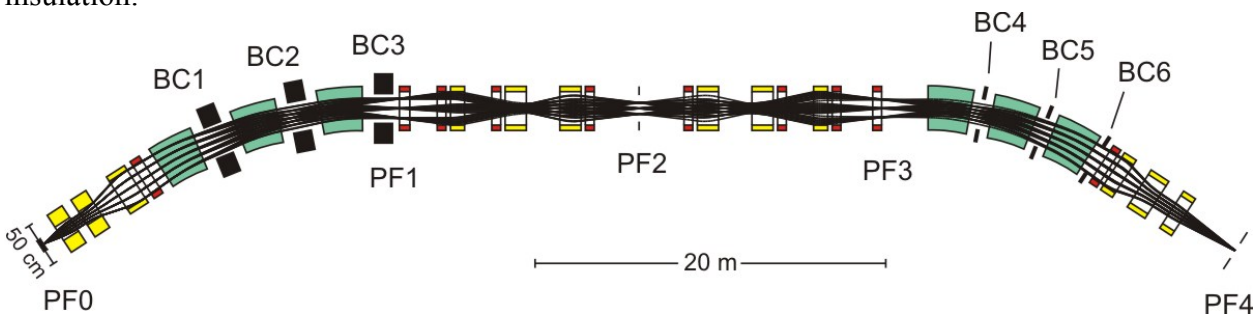

Figure 2.4-5: Layout of the Pre-Separator. The focal planes (PF1-PF4) and beam catcher (BC1-BC6) are indicated. In the standard separation mode of the Super-FRS a shaped degrader will be installed at PF2. All hexapole magnets are placed outside of the quadrupole magnets.

The standard ion-optical layout of the Pre-Separator is presented in Figure 2.4-5. The most relevant first order matrix elements are given in Table 2.4-2. In the first focal plane a focus is realized only in the x-direction whereas in the symmetrical mid plane, the position of the first degrader system, in both coordinates foci are required and a parallel dispersion line. The system is mirror symmetric with respect to PF2, firstly to have the necessary three foci to achieve the achromatic condition at PF4, secondly to minimize the geometrical image aberrations. Furthermore, one has to consider the case that a relatively high intensity component of the primary beam (up to 1%), for example uranium ions in the Li-like charge state, can impinge on the degrader. This contamination can then be removed in the corresponding slit system (BC4-6) mounted within the second dipole magnet system of the Pre-Separator.

Table 2.4-2: Calculated first-order transfer matrix elements at the focal planes PF1-PF4. The linear dimensions x and y are given in [m], a and b in [rad], and the momentum deviation δ in parts of the nominal value.

Matrix element	PF1	PF2	PF3	PF4
(x, x)	-2.93	1.72	-2.75	2.00
(x, a)	0	0	0	0
(x, δ)	4.39	-2.58	4.07	0
(a, a)	-0.34	0.58	-0.37	0.50
(a, δ)	0.52	0	-0.53	0
(y, y)	-5.62	-2.17	4.20	1.96
(y, b)	2.65	0	-2.6	0
(b, b)	-0.06	-0.46	0.03	0.51
drift length	3.6	5.0	4.4	6.0

The drift lengths between the magnetic elements and particular at the focal planes take into account the technical layout of the magnet system and accommodate the diagnostic elements.

The benefit of the design is that the higher-order aberrations are small except for the chromatic contributions, especially (x,aδ) which is responsible for an enormous focal plane tilt. The tilt angle at PF2 would be about 7 degrees (required is 90 degrees) without second-order corrections by means of hexapole magnets. Such a tilt would make a high-resolution degrader operation very difficult or even impossible. Therefore, hexapole magnets are used to correct this deficiency. However, soon as this correction is done, induced higher-order aberrations become a major challenge. Our procedure is to find an optimal position for the hexapoles where the required field strengths are minimal by means of calculated hexapole coupling coefficients along the separator. It is a necessary condition that the induced aberrations are small. This procedure was also successfully applied at the present FRS and is based on suggestions by K. Brown [6]. An example of such a system of coupling coefficients is given in Figure 2.4-6. Applying hexapole and octupole corrections we succeeded to regain about 80 % of the first-order momentum resolving power at the central plane of the Pre-Separator. This result is confirmed by higher-order calculations performed with different ion-optical codes like GICO and COSY [7].

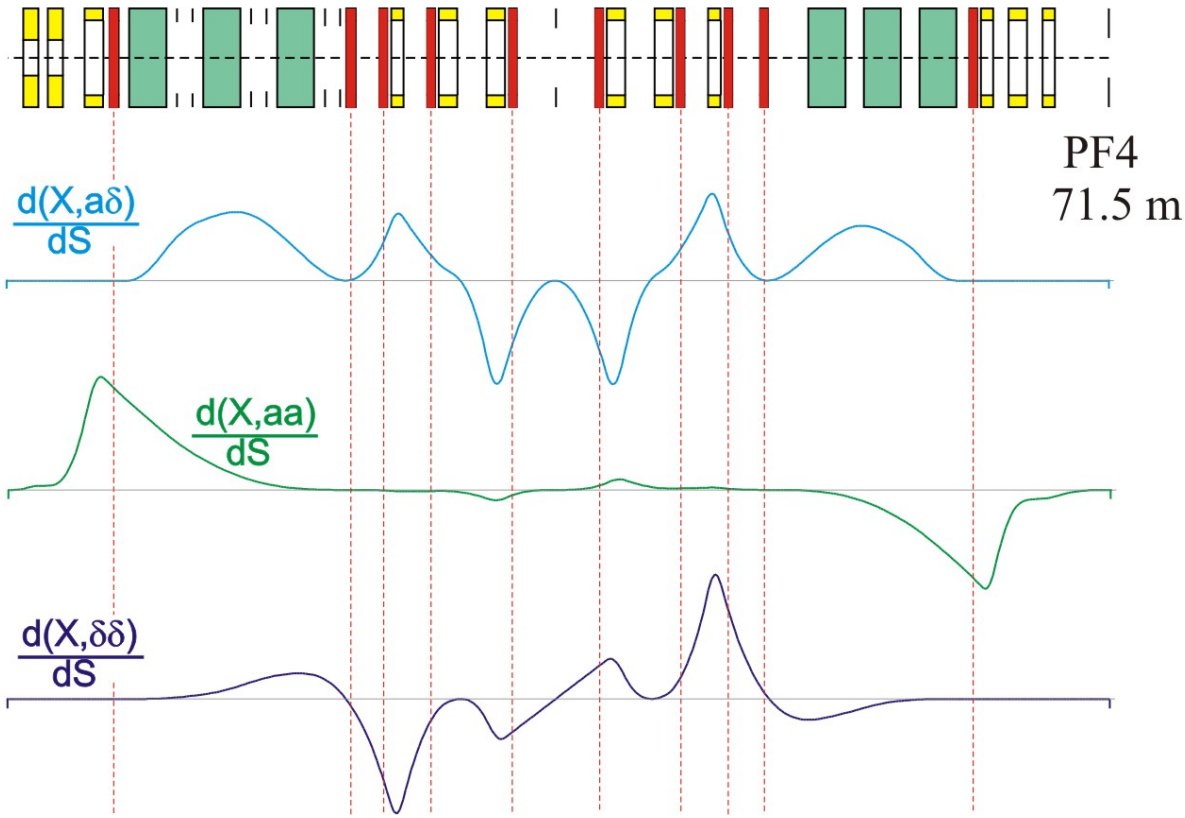

Figure 2.4-6: Example of most important 2nd-order coupling coefficients ([x,aa], [x,aδ], [x,δδ]) calculated along the Pre-Separator. The magnetic elements of the Pre-Separator are schematically shown in the upper part of the plot. The hexapole magnets are marked in red colour.

The additional foci at PF1 and PF3 can of course be shifted more towards the middle of the drift lengths between the subsequent dipole and hexapole magnets to improve the spatial separation of the primary beam from the selected fragments (see Figure 2.4-5). However, this reduces the optical resolving power at PF2 and thus the overall fragment separation power (see Figure 2.4-7). Therefore the condition has to be matched to the experimental requirement.

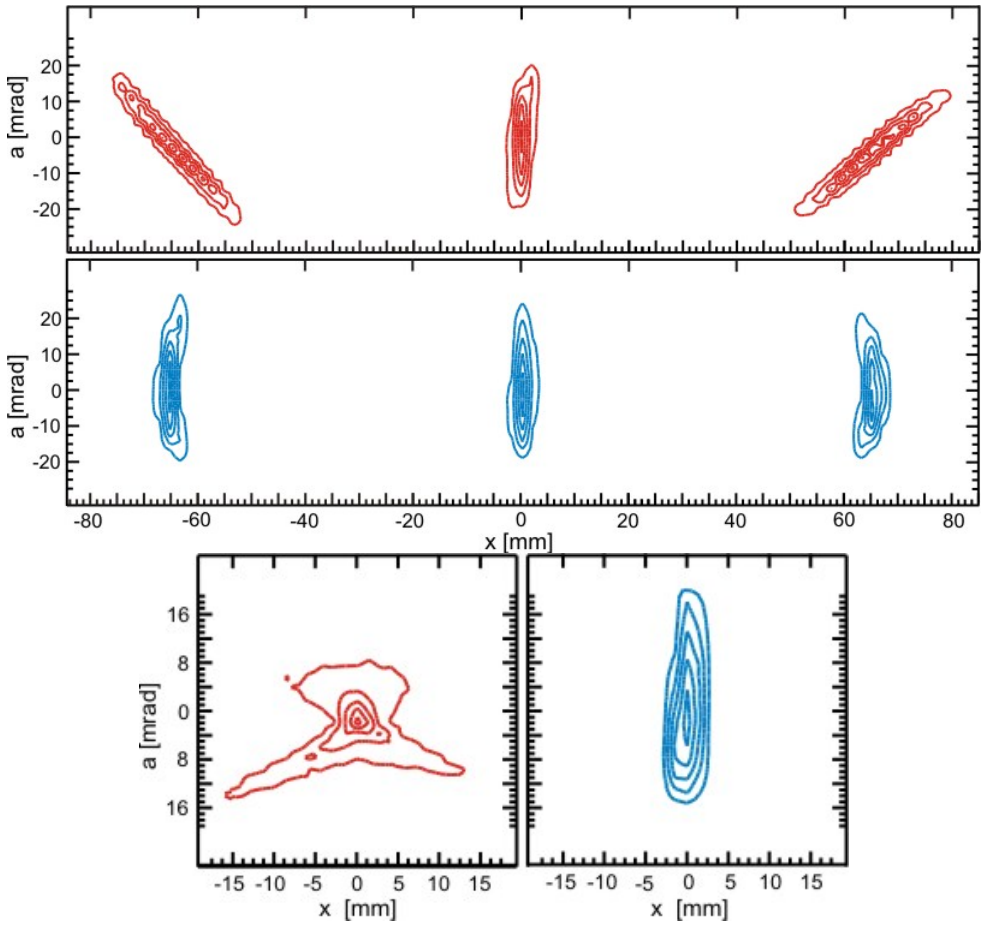

Figure 2.4-7: Upper panel: Calculated phase space in the dispersive focal plane PF2 for a beam of 40 mm mrad and three different momenta of Δp/p = ±2.5 % with (blue distributions) and without (red distributions) correction of image aberrations. Lower panel: Corresponding phase space in the achromatic focal plane PF4.

Main-Separator

The Main-Separator (see Figure 2.4-8) consists of 4 dipole stages with focusing elements in front and behind each dipole magnet system. The 29-degree dipole magnets are divided in 3 parts to facilitate the production of the iron-dominated superconducting magnets. The ion-optical design of the Main-Separator closely follows the concept applied for the Pre-Separator. However, the radiation level in this part of the Super-FRS is about two orders of magnitude lower because the primary beam and the non-desired fragments are deposited in the Pre-Separator. The Main-Separator has also 4 focal planes to accommodate an achromatic system with a degrader station in the central focal plane. The Main-Separator has 3 experimental branches to different experimental areas.

The characteristic features are outlined for the example of the High-Energy-Branch. This branch has the advantage of a symmetrical geometry and therefore, the potential for the highest ion-optical resolution and transmission. The most relevant ion-optical properties can be deduced from the first-order ion-optical matrix elements presented in Table 2.4-3.

Table 2.4-3: First-order matrix elements for the High Energy Branch (HEB) of the Main-Separator. The linear dimensions for x and y are in [m], for the angles a and b in [rad], and for the momentum deviation δ in parts of the nominal value.

Matrix Element	MF1	MF2	MF3	MF4
(x, x)	-4.23	1.93	-4.23	2.70
(x, a)	0	0	0	0
(x, δ)	6.50	-5.93	6.50	0
(a, a)	-0.24	0.52	-0.24	0.37
(a, δ)	0.09	0	0.10	0
(y, y)	-1.96	2.00	-1.96	2.70
(y, b)	0	0	0	0
(b, b)	-0.51	0.50	-0.51	0.37
drift length	4.0	6.0	4.0	6.0

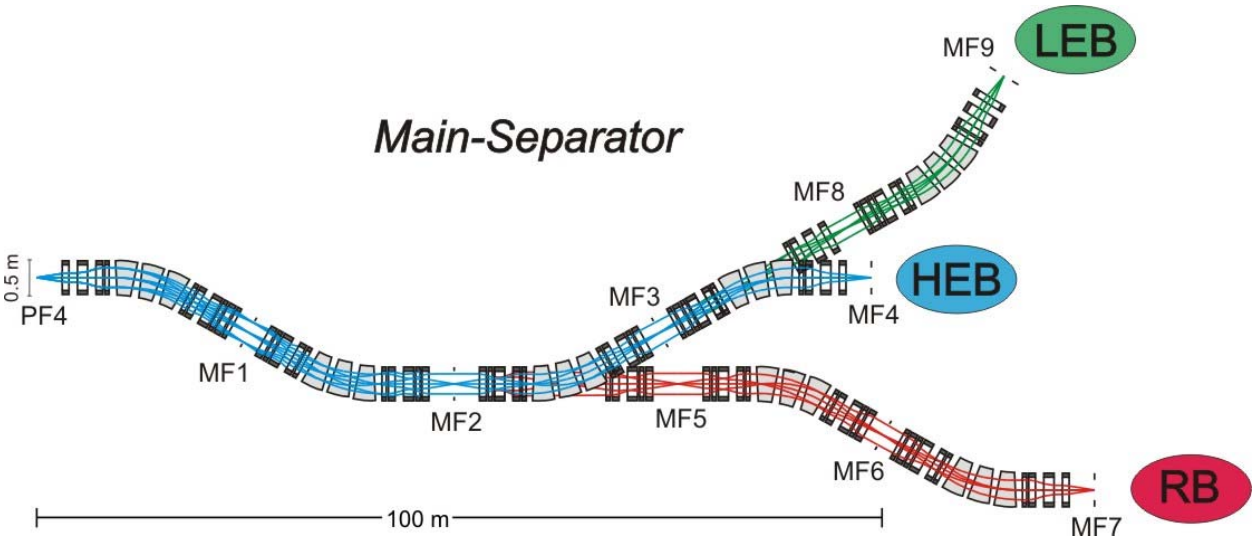

Figure 2.4-8: System plot of the Main-Separator with its branches related to the different experimental areas (LEB: Low-Energy Branch, HEB: High-Energy Branch, RB: Ring Branch). The different focal planes along the magnet system are indicated by (MF1-MF9). The main changes in respect to the FBTR have been made at the LEB, where a full focal plane including the magnetic elements was removed. As a consequence, the bending direction of the last dipole stage has been changed too.

Separation performance with two degrader stages

The two-stage system has several novel functions and features:

- reduction of the contaminants from fragments produced in the first degrader;
- optimization of the fragment rate on the detectors in the Main-Separator;
- introduction of another separation cut in the A-Z plane of the separated isotopes;
- Pre- and Main-Separator can ideally be used for secondary reaction studies if the separation of the Pre-Separator is already sufficient.

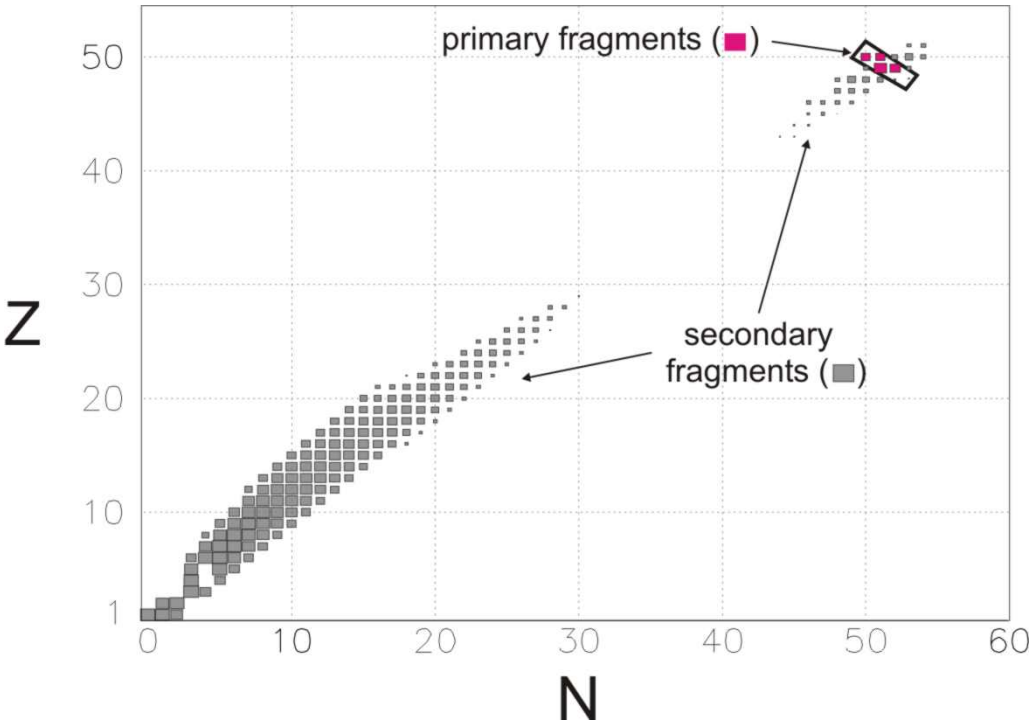

Figure 2.4-9: Separation performance of the two-degrader method compared with a one-degrader setup, for the ^{100}Sn example, taken from ref. [4]**.**

The example in Figure Figure 2.4-9 shows the separation of ^{100}Sn produced by fragmentation of ^{124}Xe at 1000 MeV/u. The large number of secondary fragments for a single degrader stage is illustrated by using the Main-Separator only (gray boxes). The total amount of unwanted secondary fragments exceeds the separated ^{100}Sn rate by a factor of 10^4. In case the Pre-Separator is used in addition, only the few primary fragments, marked with red boxes, are transported to the final focal plane.

The resulting Super-FRS system will be a powerful isotope separator and in addition a **versatile high-resolution spectrometer**. This operation mode has been very successfully applied also in several categories of experiments at the present FRS [1]. Several basic discoveries have been made with the FRS as spectrometer, e.g., new halo properties, deeply pionic states in heavy atoms, relation of fragmentation and EOS, new basic atomic collision properties at relativistic energies, etc. Such achromatic systems are ideally suited for high-resolution studies independent of possible energy fluctuations of the primary beam.

Main-Separator to the high-energy experimental area

The High-Energy Branch allows experiments with fast secondary beams up to $B\rho_{max}$ of 20 Tm. It combines the in-flight separator with an efficient reaction setup, see Figure 2.4-1 and Figure 2.4-10. The compact design will overcome the problem of low transmission of the present FRS to the experimental areas (in the SIS18 Target Hall) caused by long transport lines and beam-line magnets designed only for primary beams with small emittances.

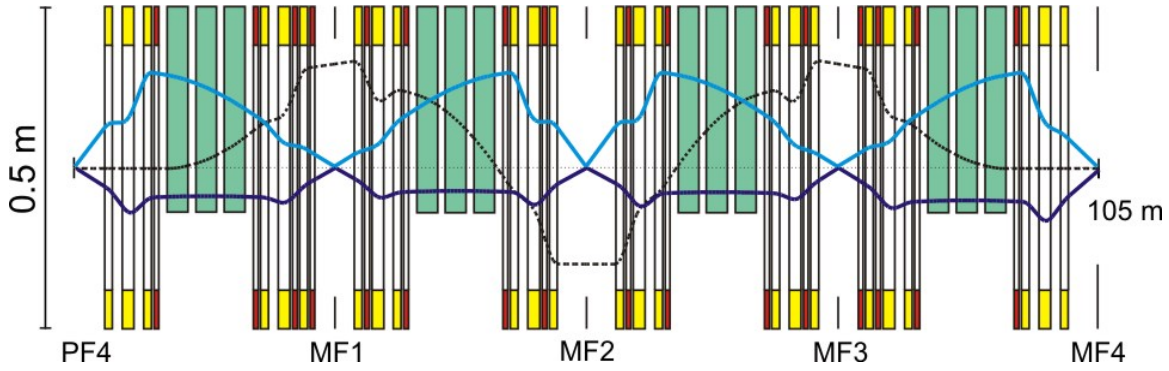

Figure 2.4-10: Ion optical layout of the High-Energy-Branch of the Main-Separator. Shown are the envelopes of a 40 π mm mrad beam in x direction (upper half), y direction (lower half) and the dispersion for a 2.5 % momentum deviation (dashed line). The main optical properties are given in Table 2.4-3.

Main-Separator to the storage rings

Of special importance is the Ring Branch (Figure 2.4-11 and Table 2.4-6) which consists of a storage-cooler ring system. Fragment pulses as short as 50 ns[1] are injected into the Collector Ring (CR) with rigidities of up to 13 Tm. The main task of the CR is to efficiently collect and stochastically precool the hot fragment beams.

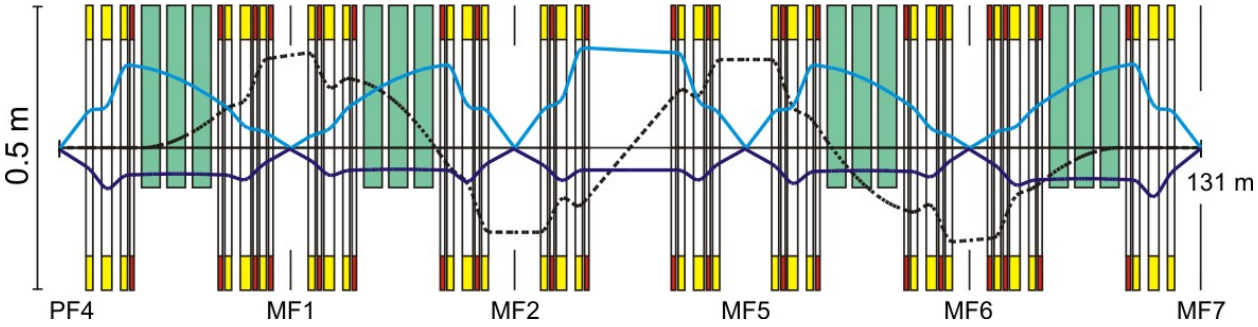

Figure 2.4-11: Ion optical layout of the Ring-Branch of the Main-Separator. Shown are the envelopes of a 40 π mm mrad beam in x direction (upper half), y direction (lower half) and the dispersion for a 2.5 % momentum deviation (dashed line).

[1] The short pulses will be available after the SIS100 rf upgrade in Phase B.

Table 2.4-4: First-order matrix elements for the Ring-Branch (RB) of the Main-Separator. The linear dimensions for x and y are in [m], for the angles a and b in [rad], and for the momentum deviation δ in parts of the nominal value.

Matrix Element	MF1	MF2	MF6	MF7
(x, x)	-4.23	1.93	4.23	-2.00
(x, a)	0	0	0	0
(x, δ)	6.50	-5.93	-6.50	0
(a, a)	-0.24	0.52	0.24	-0.5
(a, δ)	0.09	0	0.06	0
(y, y)	-1.96	2.00	2.00	-1.54
(y, b)	0	0	0	0
(b, b)	-0.51	0.50	0.50	-0.65
drift length	4.0	6.0	4.0	6.0

The Ring-Branch has been coupled in ion-optical calculations and simulations via a transport line to the Collector Ring, as illustrated in Figure 2.4-12. From the experience of the present FRS-ESR facility, such coupling is an essential part for reaction experiments with stored exotic nuclei.

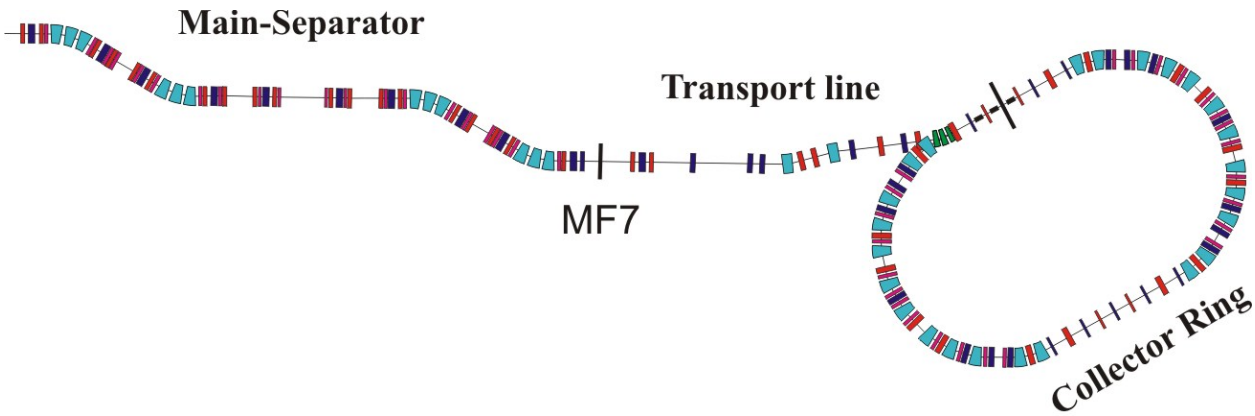

Figure 2.4-12: Layout of the Ring-Branch of the Main-Separator connected with the Collector Ring CR.

The transmission of separated fragments from the Super-FRS into the storage rings, like the CR, is an important issue. For characteristic examples the fragment production, separation and transport into the collector ring have been simulated with the MOCADI code [8]. The transmission (T) was calculated in two parts: up to the exit of the Super-FRS (MF7) and stored into the CR. Realistic target and degrader thicknesses optimized for higher rates were used for separation and slowing-down to 740 MeV/u. After this separation the beam still is not completely monoisotopic but will be with the additional m/q-separation of the CR. Four cases were selected to give a representative overview. Table 2.4-5 shows the emittance of the fragment beams after separation at MF7. The values are defined by two sigma values of the position and angular distribution. The transverse emittance is much increased due to the slowing-down and straggling in the degraders whereas the momentum spread stays about the same. The fragment beam was matched to the foreseen acceptance of the CR ($\Delta p/p = \pm 1.75$ %, $\varepsilon_x = \varepsilon_y = 200$ mm mrad).

Table 2.4-5: Transmission T of different fragments through the Super-FRS, into the CR, and the emittances and momentum spread at the exit of the Super-FRS (MF7).

fragment	**^{132}Sn**	**^{232}Fr**	**^{104}Sn**	**^{22}O**
primary beam	^{238}U	^{238}U	^{124}Xe	^{40}Ar
T to MF7 [%]	24	46	79	52
T into CR [%]	14	46	76	33
ratio MF7 / CR	0.59	0.99	0.96	0.63
ε_x [mm mrad]	169	82	90	115
ε_y [mm mrad]	151	38	64	140
2 σ_p/p [%]	3.05	1.21	1.47	3.03

At the highest projectile intensities fast extraction represents the most extreme conditions for the production target, see section 2.4.11.3. Easing of stress can be achieved if the stringent conditions for the size of the beam spot are mitigated. However, an increased size of the beam spot in the dispersive direction means that the fragment separation power is decreased as demonstrated with the detailed simulations in Figure 2.4-13. For many in-ring experiments this is no severe restriction.

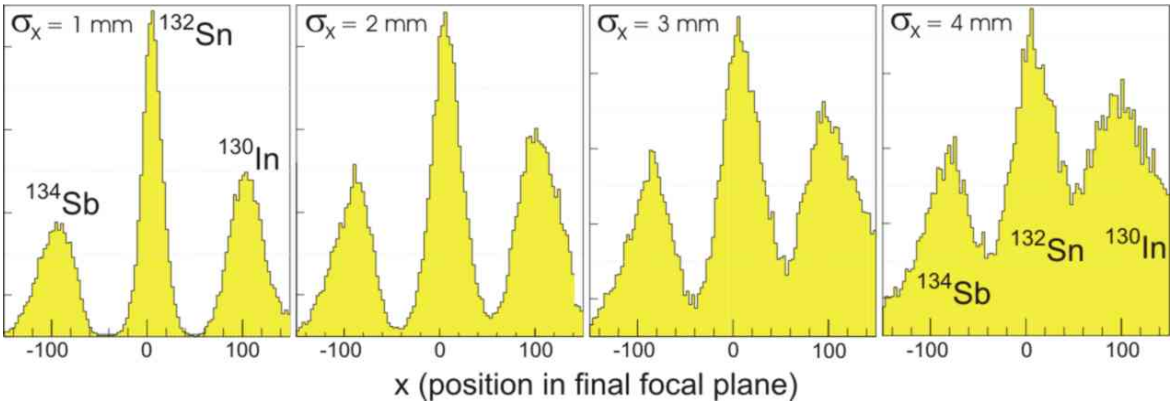

Figure 2.4-13: Calculated separation power as a function of the spot size σ_x (dispersive coordinate) at the production target. The selected example represents the separation of ^{132}Sn produced in projectile fission of ^{238}U. Both degraders at PF2 and MF2 had a thickness of half of the ^{132}Sn ion range.

Main-Separator to the low-energy experimental area

The Low-Energy Branch (Figure 2.4-14 and Table 2.4-6), which delivers secondary beams with typical magnetic rigidities up to 10 Tm, includes a high-resolution dispersive separator stage behind the achromatic Pre- and Main- Separator. In combination with a set of profiled energy degraders, including a monoenergetic degrader [9], this setup has been designed to drastically reduce the energy spread and thus the range straggling of the hot fragments. Hence, there are two operating modes for this branch. After the energy-spread reduction and absorbers to reduce the mean fragment energies, high-resolution gamma- and particle-spectroscopy research can be done. Alternatively, the exotic beams can be stopped and cooled in a gas and quickly transferred to ion or atom traps. The system will be fast and universal for all elements and be independent of the chemical properties. With the energy-buncher stage the separated fragment beams can be slowed down and their large momentum spread of up to 5 % can be reduced to a range straggling close to an ideal monoenergetic beam.

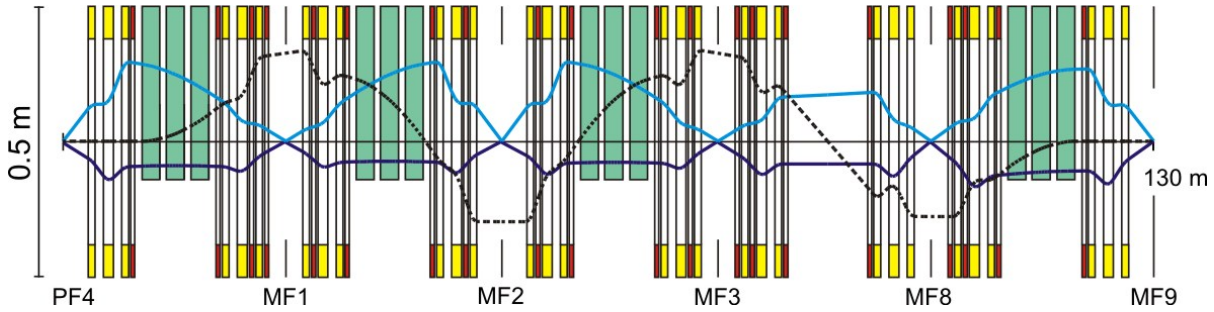

Figure 2.4-14: Ion optical layout of the Main-Separator of the Low-Energy-Branch. Shown are the envelopes of a 40 π mm mrad beam in x direction (upper half), y direction (lower half) and the dispersion in case of a ±2.5 % momentum deviation (dashed line). The ion-optical configuration beyond MF3 has been modified, with respect to the FBTR. One focal plane has been removed and as a consequence the bending direction of the last dipole stage has been changed.

Table 2.4-6: First-order matrix elements for the Low Energy Branch of the Main-Separator. The linear dimensions for x and y are in [m], for the angles a and b in [rad], and for the momentum deviation δ in parts of the nominal value.

Matrix Element	MF1	MF2	MF3	MF9
(x, x)	-4.23	1.93	-4.23	-2.00
(x, a)	0	0	0	0
(x, δ)	6.50	-5.93	6.50	0
(a, a)	-0.24	0.52	-0.24	-0.50
(a, δ)	0.09	0	0.10	0
(y, y)	-1.96	2.00	-1.96	-1.89
(y, b)	0	0	0	0
(b, b)	-0.51	0.50	-0.51	-0.53
drift length	4.0	6.0	4.0	6.0

The momentum spread of the fragment beam can be reduced if the resolving power guarantees that the spot size at the degrader is dominated by the dispersion and not by object magnification and aberrations. Since the emittances of the fragment beams are inevitably large, a large-aperture spectrometer with the necessary high resolving power is needed to compensate for the energy spread.

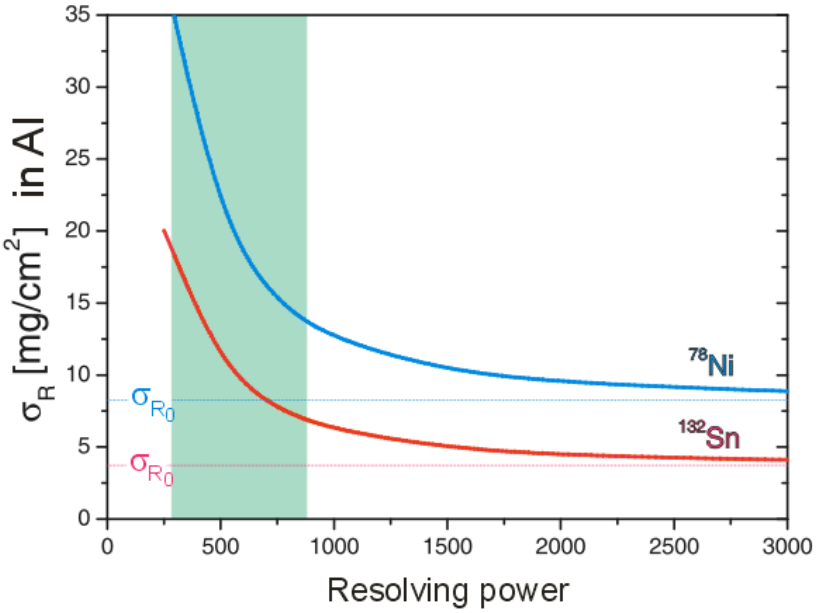

Figure 2.4-15: Resolution necessary for range bunching of ^{78}Ni or ^{132}Sn fragments produced in a fission reaction. The achievable range straggling σ_R for 300 MeV/u ^{78}Ni (blue solid curve) and ^{132}Sn (red solid curve) fragments in an aluminium stopper is plotted as a function of the momentum resolving power of the energy buncher. The dotted lines indicate the range straggling σ_{R0} of ideal monoenergetic beams of the same isotopes. The resolving-power domain which can be reached with the proposed energy buncher is marked as a green area in the figure.

In total the momentum resolving power of the dipole stage and the energy-loss straggling in a monoenergetic degrader determine how well the energy distribution can be bunched. This is shown in Figure 2.4-15 for different fragment beams compared to ideal monoenergetic beams. The area indicated in green represents the working range of the proposed energy-buncher.

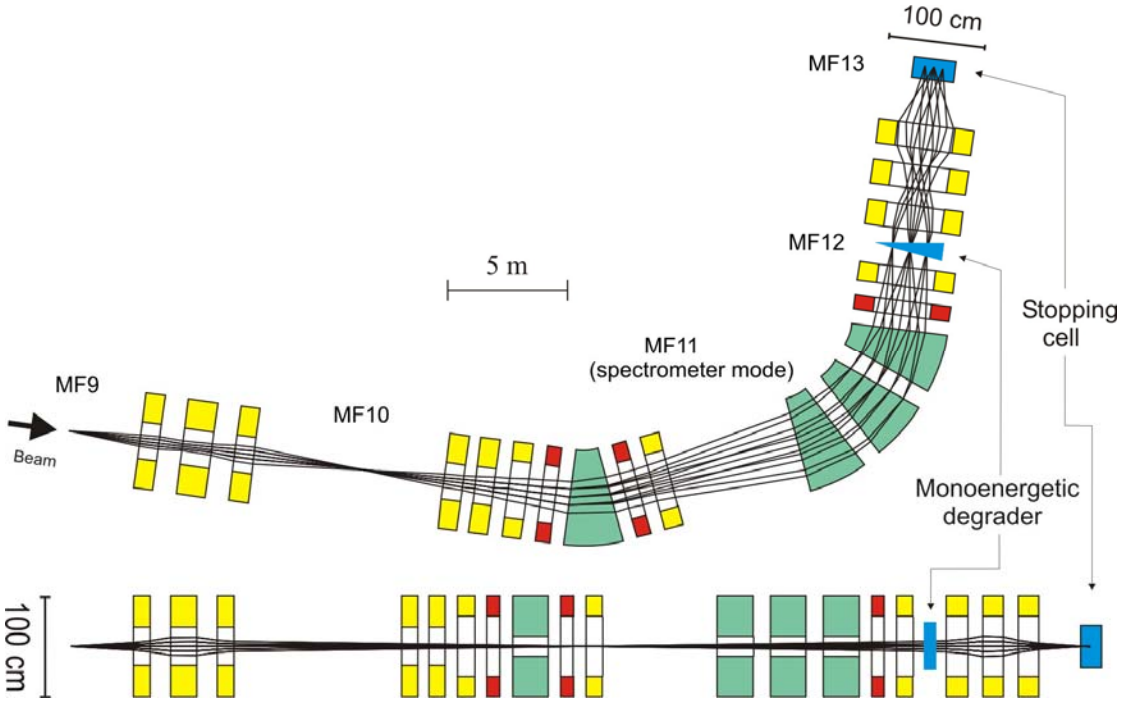

Figure 2.4-16: Ion-optical layout of the energy buncher, its main characteristics are: $B\rho_{max}$= 7 Tm, ε_x = 300 mm mrad, ε_y = 200 mm mrad, Φ_x = Φ_y = 20 mrad, $\Delta p/p$ = ±2.5 %, (transverse and longitudinal acceptance). Under these conditions a momentum resolving power of R = 600 can be achieved. The quadrupole magnets are indicated with yellow yokes, the hexapole magnets in red.

Figure 2.4-16 illustrates the ion-optical layout of the energy buncher. The spectrometer consists of a dispersive ion-optical stage with a large split dipole magnet system, quadrupole and hexapole magnets. The magnetic quadrupole triplet in front of the dipole magnet is needed to properly illuminate the field volume of the dipole magnet to reach the required resolving power and to focus the secondary beam onto a monoenergetic degrader. The quadrupole triplet behind the monoenergetic degrader guides the exotic nuclei into the gas cell or any other detector array.

It is a valuable and attractive experimental opportunity to use the energy buncher also as a high-acceptance spectrometer for particle identification after secondary reactions via magnetic rigidity analysis and tracking. The identified secondary reaction products can be measured in coincidence with gamma spectroscopy at the secondary target at MF10. For this purpose the four units of the large 90-degree dipole magnet are separated in two stages. The first unit alone has a higher momentum acceptance than the full buncher system. The ion-optical mode of this spectrometer is presented in Figure 2.4-17. In addition, an experimental scenario has been simulated to study knock-out reactions of ^{132}Sn fragments in coincidence with gamma-ray spectroscopy at MF10. The simulated mass distribution of the secondary fragments demonstrates the achieved resolving power obtained via particle tracking.

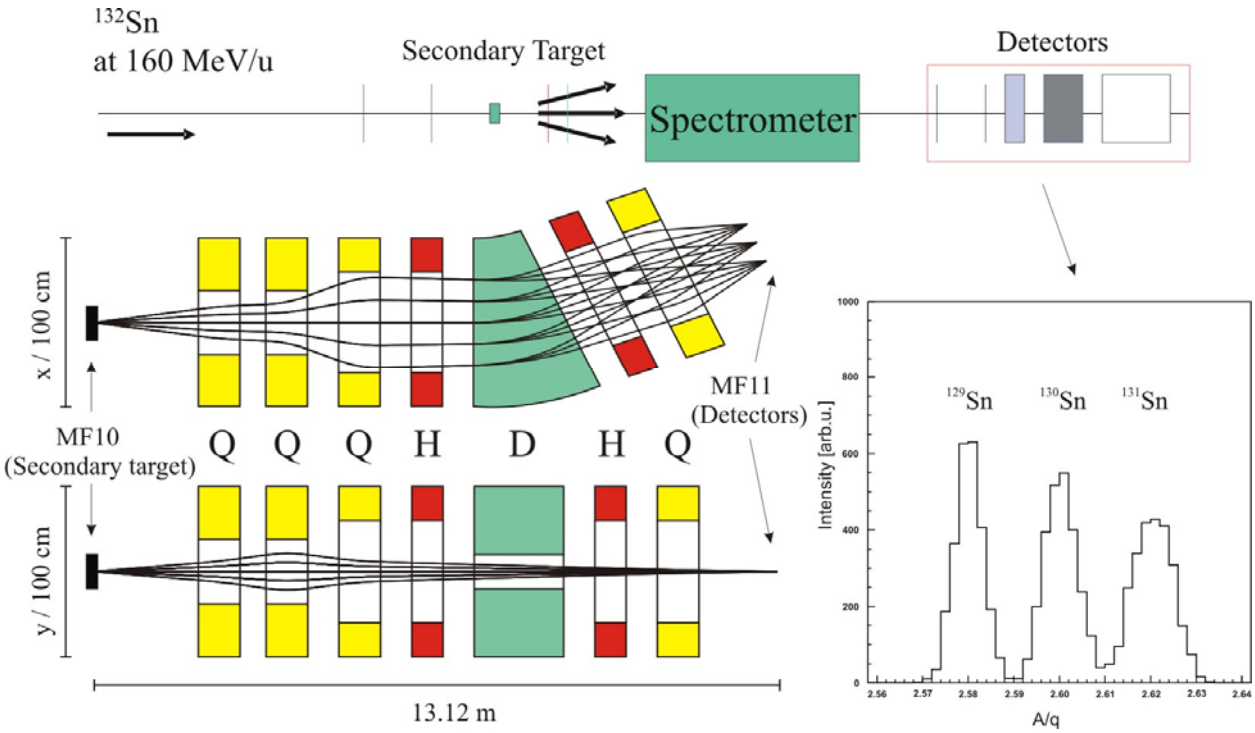

Figure 2.4-17: Spectrometer mode of the LEB Energy-Buncher. ^{132}Sn fission fragments impinge on the secondary target (C 50 mg/cm^2) placed at MF10. The secondary fragments (^{129,130,131}Sn) are analyzed by the spectrometer in combination with particle detectors. The example calculated with the MOCADI program demonstrates the achieved mass resolving power of 185, assuming a time-of-flight resolution of about 80 ps over the flight path of 13 m.

2.4.2 Magnets

Superconducting magnets

The Super-FRS has to accept fragment beams with a large phase-space volume. Therefore, it has to be equipped with large aperture magnets. In addition, the magnets have to provide high magnetic pole-tip flux densities to guide the 20 Tm ion beams. The dipole magnets of the separator will have a deflection radius of 12.5 m, a maximum field of 1.6 T, and a gap of at least 170 mm. Most of the quadrupole lenses must have a good field aperture of 380 mm with a pole tip flux density of up to 2.4 T. These specifications require the use of superconductivity. We plan to apply the superferric technology with iron-dominated lenses where the magnetic field is formed by shaped iron yokes driven by superconducting coils. This technology is already successfully applied at the A1900 in-flight fragment separator at MSU, USA [10], at the Bi-gRIPS fragment separator at RIKEN, Japan [11] and will be also applied at the future in-flight separators for RIA in the USA [12]. However, all of these facilities will work at much lower beam energies and hence the magnets are much smaller compared to those of the Super-FRS.

Radiation resistant magnets

Besides the operation of the large aperture magnets the other main challenge will be the very high radiation level, especially in the target area and the first dipole stage of the Pre-Separator where the non-reacted primary beam will be dumped. The choice of magnet technology in this area is connected to following crucial issues:

1. A principal limitation for the use of super conducting technology is that the heat load of the coils must stay below 3 mJ/g [13]. Otherwise the coil will quench. In addition the cold mass of the magnet must be sufficient small, such that the cryogenic system can provide the power to compensate the heat load.
2. Magnetic elements have to be reliably operated for the lifetime of the facility. The most radiation-sensitive part of a magnet is the electrical insulation. Conductors like copper and aluminium are many orders of magnitude more radiation resistant than organic insulators. Even the superconductors like NbTi and Nb_3Sn are at least 25 times more resistant than common organic epoxies and 10 times better than other organic insulation [14,15], see Table 2.4-7.
3. An energy deposition due to radiation of 1 mJ/g translates to a dose rate of 1 Gy. If we assume that the Super-FRS will be operated 4000 hours per year we expect an accumulated dose of 14 MGy per year. Thus for an anticipated twenty-year lifetime, the dose is close to the limit for the superconductors and beyond the lifetime of organic materials. The radiation field and an effective shielding of the magnets are described in section 2.4.A2.2.3.

Table 2.4-7: Radiation sensitivity for magnetic materials and insulations [14, 15].

Material	Radiation limit / [Gy]
NbTi	$\approx 5 \cdot 10^8$
Nb_3Sn	$\approx 5 \cdot 10^8$ (+)
Copper	$> 10^{10}$
Ceramics (Al_2O_3, MgO, etc)	$> 10^9$
Organics	10^6 -10^8

In conclusion one can state that the construction of the magnets placed in the high-radiation areas are a challenge because they require large apertures and high field gradients in the quadrupole magnets and large gaps in the dipole magnets. Designing the magnets with a re-

sistive coil option, as it would be possible in the case of the dipole magnets, leads to large magnets with a huge power consumption. The use of superconducting magnets requires a warm iron solution, in order to keep the refrigeration load (because of neutron heating) at an acceptable level. We presently consider to use resistive solutions for the magnets only in the first dipole stage of the Pre-Separator up to the hexapole behind PF1 (the location of the last beam catcher).

2.4.2.1 Dipoles

Table 2.4-8 lists the specification of the dipole magnets to be used in the Super-FRS. The table is subdivided into the radiation resistant dipole magnets needed for the 1st dipole stage of the Pre-Separator and the superferric dipole magnets for the 2nd dipole stage of the Pre-Separator, the Main-Separator, and the Energy-Buncher. Although all magnets will be operated in a DC mode the iron design must be considered to be built by laminations since the Bρ setting of the Super-FRS has to be changed frequently according to the experimental requirements.

Table 2.4-8: Design parameters for the dipole magnets of the Super-FRS.

Location of the magnet	Dim	Pre-Separator, 1st stage	Pre-Separator, 2nd stage	Main-Separator	Energy Buncher
Design		H-type, sector	H-type, straight	H-type, straight	H-type, straight
		resistive rad. resistant	superferric	superferric	superferric
Number of magnets		3	3	21	4
Maximum field	T	1.6			
Average operating field	T	1.15			
Minimum field	T	0.15			
Bending angle	deg	11	11	9.75	22.5
Edge angles (entrance / exit)	deg	0	0	0	0
Curvature radius R	m	12.5			4.375
Effective path length L	m	2.39	2.39	2.126	1.708
Useable horizontal aperture	mm	±190			±300
Useable vertical gap	mm	±70			±100
Vertical pole gap height	mm	±90	±85		±120
Field quality (over horiz. apert.)		$\pm 3 \cdot 10^{-4}$			
Overall length	m	3.2	2.8	2.5	2.1
Overall width	m	3.0	2.3	2.3	2.89
Overall height	m	2.1	1.6	1.6	1.76
Overall weight	kg	90000	56000	47500	60000
Current at max. field	A	677	246	246	200
Inductance	mH	2500	18886	16800	31250
Resistance	mΩ	320	0	0	0
ramp rate		DC Magnets (Δt_{rise} = 120 sec)			

2.4.2.1.1 Radiation resistant dipole magnets

As already mentioned above we presently consider all radiation resistant magnets needed for the 1st dipole stage of the Pre-Separator to be designed as normal conducting magnets. The most crucial part is the insulation of the coil. We intend to use Mineral Insulation Cables (MIC), where the insulation is not fabricated by organic material but by ceramics like MgO or Al_2O_3. Such kind of cable is nowadays available in various sizes, with or without hollow bores (see Figure 2.4-18) for different cooling scenarios. The cables can carry a maximum current of typically 1000 to 3000 A and an engineering current density between ≈ 2 to ≈ 5 A/mm^2 can be achieved. Magnets using MIC cable exist already in other laboratories [16].

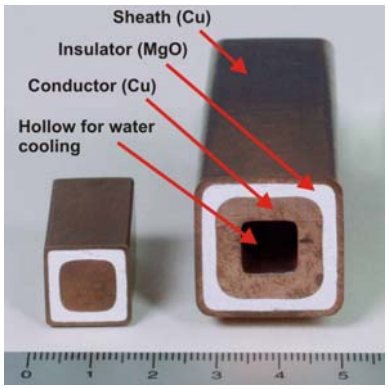

Figure 2.4-18: Mineral Insulation Cable (MIC) as produced by Hitachi Cable Ltd., Japan.

Figure 2.4-19 shows the cross section and top view of the radiation resistant dipole magnet based on a MIC cable with a conductor size of (19 x 19) mm^2. The core of the dipole magnet consists of two divisible halves (Figure 2.4-20) where each half is subdivided into three units made of steel plates and having thicknesses between 120 to 140 mm which are welded together. One unit weighs 13 tons thus the whole core weighs 78 tons.

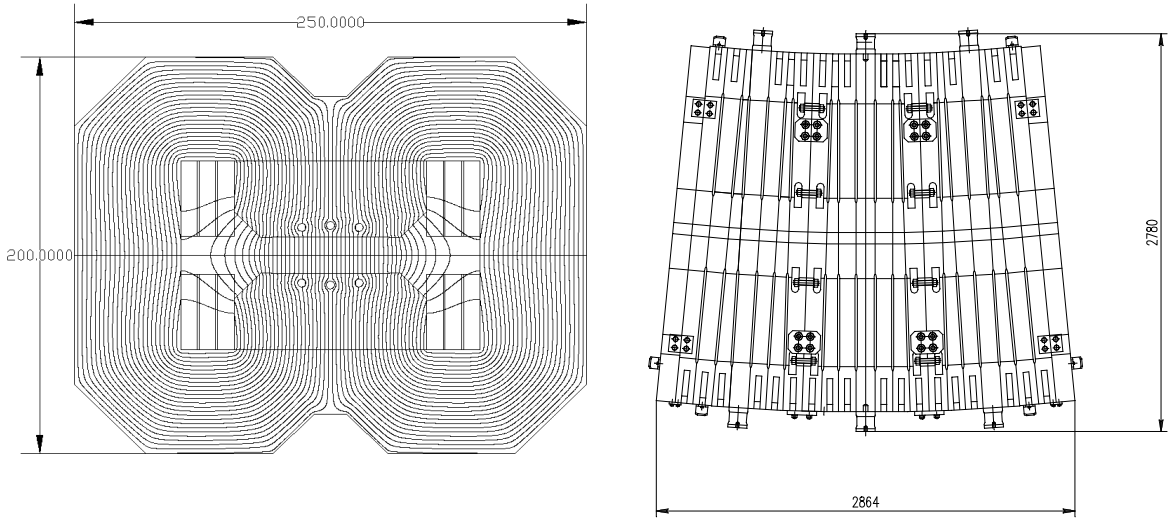

Figure 2.4-19: Magnet cross section indicating the field lines (left side) and magnet top view (right side) of a possible solution of a normal conducting radiation resistant dipole for the 1st stage of the Pre-Separator. The dimensions are given in mm.

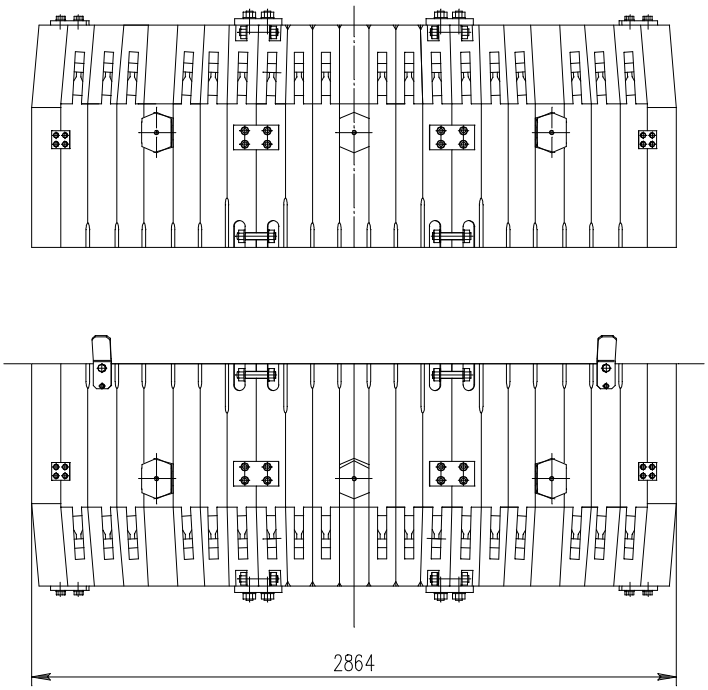

Figure 2.4-20: Side view of the two halves of the dipole magnet core. The dimensions are given in mm.

The design of the core has been chosen according to the following reasons:

1. The bending radius of the dipole magnet is 12.5 meters and the deflection angle is 11°. If a rectangular magnet were to be used this would require an increased pole width as well as an increased overall iron core to achieve the required field homogeneity (due to the beam sagitta in a rectangular magnet).
2. The units shall be rigid during their manufacture. If the units would be made out of thin sheets (about 2 mm), these sheets have to be compressed over their perimeter with a force of about 100 tons during welding. Welding is impossible over the pole surface and thus in addition thick end-plates (about 150 mm) are needed, in order to prevent the thin lamination sheets from bending outwards.
3. On the other hand, the units should not be made out of one-piece lumps because after adjusting the current, the field would not reach the steady value with a required accuracy in the requested time.

The chosen plate thickness between 100 to 150 mm thus provides rather rigid units after welding and gives an acceptable time to reach the steady value of the field. The magnet core is placed on a support allowing magnet adjustement by +/- 20 mm in the vertical and transversal horizontal directions.

The 3D simulations of the integral field homogeneity is shown in the following figure.

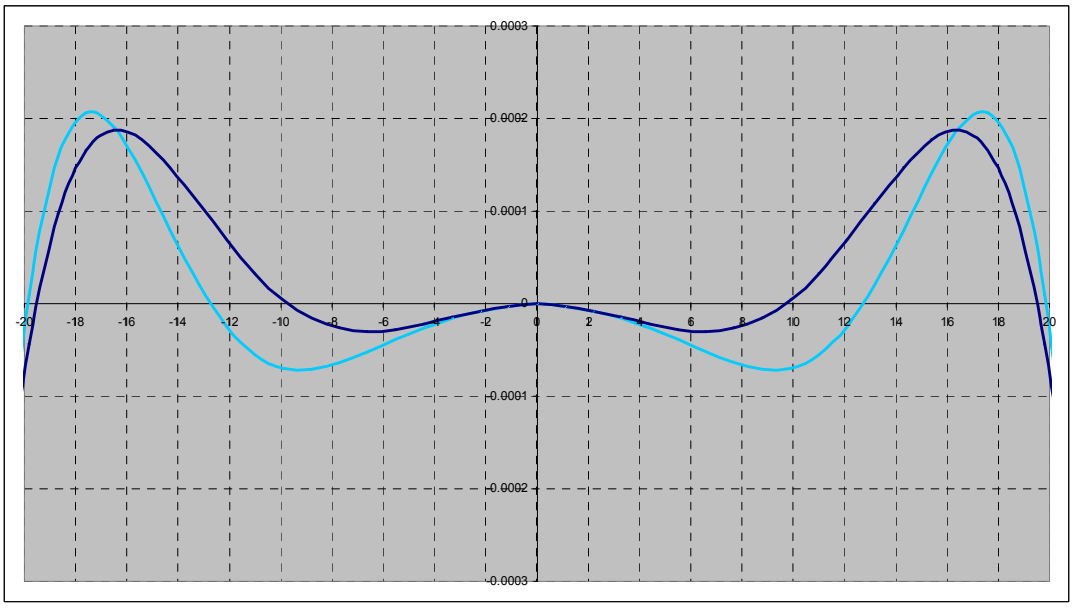

Figure 2.4-21: 3D simulations of the integral field homogeneity in the radiation resistant dipole magnet. Two cases are indicated: a high field of 1.6 T (light blue) and a low field of 0.15 T (dark blue), respectively.

To achieve B_{max} = 1.6 T for a gap height of 180 mm a total current of NI = 129 kA is required. The dipole magnet has two main current coils (Figure 2.4-22). Each coil consists of four independent sections. Each section contains a water-cooled radiator and 4 layers of radiation-resistant copper cable, two layers from each side of the radiator. The current coil section is encapsulated in tin solder in a special vacuum mould. The cross-section of current coil is shown in Figure 2.4-23.

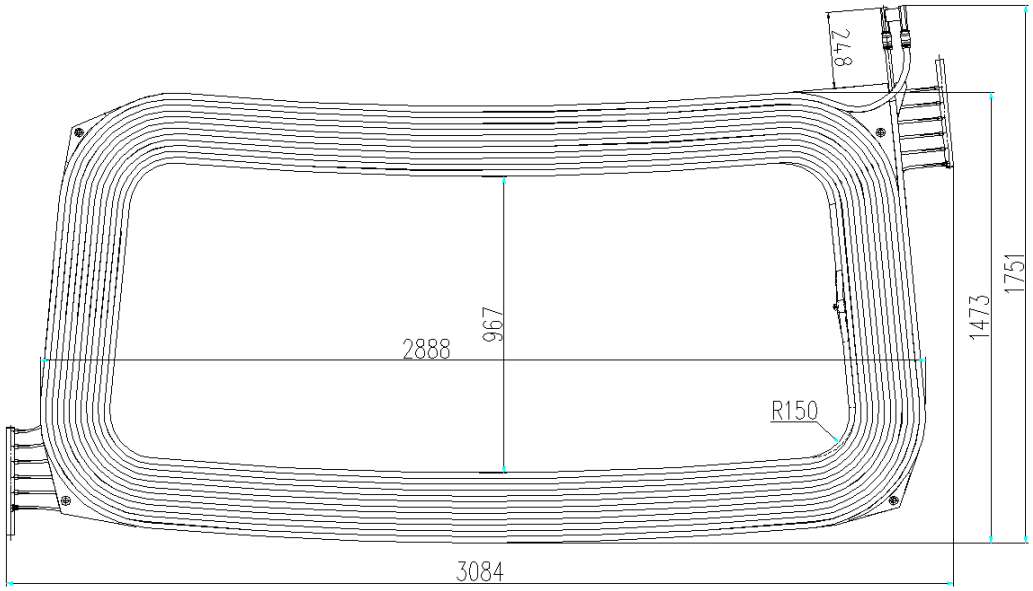

Figure 2.4-22: Top view of the coil for the radiation resistant dipole.

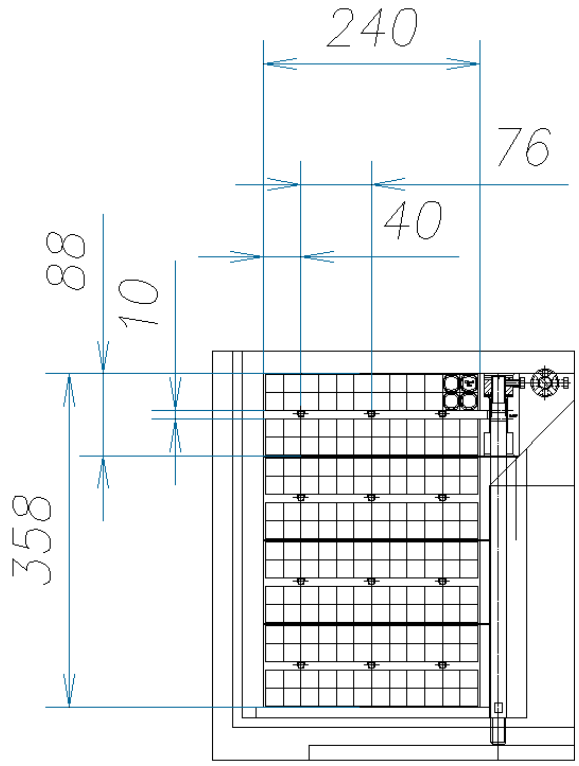

Figure 2.4-23: Coil cross-section indicating the four layers and the four water-cooled radiators.

One coil section consists of 48 turns of radiation-resistant cable with an average length of L ≈ 8.75 m. The cable length in one section is thus approximately 400 m and in total the magnet requires about 3200 m of radiation resistant copper cable. The cross-section of the radiation-resistant cable is (19 ×19) mm^2 (rectangular). The cable consists of the central copper core with a cross-section of S = 190 mm^2, a magnesium oxide interlayer of 1÷1.5 mm, and a copper envelope of approximately 1 mm thickness. The total resistance of two coils connected in series is 0.32 Ohm. The power consumption of one section of the coil will be 18 kW and thus the total power consumption of the whole magnet will be approximately 144 kW at maximum field. The voltage drop across two coils connected in series will be 215 V.

The water-cooled radiator consists of a 10 mm thick plate including three milled grooves where stainless steel tubes are incorporated (Ø 6 mm inner diameter, Ø 8 mm outer diameter). Each tube is connected independently to the water conduit but in parallel to the other tubes.
The weight of one coil section is approximately 1.4 tons, thus in total each coil weighs about 5.6 tons.

2.4.2.1.2 Superferric dipole magnets

The main design parameters of the superferric dipole magnets for the Super-FRS are:

- DC operation,
- warm iron and warm bore (including warm vacuum chamber),
- large pole gap (170 mm),
- moderate maximum field (1.6 T).

This leads to the design of a superferric magnet with warm iron (minimum cold mass, option → reduced cool down time) and potted (or vacuum-impregnated) low-current coils, wound with monolithic wire. Dipoles of this type are installed in the A1900 Fragment-Separator at MSU.

The dipole magnets in the Main-Separator of the Super-FRS have a bending radius of 12.5 m and a maximum flux density of 1.6 T. Each dipole stage is build by 3 dipoles units having a deflection angle of 11° (Pre-Separator) and 9.75° (Main-Separator), respectively, which results in an effective path length of about 2.39 m (Pre-Separator) and 2.13 m (Main-Separator). We investigated several options for the iron design such as a C-shaped magnet, a D-shaped magnet, and a straight (rectangular) magnet. Advantages and disadvantages are summarized in Table 2.4-9. Considering the short length of one magnet unit the straight version is by far the simplest to fabricate.

Table 2.4-9: Pros and cons of different magnet designs.

	C-shaped	D-shaped	Straight
Pro	'minimum iron' solution	no negative curvature winding	no negative curvature winding
Con	difficult and expensive winding process due to negative curvature coil	Variation of the lamination cross section along the magnet length	pole widened by sagitta : 'maximum iron' solution

The prototyping of a superferric dipole magnet is under way in collaboration with the Chinese FAIR Group of CAS.

Magnetic design

The 2D/3D magnetic design for the dipole units was performed using the code Opera-2D/3D [17].

Figure 2.4-24 shows the cross section of the lamination. Air slots are introduced to guarantee the required field quality over the whole range of operation from 0.1 to 1.6 T (see Figure 2.4-25). Solid iron end blocks could be used to make the entrance and exit edge angles. The coil consists of 1080 turns of a NbTi/Cu monolith conductor (Cu/SC ratios ≈ 9) with a conductor size of (1.1 x 2.2) mm^2.

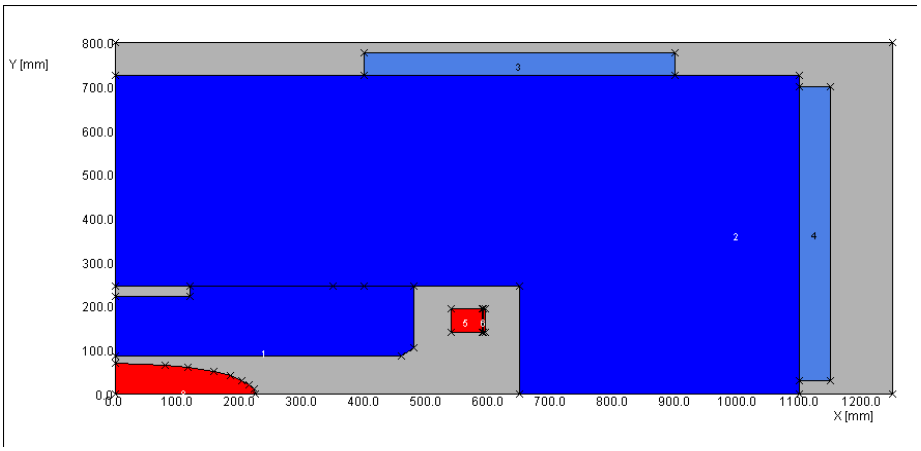

Figure 2.4-24: Cross section (1/4 part) of a superferric dipole magnet.

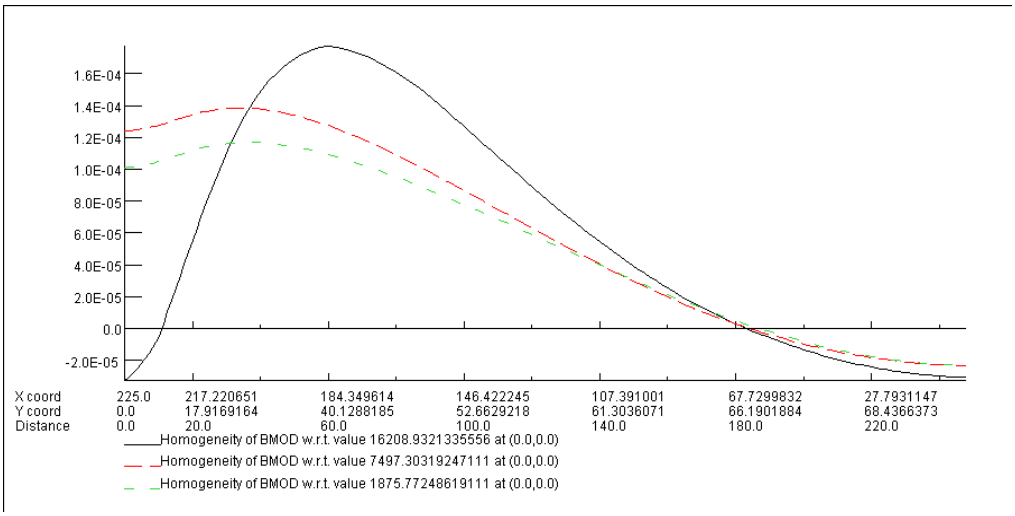

Figure 2.4-25: Flux density distribution along the border of the good field area (2D calculation) for the magnet shown in Figure 2.4-24.

The influence of the coil positioning as well as the tolerance of the pole gap was investigated. To achieve the required field homogeneity it turns out that the coil position must be better than ± 1 mm and the tolerance on punching the laminations must be less than ± 0.08 mm for the pole gap.

Punching die and punching sheets

The punching sheet width is 2200 mm, the height is 725 mm and the thickness is 0.5 mm resulting in a weight of 5.65 kg per lamination. The accuracy demand is less than ± 80 µm which requires a big punching die, whose assembly is shown in Figure 2.4-26. The tolerances of the punching sheets are measured by means of a laser tracker (accuracy of the instrument is better than 0.02 mm). With a second generation of punching die an accuracy of less than ± 0.06 mm for the magnet pole and less than ± 0.04 mm for the yoke base was achieved.

Figure 2.4-26: The different steps of the punching die assembling.

End-Block fabrication

The end-blocks of the dipole will be made of laminations which will be stacked, glued, hardened in an oven, and finally cut to the desired entrance and exit edge angles. To fabricate them efficiently a 'stair stacking' and cutting technology is applied (see Figure 2.4-27). This will be time efficient in respect of series production and the cut-off material will stay in limit (approximately 0.7 tons for each edge).

Figure 2.4-27: Fabrication of magnet end-blocks by 'stair-stacking' and cutting.

The assembling of a half-yoke of the dipole will be done using a 300 tons oil pressure stacking machine (Figure 2.4-28), where the two end blocks and the laminations will be stamped and welded. This machine needs steel casting to produce its base table, the fixing plates, and the moving plates. Finally Figure 2.4-29 shows the assembly of two half-yokes.

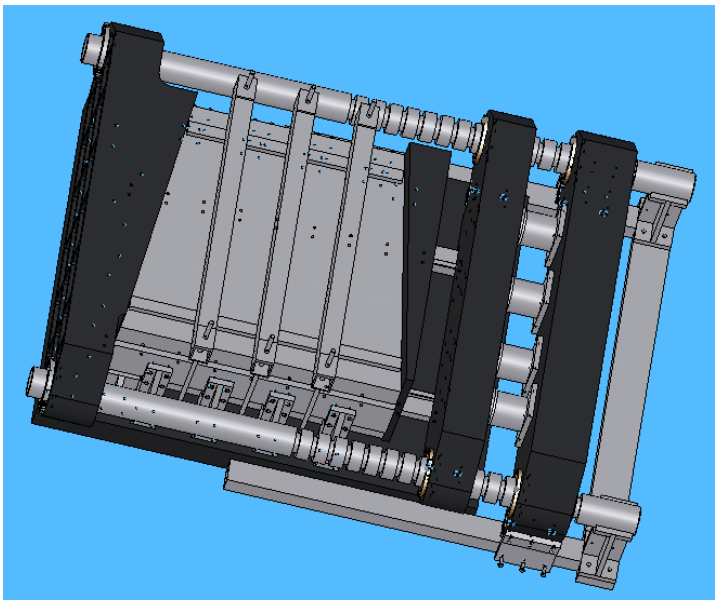

Figure 2.4-28: A 300 ton oil pressure machine for stamping and welding one half-yoke of the dipole.

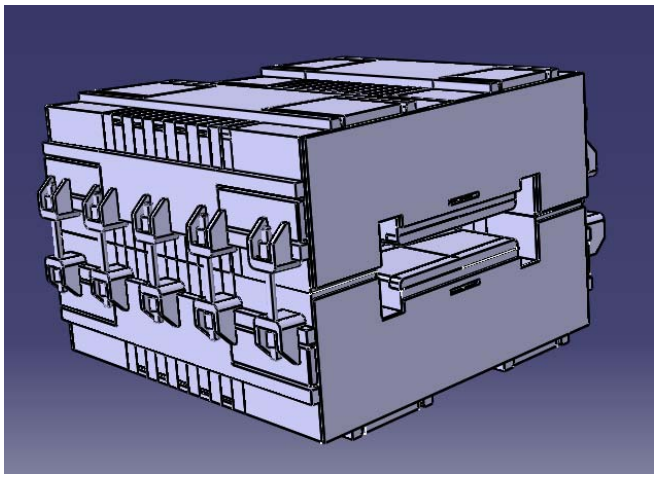

Figure 2.4-29: Assembly of two half-yokes.

Magnetic field measurement

Magnetic field measurements will be made by a Hall probe and a search coil. Driving machines for the search coil will be used which have similar function as those for the long-coil measurement of the HICAT dipoles at GSI. The maximum range in radial direction will be 600 mm and the arc length will be about 4100 mm, see Figure 2.4-30.

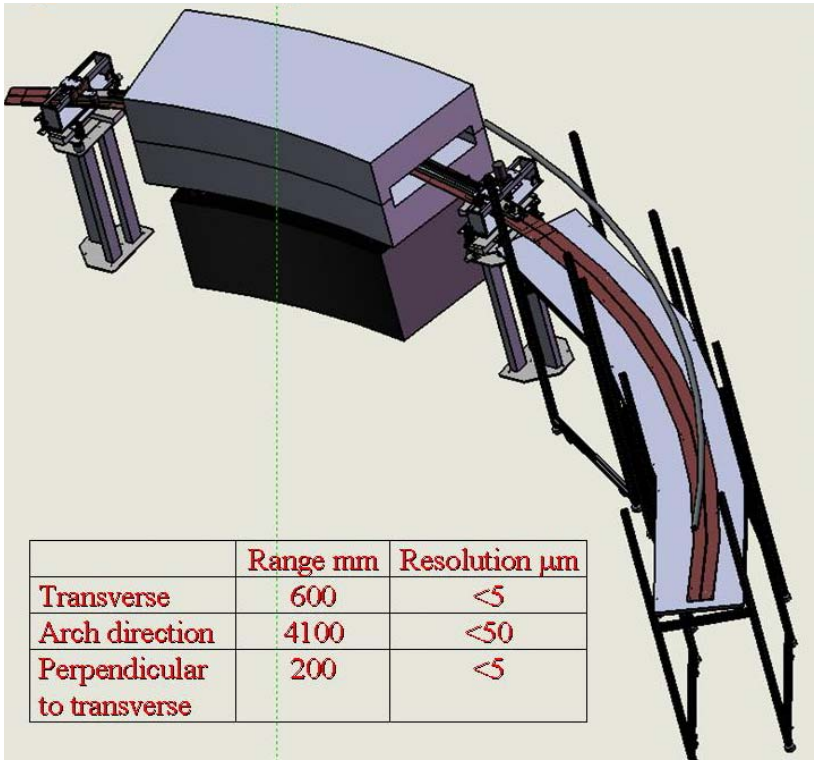

Figure 2.4-30: The long-coil driving machine for magnetic field measurements (mapping).

Engineering design of the dipole coils

Based on the requirements of the Super-FRS the superconducting coil is operated at a constant magnetic field and the maximum magnetic field in the dipole magnet is about 1.62 T. The engineering design for the dipole coil system is covered by a selection of the superconducting conductor, the structure, the fabrication technology and the quench protection.

The shape of the coil is a trapezoidal-shaped configuration with NbTi monolithic conductor of high Cu/SC ratio. The cryostat provides the necessary vacuum and cryogenic environment for operation of the Super-FRS dipole coils. The coil is surrounded by liquid helium in a coil case, and a thermal radiation shield is designed and set in the cryostat. The dipole coil with case and thermal shield are suspended by the supports.

A) Conductor

The main parameters of the conductor and the coil for the dipole magnet are listed in Table 2.4-10. Figure 2.4-31 shows the cross section of the conductor which is manufactured by Oxford company.

Table 2.4-10: Parameters for the SC coil of the dipole magnet.

		Dimension
Superconducting Strands	NbTi	
Dimension of Conductor	1.17 × 1.93	mm
Dimension of Conductor include insulation	1.43 × 2.24	mm
Filament diameter	50-105	μm
Number of the filaments in core wire	55	
Twist pitch on filaments	13	mm
Diameter of the core wire	0.0247/0.63	Inch/mm
Ratio of Cu and no Cu in core wire	1.3	
Ratio of Cu and no Cu in conductor	14	
Operating temperature T_{op}	4.2	K
n-values	84 ± 9	
RRR of Cu in strand	107 ± 11	
Thickness of the original insulation	~ 0.31 × 0.26	mm
Critical current I_{c1}	560	@4.2 K & 4 T
Critical current I_{c2}	774	@4.2 K & 2 T
Critical current I_{c3} (Calculated)	813	@4.2 K & 1.6 T
Operating current I_{op}	246	A
Density of the conductor (I_{op}/(1.17× 1.93))	109	A/mm^2
Operating fraction i=I_{op}/I_{c3}	0.3	
Critical temperature T_{cs}	7	K
Temperature margin T_{cs} - T_{op}	2.8	K

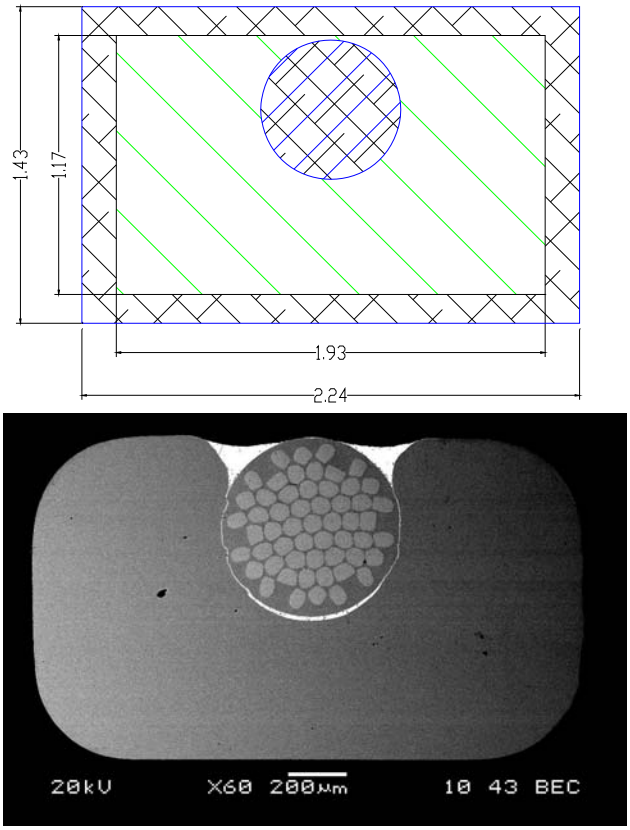

Figure 2.4-31: Cross section of the conductor of the SC coil for the Super-FRS dipole magnet (from Oxford company).

B) Coil winding

The upper and lower coils are connected as a pair. The cross section of the coil winding is shown in Figure 2.4-32. Its dimension is (52.14 × 48.8) mm^2, and it has in total 560 turns in 28 layers and 20 pancakes. The thickness of the turn-insulation is 0.26 ~ 0.31 mm, the layer insulation is 0.3 mm and the grounding insulation is 2 mm. The coil is designed using the vacuum pressure impregnate (VPI) with epoxy-resin to fix the insulation of the winding for two reasons, firstly for insulation between turns and secondly for ground insulation. The insulation after VPI holds more than 3000 Volts. The filling factor of the metal after VPI is about 49.6 %, (without grounding insulation, it would be 58.6 %).

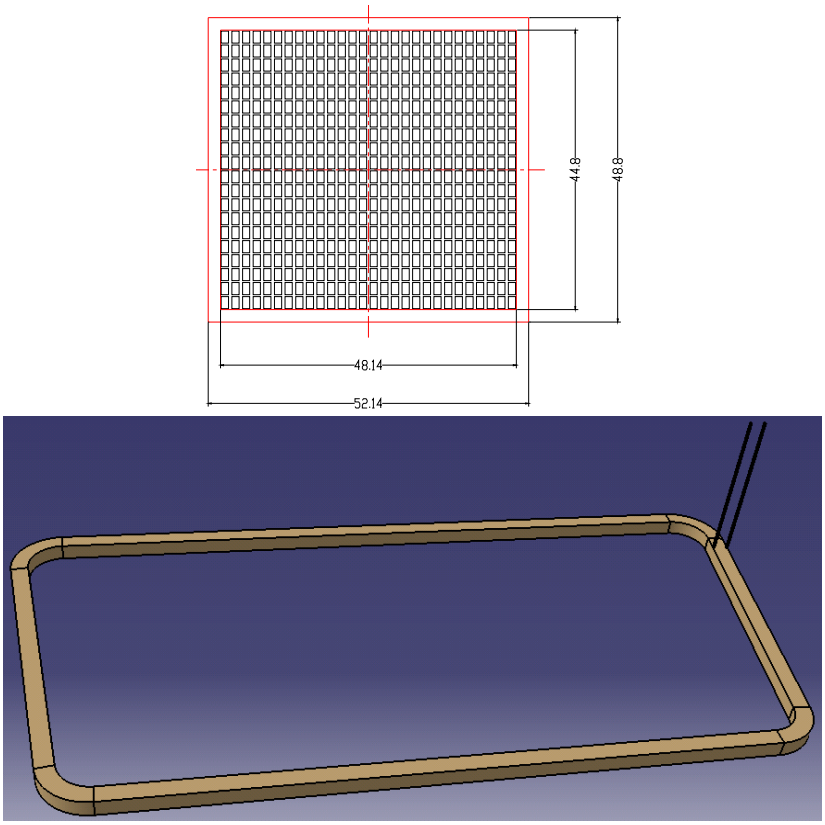

Figure 2.4-32: Cross section of the coil (upper panel) and coil top view after vacuum impregnation (lower panel)

C) Coil casing, thermal shield and cryostat

The coil casing is designed considering two main functions: one is to protect the windings against magnetic forces during operation, and the other is the use of the casing as a container for liquid helium (LHe) to cool the winding. The volume of the LHe in the casing is about 20 litres, including the LHe stored in the current leads box. In total 14 supports are fixed on the casing. The casing is made of stainless steel 316LN. Table 2.4-11 shows its mechanical properties. Its relative magnetic permeability is about 1.01 ~ 1.02. The thickness of the casing is 10 mm.

Table 2.4-11: Mechanical properties of stainless steel 316LN.

Temperature	Tensile strength	Yield strength	Elongation
	σ_b (MPa)	$\sigma_{0.2}$(MPa)	δ_5 (%)
300 K	≥650	≥350	≥35
4 K	≥1500	≥1000	≥35

To reduce the heat flux to the helium system, the outer surface of the casing will be wrapped with a multi-layer insulation. Figure 2.4-33 shows the cross section and the top view of the coil casing.

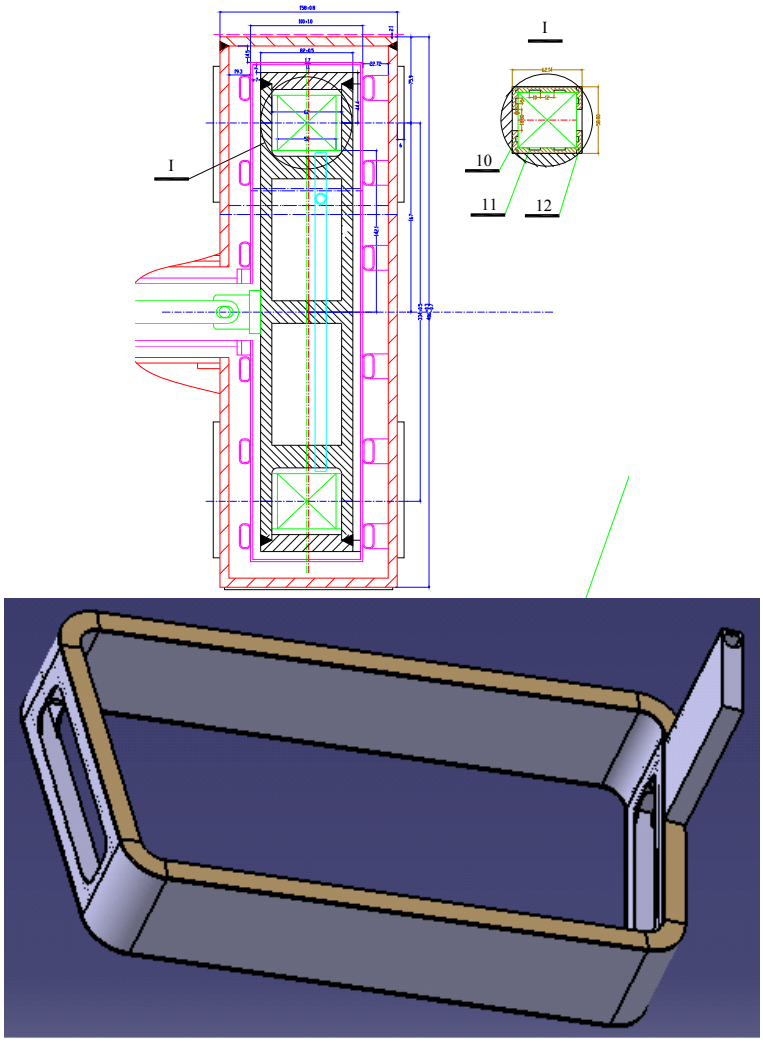

Figure 2.4-33: Cross-section (upper panel) and top view (lower panel) of the coil casing.

The thermal shield should have a good thermal conductivity, a good rigidity to weight ratio, and should be easy to fabricate and to assemble. The main part of the thermal shield consists of seven pieces: inner shield in two pieces, outer shield in two pieces, upper shield, bottom shield and a piece for the current leads box. All pieces are made of copper plates with 2 mm thickness. The forced-flow cryogen for cooling the thermal shield is cold helium gas to intercept thermal radiation from cryostat. The cooling pipes are made of 1 mm thick copper having a rectangular shape with an outer dimension of (20×8) mm^2. To reduce the heat flux to the helium system, the outer surface of the thermal shield will be wrapped with an insulation of ten layers. Figure 2.4-34 shows a sketch of the thermal shield.

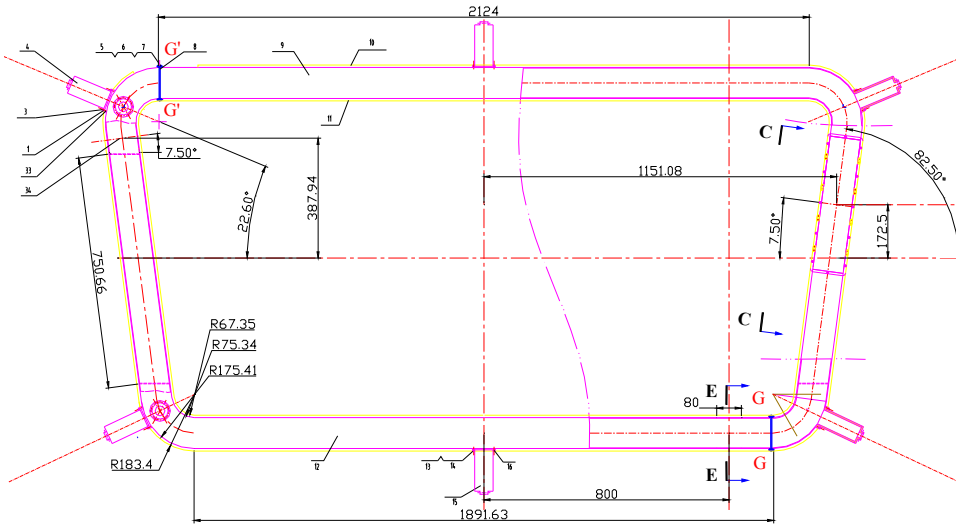

Figure 2.4-34: Sketch of the thermal shield.

The cryostat has a trapezoidal shape (see Figure 2.4-35, left panel). It provides all connections between the coil casing and the outside parts including cryogenic supply and current leads. The cryostat is a welded structure made by 316L or 304L stainless steel. It is equipped with two ports allowing the control and adjustment of the coil position during the assembly. In additions there are holes on the thermal shield as port to control the coil casing. The total weight of the cryostat including the coils is about 1730 kg. The interior volume of the cryostat for pumping is 256 litres.

D) Support and current lead box

Long rods support the thermal shield and the coil casing. They are based on the cryostat and are able to adjust the position of the coils if necessary (even at operating temperature). The rods are made of G10. The heat load to the 80 K thermal shield is about 0.3 W for each support, and to the 4.2 K LHe is about 0.1 W. Figure 2.4-35 (right panel) shows the structure of the support part. A bellows is integrated in the support to compensate the length change during the coil cool down. The loads to be supported are the self weight of the coil and the mass of the thermal shielding. The coil is suspended by twelve supports connected to the cryostat. These are placed at the outer arc section of the yoke and at the middle of the straight line to compress the coil against distortion under electromagnetic forces.

A current lead box will provide the interface to the local cryogenic line and the connection to the power line. When the magnet is powered, the low temperature heat-load for the LHe is about 0.3692 W including the joule heat produced by the resistance of the lower joint. The liquid helium consumption of one current lead is about 1.68×10^{-2} g/s**.** When no current passes through the current lead, the low temperature heat-load for the LHe is about 30-40 % of the above value, thus about 0.11-0.15 W, and the LHe consumption of one current lead is about 5×10^{-3} g/s to 6.7×10^{-3} g/s.

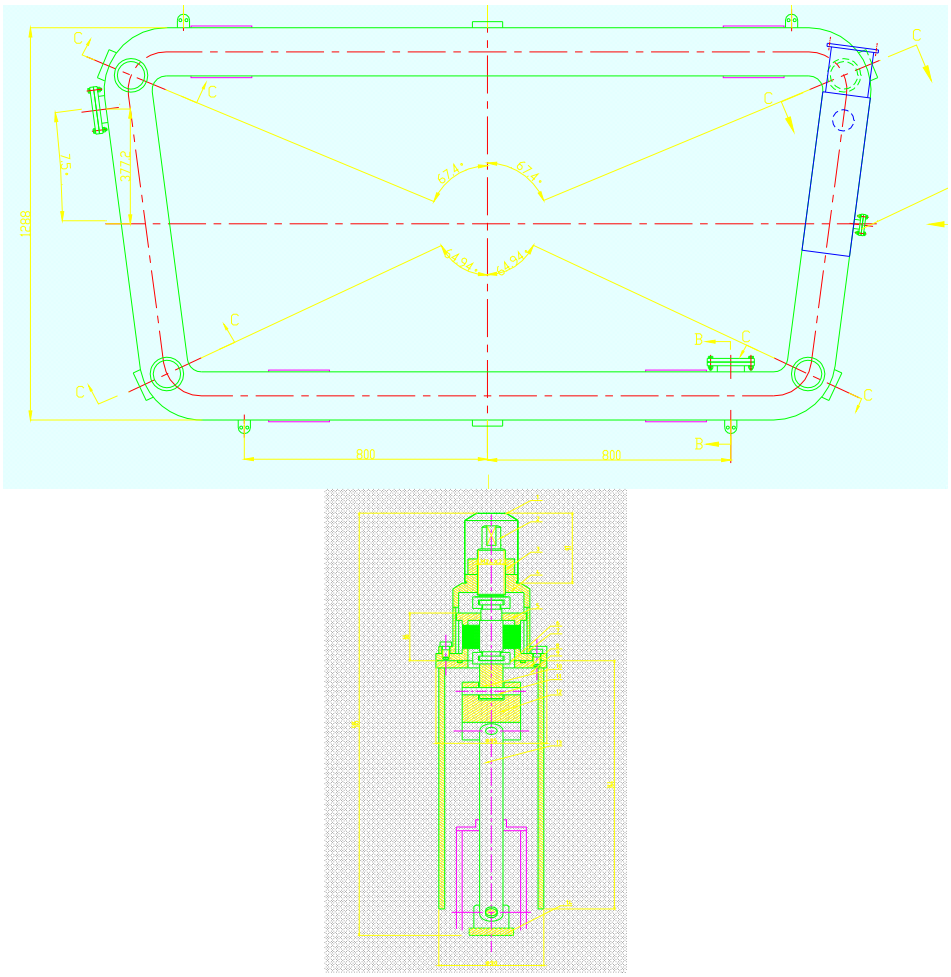

Figure 2.4-35: Upper panel: Cryostat, observation ports and supports. Lower panel: Support structure.

2.4.2.1.3 Superferric Dipole Magnets for the Energy Buncher

2D-Magnetic design

The dipoles for the Magnetic Spectrometer and Energy Buncher at the exit of the Low-Energy Branch are also superferric magnets having warm iron but SC coils. To guarantee the required resolving power of the facilities the magnets must have rather large magnetic volumes. The specifications of the dipole magnet are listed in Table 2.4-8 and its cross section is shown in Figure 2.4-36.

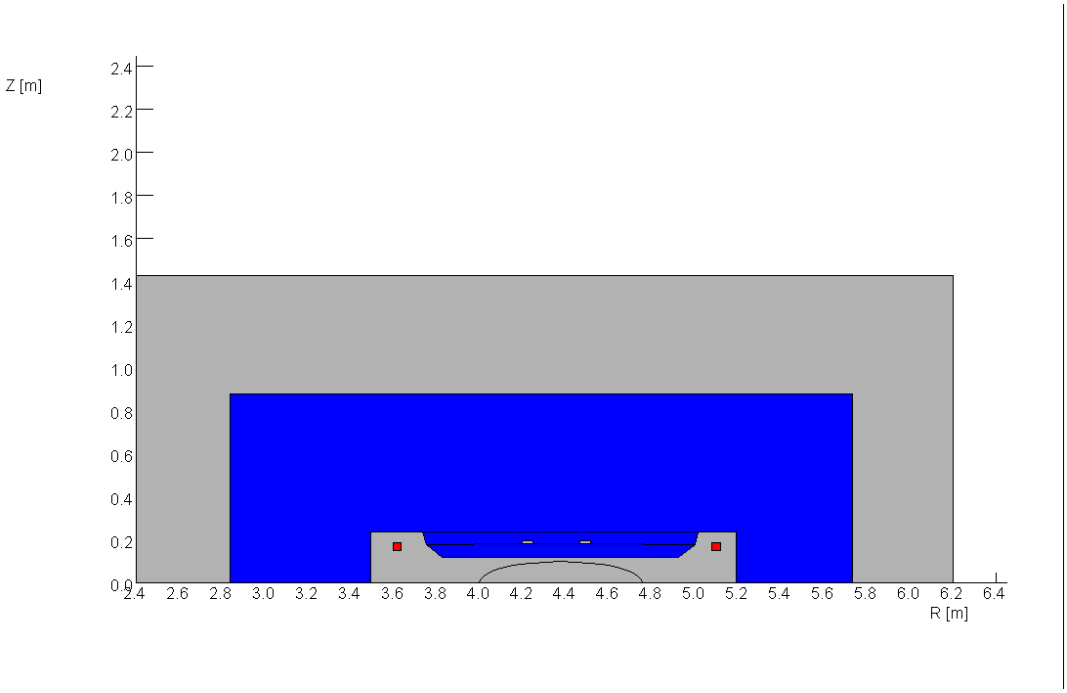

Figure 2.4-36: Cross section of one Energy Buncher dipole unit.

To fulfill the required field quality over the whole range of operation from 0.15 to 1.6 T air slots were introduced in the pole shoes. Their coordinates are given by the corners points as listed in Table 2.4-12. The air slots are not symmetrical with respect to the magnet center which corresponds to x = 4.375 m.

Table 2.4-12: Coordinates of the air slots corners.

air slot left side		air slot right side	
x [m]	y [m]	x [m]	y [m]
4.195	0.185	4.465	0.185
4.195	0.195	4.465	0.195
4.245	0.195	4.515	0.195

The coils have a dimension of 40 mm × 40 mm and their positions are given by the coil center coordinates, which are:

left side coil: $x_l = 3.615$ m, $y_l = 0.17$ m
right side coil: $x_r = 5.100$ m, $y_r = 0.17$ m

The maximum current density in the coil is 104 A/mm^2.

Figure 2.4-37 illustrates the field properties of the magnet for different B-values. Especially for low B-field values (but also for very high B-field values) the design doesn't yet fulfill the specifications. This results from the required very wide good field area and the limitation on the total width of the magnet. In principle the field quality may be improved by:

- introducing a gap between the yoke and the pole;
- arranging correcting surface coils on the pole.

These options should be analyzed additionally.

The maximum field in the coil area is 1.9 T. The load line for the magnet is shown in Figure 2.4-38 and Table 2.4-13.

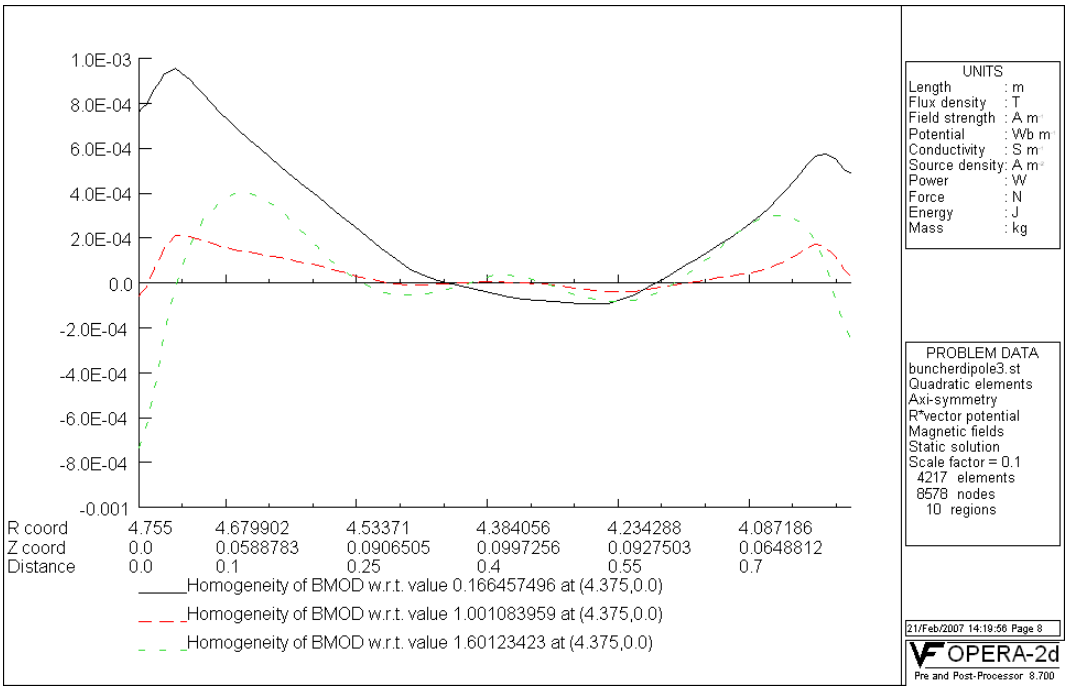

Figure 2.4-37: Field distributions in the cross section of the Energy Buncher dipole magnet.

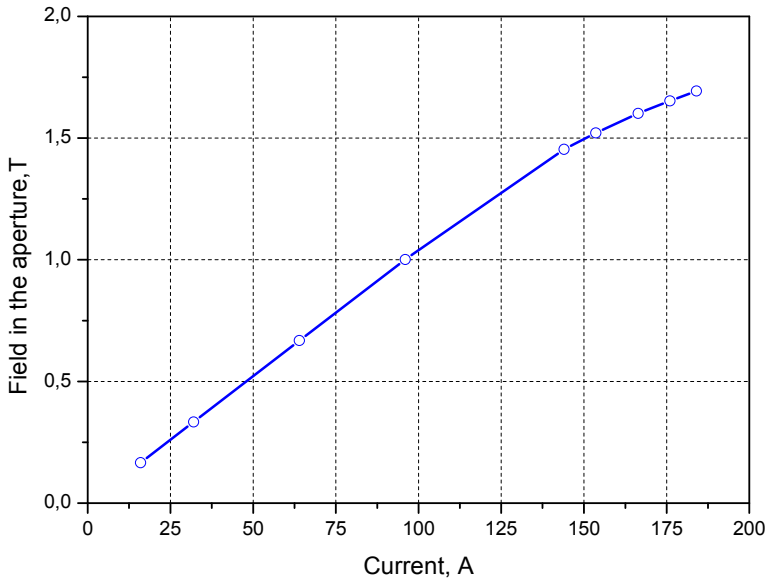

Figure 2.4-38: Load line for the Energy Buncher dipole magnet.

Table 2.4-13: Load line for the Energy Buncher dipole magnet (half coil)

I_{tot} / [kA]	B / [T]
16	0,166
32	0,334
64	0,668
96	1,001
144	1,454
153,6	1,521
166,4	1,601
176	1,653
184	1,693

3D-model of the Energy Buncher dipole

Preliminary investigations of the integral field properties of the Energy Buncher dipole were performed. A corresponding 3D model is shown in Figure 2.4-39.

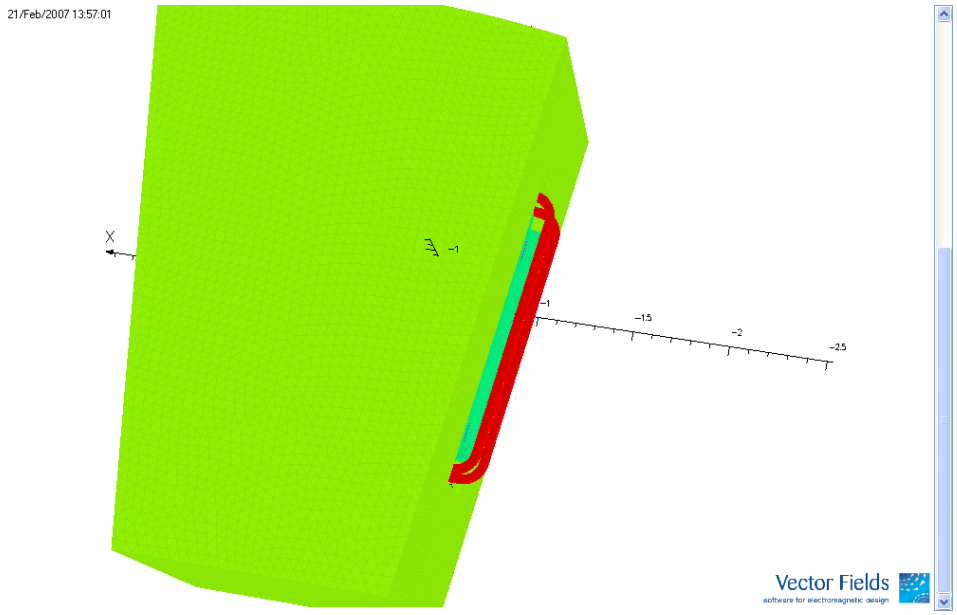

Figure 2.4-39: The 3D model of the Energy Buncher dipole.

An evaluation of the field integrals in the good field area at an intermediate field level of B = 0.9 T shows, that the distribution differs only slightly from the same distribution obtained by the 2D model. Therefore it should be easily possible to correct for it if necessary by shaping the pole end.

The possible influence of a field clamp at the entrance/exit of the magnet (Figure 2.4-40) was investigated. The calculations indicate that the field clamp changes noticeably the field integrals. These results are preliminary and a choice of an appropriate distance and profile of the clamp may change the final distributions significantly (Figure 2.4-41).

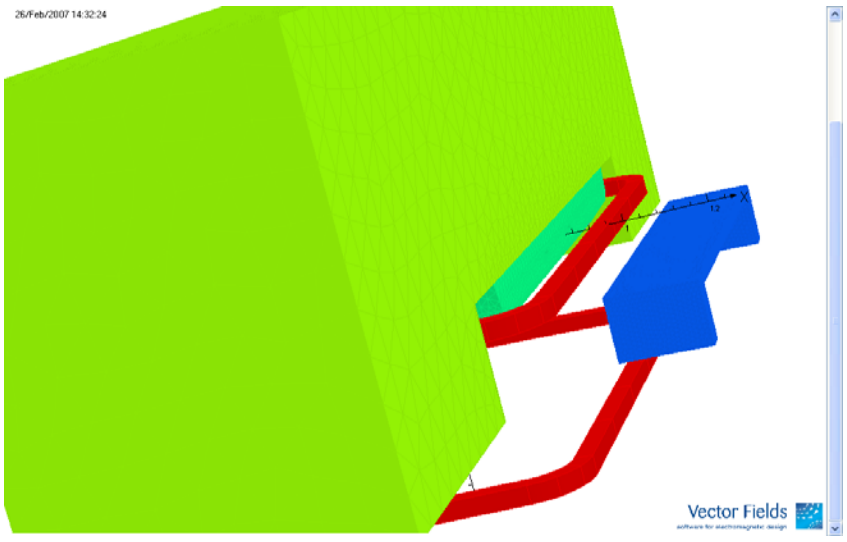

Figure 2.4-40: The 3D model of the Energy Buncher dipole with a field clamp.

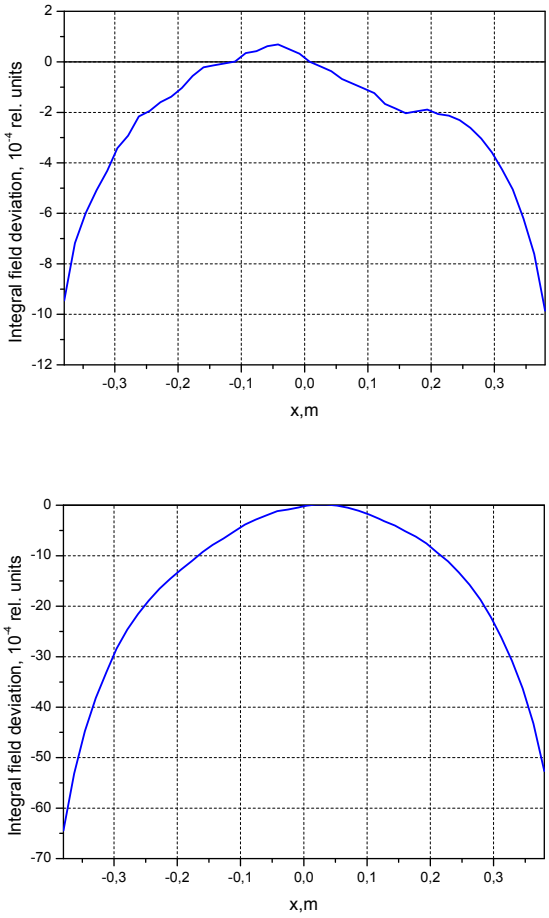

Figure 2.4-41: Field integral distribution along the central line for B = 0.9 T without (left side) and with field clamps.

2.4.2.2 Quadrupole Magnets

Table 2.4-14 lists the specifications of the quadrupole magnets used in the Super-FRS. The table is subdivided into the radiation resistant quadrupole magnets needed for the 1st dipole stage of the Pre-Separator and the superferric quadrupole magnets for the 2nd dipole stage of the Pre-Separator, the Main-Separator, and the Energy-Buncher. Although all magnets will be operated in a DC mode the iron design has to be considered to be built by laminations since the Bρ setting of the Super-FRS has to be changed frequently according to the experimental requirements.

Table 2.4-14: Design parameters for the quadrupole magnets of the Super-FRS

Location of the magnet	Dim.	Pre-Separator, 1st stage		Pre- & Main-Separator		Energy-Buncher			
Number of magnets		2	1	36	21	4	1	3	3
Design		radiation resistant		superferric					
Max. gradient	T/m	15.0	6.1	10.0		8.0	8.0	4.7	5.2
Average operating gradient	T/m	10.5	4.3	7.0		5.0	5.0	1.7	3.5
Min. gradient	T/m	1.5	0.6	1.0		0.8	0.8	0.05	0.1
Effective length L	mm	1.000	1.200	0.800	1.200	0.800	1.200	0.800	1.200
Useable horizontal aperture	mm	±90	±190	±190		±190	±190	±300	
Useable vertical aperture	mm	±90	±120	±120		±120	±120	±200	±250
Gradient field quality[a)]		$\pm 8 \cdot 10^{-4}$	$\pm 8 \cdot 10^{-4}$	$\pm 8 \cdot 10^{-4}$		$\pm 8 \cdot 10^{-4}$		$\pm 8 \cdot 10^{-4}$	
Pole radius	mm	100	210	250		250		350	
Embedded octupole component G''	T/m^3	-		105	-	105	-	-	-
Overall length	m	1.4	1.6	1.2	1.6	1.2	1.6	1.2	1.6
Overall width (w/o cryostat)	m	1.2	1.5	2.44		2.44		TBD	
Overall height (w/o cryostat)	m	1.2	1.5	3.5		3.5		TBD	
Overall weight (w/o cryostat)	kg	11200	TBD	11000	16500	11000	16500	TBD	
Current (at max gradient)	A	2500	2500	292		235		≈ 300	
Inductance	mH	35.0	70	25360	38040	25360	38040	TBD	
Resistance	mΩ	36.7	75	0					
ramp rate		DC Magnets (Δt_{rise} = 120 sec)							

[a)] Detailed requirements of integrated field quality Δg/g (at a circular radius R=190mm, with g=|B(R)|/R) depending on the field gradient are:

$\Delta g/g \leq \pm 8 \cdot 10^{-4}$ at g_{Min} (i.e. g = 1 T/m in case of Pre-/Main-Separator quadrupoles)
$\Delta g/g \leq \pm 5 \cdot 10^{-4}$ at g_{AO} (i.e. g = 6.5 T/m in case of Pre-/Main-Separator quadrupoles)
$\Delta g/g \leq \pm 60 \cdot 10^{-4}$ at g_{Max} (i.e. g = 10 T/m in case of Pre-/Main-Separator quadrupoles)

2.4.2.2.1 Radiation resistant quadrupole magnets

Like the radiation resistant dipole magnets also the radiation resistant quadrupole magnets are designed as normal conducting magnets using Metal oxide Insulation Cables (MIC). Two different types of radiation resistant quadrupoles are necessary for the Pre-Separator. The first one has a pole tip radius of 100 mm providing a useful aperture of ± 90 mm. The second one has a pole tip radius of 210 mm providing a useful aperture of ± 190 mm. Other important design parameters for the quadrupoles can be found in Table 2.4-14 and section 2.4.2.8, respectively.

Both quadrupole magnets must provide very high pole tip field considering beams with a rigidity of up to 20 Tm. Saturation effects of the yoke become of high importance, which could be partly compensated by introducing air slots in the pole. These slots could be rather easily implemented from mechanical point of view, since we intend to use laminated iron. These slots imitate the saturation of the pole's central part at high flux density levels and homogenize the field distribution in the aperture. Also the use of special magnetic material like Armco etc. is considered in order to overcome saturation effects.

The present design considers a coil which is powered by a MIC cable assuming 2500A. Figure 2.4-42 and Figure 2.4-43 show the present layout of both quadrupole types.

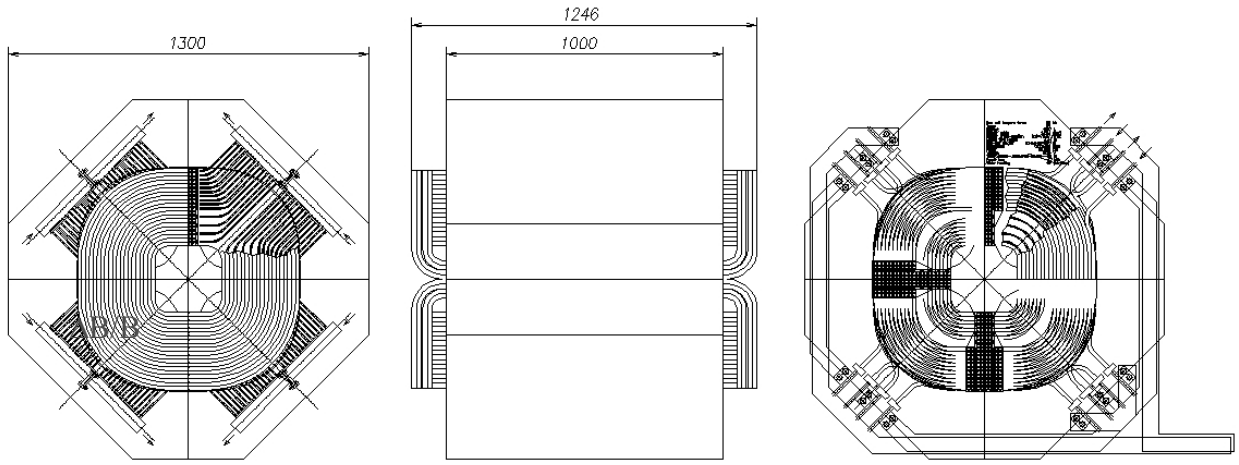

Figure 2.4-42: Front, side, and back view of a normal conducting radiation resistant quadrupole having a pole tip radius of 100 mm for the 1st stage of the Pre-Separator. The dimensions are given in mm.

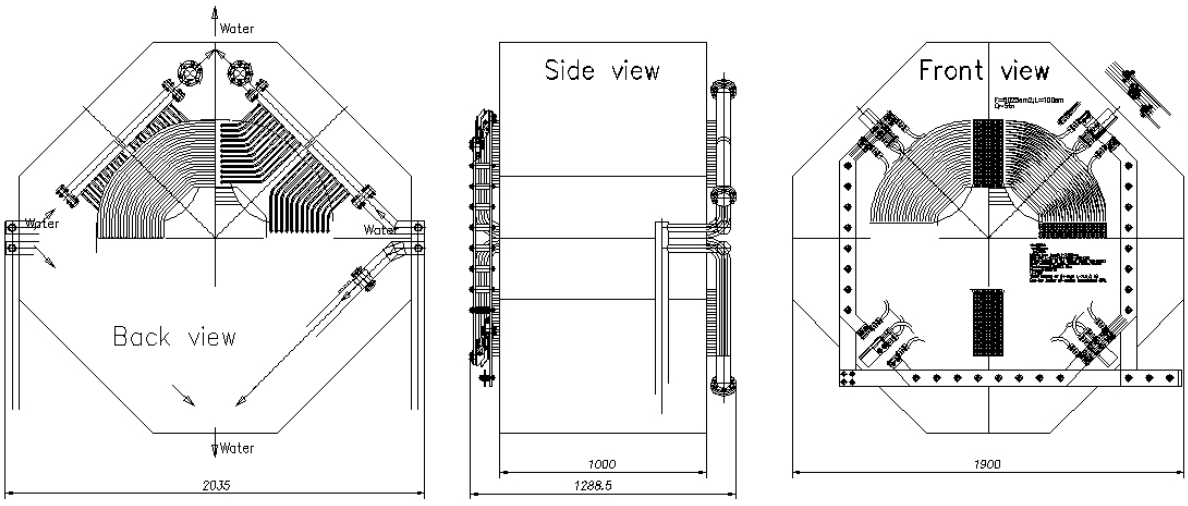

Figure 2.4-43: Front, side, and back view of a normal conducting, radiation resistant quadrupole having a pole tip radius of 210 mm for the 1st stage of the Pre-Separator. The dimensions are given in mm.

2.4.2.2.2 Superferric quadrupole magnets

Each dipole stage of the Super-FRS is equipped with a quadrupole triplet in front and behind the dipole magnet. The standard quadrupole triplet consists of 3 cold-iron, superferric quadrupole magnets with the same warm aperture radius of ± 190 mm. They have lengths of 800 mm, 1200 mm, and 800 mm and provide a maximum field gradient of 10.0 T/m. The distance between two quadrupoles is 1000 mm. Octupole correction coils are embedded in the 800 mm long quadrupole magnets to allow corrections of image aberration. The three quadrupole magnets will be assembled in one common cryostat together with up to three 500 mm long superferric hexapole magnets and 500 mm long superferric steering dipoles. One example for such a multiplet consisting of three quadrupoles and two hexapoles is schematically illustrated in Figure 2.4-44. All magnets in the cryostat are cooled with liquid helium in a common helium bath. The same principle is used for the A1900 quadrupole triplet [18] and the quadrupole triplet for the BigRIPS [19].

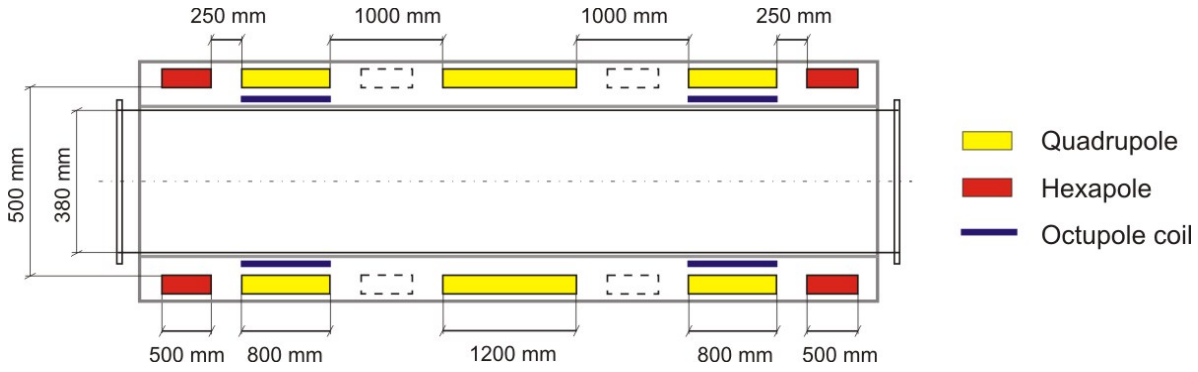

Figure 2.4-44: Schematic view of a Super-FRS multiplet structure consisting of a quadrupole triplet with octupole correction coils and two hexapole magnets. All magnets are located in a common cryostat. Hexapole magnets can also be inserted between two quadrupoles (indicated with dashed lines).

The magnets will be operated in DC mode but it must be guaranteed that all magnets in a multiplet can be ramped up from g_{min} to g_{max} and ramped down from g_{max} to g_{min} three times consecutively, i.e. within 12 minutes and without quench. This is necessary in order to guarantee a frequent changing of the magnet setting due to experimental requirements. The

maximum current of one magnet must not exceed 300 ampere. All magnets are individually powered. The breakdown voltage, V_{bd}, against ground of all magnets, sensors and connections must be:

$$V_{bd} > 2 \cdot V_{qm} + V_{sm}$$

where V_{qm} is the maximum quench voltage to ground and V_{sm} = 500 V is a safety margin.

Magnetic design

The 2D/3D magnetic design for the quadrupoles was performed using the code Opera-2D/3D [17]. Figure 2.4-45 shows the cross section of a standard quadrupole magnet for the Super-FRS. The pole tip radius of 250 mm was chosen in order to provide sufficient space for the beam pipe (190 mm inner diameter + 10 mm expected wall thickness), for the cryostat (expected thickness of 30 mm), and for the octupole correction coils (about 5-15 mm), which are needed to correct the ion-optical 3rd-order image aberrations. For simplicity of winding the main coil is designed as a race track coil with a cross section of (55 × 50) mm^2.

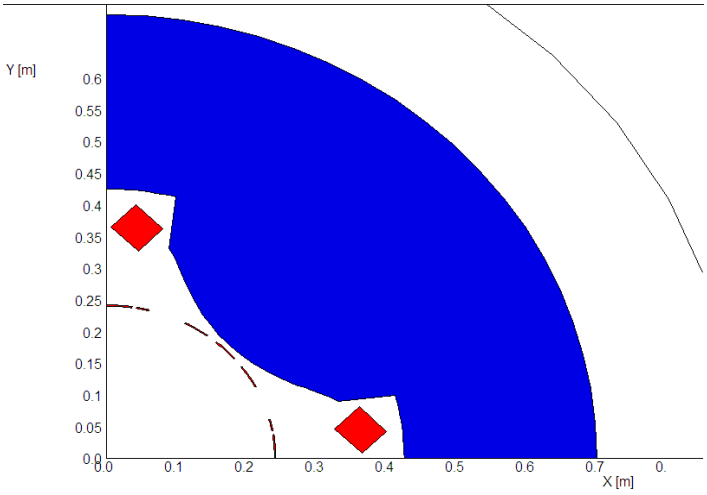

Figure 2.4-45: Cross section (1/4 part) of the standard superferric quadrupole magnet for the Super-FRS including octupole correction coils (dashed circle).

Figure 2.4-46 shows the dependencies of the average field gradient along the elliptical aperture for a quadrupole magnet. It presents the field quality distributions for the medium/high field gradients of 5.6, 7.7 and 8.7 T/m. The field gradient deviation is still inside the requirements of $\pm 8 \cdot 10^{-4}$ relative units. For the highest field gradients of 10 T/m, however, the 6th harmonics increases exponentially such that field quality distribution reduces to few ‰ (see Figure 2.4-47). These errors could only be corrected by additional 12-pole correction coils also embedded into the quadrupole like the octupole correction coils. The present layout of the quadrupole magnet still leaves enough space to include these correction coils if necessary which would allow to reduce the field gradient deviation to $\approx \pm 4 \cdot 10^{-4}$ even for the highest gradient of 10 T/m.

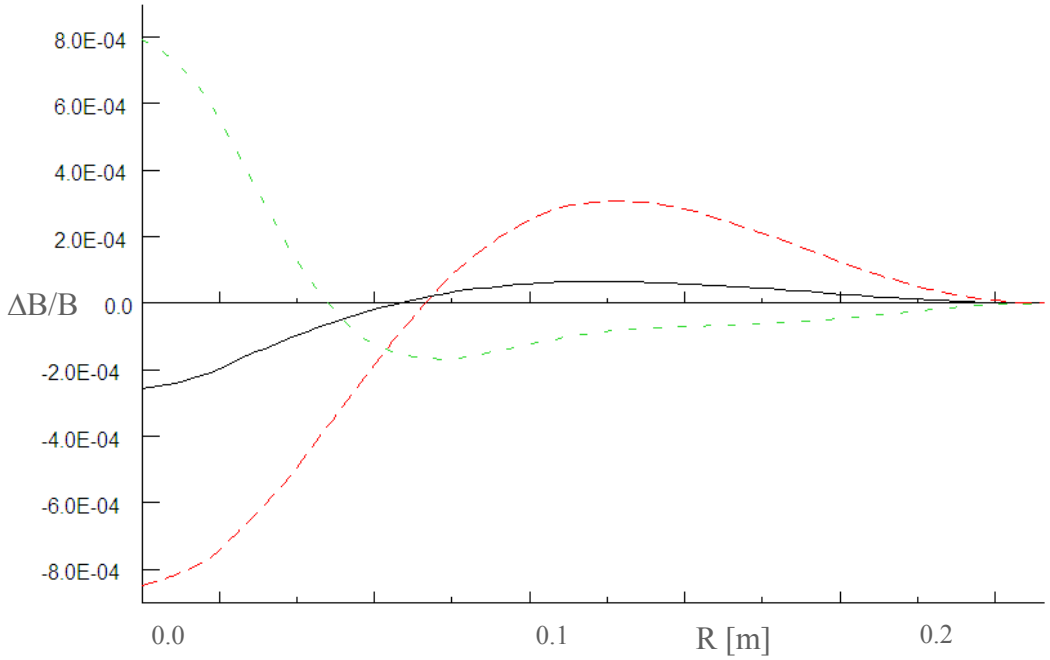

Figure 2.4-46: Average field gradient distribution along the border of an elliptical aperture of ± 0.19 m × ±0.10 m (colour code: black full line indicates gradient g = 5.6 T/m, red dashed line g = 7.7 T/m, green dashed line g = 8.7 T/m).

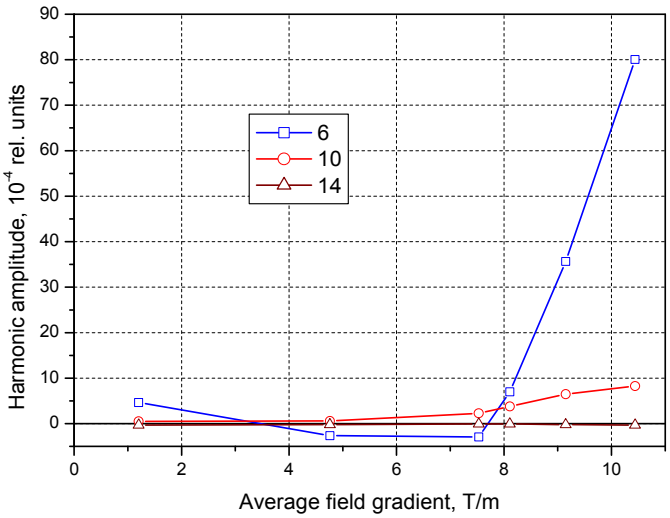

Figure 2.4-47: Field harmonics along a circle of 190 mm radius in the quadrupole magnets.

Figure 2.4-48 shows a 3D view of the quadrupole magnet and the main coils. 3D calculations indicate that the effective length of the magnet is approximately 76 mm longer than the iron yoke length for a 800 mm long magnet and 72 mm longer for a 1200 mm long magnet. To correct the field integral distribution end chamfers were added using the geometry shown in Figure 2.4-49.

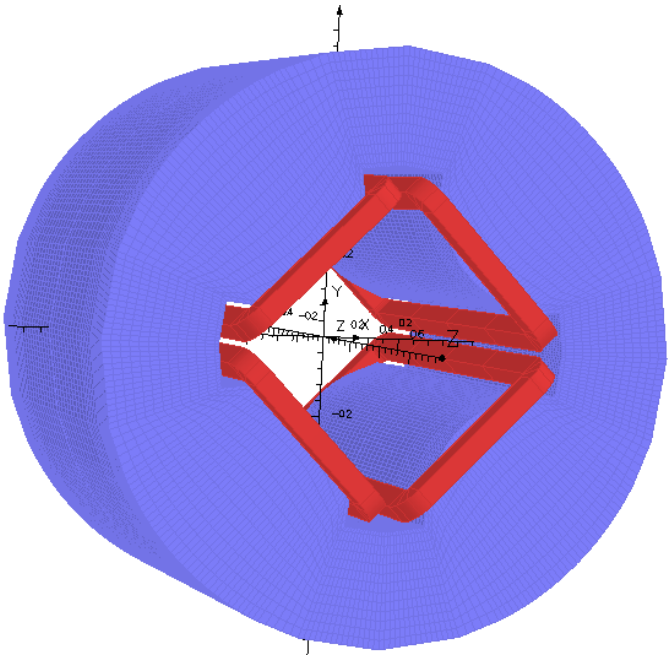

Figure 2.4-48: 3D view of the superferric quadrupole magnet with main coils and a yoke diameter of 1.4 m.

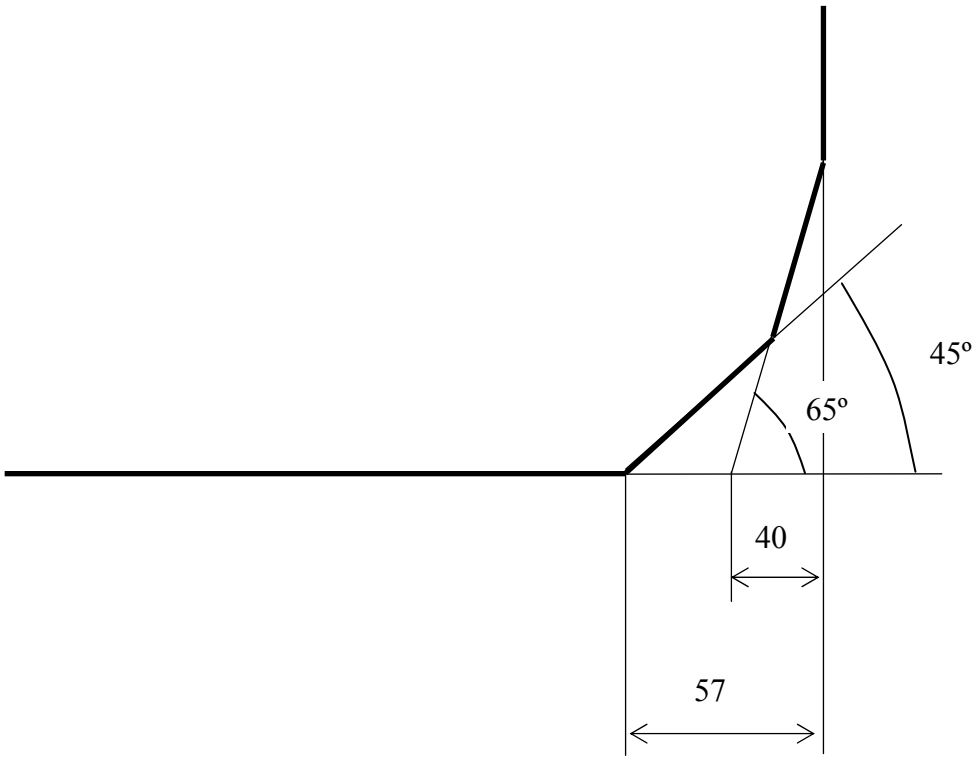

Figure 2.4-49: Geometry of the end chamfer for the Super-FRS quadrupoles**.**

The properties of the Super-FRS quadrupoles were also calculated for a 3D model including special construction details like round holes and grooves. Such a model for a quadrupole is shown in Figure 2.4-50. The calculations indicate that these additional construction elements do not influence the field distributions in the aperture noticeably. For all calculations the B-H curve as shown in Figure 2.4-51 was used.

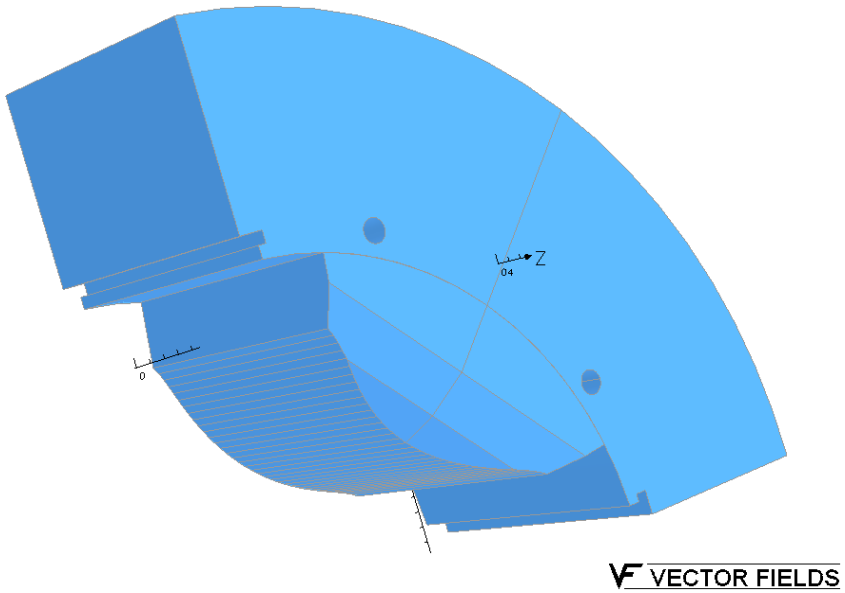

Figure 2.4-50: 3D model of the Super-FRS quadrupole magnet including holes and grooves. Indicated are also the end chamfers.

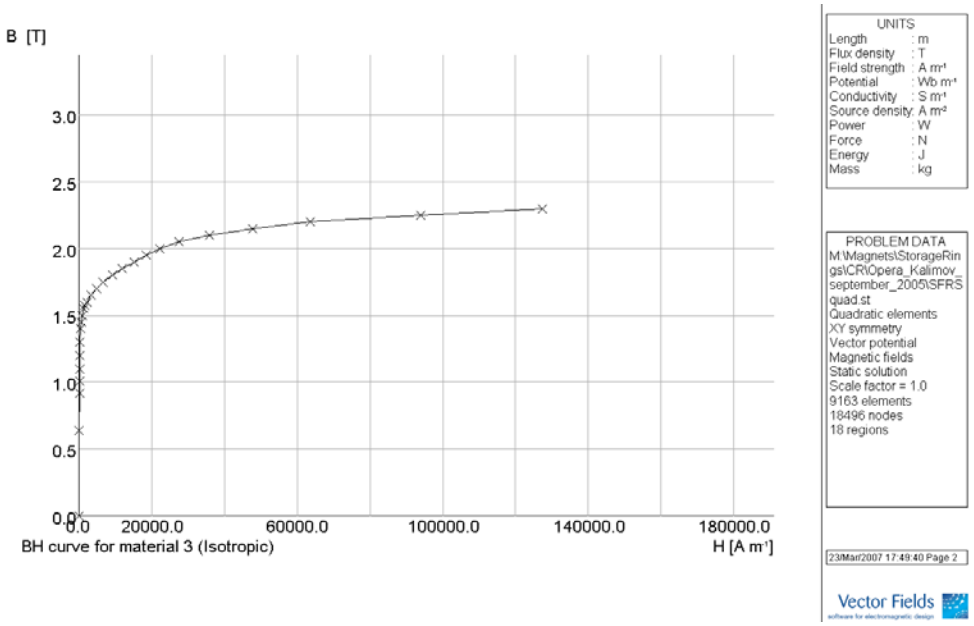

Figure 2.4-51: BH-curve used in the 2D and 3D magnetic field calculations. The option 'laminated' is used in all 3D models.

2.4.2.2.3 Superferric quadrupole magnets for the Energy Buncher

2D-Magnetic design

The quadrupole magnets for the Magnetic Spectrometer and Energy Buncher at the exit of the Low-Energy Branch are superferric magnets having cold iron. The specifications of the quadrupoles are listed in Table 2.4-14 and its cross section is shown in Figure 2.4-52.

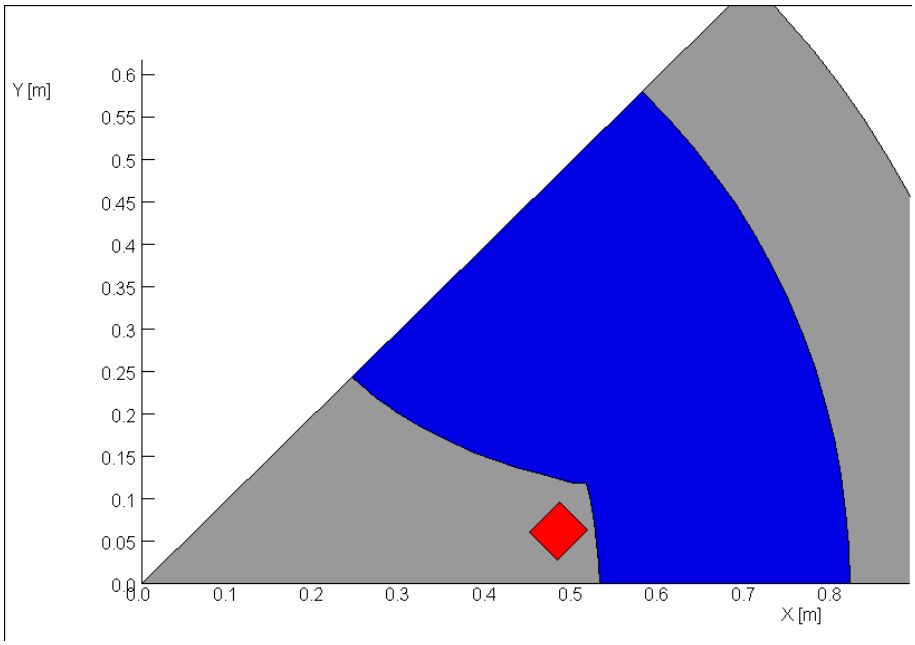

Figure 2.4-52: Cross section of the Energy Buncher quadrupole.

The cross section of the coil is 45 mm × 50 mm. Its position is given by its centre coordinates, which is: x_0 = 0.4826 m and y_0=0.061872 m. The maximum current density in the coil is 110 A/mm^2 which yields a maximum field in the yoke of 1.98 T and a maximum pole-tip field of 1.75 T.

Field properties:

Generally the field deviation inside the circle with a radius of 300 mm is less than $3 \cdot 10^{-4}$ relative units in the whole operation range from 0 ÷ 5 T/m. The corresponding field distributions along a circle with a radius of 300 mm are shown in Figure 2.4-53.

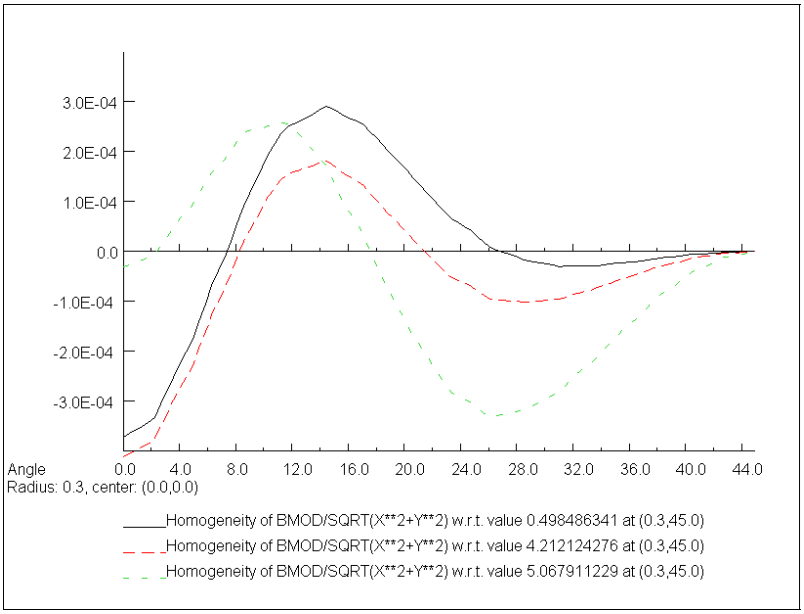

Figure 2.4-53: The distribution of the relative field gradient of an Energy Buncher quadrupole along a circle with a radius of 300 mm.

Figure 2.4-54 and Table 2.4-15 illustrate the dependence of the main field harmonics at the circle along a radius of 300 mm.

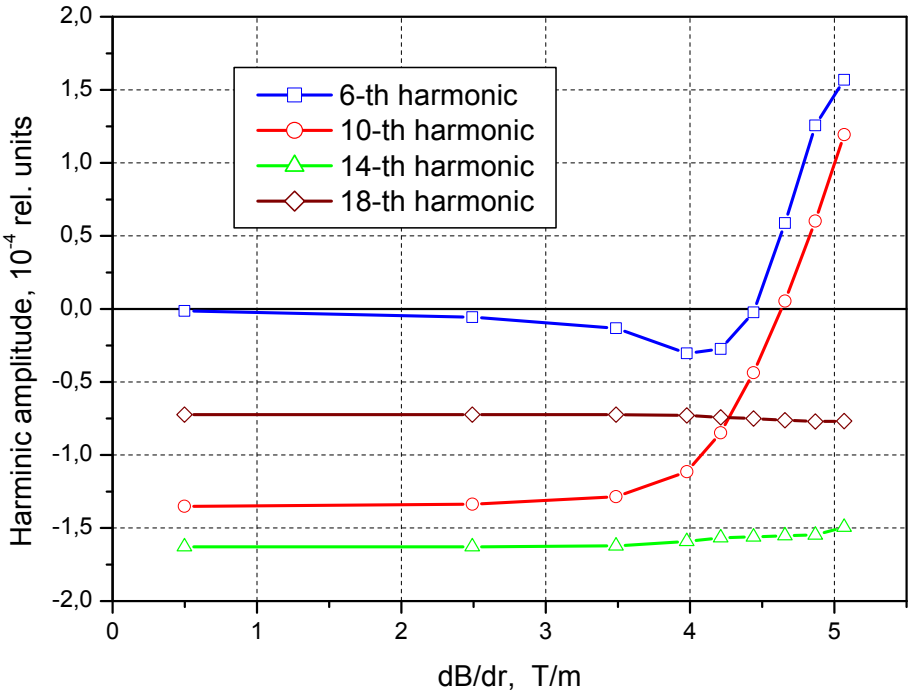

Figure 2.4-54: Amplitudes of the higher harmonics for different field gradients. The harmonics are calculated along a circular with a radius of 300 mm.

Table 2.4-15: Amplitudes of the higher harmonics for different field gradients (in 10-4 relative units). Harmonics are calculated along a circular with a radius of 300 mm.

dB/dR / [T/m]	6^{th}-harmonics	10^{th}-harmonics	14^{th}-harmonics	18^{th}-harmonics	22^{th}-harmonics
0,498	-0,0137	-1,3508	-1,6290	-0,7237	-0,1835
2,492	-0,0563	-1,3371	-1,6286	-0,7232	-0,1833
3,487	-0,1323	-1,2852	-1,6235	-0,7241	-0,1836
3,977	-0,3049	-1,1151	-1,5922	-0,7294	-0,1851
4,212	-0,2743	-0,8472	-1,5667	-0,7422	-0,1852
4,439	-0,0239	-0,4368	-1,5608	-0,7506	-0,1854
4,657	0,5876	0,0539	-1,5525	-0,7621	-0,1884
4,867	1,2559	0,6019	-1,5484	-0,7701	-0,1883
5,068	1,5695	1,1936	-1,4946	-0,7686	-0,1961

2.4.2.3 Multipoles

Table 2.4-16 lists the specification of the higher order magnets used in the Super-FRS. The table is subdivided into hexapole magnets (radiation resistant as well as superferric) and into the octupole correction coils, which are embedded into the 0.800 m long superferric quadrupole magnets. Although all magnets will be operated in a DC mode the iron design has to be considered to be build by laminations since the Bρ setting of the Super-FRS has to be changed frequently according to the experimental requirements.

Table 2.4-16: Design parameters for the higher order multipole magnets of the Super-FRS.

Location of the magnet	Dim.	Pre-Separator, 1st stage	Pre- & Main-Separator		Energy-Buncher	
Number of magnets		2	39	36	3	4
Type		Hexapole magnet	Hexapole magnet	Octupole correction coil	Hexapole magnet	Octupole correction coil
Design		resistive, rad. resistant	superferric	superferric		
Max. hexapole component	T/m^2	34	40	-	15	-
Max. octupole component	T/m^3	-	-	105	-	105
Effective length L	m	0.600	0.500	0.800	0.800	0.800
Useable horizontal aperture:	mm	±190	±190	±190	±300	±190
Useable vertical aperture:	mm	±100	±120	±120	±200	±120
Pole radius:	mm	±200	±235	±235	TBD	±235
Overall length	m	0.95	0.7	(embedded)	TBD	(embedded)
Overall width	m	Ø 0.8	2.03		TBD	
Overall height			3.5		TBD	
Overall weight	kg	1800	1200	(embedded)	TBD	(embedded)
Max. Current	A	600	171	TBD	TBD	TBD
Inductance	mH	15	1776	TBD	TBD	TBD
Resistance	mΩ	7.2	0	0	0	0
Ramp rate		DC Magnets (Δt_{rise} = 120 sec)				

2.4.2.3.1 Radiation resistant hexapole magnets

It is foreseen be built the radiation resistant hexapole magnets as normal conducting magnets using MIC cables, like it will be done for the radiation resistant dipole and quadrupole magnets. Two of such hexapole magnets are necessary, one before the first dipole unit and one behind the third dipole unit, close to the first focal plane PF1. The hexapole magnets have a pole tip radius of 200 mm (useful aperture is 190 mm) achieving a hexapole component of 34 T/m^2.

Design of the sextupole magnet

Figure 2.4-55 shows a 3D view of the radiation resistant hexapole. The iron yoke is divided into 6 parts, fixed together with bolts and dowels. Each part of the iron yoke consists of separate lamellae with radiation-resistant insulation on their surfaces. The lamellae are welded together over the external surface of the hexapole magnet and special studs and hooks additionally tighten them together in the pole area. Thus the magnetic field in the hexapole magnet does not pass through close circuits in the iron yoke.

The diameter of the circle inscribed between the magnet poles should be observed with accuracy better than ±100μ. The distances between neighboring poles should be observed with accuracy better than ±50μ.

It is planned to equip the hexapole magnet with two water feeding and discharge collectors, allowing separate supply of water to each current coil cooling pipe (see Figure 2.4-56). The coils are connected in current so that when assembling or dismantling two halves of the hexapole magnet it will be enough to assemble or dismantle one connection of the copper bus (see Figure 2.4-55). That significantly simplifies assembling and dismantling the lens on the accelerator.

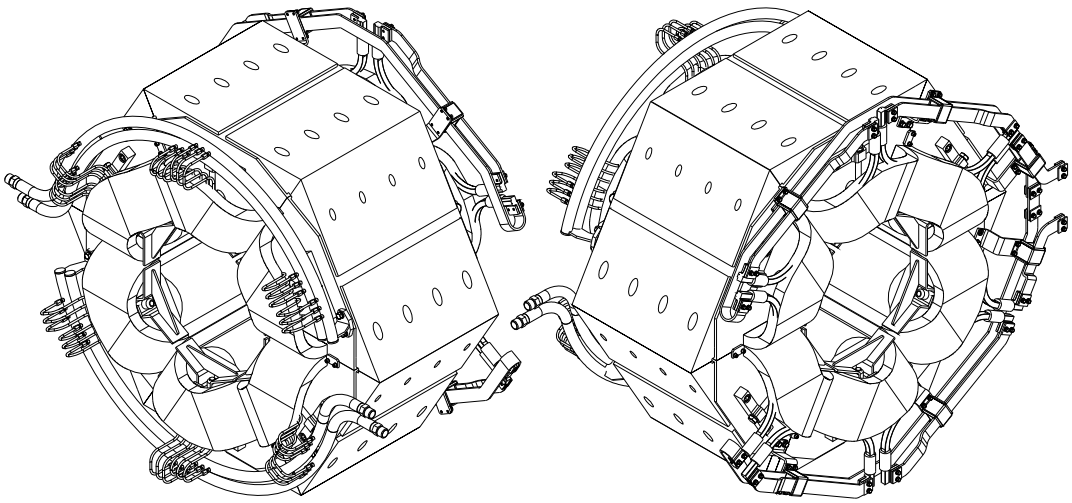

Figure 2.4-55*:* 3D view of the radiation resistant hexapole magnet. Electric circuit (right side) and water cooling circuit (left side) are separated from each other.

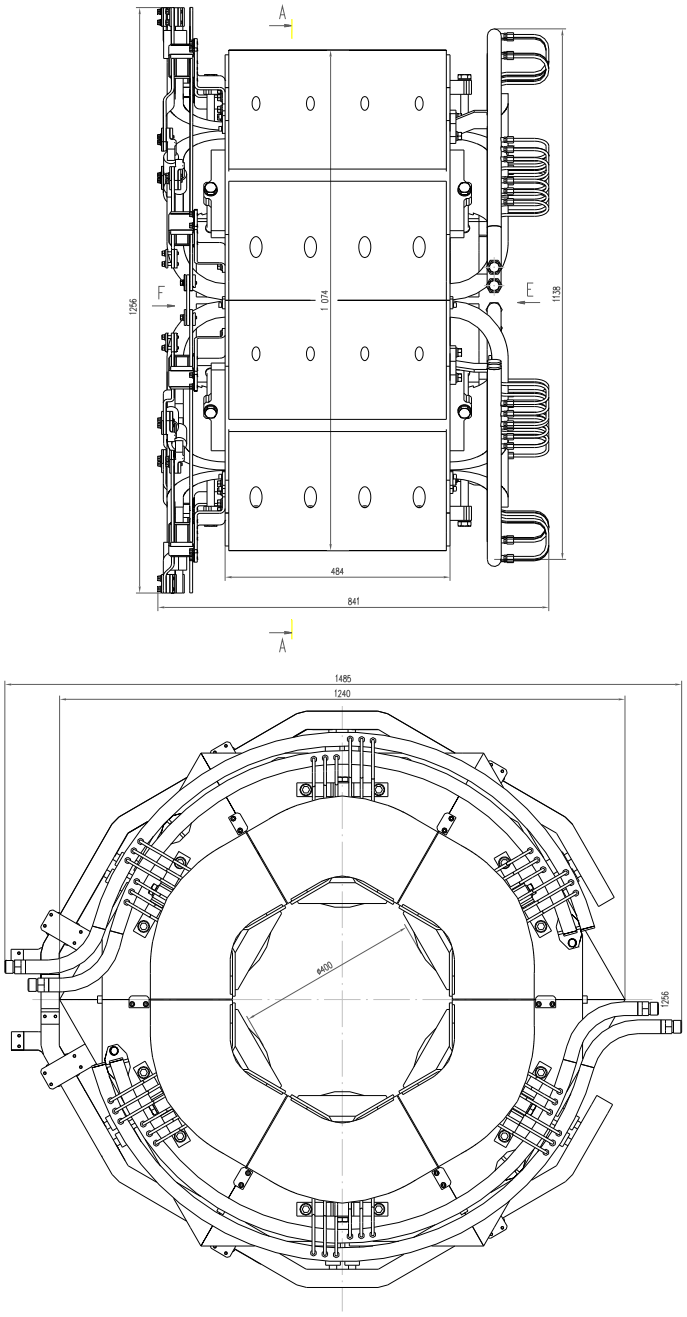

Figure 2.4-56*:* Side view and front view (showing the water connection) of the hexapole magnet.

Specification of the current coils

The hexapole magnet consists of 6 current coils. The current in the coil is $N \cdot I = 14.855A$; the number of copper wire turns is $N = 24$; thus the current in the wire is $I = 619A$. The maximal consumed electrical power of the sextupole magnet is 20 kW.

Each coil consists of a water-cooled radiator and 1 segment of copper, radiation-resistant wire wound in 2 layers. The section of the current coil is covered by tin-lead solder in a special vacuum mould. The cross-section of the current coil is shown in Figure 2.4-57.

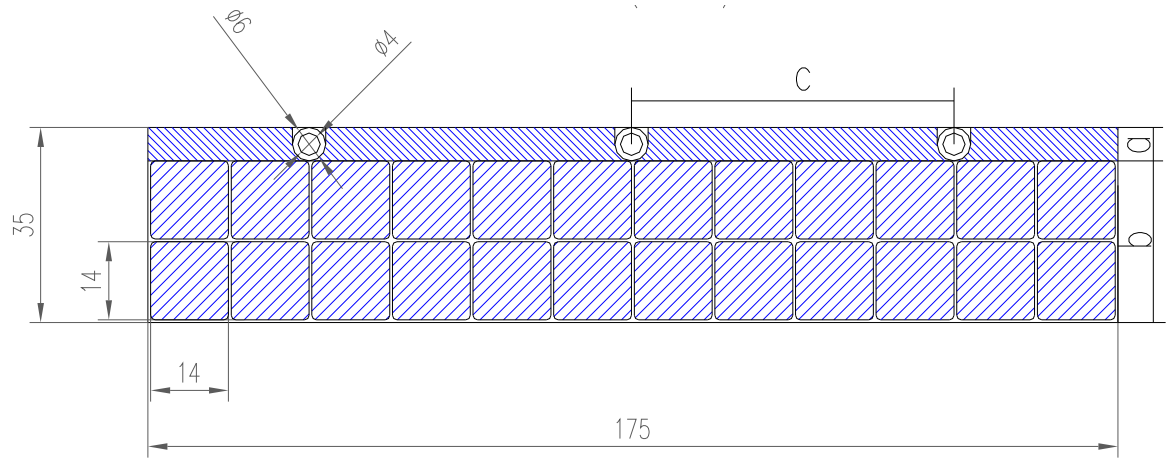

Figure 2.4-57*:* Cross-section of the radiation-resistant current coil.

The water-cooled radiator consists of a 8 mm thick copper plate with grooves comprising 3 Ø6mm stainless steel pipes with a Ø4mm inner hole. The pipes are independently connected with water supply.
The segment of the current coil consists of 24 turns of radiation-resistant wire with an average length of $l \approx 2.12$ m. The length of one segment wire is $L \approx 51$ m. In total, one magnet needs 306 m of the copper wire.
The radiation-resistant wire has a rectangular cross-section of 14mm×14mm. It consists of the central copper bus with the cross-section S=1.09 cm^2, the magnesium oxide layer 1 mm thick and copper envelope 0.5mm thick.

2.4.2.3.2 Superferric hexapole magnets

We decided to use standalone hexapole magnets in the Super-FRS for two reasons:

- the hexapole components which are required for 2^{nd}-order image aberration correction have a rather high field (at least for some hexapole magnets),
- the ion-optical coupling coefficients guide the positioning of correction elements.

Most of the required hexapole magnets will be technically realized as superferric magnets and they will be installed in a common cryostat together with the quadrupole magnets. Figure 2.4-58 shows the cross section of the magnet and Figure 2.4-59 shows the 3D model. Its pole tip radius is 235 mm and the yoke diameter is 800 mm. The coil has a cross section of (20 x 20) mm^2 and a maximum current density of 132 A/mm^2 is required. The calculated field quality in the aperture is found to be less than $\pm 1 \cdot 10^{-4}$, see Figure 2.4-60.

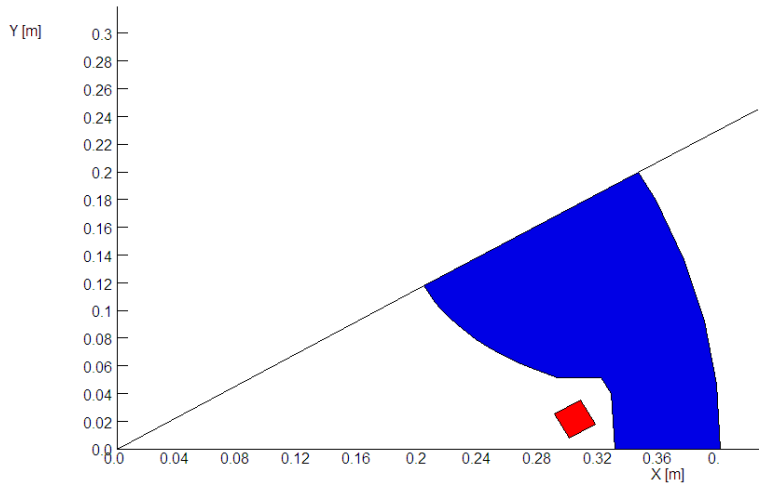

Figure 2.4-58*:* Cross section of the superferric hexapole magnet (1/6 part).

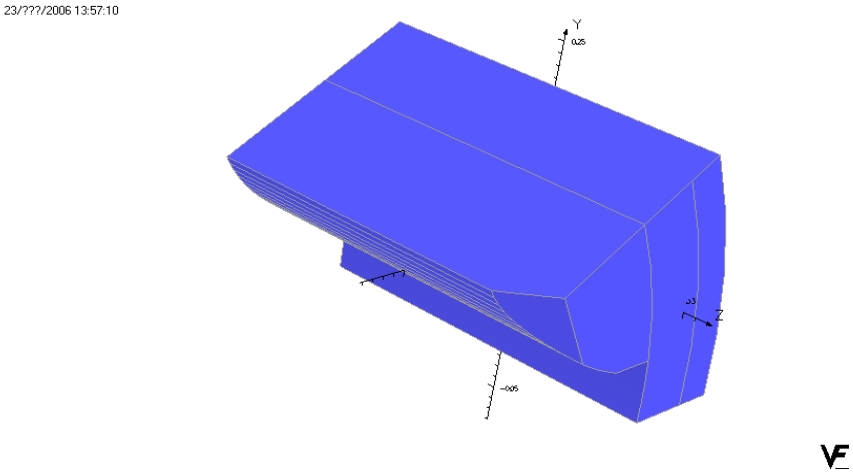

Figure 2.4-59*:* 3D model of the superferric hexapole magnet.

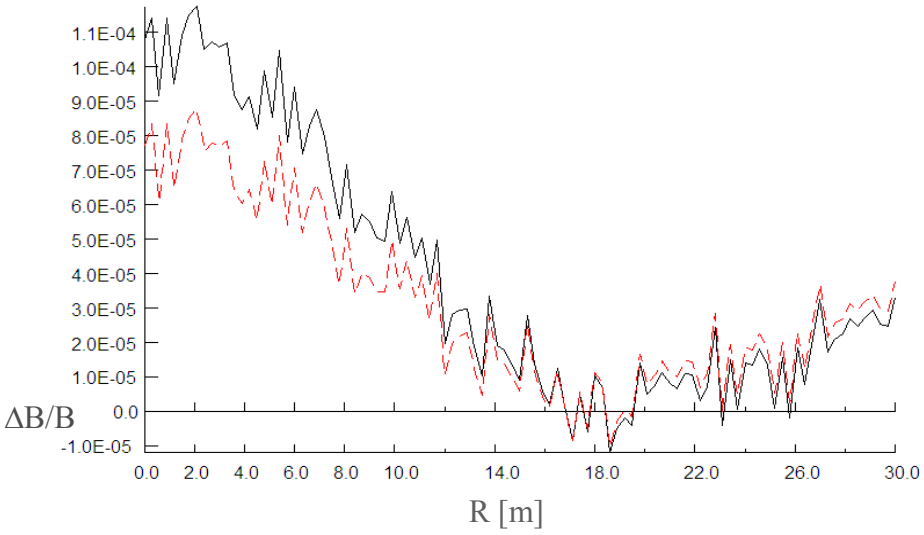

Figure 2.4-60*:* Flux density deviation in the hexapole magnet along a circle of 190 mm radius for a low (≈ 1 T/m^2) and a high (≈ 15 T/m^2) hexapole component.

2.4.2.3.3 Octupole correction coils

The Super-FRS requires rather small octupole components in order to correct for 3rd order image aberrations. Using superferric quadrupole magnets these correction elements can be advantageously built as simple surface coils (few mm thick) and embedded into the quadrupole magnet as already indicated in Figure 2.4-45. The creation of higher harmonics can be kept small by optimizing the current distribution in the surface coils. The parameters for a one-layer super conducting coil are summarized in Table 2.4-17. The maximum linear current density in the coil is 54 A/mm. In the performed calculations the octupole coil was described as a set of sector shape areas. The thickness of these sectors was chosen to be 2 mm, but it may be changed to another thickness depending on the available and necessary superconducting wire diameter. Figure 2.4-61 shows the 3D view of the complete coil.

Table 2.4-17*:* Coil parameters for the octupole correction coil (one quadrant).

Segment	Radius 1 [mm]	Radius 2 [mm]	Angle 1 [deg]	**Angle 2 [deg]**
1	240	242	0	**8.8**
2	240	242	10.3	**14.7**
3	240	242	27.9	**36.7**
4	240	242	40.6	**49.4**
5	240	242	53.3	**62.1**
6	240	242	75.3	**79.7**
7	**240**	**242**	**81.2**	**90**

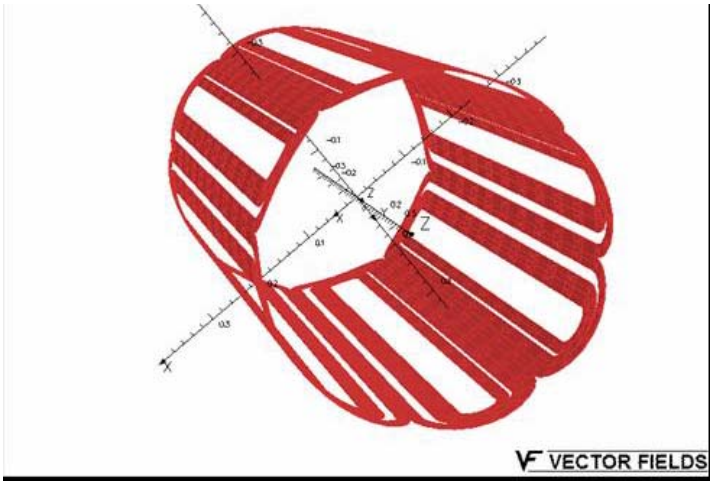

Figure 2.4-61*:* 3D view of the octupole correction coil to be embedded into the superferric quadrupole magnet.

2.4.2.4 Steerers

The total flight path of the Super-FRS is more than 170 m. Therefore, based on the experience on the present facility, one needs the possibility of position corrections in y-direction. Altogether we plan to install 6 pairs (position and angle correction) of y-steerers in the 3 branches of Super-FRS. The steerers can be rather short and will be implemented as superconducting dipole correction coils located between two successive quadrupole magnets.The main requirements to a short Super-FRS y-steerer are summarized in Table 2.4-18.

Table 2.4-18: Main requirements to a short Super-FRS y-steerer

	units	Value
Maximum field	T	0.2
Length	m	0.5
Useable horizontal aperture	m	±0.1
Useable vertical aperture	m	±0.2
Field quality	rel. units	TBD

A 2D design of a short superferric magnet was developed. A cross section of the magnet is shown in Figure 2.4-62. Coils are supposed to be arranged by surface winding. The parameters of the coil were optimized so that the first 11 higher harmonics (B_3, B_5, …B_{23}) at the circle of 0.2 m radius are very small. Only harmonics with the numbers $n \geq 25$ have relatively big amplitudes. A whole winding consists of 6 sectors, symmetrical in horizontal and vertical planes. The coil average radius is 235 mm.

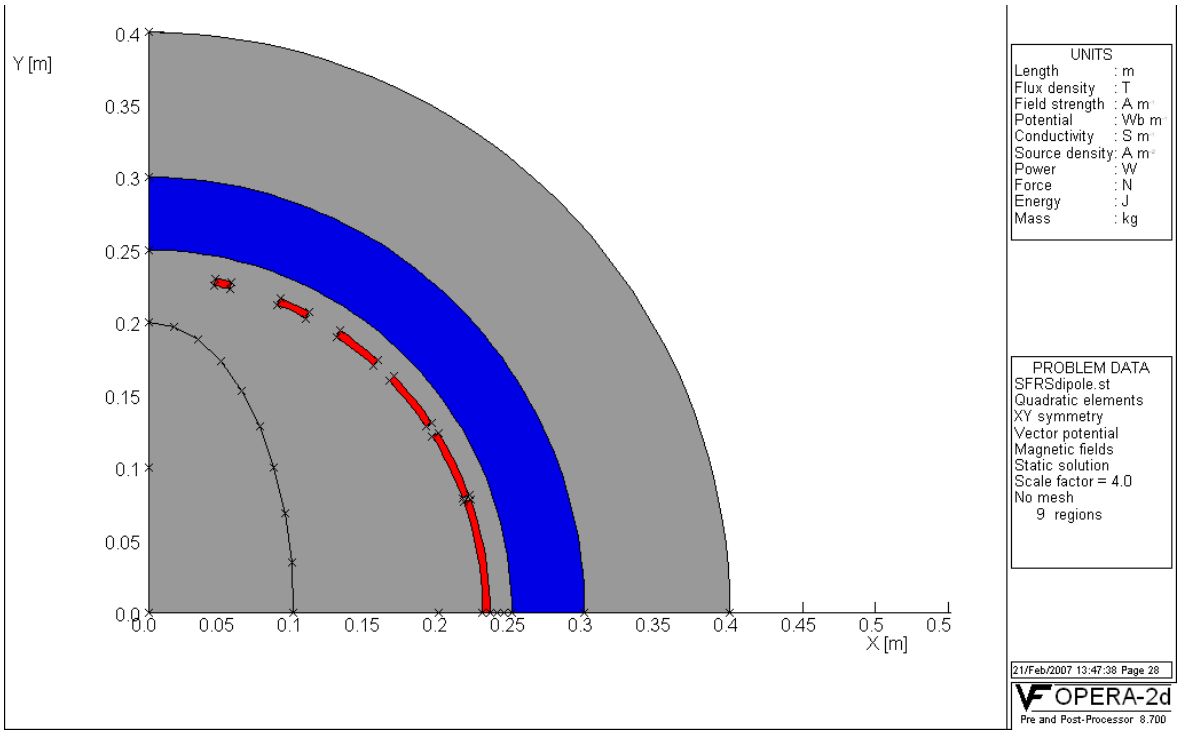

Figure 2.4-62: Cross section of the short Super-FRS y-steerer.

The calculated field harmonics demonstrate that the low field components are really eliminated. At the same time the maximum field deviation at the circle of 200 mm radius reaches $14 \cdot 10^{-4}$, but this deviation corresponds to harmonics with very big numbers $N \geq 25$ (see Figure 2.4-63 and Table 2.4-19).

A simple transformation of a 2D design to a 3D geometry demonstrated, that the integral field quality does not correspond to the same properties of a 2D model. In principle it is understandable because the magnet diameter and the magnet length are approximately equal and thus the magnet is sufficiently a 3D object. Calculations demonstrated that the field distribution in the central cross section and the integral field distribution differ significantly. That is why main geometric parameters of the coil are optimized in order to provide best possible integral field homogeneity. The final parameters of the coil are shown in Table 2.4-20 and the general view of the model is shown in Figure 2.4-64.

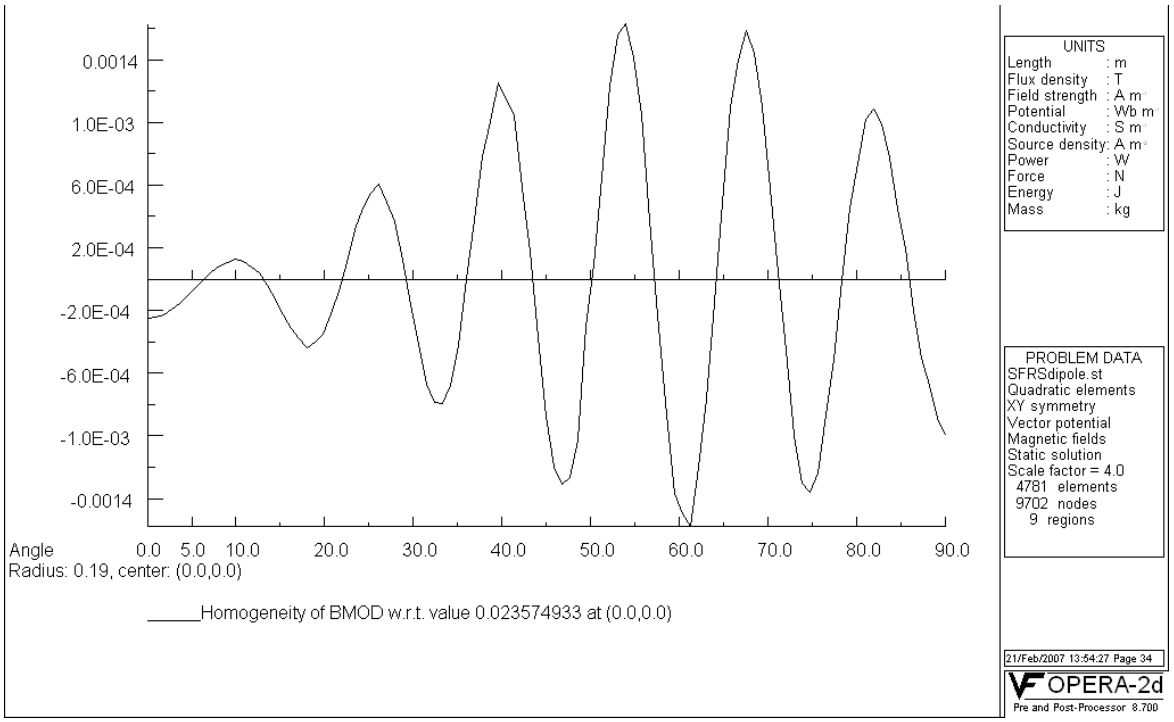

Figure 2.4-63*:* Field distribution along a circle of 190 mm radius.

Table 2.4-19*:* Field harmonics (in 10-4 relative units) for the y-steerer at the circle of 200 mm radius

Harmonics	
3rd	-0,33603
5th	-0,7285
7th	-0,27517
9th	0,27377
11th	0,21706
13th	-0,02622
15th	-0,07961
17th	-0,16504
19th	-0,07655
21st	0,04899
23rd	0,16384
25th	-27,0675
27th	25,73807
29th	8,26473
31st	-13,8634
33rd	3,35416
35th	-0,5094

Table 2.4-20: Coil parameters for a y-steerer as shown in Figure 2.4-64. The coil type is “constant perimeter end”.

Coil number	Central angle [deg]	width [m]	Length of a straight part [m]
1	9.7125	0.0788	0.28
2	25.991	0.0477	0.234
3	38.911	0.042	0.186
4	51.763	0.033	0.15
5	64.549	0.036	0.144
6	77.288	0.017	0.106

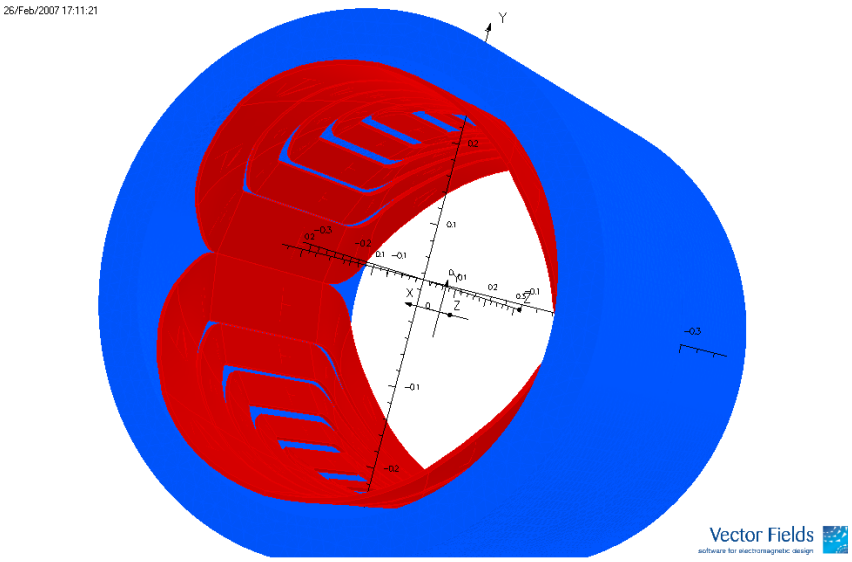

Figure 2.4-64: 3D model of the short Super-FRS y-steerer.

2.4.2.5 Multipole configuration

Indeed several different multipole configurations are used in the Super-FRS. These are in detail 2 different multipole configurations for the Pre-Separator consisting of only one quadrupole and one hexapole magnets (see Figure 2.4-65) and 4 different multipole configurations used in the Main-Separator. A complete overview of those configurations is given in Figure 2.4-66.

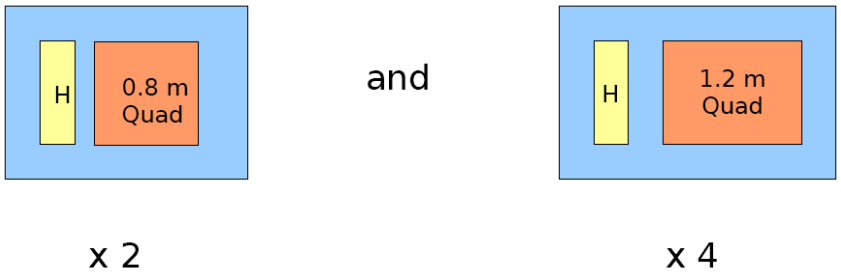

Figure 2.4-65: Multiplet configuration in the Pre-Separator of the Super-FRS.

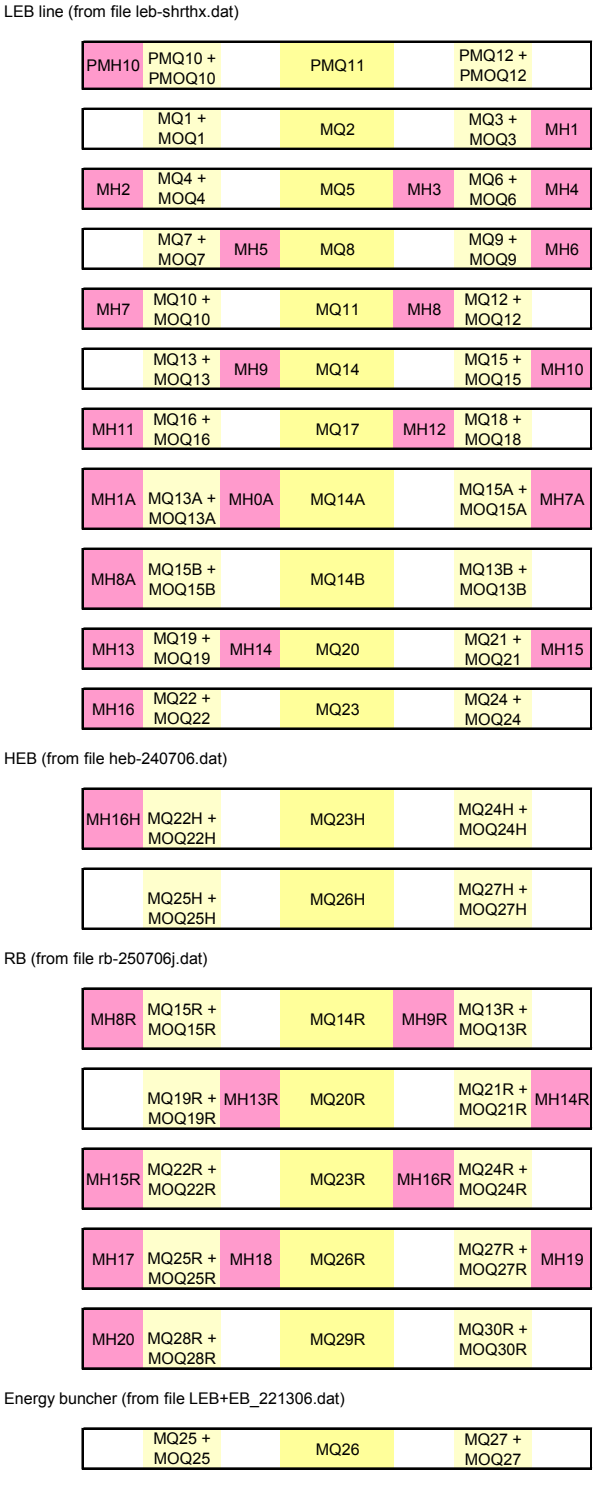

Figure 2.4-66*:* Multiplet configuration in the Main-Separator of the Super-FRS. The colour code is the following: yellow is for 1200 mm long quadrupole, light yellow is for 800 mm long quadrupole including octupole coil, pink is for 500 mm long hexapole.

The steering dipoles also could be installed also in the multipoles in locations which are not occupied by hexapole magnets.
The distance between the quadrupole and hexapole magnets is not still fixed, but the tendency is to make it as short as possible in order to save space and to get a rigid structure. A series of calculations have been performed to define a mutual influence of these two magnets on the induced magnetic fields. A 3D model of quadrupole hexapole combination was created as shown in Figure 2.4-67. Each of the magnets is presented by a quarter of the yoke. The boundary conditions at the two top planes were stated as the "magnetic tangential".

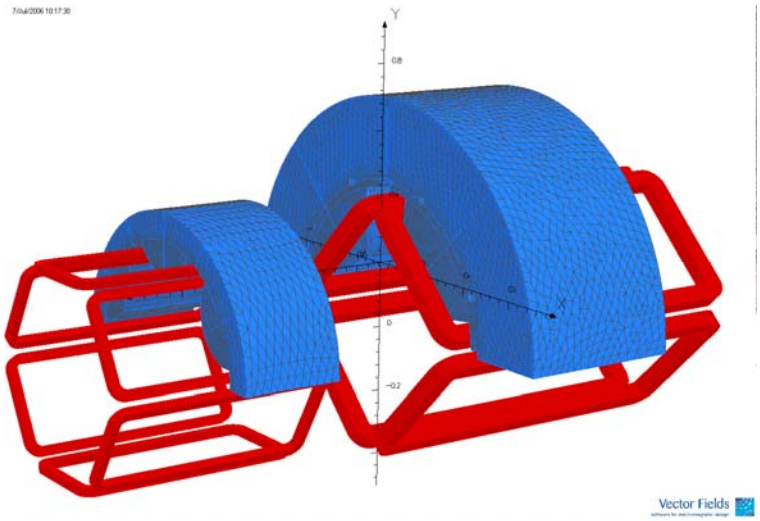

Figure 2.4-67*:* 3D model of the system quadrupole – hexapole.

To define the properties of such a system the field integrals along the optic axis were calculated twice: a) both magnets are excited to the maximum field independently; b) they are excited to the maximum field together.
The results were expanded in Fourier series and the derived sets of harmonics were compared for both cases. For a separation distance of 500 mm between the quadrupol and hexapole magnet it can be concluded that they are absolutely independent and the harmonic amplitudes may be presented as a superposition of individual magnets with a high accuracy.

Table 2.4-21*:* Amplitudes of the field integral harmonics for the system quadrupole – hexapole on the circular line of 0.19 m radius. The distance between the yokes is 250 mm. All data are normalized to the amplitude of the quadrupole harmonic. The field gradient in the quadrupole is dB/dr = 10 T/m.

	Quad. + Hexapole	Quadrupole	Hexapole
2	1.0000000	1.0000000	0.0000000
3	$-1.8237\cdot10^{-1}$		$-1.8212\cdot10^{-1}$
4	$-4.0895\cdot10^{-4}$		
6	$6.8049\cdot10^{-3}$	$6.7903\cdot10^{-3}$	
8	$9.0526\cdot10^{-5}$		
9	$9.3193\cdot10^{-5}$		$9.9534\cdot10^{-5}$
10	$7.3875\cdot10^{-4}$	$6.9748\cdot10^{-4}$	
14	$-3.3380\cdot10^{-5}$	$-2.5288\cdot10^{-5}$	
15	$2.7728\cdot10^{-5}$		$1.3503\cdot10^{-5}$
18	$-2.4137\cdot10^{-6}$	$-1.6561\cdot10^{-5}$	

Table 2.4-21 summarizes the results of such a harmonic analysis for a separation distance between the quadrupole and hexapole magnet of d = 250 mm, which corresponds to the present layout. It can be concluded, that the magnets are almost independent. The 4-th (especially) and

8-th harmonics are observed, which are forbidden for the 'stand alone' hexapole and quadrupole magnet due to symmetry reasons. Appearance of these harmonics is a direct result of mutual influence of the magnets on a magnetic field distribution. Reducing this separation distance even further amplify this effect. Figure 2.4-68 summarizes the results of the simulations and it can be seen that the separation distance should not become less than d = 250 mm, in order to keep the coupling coefficients under reasonable limits.

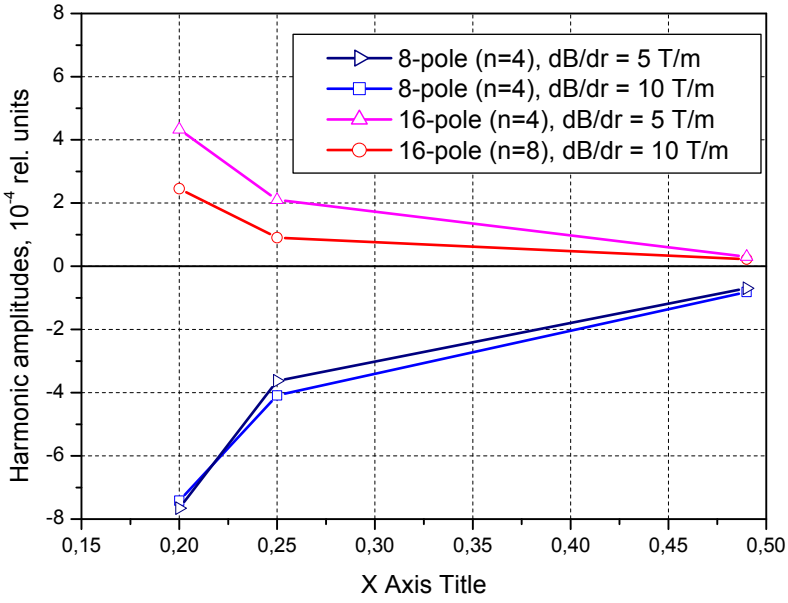

Figure 2.4-68: Strength of the "forbidden harmonics" depending on the separation distance between a Super-FRS quadrupole and hexapole magnet. In practice, the separation should be larger than 250 mm.

2.4.2.5.1 Multiplet Assembly

For the manufacturing and assembly of the multiplets the following has to be considered:

- filling factor: 98% (Metal sheets tend to have a convex cross section. The laminations should be stamped/cut in a way, which allows compensating this effect by rotating the laminations. Otherwise it might be necessary to add thin metal sheets in the back leg region for getting the requested packing across the magnet.
- the possibility to construct removable end blocks must be considered.
- the sag of the yoke should be limited by 0.2 mm.
- thickness variation of the block over the cross section must be less than 0.3 mm
- stainless steel structure: all structural elements (endplate, brackets, structural plates) will be made out of SS316LN or SS316L.

The centre of field is defined by the position of the yoke laminations. Locating the magnet, and thus the position of the dipole field, is initially reached by precise mechanical references given on the yoke. For the purpose of making fiducial references the outer side of the lamination should have a groove of 20 mm width (±0,02 mm) and 10 mm height which represents to the ideal beam path on the upper and lower yoke. Furthermore three fit drill-hole in the yoke surfaces, representing precisely the intersection point of the path tangents and their direction, and some reference planes, well defined relative to the pole surface, are required.

The reproducibility of the position of the upper and lower yoke among each other after disassembling and reassembling must be better than 0.050 mm. Reference planes, fit drill-holes and groove have to be protected against corrosion, but not varnished. Voltage taps are placed along the coil to detect where a possible quench starts and to measure joint resistances. Voltage and current taps are connected to the high voltage socket. The wires of the temperature sensors are connected to the low voltage socket.
Accurate support and stable positioning of the superconducting magnets within their cryostats is essential for the machine alignment. High flexural stiffness of the supports is therefore the basic mechanical requirement in order to guarantee that magnets are stable within 0.2 mm under variation of external forces; respectively the position of the cold mass with respect to cryostat fiducials should be reproducible to within 0.2 mm.

The cryostat – wherein the magnet must move with - must be capable to be positioned in x, y, z direction independently, and to be corrected for rotation errors of the magnetic field. Three adjustable feet should support the cryostat and should provide a controlled motion in the vertical and horizontal direction. Parameter for the alignment feet are:

- Adjustable range in horizontal / vertical direction: ± 20mm;
- Setting resolution: 0.05 mm;
- Long term stability < 0.1 mm/year;
- Maximum loads on alignment feet: to be customised according to arising overall weight of cryostat incl. cold mass etc.

The most important tolerances of the quadrupole iron yoke are shown in the following table:

parallelism of contact surfaces	±20 μm
coordinates of pole profile	±20 μm
tolerance of remaining dimensions of lamellas	0.1 mm
tolerance of width of reference groove	+20 μm / 0
height of burr at the lamellas	max. 0.1 mm
filling factor of yokes	98%
tolerance of weight	weight of lamella
flatness of stack	0.1 mm
maximum twist of stack	0.1 mm
maximum height of the bur	0.1 mm

2.4.2.6 Current Leads

The current leads provide the electrical link between the normal conducting cables connected to the power converter at ambient temperature and the superconducting cables connected to the magnets at liquid helium temperature and must therefore operate in the temperature range from 300 K to 4.5 K.
The large heat load introduced by the currents leads into the magnet cryostat is attributed to heat conduction down the lead from ambient to liquid helium temperature and ohmic heat generation within the leads. The attempt to minimise both thermal conductivity and electrical resistivity is constrained by the fact that most materials obey the Wiedemann-Franz Law. This results in the existence of a minimum heat leak which is practically independent of material properties, but is determined by the optimum shape of the leads [20].

The magnets of the Super-FRS will be powered via vapour-cooled current leads at currents ranging from 170 A up to 300 A. Every magnet will have an individual pair of current leads located on the magnet cryostat. The total numbers of leads required and the correspondent currents are listed in Table 2.4-22 [21].

Table 2.4-22*:* Number and currents of current leads required for the Super-FRS

	No. of current lead pairs	Current [A]
Dipoles (separator)	24	246
Dipoles (Energy Buncher)	4	200
Quadrupoles	68	292
Hexapoles	41	171
Octupoles	36	

Vapour-cooled leads are usually designed as high efficiency heat exchangers made of copper or brass. The lower end of the lead, which is directly connected to the low temperature superconductor (LTS), is immersed in liquid helium. The heat conducted down the lead causes evaporation of the helium and the vapour is used as cooling gas for the conductor, see Fig.1. The gas escaping the lead at the warm end is controlled by a valve.
Thus the full cooling capacity of the helium can be utilised, not only the latent heat of vaporization but also the change in enthalpy of the gas as it warms up to room temperature.
Nowadays there exist standard designs (as shown in Figure 2.4-69) commercially available for vapour-cooled current leads and they can be optimised for different current ratings with a minimum heat leak which is close to the optimum value of 1.1 mW/A per lead.

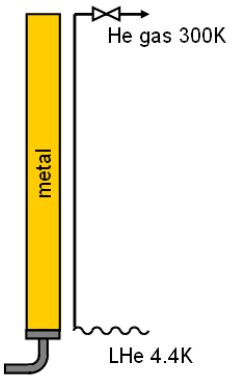

Figure 2.4-69: General layout of vapour-cooled leads.

2.4.2.7 Quench detection

A single superferric magnet is self-protecting. This means that if it is short-circuited with a superconducting bypass, it does not need any external protection. In case of quench, the magnetic energy will be used to heat up the coil. If all the magnetic energy is converted as heat at the end of the quench, when the current is null, the maximum temperature T_{max} would be between 250 and 350 K. We fear that this level of temperature will be accompanied by large thermal stresses that may destabilize the coil. It seems more reasonable to keep T_{max} lower than 200 K. To limit the temperature rise the current will be dumped by means of an external resistor with a time constant τ. Each superferric magnet will have two copper current leads. They will be

designed so that if one lead faces a thermal runaway, it will withstand the current during the runaway detection time plus the dumping time with the time constant τ.

Super-FRS dipoles will be powered in series of three. All the other magnets types are expected to be powered individually. Figure 2.4-70 presents how the quench protection will be done. In all cases, the current will be dumped by means of a resistor. The current link from one magnet to another will be warm. The quench detection material for one magnet is: 1 bridge for the magnet and 2 CL1 units (that detects the thermal runaway in the current leads). We note that the magnet has only one voltage tap. The two other bridge taps are taken from the current leads which enables to take into account the very small bus bars that connect the magnet to the leads. Steerers will also be self-protecting magnets. Their protection scheme will be the same as the one presented in Figure 2.4-70.

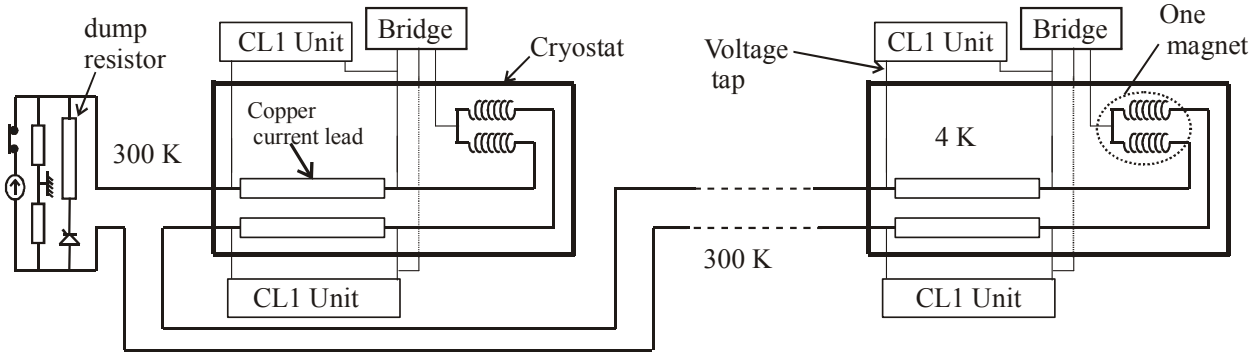

Figure 2.4-70*:* Power circuit and quench detection for 1 to 3 Super-FRS superferric magnets.

Table 2.4-23 presents the list of the superferric magnets in the Super-FRS and also in the associated beamlines (focusing system, experimental caves, connection to the rings). Table 2.4-24 gives the corresponding electronics for quench detection.

Table 2.4-23*:* List of the superferric magnets in the Super-FRS and the associated beamlines

location	dipole	quadrupole (long)	quadrupole (short)	octupole	hexapole	steerers
between PF1 and PF2	0	2	1	1	3	0
between PF2-PF3	0	2	1	1	4	1
between PF3-PF4	3	1	2	2	1	1
between PF4-MF1	3	2	4	4	4	1
between MF1-MF2	3	2	4	4	4	1
between MF2-MF3	3	2	4	4	4	1
between MF3-MF8	0	2	4	4	4	1
between MF8-MF9	3	2	4	4	4	2
between MF9-MF10	0	1	2	2	0	0
between MF10-MF11	1	0	4	2	2	1
between MF11-MF12	3	0	1	0	1	0
between MF12-MF13	0	0	3	0	0	0
MF3-MF4 (add.)	3	1	2	2	1	0
MF2-MF5 (add.)	0	1	2	2	2	1
between MF5-MF6	3	2	4	4	4	1
between MF6-MF7	3	2	4	4	4	1
Total Super-FRS	28	22	46	40	42	12
Grand Total	190					

Table 2.4-24*:* Quench detection electronics in the Super-FRS

Super FRS	No. of magnets	No. of Bridge	No. current lead Unit (CLU_1)
	190	190	380

2.4.2.8 Parameters for the Magnets of the Super-FRS

PSP	Magnet	Number of magnets	nc/ sc	Magnet type	Field or Gradient	Effective Length (m)	Bending angle(mrad) /radius (m)	*Usable Aperture/m m	Rise time (s)	Pole gap height or pole radius (iron magnet) (mm)	physical length/width/ height (m)	Cur- rent (A)	Induc- tance (mH)	Resist- ance (Ohm)
2.4.2.1	*Dipoles*													
2.4.2.1.1	Dipole 1	3	nc	Radiation resistant	0.15 ... 1.6 T	2.39	191 / 12.5	1000 x 140	120	180	3.2 / 3.0 / 2.1	677	2500	0,402
2.4.2.1.2	Dipole 2	3	sc	H-type, superferric	0.15 ... 1.6 T	2.39	192 / 12.5	380 x 140	120	170	2.8 / 2.3 / 1.6	246	18886	0
2.4.2.1.3	Dipole 3	21	sc	H-type, superferric	0.15 ... 1.6 T	2.126	170.2 / 12.5	380 x 140	120	170	2.5 / 2.3 / 1.6	246	16800	0
2.4.2.1.4	Dipole 4	4	sc	H-type, superferric	0.15 ... 1.6 T	1.708	392.7 / 4.35	760 x 200	120	240	2.1 / 2.89 / 1.76	200	31250	0
2.4.2.2	*Quadrupoles*													
2.4.2.2.1	Quadrupole 1	2	nc	Radiation resistant	1.5 ...15 T/m	1.0	—	Ø 180	120	100	1.4 / 1.2 / 1.2	2500	35	0,0367
2.4.2.2.2	Quadrupole 2	1	nc	Radiation resistant	0.6 ... 6.1 T/m	1.2	—	380 x 240	120	210	1.6 / 1.5 / 1.5	2500	70	0,075
2.4.2.2.3	Quadrupole 3	36	sc	Superferric	1 ... 10 T/m	0.8	—	380 x 240	120	250	1.2 / 2.44 / 3.5	292	25360	0
2.4.2.2.4	Quadrupole 4	21	sc	Superferric	1 ... 10 T/m	1.2	—	380 x 240	120	250	1.6 / 2.44 / 3.5	292	38040	0
2.4.2.2.5	Quadrupole 5	4	sc	Superferric	0.8 ... 8 T/m	0.8	—	380 x 240	120	250	1.2 / 2.44 / 3.5	292	25360	0
2.4.2.2.6	Quadrupole 6	1	sc	Superferric	0.8 ... 8 T/m	1.2	—	380 x 240	120	250	1.6 / 2.44 / 3.5	292	38040	0
2.4.2.2.7	Quadrupole 7	3	sc	Superferric	0.05 ... 4.7 T/m	0.8	—	600 x 400	120	345	TBD	TBD	TBD	0
2.4.2.2.8	Quadrupole 8	3	sc	Superferric	0.1 ... 5.2 T/m	1.2	—	600 x 500	120	345	TBD	TBD	TBD	0
2.4.2.3	*Multipoles*													
2.4.2.3.1	Sextupole 1	2	nc	Radiation resistant	3.5 ... 34 T/m^2[§]	0.6	—	380 x 200	120	200	0.95 / 0.8 / 0.8	650	15	0,0072
2.4.2.3.2	Sextupole 2	39	sc	Superferric	4 ... 40 T/m^2[§]	0.5	—	380 x 240	120	235	0.7 / 2.03 / 3.5	171	1776	0
2.4.2.3.3	Sextupole 3	3	sc	Superferric	TBD	TBD	—	600 x 400	120		TBD	TBD	TBD	0
2.4.2.3.4	Octupole 1	0	nc	Radiation resistant	50 T/m^3[§]	0.4	—	380 x 240	120	200	TBD	TBD	TBD	TBD
2.4.2.3.5	Embedded Octupole2	36	sc	Surface coils	10 ... 105 T/m^3[§]	0.8	—	380 x 240	120	235	embedded in Q3	TBD	TBD	0
2.4.2.3.6	Embedded Octupole3	4	sc	Surface coils	10 ... 105 T/m^3[§]	0.8	—	380 x 240	120	235	embedded in Q5	TBD	TBD	0
2.4.2.4	*Steering magnets*													
2.4.2.4.1	Steerers 1	12	sc	Superferric	-0.2 ... +0.2 T	0.5	—	380 x 240	120	235	TBD	TBD	TBD	0

2.4.3 Power Converters

The power converters for the Super-FRS magnets are determined by the requirements of field homogeneity and stability. Experience is available from the operation of the present FRS facility. While for superconducting magnets the power converters need only provide the requested current, rather large power converters are needed for the power-consuming normal conducting, radiation resistant magnets in the 1st stage of the Pre-Separator. For all types of power converters appropriate devices are available on the market and no special R&D work on this topic is foreseen.

Although the magnets of the Super-FRS are operated in a DC mode the currents are required to be ramped up to the maximum current and down to zero within ≈120 s to allow for a fast change between different Bρ settings according to the experimental requirements. The basic parameters of the power converters are listed in section 2.4.3.7. The data on power cabling and cable terminals are included. Information on the number of cabinets and the floor space required are also given. Figure 2.4-76 shows the arrangement of the cabinets. The length of the power cables is derived from this arrangement.

2.4.3.1 General Aspects of Power Converters

2.4.3.1.1 Definition of Power Converters

In this report the term Power Converter is used with the following meaning:

- A Power Converter is a device with power part and control part for supplying current and voltage to a load in a controlled way.
- The power part can be a single inverter or a distributed system of inverters.

2.4.3.1.2 Interfaces of Power Converters

There are interfaces for electrical power, for cooling, for protection and for control and display. Some basic considerations are listed:

- Electrical power input:

  Small power converters are connected to the common 400 V three phase supply of the accelerator (not loaded by pulse power).

  Medium power converters are connected to the common 400 V three phase supply or to the 400 V three phase supply derived from the pulse loaded 20 kV system.

  All input contactors are part of the power converter.

  Power converters of high power have usually own 20 kV transformers (part of power converter) which are connected via 20 kV switch gear either to the common 20 kV supply system or to the pulse loaded 20 kV supply system.

  However the 20 kV switch gear is not part of the power converter, and the transformer has to be placed in a nearby transformer box of the building.

  The electrical supply for the control electronics of pulsed medium or high power converters is derived from the common supply system (not pulsed, 230V or 400V) via a miniature circuit breaker in the power converter.

- Cooling arrangements:

  Both, air cooling and water cooling can be used. In the case of air cooling all necessary fans are parts of the power converter.

  In the case of water cooling all water flow meters are included and all material of the cooling circuits must be suited for non conductive water.

- Control and Display:

  All power converters for magnets are equipped with a high precision current measuring device, i.e. DCCT.

  Digital control algorithms are implemented whenever possible.

  Full manual control is possible at the power converter without external control system. Full remote control is possible. Therefore all electronics are included to communicate on a basic digital level with the external control system. The external control system must be able to load or read all parameters of the implemented control algorithm.

  Appropriate displays are provided to show the controlled quantities. Status and fault indications are mandatory.

- Protection:

  The power converters must be self protecting from internal and external faults. There are fault detecting devices: for instance over current detection.

  There are fault clearing devices: for instance fuses and predefined actions.

  There are direct protecting devices: for instance voltage limiters.

  The power converter must protect the load:

  from overcurrent

  from overvoltage

  by predefined reactions to interlocks of the load such as temperature interlocks, water interlocks, quench detection signals.

2.4.3.1.3 Locations of Power Converters

The basic concept is to place all power electronics outside the restricted area of the beam transport system whenever possible. The advantages are:

- Measurements, repairs and service are possible without accessing restricted areas, thus avoiding machine shut downs.
- There is no waiting time to have access to faulty power converters.
- There is no uncertainty on the influence of radiation on the proper operation of components of power electronics and on the impact on life time of the components
- There is no need for automatic redundancy.

2.4.3.1.4 Choice of Power Converter Circuit Configurations

Every selected power converter configuration must fulfil the criteria listed below:

- it meets the specifications
- it is reliable
- it is circuit structure is as simple as possible.

SCR structure

Regarding high power requirements combined with high currents and energy recovery as in the case of SIS100 a line commutated converter (SCR) is the best choice. High amounts of energy can be transmitted in two directions by using one active semiconductor circuit only. Reactive power can be reduced by adding freewheeling thyristors while an active switch mode filter circuit (PE, 50...100 kHz) will improve the poor dynamics of the SCR as well as it reduces the ripple content of the load current. The SCR will be set up as a line commutated 12-pulse system in series or parallel connection as shown in Figure 2.4-71.

Switch Mode structure (SM): hard switching

For small and medium power requirements with energy recovery capability switch mode circuits in hard switching configuration are well suited. Limits are given by high load currents because of the number of parallel IGBTs and the switching current capability of the storage capacitor in the DC-link.

The benefits are the small filter for blocking the switching frequency from the load, the good dynamics and the energy storage which allows reduction of grid loading by pulsed currents. Switch mode circuits can be designed for 1-quadrant (chopper), 2-quadrant (half bridge) or 4-quadrant (full bridge) operation. The full bridge enables precisely controlled zero crossing of currents for bipolar applications. The full bridge configuration is already given in Figure 2.4-71. Half bridge and chopper configuration are given in Figure 2.4-72. Typical switching frequencies are 20 kHz.

Switch Mode structure (SM-s): soft switching

For DC applications demanding nearly noise free load currents soft switching circuits are well suited. Using medium frequency transformers to adapt to the wanted load voltage allows very compact construction of power converters. However the current of one circuit is limited to about 200A because of the Schottky diodes in the output rectifier. For higher load currents several circuits have to be connected in parallel.

2.4.3.1.5 Accuracy and current ripple

The requirements for current control performance in respect to accuracy, stability, ripple and time lag of actual current to the set value are summarized in the total deviation. The definition of total deviation is illustrated in Figure 2.4-73 and can be expressed as a relative or absolute quantity. For bipolar power converters which can be operated at zero current the total deviation can only be given as an absolute quantity. In the relative definition the reference is always the actual value while in the absolute definition the reference is the nominal value.

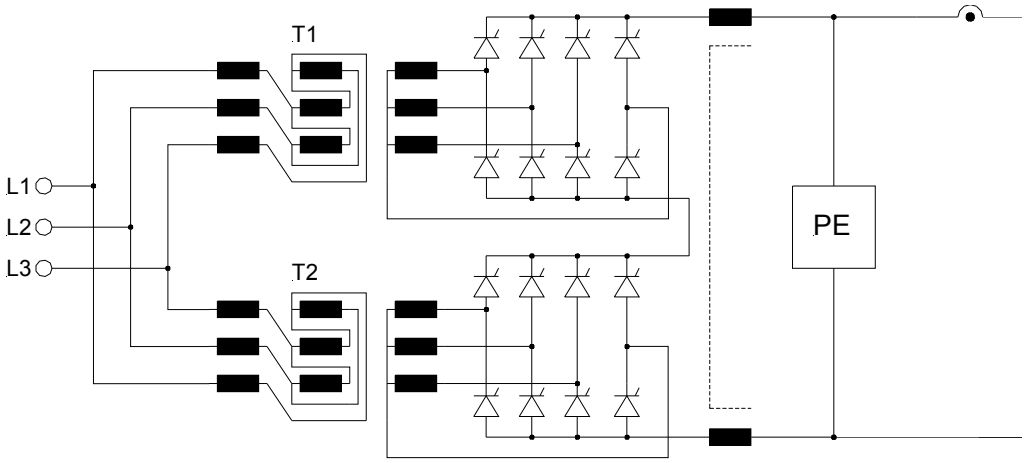

a) series connection

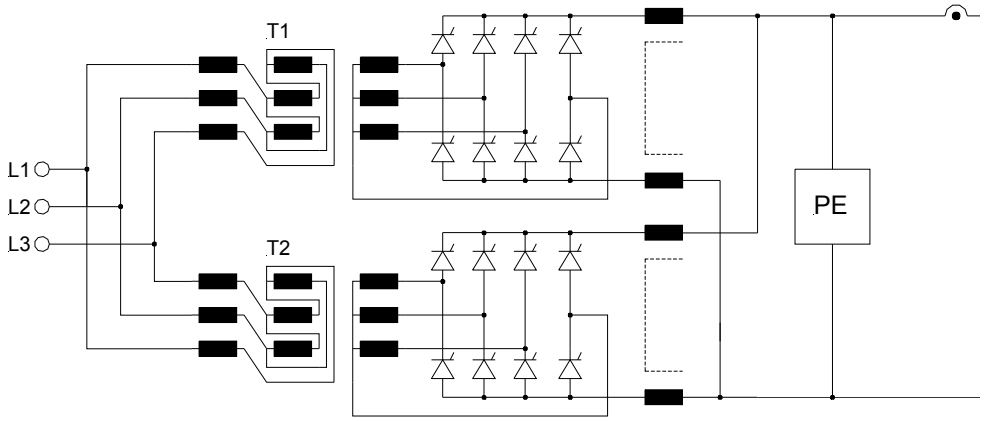

b) parallel connection

T1, T2 identical transformers : phase shift of +/-15° el by interchange of L1,
PE : active parallel filter

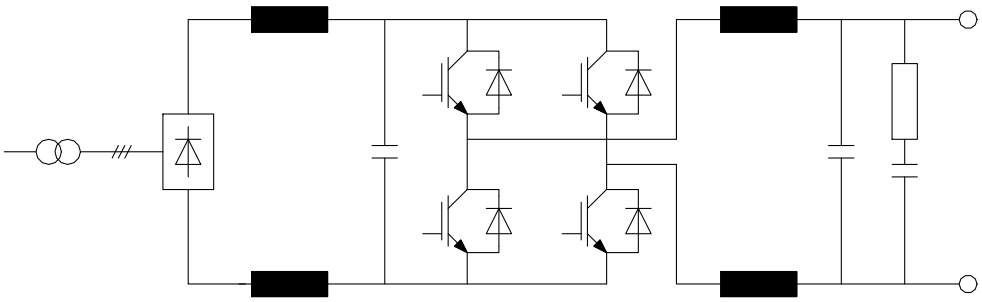

c) 4 quadrant switch mode converter as active parallel filter

Figure 2.4-71*:* 12 pulse SCR in series or parallel connection with freewheeling Thyristors and active parallel filter PE.

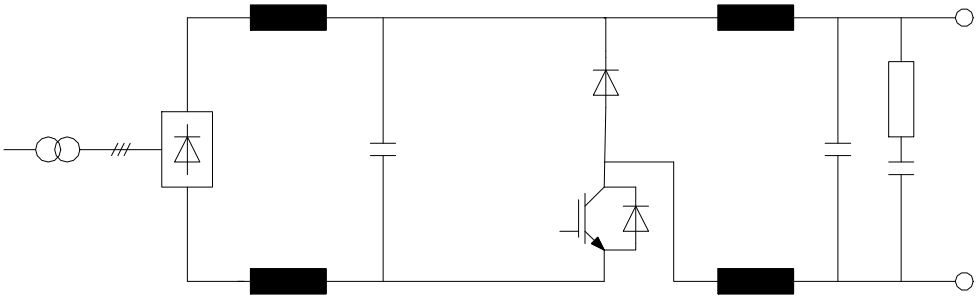

a) Chopper circuit

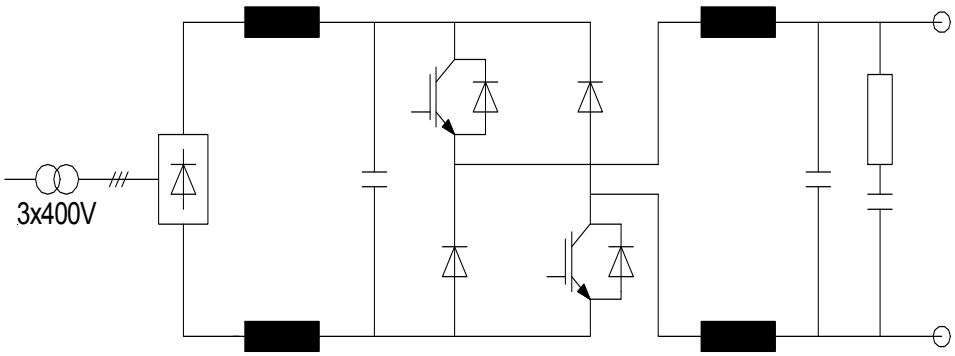

b) Half bridge

Figure 2.4-72*:* Basic circuit diagram for switch mode converter (hard switching).

For converters with one current polarity and defined minimum current there is a relative total deviation defined.

$W = Set\ value$
$X = Actual\ value$

$\Delta X = W - X$

$$\Delta I / I$$

For bipolar currents there is an absolute total deviation defined.

I_N = nominal current

$$\Delta I / I_N$$

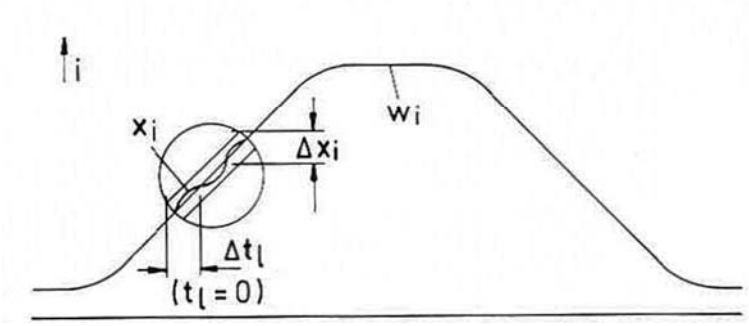

Figure 2.4-73*:* Definition of total deviation.

2.4.3.1.6 Proposed Control of Power Converters

In Figure 2.4-74 the general structure of a power converter is presented. There are three main components: the Power Part, the Power Converter Control and a Basic I/O-system.

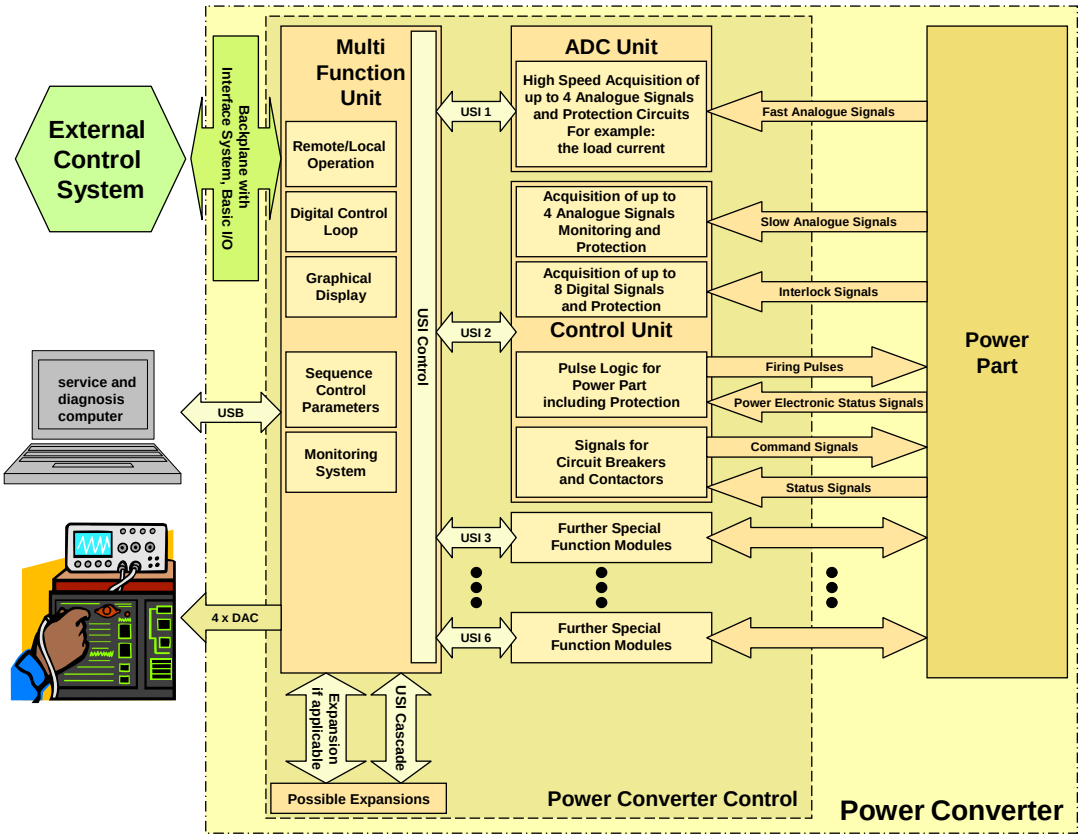

Figure 2.4-74: General structure of power converters.

The Power Converter Control is a modular system consisting of a Multifunction unit, an ADC unit for fast analogue signals and a Control unit. The Multifunction unit is the user interface for manual operation and service and diagnosis by computer or oscilloscope. It also contains the communication ports to the external accelerator control system via the basic I/O-unit, and the control loops and the control topology of the power converter are also implemented in the Multifunction unit. The ADC unit acquires fast analogue signals of the power part, for example the load current, for control, protection and documentation purposes.
The Control unit generates command signals and firing pulses for the power electronics of the power part. Additionally it handles status and interlock signals and slow analogue signals for protection purposes

As illustrated in Figure 2.4-75 the power converter can communicate on a basic digital I/O-level in real time with a link to the external control system. This link generates the real time data of the set value for the power converter from data provided by the external control system. Thereby the communication to the external control system is not in real time. The link mentioned before is an electronic card which is not part of the power converter. However it can be integrated into the power converter.

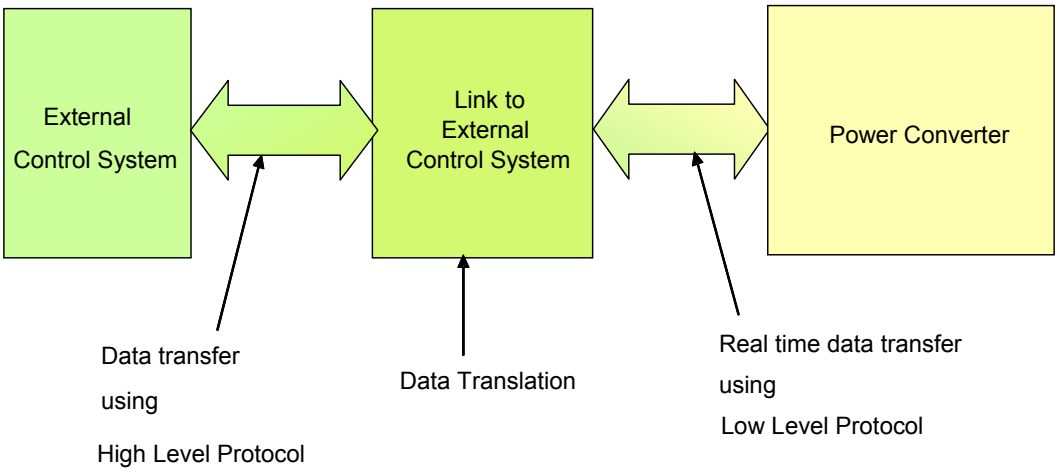

Figure 2.4-75*:* Communication to external control system.

The controller for the load quantities can be realized by analogue electronics or by digital control algorithms. Where ever possible digital control is preferred. Excellent results have been achieved with digital control algorithms based on analogue control strategies enhanced by the possibilities of digital signal processing.

The link to the external control system as well as the power converter control have been decided to have the same design and the same technical realisation in all power converters of FAIR. That applies to the load current measuring devices, the DCCTs, too.

2.4.3.2 Dipole Power Converters

4-quadrant converters will be used to allow for bipolar currents which are required for different particle modes of the Super-FRS. Part of the magnet energy has to be dumped in a brake chopper parallel to the capacitor of the DC-link. A basic circuit diagram is given in Figure 2.4-71.

2.4.3.3 Quadrupole Power Converters

The quadrupole magnets are normal or superferric conducting magnets. 1-quadrant (including mechanical reversing switch) and 4-quadrant converters will be used to allow for bipolar currents which are required for different ion-optical modes of the Super-FRS depending on the specific experimental condition. Part of the magnet energy has to be dumped in a brake chopper parallel to the capacitor of the DC-link.

2.4.3.4 Multipole Power Converters

The hexapole magnets are normal or superferric conducting. The power supplies are equipped with 4-quadrant switching circuits. The capacitor of the DC-link can absorb the small amount of magnet energy.

2.4.3.5 Steerer Power Converters

The steering magnets perpendicular to the dispersive coordinate are all superferric conducting. The power supplies are equipped with 4-quadrant switching circuits. The capacitor of the DC-link can absorb the small amount of magnet energy.

2.4.3.6 Power Distribution

The magnet power cables needed for the Super-FRS are included in section 2.4.3.7. Altogether two power transformers will be needed for Super-FRS, one is planned to be located in the Target Building (FAIR Building #18, Figure 2.4-76), the other is planned to be located in the Super-FRS Supply Building (FAIR Building #6a, Figure 2.4-77).

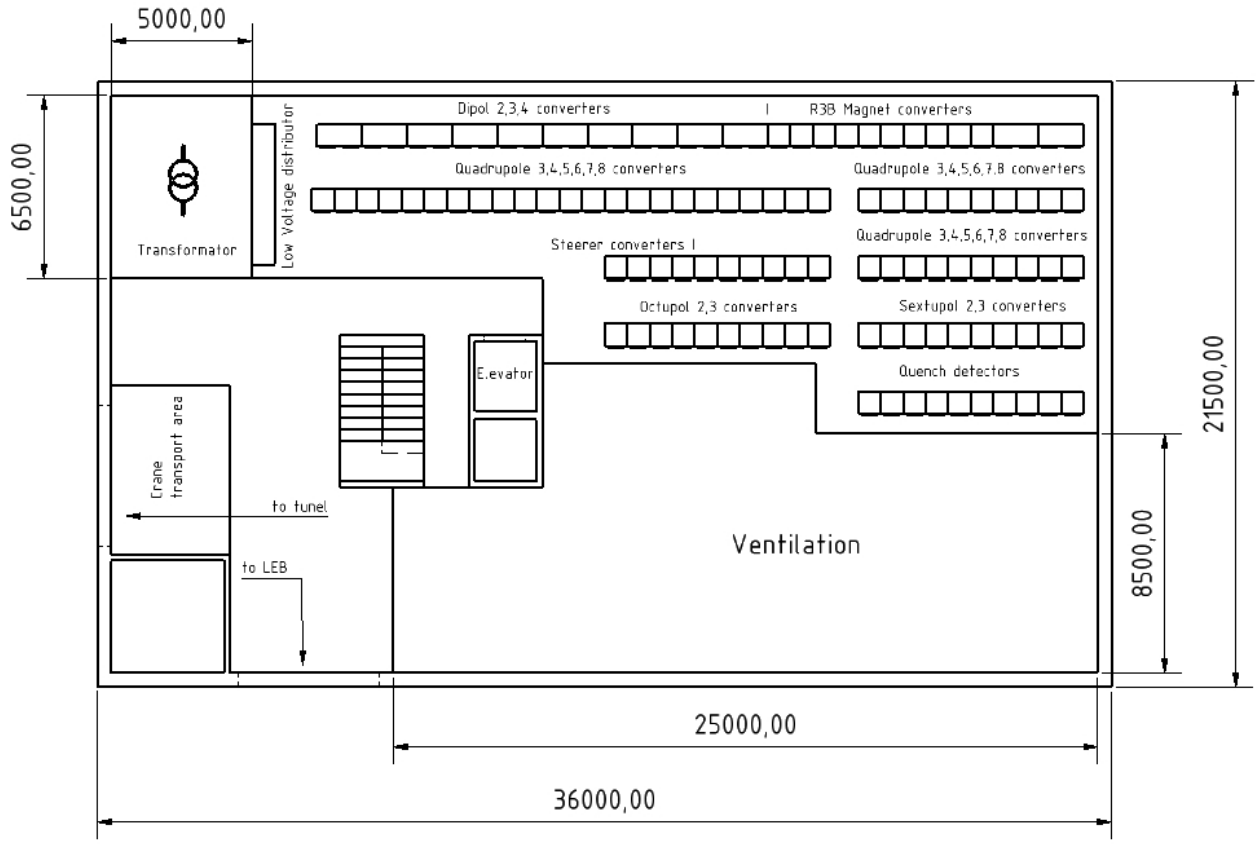

Figure 2.4-76*:* Planned arrangement of power supplies in Service-Building (building #6a), Level 0.

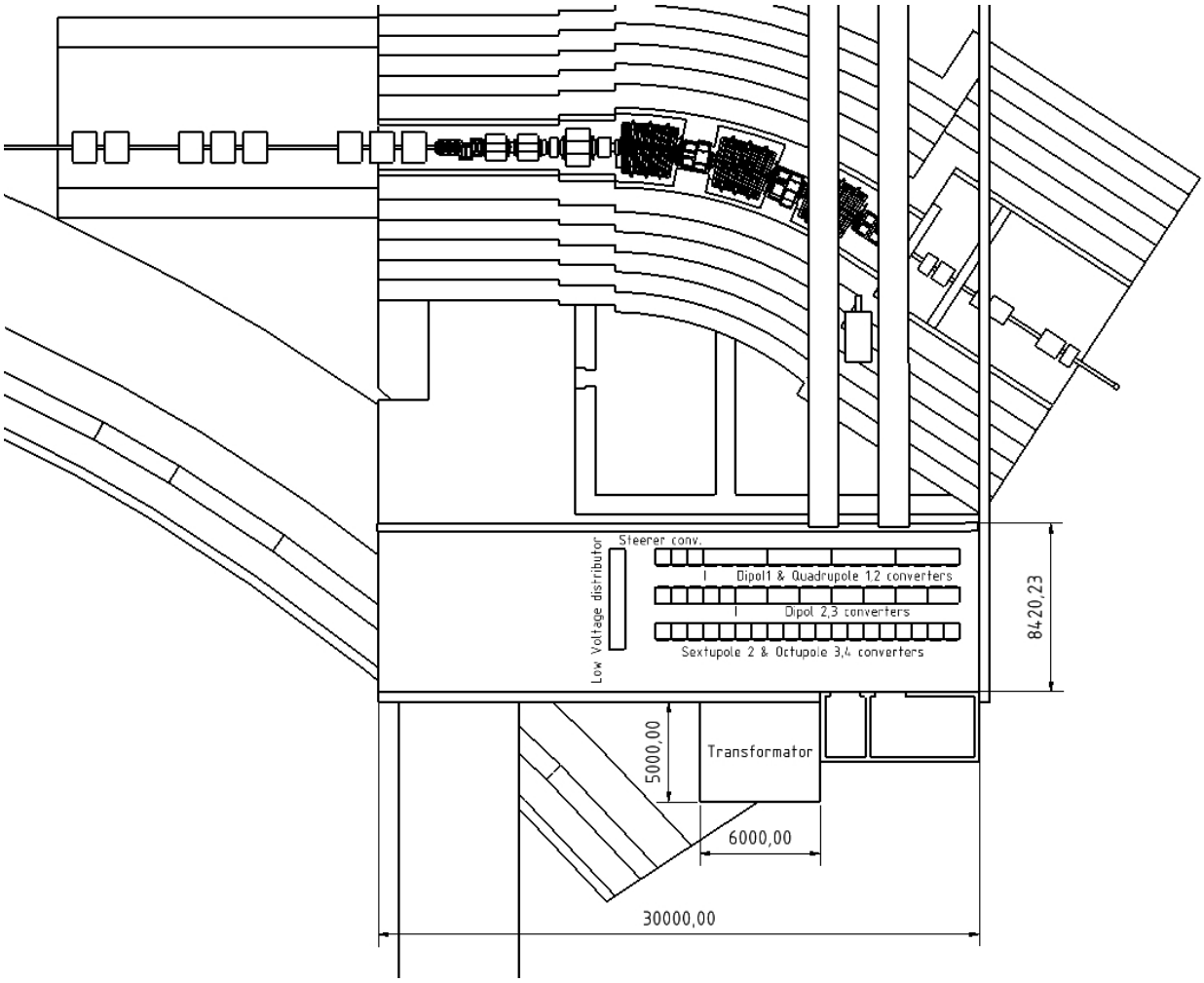

Figure 2.4-77*:* Planned arrangement of power supplies in Target-Building (building #18), level 1.

2.4.3.7 Parameters for Power Converters

SuperFRS	Power Converters	Design of PS	No. of PS	No. of Cab.	No. of Dump Units	Floor space per Cab.	Min. Current	Rated Current	Max. Current Rate	Flattop Voltage	Max. Voltage	Max. Active Power	Max. Apparent Power
						[m x m]	[A]	[A]	[A/s]	[V]	[V]	[kW]	[kVA]
2.4.3.1	*Power Converters Dipoles*												
2.4.3.1.1	Dipol 1	SM_4	1	1	-	3,2 x 0.8	67,7	+/- 677	+/- 5,6	654	+/- 696	471	575
2.4.3.1.2	Dipol 2	SM_4	1	1	1	1,6 x 0.8	24,6	+/- 246	+/- 2,1	22	+/- 138	34	41
2.4.3.1.3	Dipol 3	SM_4	7	7	7	1,6 x 0.8	24,6	+/- 246	+/- 2,1	18	+/- 121	30	36
2.4.3.1.4	Dipol 4	SM_4	1	1	1	2.4 x 0.8	20	+/- 200	+/- 1,7	7	+/- 215	43	53
2.4.3.2	*Power Converters Quadrupoles*												
2.4.3.2.1	Quadrupole 1	SM_1	2	2	-	3.2 x 0.8	250	+/- 2500	+/- 20,8	94,7	+/- 95,4	239	291
2.4.3.2.2	Quadrupole 2	SM_1	1	1	-	3.2 x 0.8	250	+/- 2500	+/- 20,8	190	+/- 192	480	585
2.4.3.2.3	Quadrupole 3	SM_4	36	36	36	0.8 x 0.8	29,2	+/- 292	+/- 2,4	7	+/- 69	20	25
2.4.3.2.4	Quadrupole 4	SM_4	21	21	21	0.8 x 0.8	29,2	+/- 292	+/- 2,4	7	+/- 100	29	36
2.4.3.2.5	Quadrupole 5	SM_4	4	4	4	0.8 x 0.8	29,2	+/- 292	+/- 2,4	7	+/- 69	20	25
2.4.3.2.6	Quadrupole 6	SM_4	1	1	1	0.8 x 0.8	29,2	+/- 292	+/- 2,4	7	+/- 100	29	36
2.4.3.2.7	Quadrupole 7	SM_4	3	3	3	0.8 x 0.8	TBD	+/- TBD	+/- TBD	TBD	+/- TBD	TBD	TBD
2.4.3.2.8	Quadrupole 8	SM_4	3	3	3	0.8 x 0.8	TBD	+/- TBD	+/- TBD	TBD	+/- TBD	TBD	TBD
2.4.3.3	*Power Converters Multipoles*												
2.4.3.3.1	Sextupole 1	SM_4	2	2	-	0.8 x 0.8	65	+/- 650	+/- 5,4	+/- 10	+/- 11	6,9	8,4
2.4.3.3.2	Sextupole 2	SM_4	39	10	39	0.8 x 0.8	17,1	+/- 171	+/- 1,4	+/- 5	+/- 8	1,3	1,6
2.4.3.3.3	Sextupole 3	SM_4	3	1	3	0.8 x 0.8	TBD	+/- TBD	+/- TBD	+/- TBD	+/- TBD	TBD	TBD
2.4.3.3.4	Octupole 1	SM_4	0	0	0	0.8 x 0.8	TBD	+/- TBD	+/- TBD	+/- TBD	+/- TBD	TBD	TBD
2.4.3.3.5	Octupole 2	SM_4	36	9	36	0.8 x 0.8	TBD	+/- TBD	+/- TBD	+/- TBD	+/- TBD	TBD	TBD
2.4.3.3.6	Octupole 3	SM_4	4	1	4	0.8 x 0.8	TBD	+/- TBD	+/- TBD	+/- TBD	+/- TBD	TBD	TBD
2.4.3.4	*Power Converters Steerers*												
2.4.3.4.1	Steerers 1	SM_4	12	3	12	0.8 x 0.8	TBD	+/- TBD	+/- TBD	+/- TBD	+/- TBD	TBD	TBD

SuperFRS	Power Converters	Effective Apparent Power	Tolerable Ripple		Magnet Type (nc/sc)	No. of Magnets in Series	L per magnet	R per magnet	Rmax of cable	Cable type				max Cable length	Sum of cable length	average cable length	cable Power loss	sum of cable Power loss
		[kVA]	[10^{-4}]				[mH]	[m□]	[m□]					[m]	[m]	[m]	[KW]	[KW]
2.4.3.1	*Power Converters Dipoles*																	
2.4.3.1.1	Dipol 1	553	+/-	0.5	nc	3	2500	320	6	3	x (4 x	50	mm²)	50	150	40	2,18	2,18
2.4.3.1.2	Dipol 2	25	+/-	0.5	sc	3	18886	0	89	1	x (4 x	50	mm²)	250	250	110	2,38	2,38
2.4.3.1.3	Dipol 3	22	+/-	0.5	sc	3	16800	0	71	1	x (4 x	50	mm²)	200	1400	110	2,38	16,64
2.4.3.1.4	Dipol 4	32	+/-	0.5	sc	4	31250	0	36	1	x (4 x	50	mm²)	100	100	70	1,00	1,00
2.4.3.2	*Power Converters Quadrupoles*																	
2.4.3.2.1	Quadrupole 1	291	+/-	1	nc	1	35	36,7	1	8	x (4 x	95	mm²)	50	800	40	5,87	11,75
2.4.3.2.2	Quadrupole 2	585	+/-	1	nc	1	70	75	1	8	x (4 x	95	mm²)	50	400	40	5,87	5,87
2.4.3.2.3	Quadrupole 3	15	+/-	1	sc	1	25360	0	26	2	x (4 x	70	mm²)	200	14400	110	1,20	43,07
2.4.3.2.4	Quadrupole 4	21	+/-	1	sc	1	38040	0	26	2	x (4 x	70	mm²)	200	8400	110	1,20	25,12
2.4.3.2.5	Quadrupole 5	15	+/-	1	sc	1	25360	0	26	2	x (4 x	70	mm²)	200	1600	110	1,20	4,79
2.4.3.2.6	Quadrupole 6	21	+/-	1	sc	1	38040	0	26	2	x (4 x	70	mm²)	200	400	110	1,20	1,20
2.4.3.2.7	Quadrupole 7	TBD	+/-	1	sc	1	TBD	0	TBD	1				100	300	110	TBD	TBD
2.4.3.2.8	Quadrupole 8	TBD	+/-	1	sc	1	TBD	0	TBD	1				100	300	110	TBD	TBD
2.4.3.3	*Power Converters Multipoles*																	
2.4.3.3.1	Sextupole 1	8,0	+/-	1	nc	1	15	7,2	9	2	x (4 x	50	mm²)	50	200	40	3,02	6,04
2.4.3.3.2	Sextupole 2	2,0	+/-	1	sc	1	1776	0	31	2	x (4 x	50	mm²)	175	13650	110	0,57	22,40
2.4.3.3.3	Sextupole 3	TBD	+/-	1	sc	1	TBD	0	TBD	2				175	1050	110	TBD	TBD
2.4.3.3.4	Octupole 1	TBD	+/-	1	sc	1	TBD	0	TBD	2				175	0	110	TBD	TBD
2.4.3.3.5	Octupole 2	TBD	+/-	1	sc	1	TBD	0	TBD	2				175	12600	110	TBD	TBD
2.4.3.3.6	Octupole 3	TBD	+/-	1	sc	1	TBD	0	TBD	2				175	1400	110	TBD	TBD
2.4.3.4	*Power Converters Steerers*																	
2.4.3.4.1	Steerers 1	TBD	+/-	1	sc	1	TBD	0	TBD	1				175	2100	110	TBD	TBD

2.4.4 RF-Systems

n/a

2.4.5 Injection/Extraction

n/a

2.4.6 Beam Diagnostics

Based on the operating experience gained at the FRS, it is planned to implement a detection system that can be commonly used for all experiments at the different Super-FRS branches and comes with its associated data acquisition scheme. The main task of this combined system is threefold:

(i) it can be used to set up and adjust the separator,
(ii) it provides the necessary measures for machine safety and monitoring,
(iii) it allows for an event-by-event particle identification, tracking and characterization of the produced rare ion species.

Furthermore, the beam intensities at different locations in the separator are to be monitored, e.g. to normalize measured rates in order to extract absolute cross sections. The modi operandi depend strongly on these given tasks and the necessary requirements for the combined detector and acquisition systems will be given:

Setting up and adjusting the separator can be done at a low rate for almost any detector system. The main design goal is to get an easy to maintain, reliable system.
An online monitoring has to be performed, especially in the target and beam catcher areas. Any deviation of the primary beam from its nominal position should lead immediately to an interlock condition. The main challenge is to cope with the very high intensities and background radiation here. The design of the detector systems should allow extended periods of operation without hands-on maintenance.

For almost all experiments, the separator is to be treated as the first part of the experimental setup. The beam particles entering the different branches have to be identified and their longitudinal and transverse momentum components should be known. For tracking experiments to be carried out in the Low-Energy Branch and the High-Energy Branch, the measurement has to be performed on an event-by-event basis. This implies that the data acquisition system of the particular experiments and the Super-FRS should be closely coupled if not identical. The Super-FRS data taking will therefore be designed in accordance with the common NUSTAR data acquisition scheme. The implication on the location of electronics and readout systems will be discussed in section 2.4.6.5. The requirements on the detector systems are demanding at the entrance of the main separator, where rates up to 10^9 particles /sec can be expected.

The locations for the different detection systems are shown in Figure 2.4-78. The special conditions in the target area require a design of the detection system that takes into account the radiation level of the area; it is foreseen to be able to run for about one year without opening the section from PF0 to PF1. Generally we foresee UHV material although a pressure of 10^{-7} mbar is sufficient. The choice of the particular detector systems is driven by the idea of benefiting from the various developments that are currently done in the detector laboratory (e.g. diamond detectors) and accelerator division (beam diagnostic systems) in conjunction with the FAIR project.

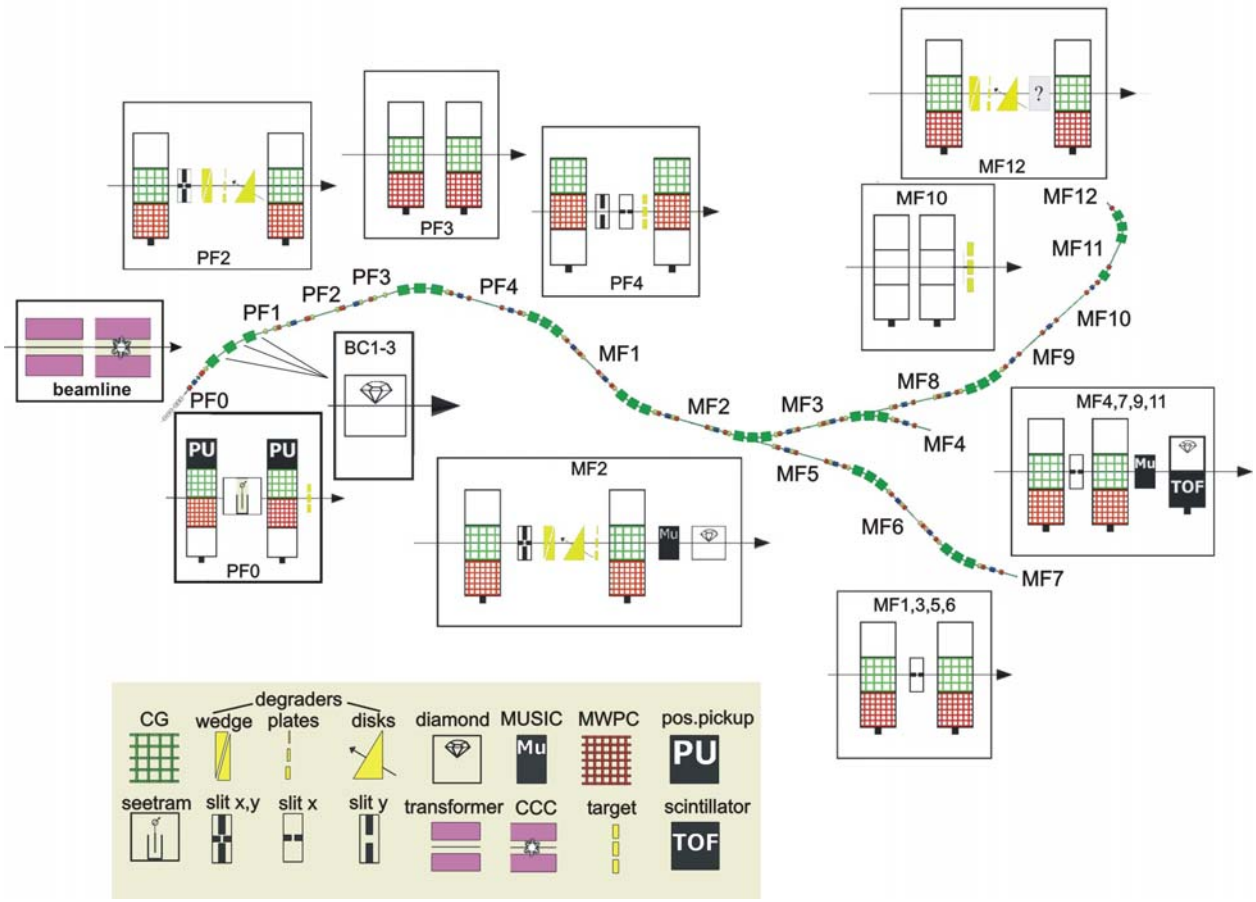

Figure 2.4-78: Detector systems and their positions in the Super-FRS. The particular areas and setups are described in the text.

Radiation environment

The envisaged intensities of up to 10^{12} uranium ions / spill are demanding for the design of detector components in the first part of the Pre-Separator of the Super-FRS. Readout electronics has to be placed away from the beam axis for at least 1 m (in y-direction), where the flux stays below 10^{15} neutrons/cm^2 (see also Figure 2.4-79). The end of the Pre-Separator (PF4) denotes the area where ion intensities are down to 10^9/s, thus, being comparable with the rates at the present FRS.

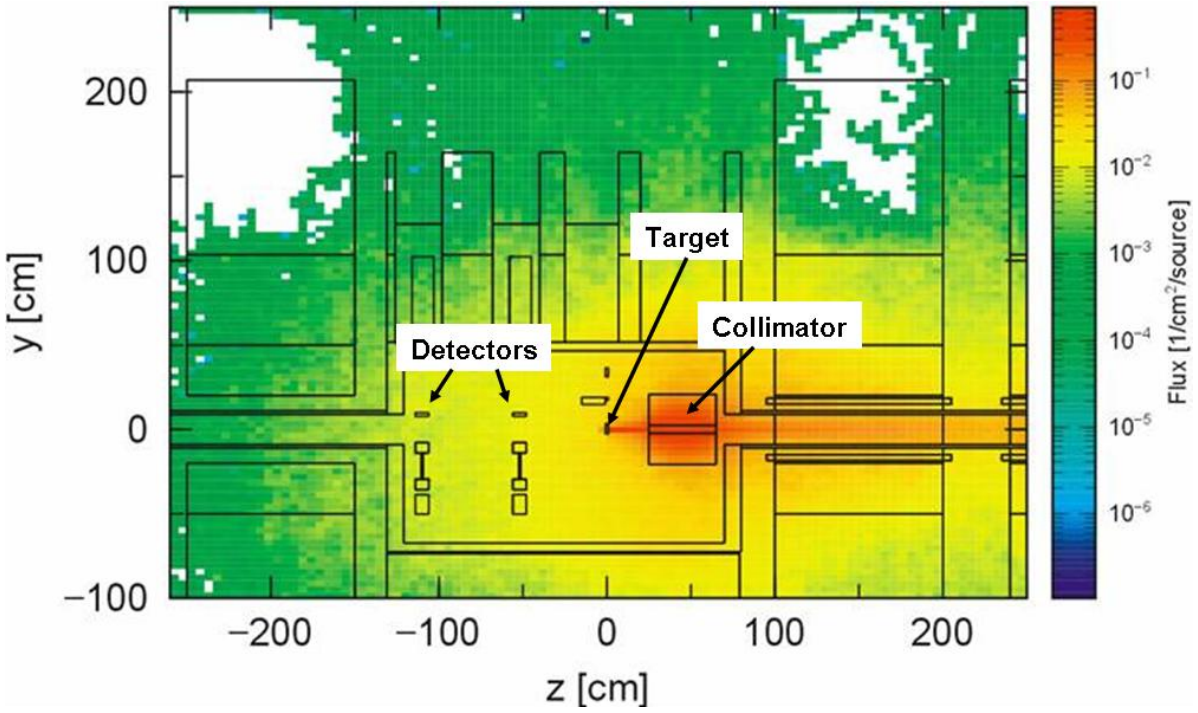

Figure 2.4-79*:* Total Neutron Flux (all energies) per incident particle in the target area of the Super-FRS (detector positions at z = -55 cm and z = -110 cm, target at z = 0 cm, beam collimator starts at z = 30 cm). The values are given for 1500 MeV/u ^{238}U ions hitting a 4 g/cm^2 carbon target. The material of the target chamber and nearby shielding is iron, the outside is concrete.

2.4.6.1 Diagnostics Target Area and Beam Catchers

For the target and beam catcher area it is foreseen to have a safety interlock on the nominal beam position on target and beam catcher to avoid damage to any component in the high radiation areas. It is clear, especially for the short extraction with 50 ns pulses, that any detector material or foil will fail if hit by the full beam intensity. Therefore, contact-free measurement methods have to be used.

Target monitor

For the beam spot on target monitoring an optical imaging technique in the infrared spectrum is to be developed together with the target types. As the camera has to be placed a reasonable distance from the target to avoid radiation damage, a fibre or mirror optics has to be developed and tested. The camera images are than analyzed using standard methods.

Another interesting method to visualize and monitor the beam spot on the target makes use of the surrounding residual gas. The induced fluorescence in the residual-gas volume may be used to deduce the profile of the incoming beam. This method has been successfully applied (Figure 2.4-80) at the UNILAC at GSI [22]. For application to the Super-FRS a camera and image intensifier have to be placed in safe distance from the target and a suitable telescope or fibre optics has to be developed.

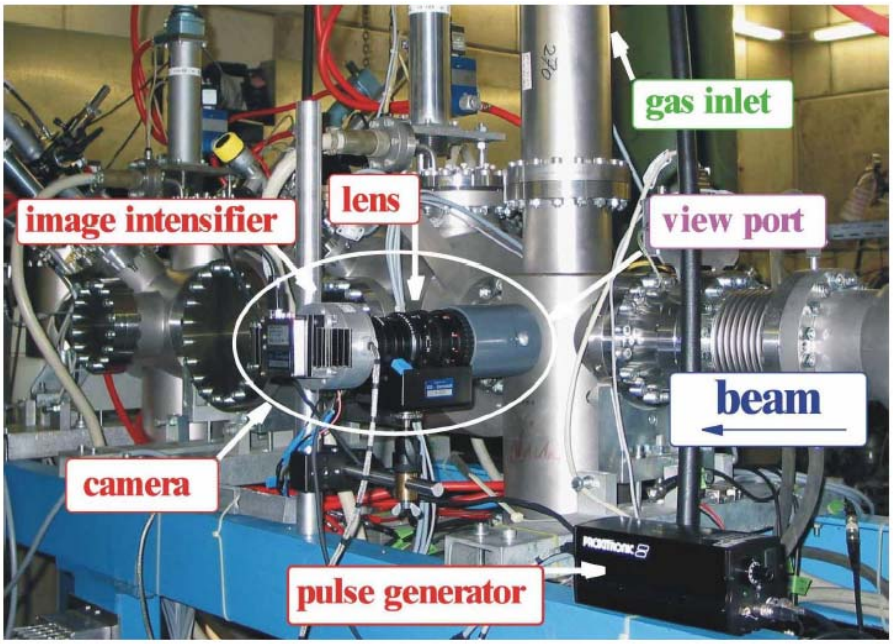

Figure 2.4-80: Beam induced fluorescence setup that has been used to measure beam profiles at the UNILAC accelerator. Uranium $q=28^{+}$ ions at 4.7 MeV/u with an intensity of 10^{8} - 10^{9} / macro-pulse can be detected.

Beam catcher diagnostics system

The beam catchers of the Pre-Separator are described in section 2.4.11.1. It is desirable to perform an on-line monitoring of the dumped beam intensity for security reasons. The simplest way would be to measure the transferred charge of the dumped ions directly by means of commercially available Ampere meters (current integrators), thus, use them like a Faraday cup. However, in practice this method becomes cumbersome for these rather extended movable and cooled devices. Apart from the optical methods already mentioned, where one could monitor the deposition of the primary beam intensity on the beam catcher, there is another option that recently became available and is subject to intense ongoing development.

Diamond has superior material properties; a large thermal conductivity and high shock wave resistance that are ideally suited for their use in the hostile environment of the Pre-Separator. Commercially, artificially grown diamond films (CVD-D) are used as windows but became recently also available to build detectors. They are available as PolyCrystalline (PC) films, or even Single Crystal (SC) films, depending on how close the substrates properties, where they are grown on, are equal to the diamonds lattice. If nowadays, monolithic large area diamond detectors of a size > (8 x 8) mm^2 are needed, PC-CVD-D must be used. This material is available in wafers of up to 100 mm in diameter. High quality, i.e., Electronic Grade (EG) CVD-D can be used As Grown (AG) or polished to Detector Grade (DG) quality. AG CVD-D shows inhomogeneity in both, the charge collection efficiency which increases linearly along the crystals growth and the structure of the two opposite surfaces, i.e. a smooth substrate side with a bad charge collection efficiency and a rough growth side with a high efficiency. The average charge collection efficiency of AG PC diamond is 20 % - 40 %, meaning that more than half of the material thickness is electronically inactive. On the other hand this type of diamond provides the fastest detectors and, if needed, the thinnest free standing sensors. They can be ordered in layers of about 50µm to 2 mm thickness. DG material is post processed, i.e. lapped down from 1 mm EG thick wafers by removing several hundreds of micrometers from the bad substrate side. These much more homogeneous DG-PC-CVDD films with a charge collection efficiency ≈ 65 % are available between 300 µm and 600 µm thickness. In the next 2-3 years,

(10 x 10) mm^2 SC-CVDD samples have been announced for sale. Intense R&D is going on to achieve areas as large as 2 inch wafers. All those prices mentioned above are forced at the time being by decisions which do not correspond to real production costs. It has been demonstrated that PC-CVD-DD operating with low-noise low-impedance broadband amplifiers are able to measure linearly heavy ion rates in a broad range from 1 Hz up to > 500 MHz by single particle readout of one detector channel. This value has been obtained with a detector of large capacitance of 8 pF and a scaler which limited the measurement due to its 500 MHz bandwidth. The s-p rate capability is higher for reduced strip capacitance and GHz electronics signal processing [23]. If two-dimensional position resolution on thin detectors is needed, crossed strips can be applied on opposite sides of the diamond substrate. Note, that although this type of detector is of high interest for different experimental groups and the expectations for a successful realization are good, no such a detector has been developed up to now at GSI. Thus, joined R&D e.g. with the Atomic Physics and R³B collaborations is foreseen. Figure 2.4-81 shows the microscopic image of a pixel structure, which has been processed by sputtering a 1000 Å Si_3N_4 layer on a metallized surface. PC-CVDD micro-strip and micro-pixel detectors have been developed (Figure 2.4-82) and excessively tested by the RD42 Collaboration at CERN [24] (GSI is a member), striving for MIP tracking at high luminosity colliders.

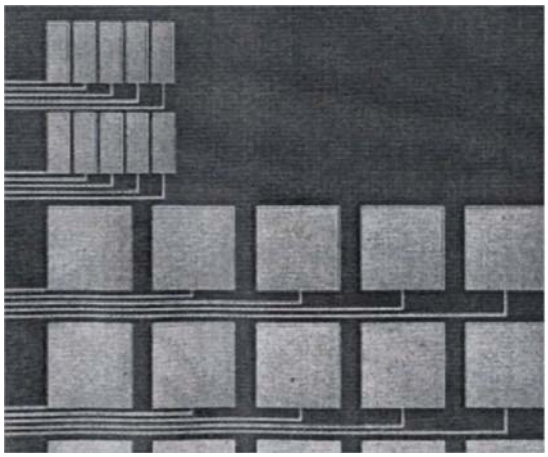

Figure 2.4-81*:* Pixel readout by Si_3N_4 - isolated micro tracks. Microscopic image of a pixel structure on a 1.3 µm thick diamond membrane. The small pixels are (110 x 290) $µm^2$ and the large ones (400 x 400) $µm^2$. The width of the tracks is 15 µm and their pitch is 30 µm.

For fast micro-electrode readout providing a large dynamic range as needed for HI measurements no suitable ASIC exists yet. For CBM at FAIR solutions to readout the diamond start detector, which will be a (20 x 20) mm^2 micro-strip detector of a pitch of 50 µm at a strip width of 25 µm, are currently developed. The electronics would fit also for beam monitoring and tracking at Super-FRS.

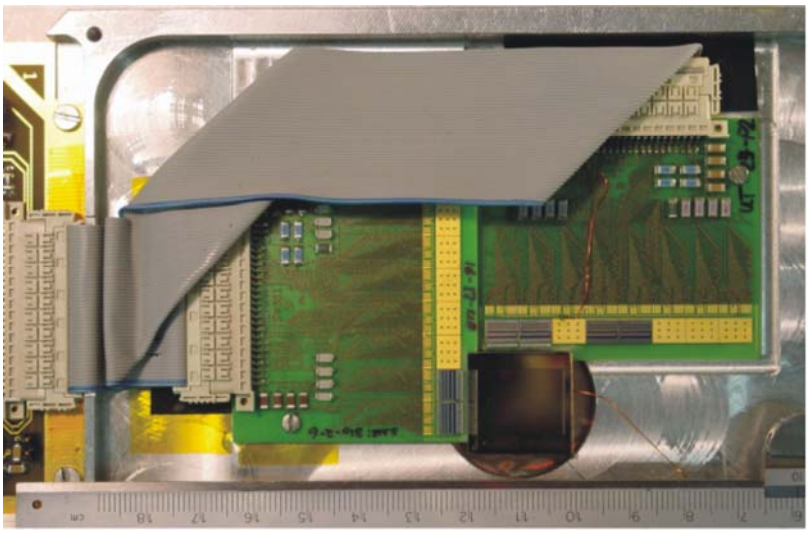

Figure 2.4-82*:* Two hybrids carrying PC diamond strip detectors and readout chips. The (2 x 2) cm² big sensors of a strip- and readout pitch of 50 µm are centred over a hole in the aluminium frame (from RD42 collaboration).

The APV25 ASIC [25] has been tested and used for the readout of diamond signals stemming from heavy ion signals and the Hades TRBv2 [26] board can be used with a GTB or Ethernet based readout (see Figure 2.4-83). The board is equipped with an ETRAX processor running an embedded Linux and can be readily used as EPICS instrument in a slow control chain. A Virtex 4 FPGA coupled to a 500MHz Tiger Shark digital signal processor and 128MByte SDRAM is installed on the readout board, so that complex tracking algorithms together with automated calibration and monitoring processes can be implemented.

Figure 2.4-83*:* APV25 based readout board for diamond detectors to be coupled with the HADES TRBv2 readout board.

The expected radiation hardness of CVD diamond is the most important material property initiating the research and development of diamond detectors. For the tracking of minimum ionizing particles (mip) in the LHC experiments ATLAS and CMS [27] as well as for a variety of heavy ion applications with high luminosity beams [28] diamond detectors have been already developed. In the case of mips no increase in leakage current and unchanged collected

charge is obtained for all kind of particles up to a fluence of about 10^{15} particles/cm². However, the heavy ion dose which starts damaging CVD diamond is still unknown. Currently as a lower limit about 10^{13} cm^{-2}, ^{12}C ions (at 1-2 GeV/u) and ^{131}Xe ions that were even stopped in the detector material have been already applied without any degradation of these detectors.

According to the fragment distribution as shown in Figure 2.4-106 we would expect an intensity of 10^{12} uranium ions per spill on a (10 x 20) mm² area which corresponds to an annual dose of $10^{18}/cm^2/y$. Our calculations have shown that the material as such will survive such intensities; the question to be investigated is now whether a thin detector film can stand such a dose without getting blind. The beam catcher detector arrays would then have an active area of (40 x 20) cm² build from the cheapest poly crystalline as grown CVD-D material. They will be freely movable over the full aperture of the Pre-Separator. A spatial resolution of about 1mm is considered to be ideal for monitoring the fragment distributions. It has been already demonstrated, that the readout electronics can be safely placed about 1m away from the detector system without degradation of the electronic signals. However, a detailed study has to be performed how to build a 600-channel readout and cabling for these detectors.

2.4.6.2 Diagnostics for Slowly Extracted Beams

We define slow extraction as extraction times that are above 100ms for the Super-FRS. Beam diagnostics systems will be installed in all intermediate foci PF(0-4), MF(1-12) with a standardized active area of (40 x 20) cm² whenever possible (at MF11 (90 x 20) cm² will be needed for the LEB). Two systems will be placed at PF(0, 2, 4) and MF(1-12) to allow an angular measurement. At intensities above 1 nA in the Pre-Separator, beam induced fluorescence (see section 2.4.6.1) has to be used. If the energy deposit/mm stays below 100 mW current grids [29] are routinely used to measure beam profiles. At even lower intensities (< 100 kHz) usually multiwire chambers or gems [30] with single wire or single pad front-end readout boards will be used to measure beam particles event-by-event, thus allowing tracking through the separator (see also section 2.4.6.5). This standard instrumentation is chosen for its moderate system cost. Whenever possible a continuous recording of the beam positions will be done to allow automatic steering of the beam to the nominal position.

Additional standard tracking detectors, presently operating at the FRS, are the Time Projection Chamber (TPC). The high efficiency at 100-200 kHz (see Figure 2.4-84) allow them to be used as in-beam detectors for experiments using slow-extraction beams, Available drift volumes are (20 x 6,8,10) cm^2. They are filled with a P10 gas mixture at 1 bar pressure. Using a standard VME readout (see Figure 2.4-84), reading two x-position and 4 y-position measurements, σ_x=0.1 and σ_y=0.05 mm can be achieved, respectively. Such detectors are ideal for precise momentum-measurements experiments.

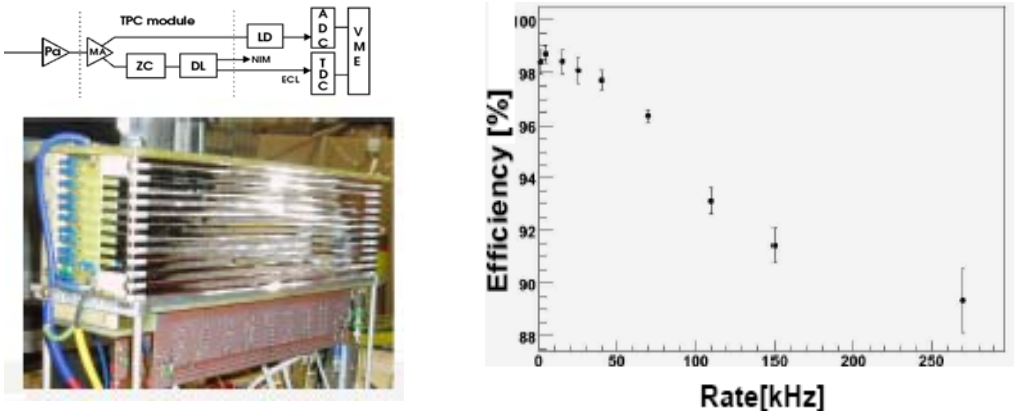

Figure 2.4-84*:* Left panel: TPC detector and associated electronic scheme. Right panel: TPC efficiency measured for ^{129}Xe beam at 500 MeV/u as a function of the particle rate.

In this case (momentum measurement) the detector is working as position-sensitive detector recording single ions. The readout can be improved to reach a dead-time free readout speed of 160 kHz/wire by making use of the CBM-XYTER ASIC and readout boards. These boards are based on the N-XYTER [31] ASIC for the DETNI project, and are being currently developed at GSI.

2.4.6.3 Diagnostics for Fast Extraction

For fast extraction mode and intensities above 1 nA capacitive pickups [32] are routinely used to deduce the beam position at GSI for the ESR experiments. We will use these pickups for the Pre-Separator of the Super-FRS. The usual current grids and multi wire chambers (see section 2.4.6.2) can be used to measure fast extracted beams at lower intensities. For beams with a spill length as short as 50 ns, single ion tracking is no longer feasible, and only measurements of the bunch profile can be performed. This problem arises from the large amount of charge (up to several nC) which is deposited in the detector. The use of a gas detector leads to a long integration time for complete charge collection (~ μs). This causes a spreading of the charge and thus strongly affects the measurement of the beam profile. Therefore the use of fast electronics and lower gas pressure has been proposed. Recent investigations, which are still ongoing have shown that it is advantageous to operate the gas filled current grids at reduced pressure or even without gas for fast extracted beams. The gas supply system for the relevant detector systems should therefore provide gas mixtures at reduced pressure down to 1 mbar.

A Beam Profile Detector (BPD) prototype using a variable gas pressure and delay-line read-out was developed in collaboration with the University of Bratislava within the NUSTAR 3 task of the FP6 EU Design Study for the Super-FRS facility. It was successfully tested in November 2007 at the FRS with fast extracted carbon beams at the highest intensities (several 10^9 ion/spill) from SIS18. On-line measurements showed excellent stability of the response (beam profile in both x and y) with still considerable reserves for even higher beam intensities. The detector has a modular design with a basic module size of (100x100) mm^2. In Figure 2.4-85 (left panel) a BPD of (200x100) mm^2 active area made by two basic modules is shown together with the front-end electronics. The detector volume is filled with a gas of Ar + 10 % CO_2. It contains 3 x 50 wires. Each wire with 2 mm pitch is directly connected to 3 integrated passive delay lines for x and y position measurements. The integrated electronics containing pre-amplifiers, amplifiers and zero crosser worked reliably. The digitalization of the fast signal was obtained by using a Flash ADC SIS3301. An example of measured beam profile in x is shown in Figure 2.4-85 (right panel).

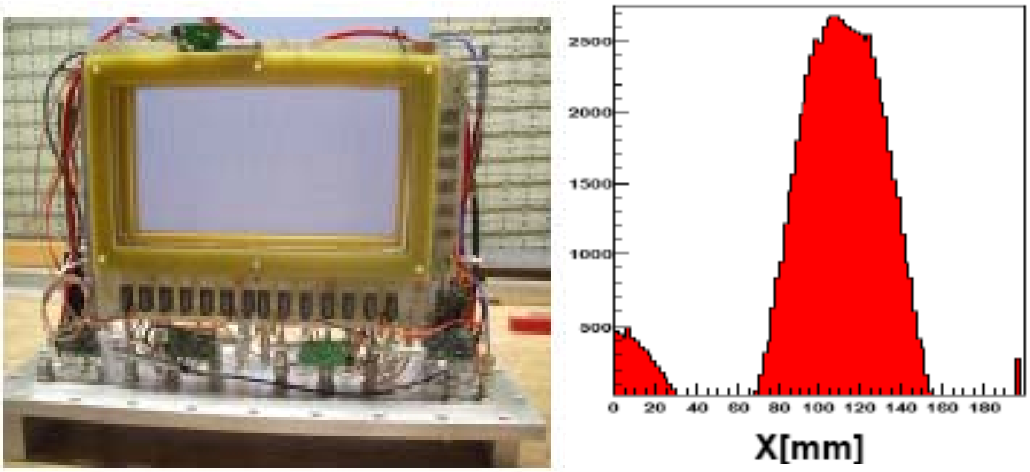

Figure 2.4-85*:* Left panel: BPD prototype with front-end electronics. Right panel: Measured x-direction beam profile of ^{12}C ions at 400 MeV/u with an intensity of $1.6 \cdot 10^9$ ion per 300 ns.

In addition, the BPD was tested as in-beam detectors for experiments using slow-extraction beams at 3 MHz rate. Similar to time projection chamber (TPC) detectors, in this case it was working as position-sensitive detector recording single ions.

As in the case of the TPC described in section 2.4.6.2 the readout can be improved to reach a dead-time free readout speed of 160 kHz/wire by making use of the CBM-XYTER ASIC readout boards.

2.4.6.4 Luminosity Monitor (SEETRAM)

We want to perform luminosity measurements at two positions in the Super-FRS:

(i) in front of the quadrupole triplet prior to the target area,
(ii) at the entrance of the main separator (PF4).

(i) The intensity of the primary beam delivered by SIS12/18 or SIS100/300 will be measured outside the target zone. The advantage of this arrangement is the enhanced accessibility, and to keep the hot zone technically as simple as possible. Two ladders for mounting are foreseen in this diagnosis box, both covering detectors with an active area of (10 x 10) cm². The first one will be equipped with a Resonant Beam Transformer and a Diamond counting detector. The second one houses a SEETRAM (Secondary Electron Emission TRAnsmission Monitor) counter and a Cryogenic Current Comparator. Resonant Beam Transformers [33] are the work-horses at the current GSI facility. They can be used from 1 nC up to 1 µC with a resolution 10 pC (rms) for bunches with a maximum pulse length of 1.5 µs. Thus, they are perfectly suited for the detection of fast extracted pulses. Cryogenic Current Comparators are usable for DC currents down to about 100 pA [34] and can be used for the slow extracted beams. The SEETRAM counter [35] was developed for the FRS. Its operation is based on the emission of secondary electrons from thin metal foils (see Figure 2.4-86) by the passage of the projectiles. It can be used for slow and fast extracted beams. Its use for the Super-FRS is limited to intensities up to about $10^{10\text{-}11}$ particles/spill to avoid damaging of the detector.

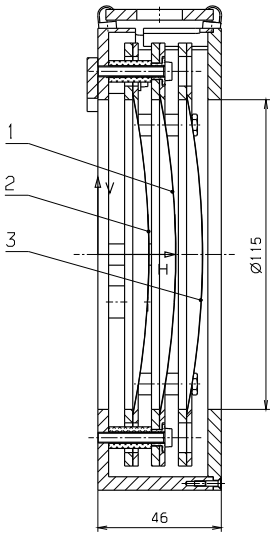

Figure 2.4-86*:* Layout of the SEETRAM counter. It consists of three titanium foils with 10 µm thickness each. Each foil has a diameter of 11.5 cm. They are mounted perpendicular to the beam axis. The outer foils (#2 and #3) are connected to a voltage of +80 V. They and their supporting aluminium rings form the detector housing. The middle foil (#1) is supported by two Teflon rings and is insulated against other parts of the detector. The foils are curved in order to reduce the sensitivity to mechanical vibration of the beam line. Secondary electrons emitted from the middle foil are collected by the two outer foils. The created current in the middle foil is measured by a current digitizer (CD1010 developed at GSI).

In order to calibrate the current measurement up to now the calibration proceeds via two steps: first a scintillator detector is used in counting mode; second an ionization chamber takes over in order to calibrate the SEETRAM detector. For the Super-FRS we will benefit from the high counting rates that can be taken by a diamond detector (10 x 10 cm², PC-CVC-DD (AG)) and thus be able to leave out the ionization chamber. Thus we will be able to reduce the setup and calibration phase for the experiments. The diamond detector here can also be used at reduced rates of $10^{9...10}$/spill – as has been done already for the SIS18 – to analyze the spill structure after slow extraction from the different SIS rings.

(ii) For the entrance of the main separator a SEETRAM counter and a diamond detector are planned to be used for the luminosity measurements. The diamond counter can be used (as shown in section 2.4.6.5) also as start counter for a time-of-flight measurement. The expected spot size is here about (2 x 3) mm² as given by the magnification ($M_x = 2$, $M_y = 1.5$) of the Pre-Separator optics. With rates up to 10^9 /s uranium ions, this is just at the limit of what can be counted using a PC-CVD-DD. One may consider using single crystal material here. The recent available SC-CVD-D material is presently investigated by NoRHDia [36]. The charge collection efficiency of SC-CVD-D detectors amount to almost 100 %, and the signal amplitudes are uniform over the detector area, which is not the case for PC-CVC-DD. However, due to much lower concentration of traps the detectors behave as fast drift chambers. Therefore, the count rate capability is lower and only 50 MHz are manageable. Instead of single particle counting one should investigate the possibility to perform a current measurement here, which becomes favourable due to the uniformity of the pulse heights.

2.4.6.5 In-Flight Fragment Identification (Bρ, ΔE, ToF)

Magnetic rigidity measurement

The magnetic rigidity can be deduced from a position measurement in the dispersive planes, two scenarios are considered: (a) determination during setup (b) continuous monitoring. Option (a) requires a good knowledge of the relative magnetic field as a pilot beam is centred with known Bρ, and the measured B-field can be calibrated using an effective radius for the dipole magnets. Unknown magnetic rigidities can thus be determined. The centring process can be done at reduced rate using the standard detectors (see sections 2.4.6.2 and 2.4.6.3). Option (b) is more demanding but also required by several NUSTAR experiments (e.g. the R³B collaboration). The idea is here to gather additional information on the incoming beam by measuring its displacement in the dispersive plane (MF2) of the separator event-by-event. This method [37] has been successfully applied at the FRS to improve the mass resolution in the ALADIN-LAND reaction setup for fission fragments that were transferred to Cave B, by using a scintillator strip array. The granularity of the strip setup determines the maximum rate that can be dealt with typically a few MHz/strip. Instead of this conservative approach the use of PC-CVC-DD would be advantageous.

For this latter approach, a rate capability of 100 MHz/mm could be reached with a 300-500 μm thick detector array, polished to a roughness that is below 10 μm – which is consistent with the 3 % accuracy specified by the manufacturers – to avoid a degradation of resolution due to a lack of detector homogeneity. Precise water-dive measurements performed in early PC-CVD-DD research show that even PC-CVD as grown diamond material is tight, meaning without serious amount of pinholes: no water absorption has been measured [38]. This is an indication that it is valid to assume roughly the diamond mass density to 3.5 g/cm^3 over the whole bulk. However, the much higher concentration of grain boundaries in the nucleation side of the film may lead to residual graphite material ($\rho_{graphite} \approx 2.2$ g/cm^3) on this side which can reduce the average density. R&D work is underway at the FRS to ensure quality of the PC-CVD material. Details for the diamond detector setup can be found below. The online monitoring of the stability of the separator settings will be used for feedback loops to perform e.g. automatic centring through the setup. This requires a combined analysis and simulation framework in order to be able to determine the offsets and compute the corrections. Here accelerator controls and Super-FRS instrumentation have to be coupled in the most efficient way.

Specific energy loss measurement

For the required charge resolution via the specific energy loss we consider MUSIC (multiple sampling ionization chamber [39] detectors as the optimal choice. These detectors can currently measure rates up to 200 kHz. There are developments underway to increase these rates up to a few MHz [40]. These detectors will be positioned at the foci MF(2, 4, 7, 10) with an active area of (40 x 8) cm², and be operated continuously at the final focal planes to identify fragments during experiments.

Time of Flight measurement

At present plastic scintillator detectors are being used in the FRS to perform the TOF measurement, leading to a restriction in rate of a few MHz on the detector. In the dispersive plane of the FRS this problem can partly be overcome by using a segmented scintillator strip detector. For the Super-FRS, we will investigate also the possible use of diamond detectors, providing both position information and timing signals at the MF(2, 4, 7, 10) focal planes with an active area of (40 x 5) cm² using a pitch of 1 mm. For the foreseen rates these detectors would be optimal with respect to rate capability and radiation hardness. Using various heavy projectiles the intrinsic time resolution of PC-CVD-DDs has been measured frequently to be well below 50 ps. Recently, the FOPI collaboration achieved a σ_{intr} = 22 ps with ^{181}Ta ions of 1 GeV/u (Figure 2.4-87). A similar value (σ_{intr} = 29 ps) has been measured in the HADES setup using ^{52}Cr ions of 650 MeV/u.

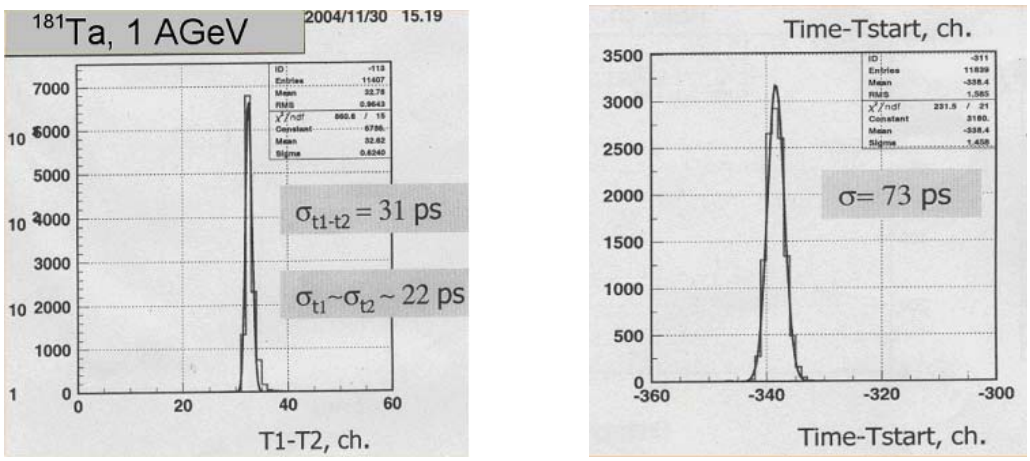

Figure 2.4-87*:* Intrinsic time resolution of PC-CVD-DDs demonstrated using ^{181}Ta ions at 1 GeV/u. (PRELIMINARY data, measured by the FOPI Collaboration). Time spectrum measured with two PC DG diamond detectors of a thickness of 500 µm mounted perpendicular to the primary beam (left), compared to the time spectrum measured with one diamond against the time given by the currently used FOPI start detector (plastic scintillator detector, right).

At PF4 (see section 2.4.6.3) a (4 x 4) cm² PC/SC-CVD-DD can be used also as time-of-flight detector whenever suitable. The time resolution of SC-CVD-DDs is expected to be at least as good as for PC material. The electronics used in the FOPI run consisted of a 16 channel front end board with preamplifiers designed for RPC readout, and a version for scintillator detectors also exists. These boards can be coupled to the GSI Tacquila front end readout system [41], that provides excellent time resolution at a moderate channel costs of about 55 €/channel. Apart from TAC based systems, the GSI ASIC group is developing DLL based solutions [42] for fast timing measurements that provide the envisaged resolutions with the advantage of being inherently free from the need of an external calibration.

2.4.6.6 Data Acquisition

The main task of the Super-FRS data acquisition (DAQ) is to provide on-line data about the production and separation process in the separator. It is clear from the beginning, that there are rate limitations, that will set the limit between event-by-event and integrated data. For different experiments in the experimental branches different classes of information are required.

Fragment Monitoring

As example, the ring experiments only depend on the history of the pulses delivered to the CR/RESR/NESR complex, e.g.:

- intensity,
- charge and mass distributions,
- contaminants,
- deviations from nominal beam optics.

They are of interest as for bunches all event-wise information gets lost in the transfer processes. However, this is also the information that is needed as slow control feedback data, which is described in the general NUSTAR-DAQ section. The collection of these data will be done by the local stand-alone Super-FRS DAQ together with an on-line analysis process that runs as data server for the Super-FRS's slow control and the experiments bunch monitoring. The data server should provide a list of information it can deliver and provide a selection mechanism. Together with the information provided by the accelerator sections one is then able to monitor the full production process. This will also allow the accelerator controls to get specific feedback information from the experiments, allowing a very effective optimization of the setup data (see general NUSTAR-DAQ section). The necessary R&D will be done in close relation with the accelerator controls group.

Tracking experiments

Another class of experiments requires tracking ions through the separator, e.g.:

- experiments performed at the final focus (MF4) of the Super-FRS,
- experiments in the high energy branch R^3B.

Here the main issue is to record event-wise information about individual particles through the setup. As the selection process leads to substantial reduction factors (typ. 10^{-6} PF4 → Caves, typ. 10^{-3} MF2 → Caves), coincidences have to be build from the end of the beam line. This means, especially for the diagnostic detectors at the entrance of the main separator, that at rates of several 10 MHz the spread in velocities for different isotopes with similar Bρ will lead to overlapping events. This problem corresponds to the task of tracking particles with small yields while reconstructing their interaction vertices as in high energy physics. Here this is usually overcome by storing the data first in the front-end electronics while subsequently transferring and reducing it in a multi step triggering process. In our case this problem can be reduced to the problem of finding a plausible candidate in a certain time interval for an identified particle at one of the experiments.

There are several solutions, as discussed below, which have to be evaluated in close collaboration with the planned experiments:

i. a suitable reduction rate can be achieved already by demanding a coincidence window, where events are taken. The particular coincidences are evaluated off-line.
ii. Coincidences are fully evaluated on-line.

Option (i) can be realized in several ways. The conventional approach is to adjust cable delays to digitize all data from the experiment within a coincidence time (e.g. given by a gate). This is,

however, also the most inflexible approach in view of the different DAQs that should be coupled together. Another option is to perform full data readout with subsequent selection of suitable events. This requires efficient way of addressing data into the past, corresponding to a certain delay time. The detector system at the two locations PF4 and MF2 should provide both absolute times for a time-of-flight measurement in addition a position in horizontal direction for MF2. This can be realized using a circular ring buffer to store timestamps and positions for the detector systems. Typically one would expect some 10...20 Bytes/event information here. Given a sampling frequency of about 100 MHz this corresponds to a data rate of 1-2 GByte/s for the buffer input. A similar system has been already realized for the mass measurements at the ESR, using commercially available oscilloscopes for sampling. We want to develop a dedicated readout board using contemporary FPGA designs. The design will be an extension of the existing GSI taquila system (see NUSTAR-DAQ section). The board should be synchronized by the common time distribution system (see NUSTAR-DAQ section). It should store all channels synchronously with the time-stamp given by the sampling clock into its circular ring buffer. The relative time within the samples is then given for every hit by the ADC value form the TAC. Such, a precision of 50-100 ps can be reached for the timing information. The digital delay can then be realized by reading out the circular buffer with a certain offset of the readout pointer as the data is stored in fixed time intervals. The reduced data rate is then expected to be a few MByte/sec (given by the suppression factor to the cave) only. Apart form this option we will look for other developments for the different FAIR experiments.
In order to avoid long storage times, we foresee to place this readout system in the Super-FRS DAQ electronics-room, which should be nearby the R^3B and LEB counting rooms. In that case signal propagation and beam propagation downstream would be aligned and the trigger information could be provided directly to the readout modules, thus saving additional delay times.

Standard electronics

The remaining particle identification and tracking can be realized, using a conventional trigger scheme. The existing VME readout scheme will be gradually updated with the upcoming novel developments described in the NUSTAR DAQ section. In order to come up with a fast readout scheme we will investigate the possibility already to reduce the data before building events to be written to mass storage for all detector systems (e.g. tracking detectors could already deliver pre-processed positions instead of raw times). We expect about 100 words of data at a rate up to 1-10 MHz corresponding to 100 MByte/sec up to 1 GByte/sec.

2.4.7 Vacuum

2.4.7.1 General Layout

The high-intensity primary beams that will be delivered by SIS100/300 in the final stage of FAIR require a special layout of the first section of the Super-FRS that contains the production target(s) and the beam catchers. Following concepts developed at other radioactive-beam facilities (e.g. PSI, TRIUMF-ISAC, RIKEN-RIBF and GANIL-SPIRAL), we will apply the "plug" concept in the Pre-Separator up to PF1. This concept involves:

- a combination of beam-line inserts (targets, beam-catchers, slits, diagnostic detectors etc.) with local mobile shielding that can be removed as one unit ("plug");
- a compact shielding of the beam lines and vacuum chambers;
- vertical insertion of the plugs along rails into the vacuum chambers;
- vacuum seals and media connection in a moderate-radiation area above the local shielding that can be serviced manually after shutdown.

Schematically, this concept is depicted for the production-target area in Figure 2.4-126. The compact shielding reduces the shielding volume (and thus cost) and avoids air activation. Plugs can be removed individually from their common vacuum chamber. The vacuum chamber itself can be separated from the beam line by inflatable “pillow seals”. A similar scheme will be applied to the beam-catcher modules which are located in the sections between the first dipole magnets and at the Pre-Separator degrader unit.

The positions of the pillow seals in the Super-FRS are indicated by the positions 1 to 13 in Figure 2.4-88. Elastomer seals can not be used because of the radiation level in this area. A test stand to measure the leak rate of a 200 mm pillow seal is shown in Figure 2.4-89.
The leak rate of the pillow seal was determined in dependence of the contact pressure and the surface roughness of the seal and the counterplates, respectively. The best achieved leak rate so far is approximately 3×10^{-6} mbar·l/s.

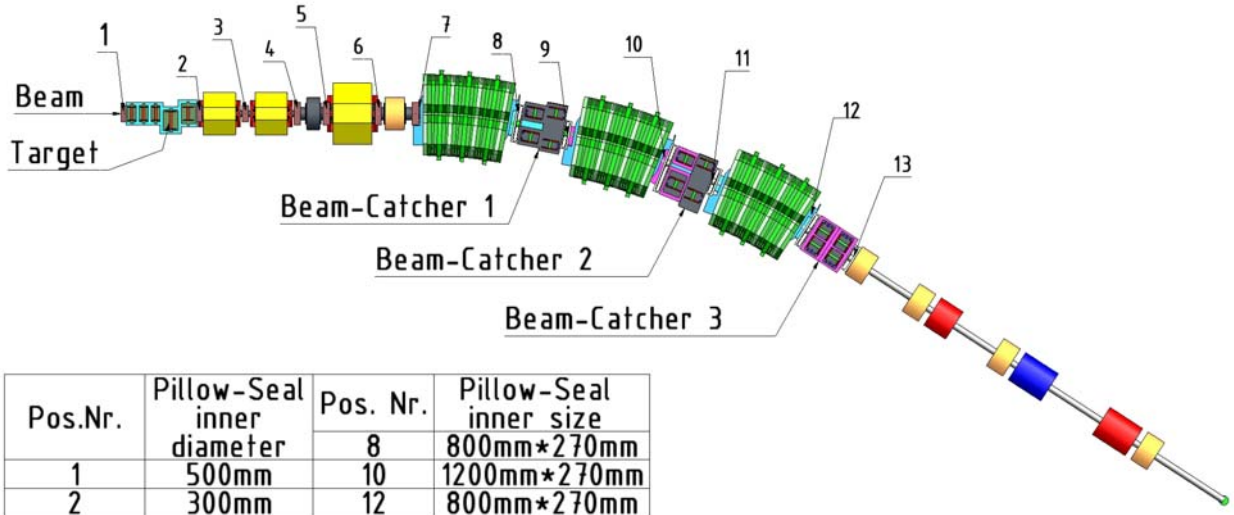

Pos.Nr.	Pillow-Seal inner diameter
1	500mm
2	300mm
3	300mm
4	500mm
5	500mm
6	500mm
7	500mm
9	500mm
11	500mm
13	500mm

Pos. Nr.	Pillow-Seal inner size
8	800mm*270mm
10	1200mm*270mm
12	800mm*270mm

Figure 2.4-88*:* Pillow seal positions in the Super-FRS Pre-Separator and required sizes.

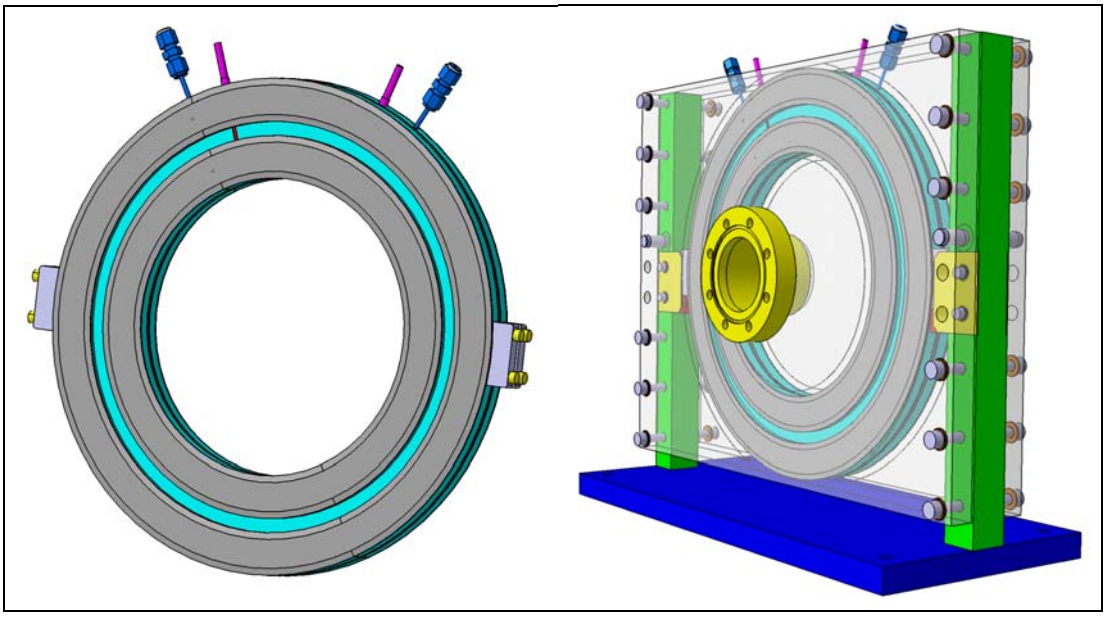

Figure 2.4-89*:* Pillow seal test stand.

It is expected that downstream from the mid-plane of the Pre-Separator (PF2) much less activation can be expected (at least 2-3 orders of magnitude), which is equivalent to dose rates similar to the present FRS. Consequently, the same concepts developed and applied successfully for FRS will be foreseen there.

2.4.7.2 Maintenance and Handling of Highly-Radioactive Components

The service platform mentioned above, where all radiation-sensitive devices are located (pumps, polymer vacuum seals, media connectors) allows manual intervention during shut-down periods. After media and vacuum disconnection, plugs will be removed vertically by

a heavy-load crane and will be inserted in shielded transport containers in which they can be safely transported to either a storage position (in case a new module is to be inserted) or a hot cell (in case repairs have to be performed on a module). The transport container ensures that highly-activated components are never exposed to the surrounding areas and that manual intervention is possible e.g. in case of crane malfunction.

2.4.7.3 Maintenance and Handling in Low-Radiation Areas

Contrary to the high-radiation areas, the less activated areas in the Super-FRS will be placed in a wide tunnel (approximately 7 m). Maintenance here can be done by using an industrial robot equipped with appropriate tools to disconnect devices from the vacuum containers and the media and to remove them from their respective flanges. A well-shielded storage area has to prevent radiation damage to the robot during beam-on periods. All other concepts can be easily adapted from current FRS robot operation techniques.

2.4.7.4 Vacuum System

The vacuum system, pumps, valves and controls, will be based on the experience gained at the present FRS. The requirements for the vacuum system of the Super-FRS are mainly determined by the necessity to be coupled to the UHV systems of the storage rings and to the driver accelerator without applying any separation foil. At the relatively low primary beam intensity at the present FRS a thin titanium window is used between the separator and the vacuum of the beam line to the SIS18. At the Super-FRS such a window would not survive the interaction of the high-intensity fast extracted beam. A foil between the achromatic final focal plane and the collector ring would severely disturb the experimental conditions, especially for the heaviest fragments which are not fully ionized at a kinetic energy corresponding to 13 Tm. In summary, we aim at pressures of better than 10^{-7} mbar and will use UHV compatible materials inside the vacuum chambers. For the pump-down a combination of turbo molecular pumps and dry roughing pumps will be used. The residual gas pressure will be of course slightly higher in the Pre-Separator with the pillow seals, the hot materials due the energy deposition of the primary beam and the plug system compared to other sections of the Super-FRS. The vacuum system of Super-FRS will be divided into 15 vacuum sectors. They will be separated from each other by 14 gate valves and 2 quick closing valves.

Two typical vacuum chambers including the corresponding valves, pumps and focal-plane equipment are shown in Figure 2.4-90 and Figure 2.4-91. Standard stainless steal (AISI 304) will be used for vacuum chambers (pumping, diagnostic, etc.).

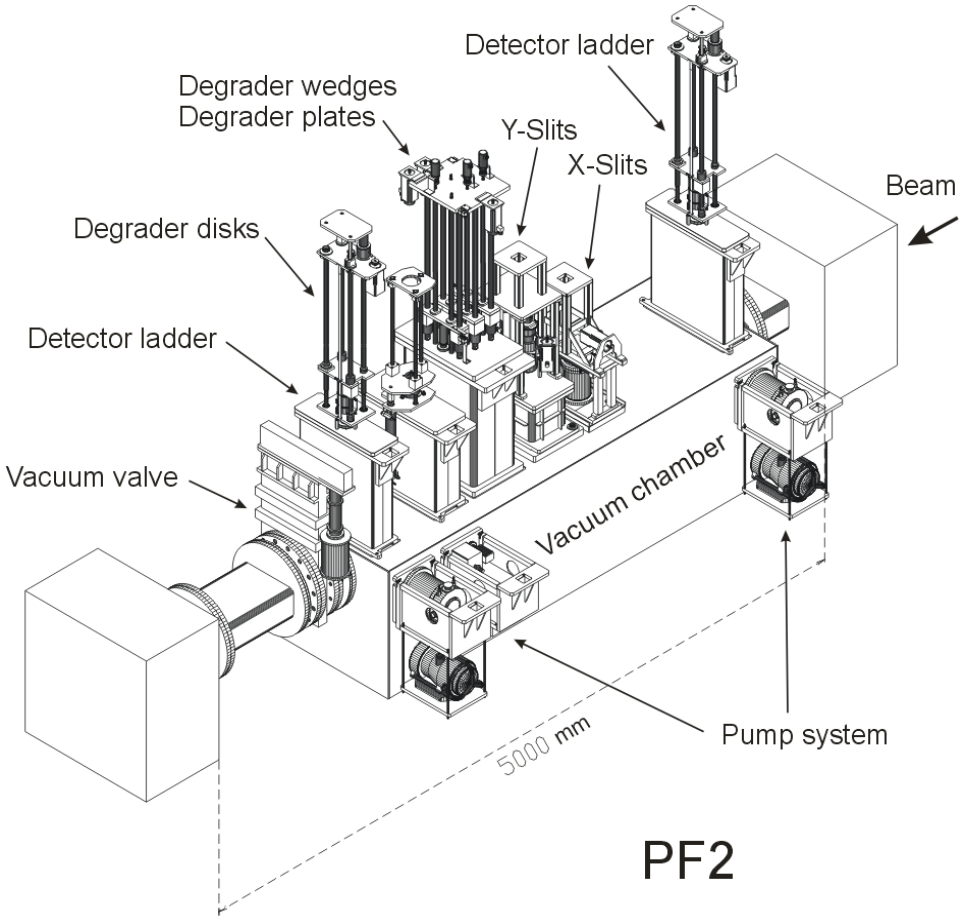

Figure 2.4-90*:* Setup at the mid focal plane of the Pre-Separator (PF2). A complete degrader system is depicted, the vacuum chamber equipped with valve and pumps. In front of the degrader system a pair of slits in x- and y-direction is mounted. Two universal detector systems have been placed at suitable distance in the vacuum chamber to measure the position and angles of the ions at the different intensities. All movable components can be remotely operated.

Since PF2 can have a significant radiation field any maintenance will be done with a robot system. First experience with such robots is presently gained at the FRS, where one device has been installed at the first focal plane. A photograph of the robot at the first focal plane of the FRS is shown in Figure 2.4-93.

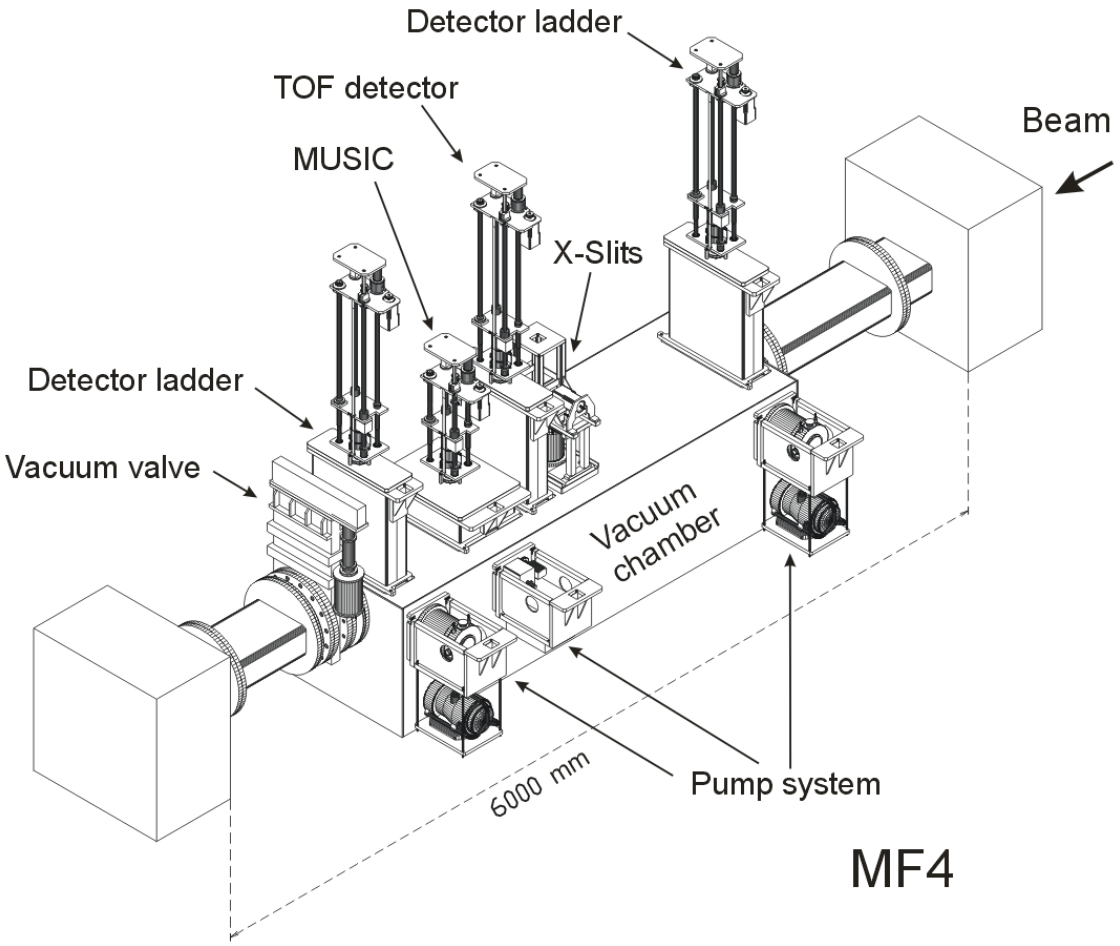

Figure 2.4-91*:* Setup at the final focal plane of the Main-Separator (MF4). The vacuum setup is quite similar to all other focal planes, here at MF4, mainly detectors for in-flight particle identification are installed.

An overview of the total vacuum system of the Super-FRS is schematically shown in Figure 2.4-92.

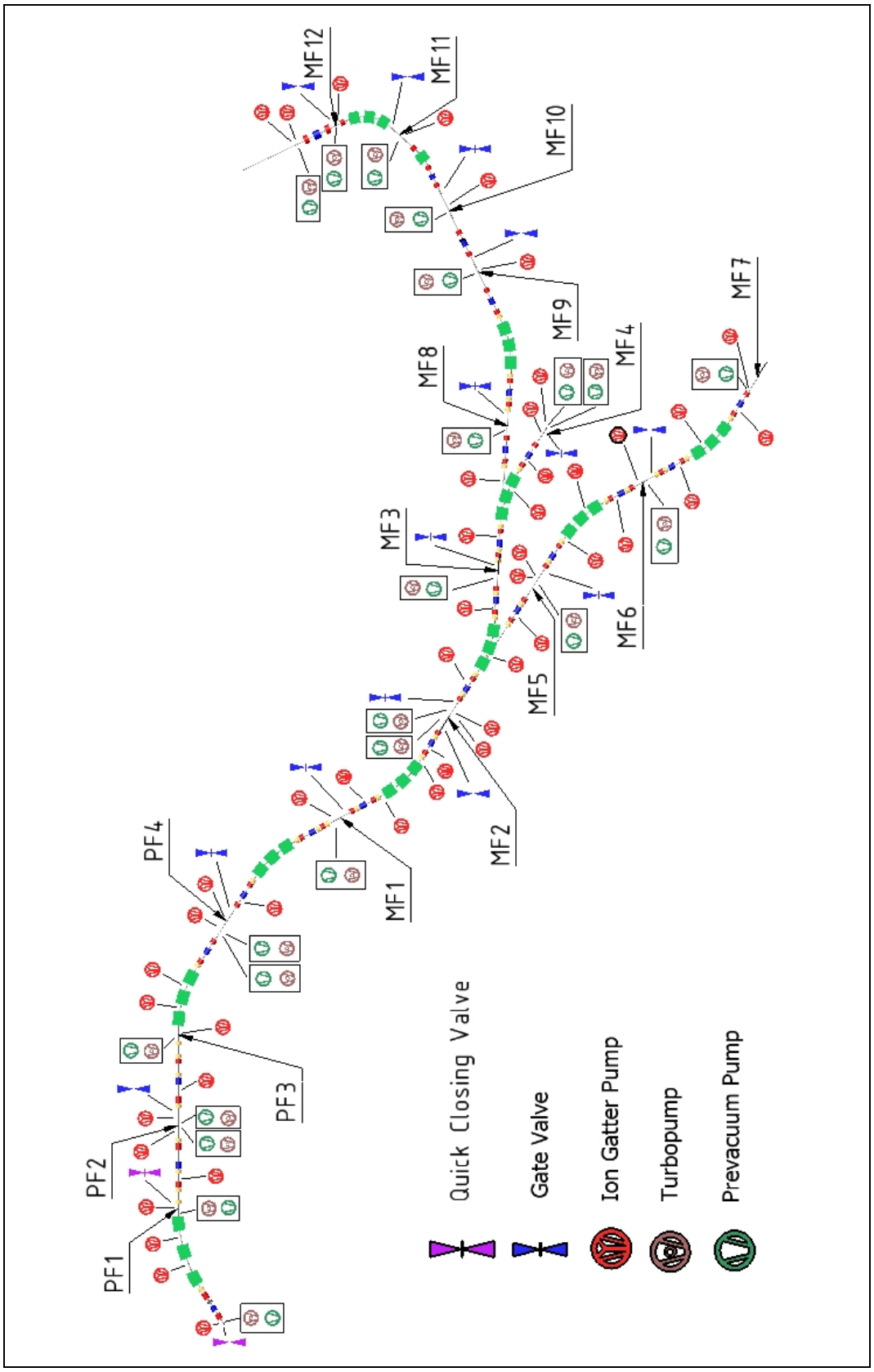

Figure 2.4-92*:* Schematic overview of the Super-FRS vacuum system including dry (oil-free) roughing pumps and valves.

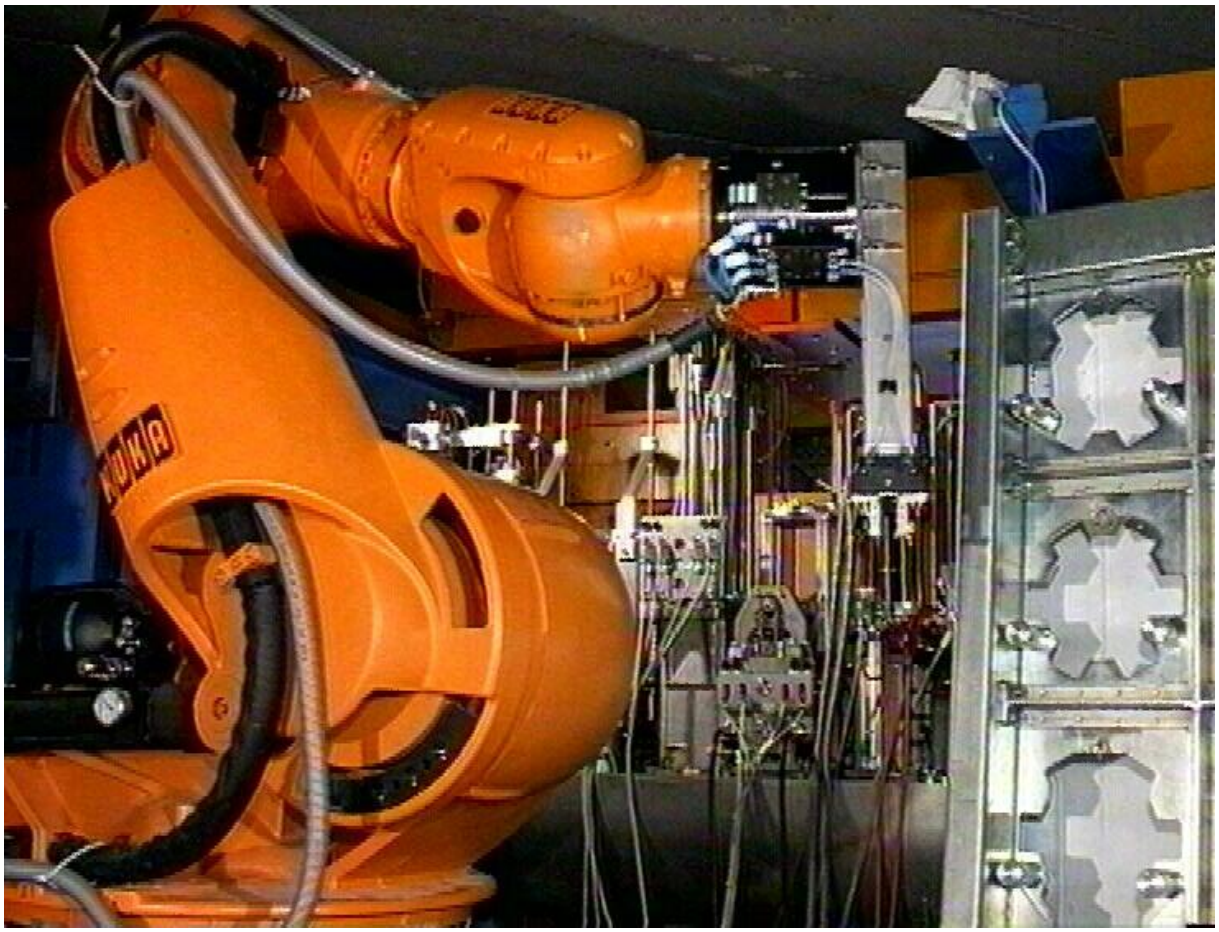

Figure 2.4-93*:* Robot for remote maintenance installed at the first focal plane of the present FRS. A magazin of special tools has been constructed and installed to perform the required maintenance tasks.

Table 2.4-25*:* Vacuum chambers for magnets and diagnostics

Part	Numbers	L*B*H Ø
Target Area		
Target chamber	1	2200*1100*2700
Beam catcher chamber	3	1430*1730*2500
Magnet Chambers		
Radiation Resistent Dipol 1+3 Chamber	2	3200*800*140
Radiation Resistent Dipol 2 Chamber	1	3200*1200*140
Superferric Dipol Chamber long	3	2800*400*140
Superferric Dipol Chamber short	21	2550*400*140
Radiation Resistent Quadrupol 1 Chamber	2	1400 Ø200
Radiation Resistent Quadrupol 2 Chamber	1	1900 Ø400
Radiation Resistent Sextupol Chamber	2	800 Ø400
Superferric Multiplet short	8	2000 Ø380
Superferric Multiplet long	18	7000 Ø380
Pumping and Diagnostic Chambers		
Chamber Type 1	13	3400*1000*900
Chamber Type 2	1	2240*1000*900
Chamber Type 3	1	3400*1300*900
Chamber Type 4	6	1500*1000*900
Miscellaneous		
Bellows	18	Ø400
Pillow Seals (different sizes)	13	Ø500 / 1200*200
Straight vacuum pipes (different length)	13	Ø 400

Table 2.4-26*:* Pumps and valves.

Pump Type	Numbers	Pumping speed	comments
Pumping station roughing	22	1000l/s & 35m³	TMP & dry fore-pump
Ion Pumps (warm)	48	300l/s	DN 160CF
Pumping station roughing for insulation vacuum	60		

Valves	Numbers	Type	comments
Gate Valves	12	Viton	DN 400 CF
Gate Valves	4	all-metal	DN 400 CF
Fast Valves	2	all-metal	DN 400 CF
Valves for insulation vacuum	60	viton	DN 160 CF

2.4.7.5 Technical Drawings

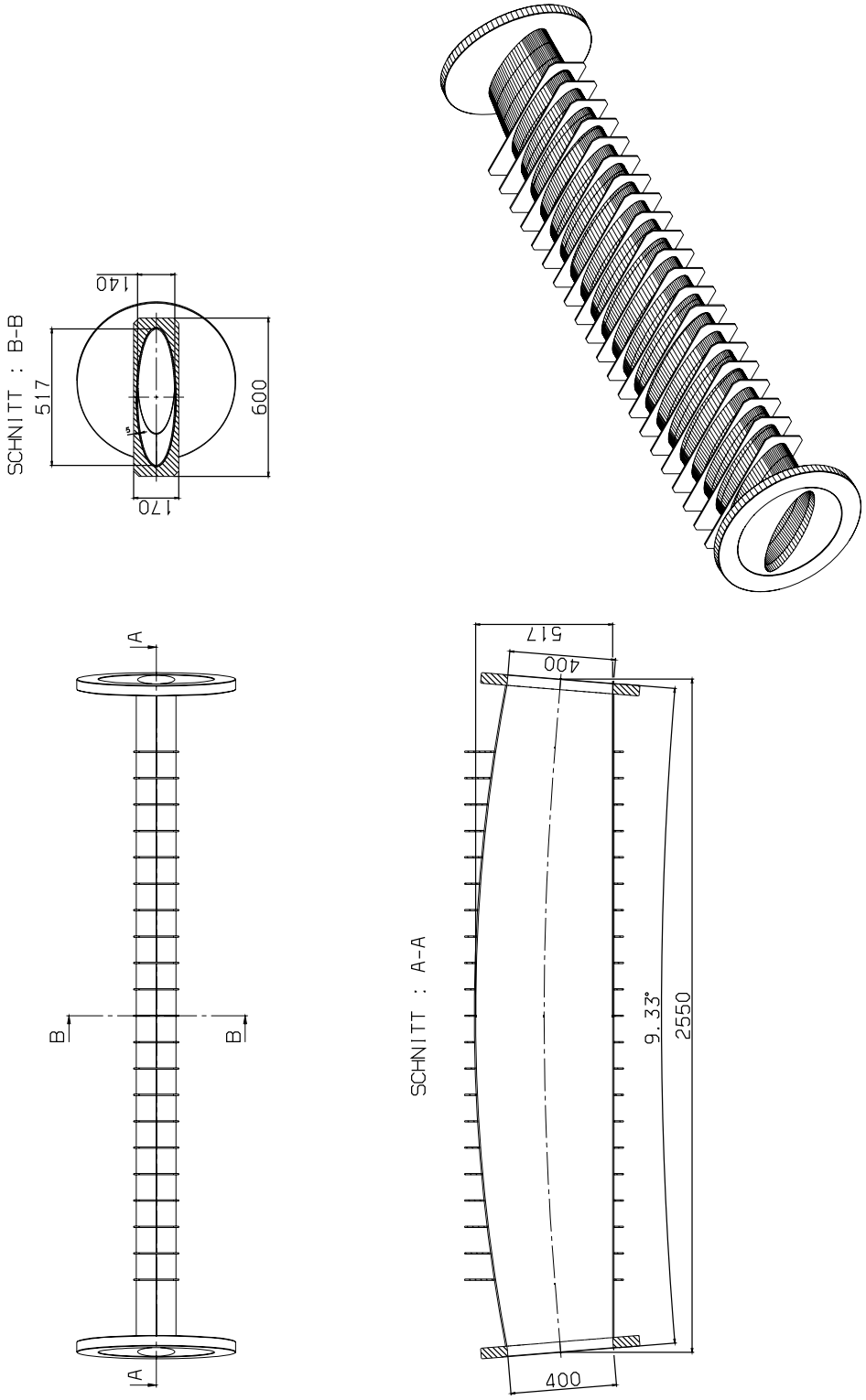

Figure 2.4-94*:* Vacuum chamber of a superferric dipole.

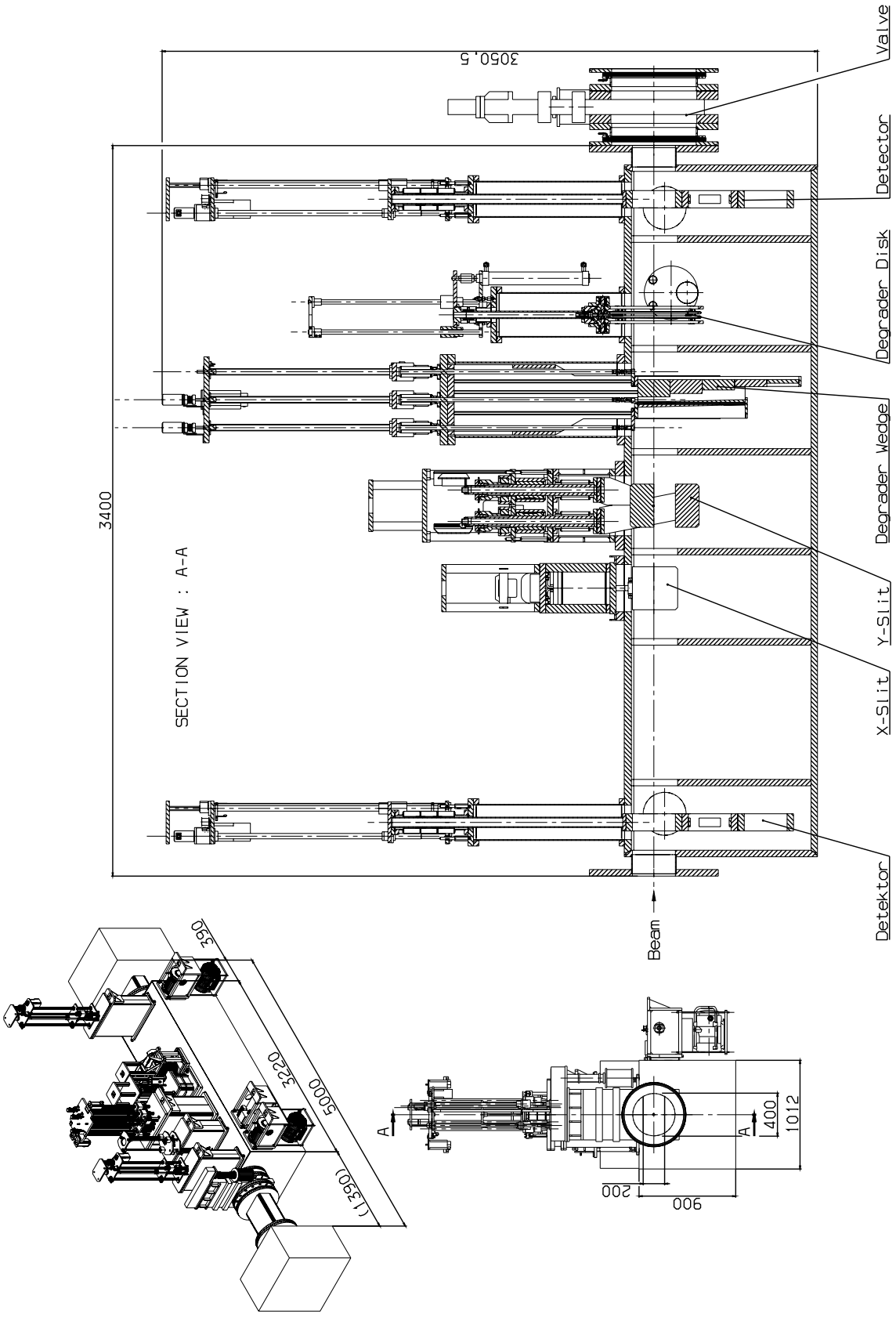

Figure 2.4-95: Diagnostic chamber including the setup at the PF2 focal plane (middle plane of the Pre-Separator).

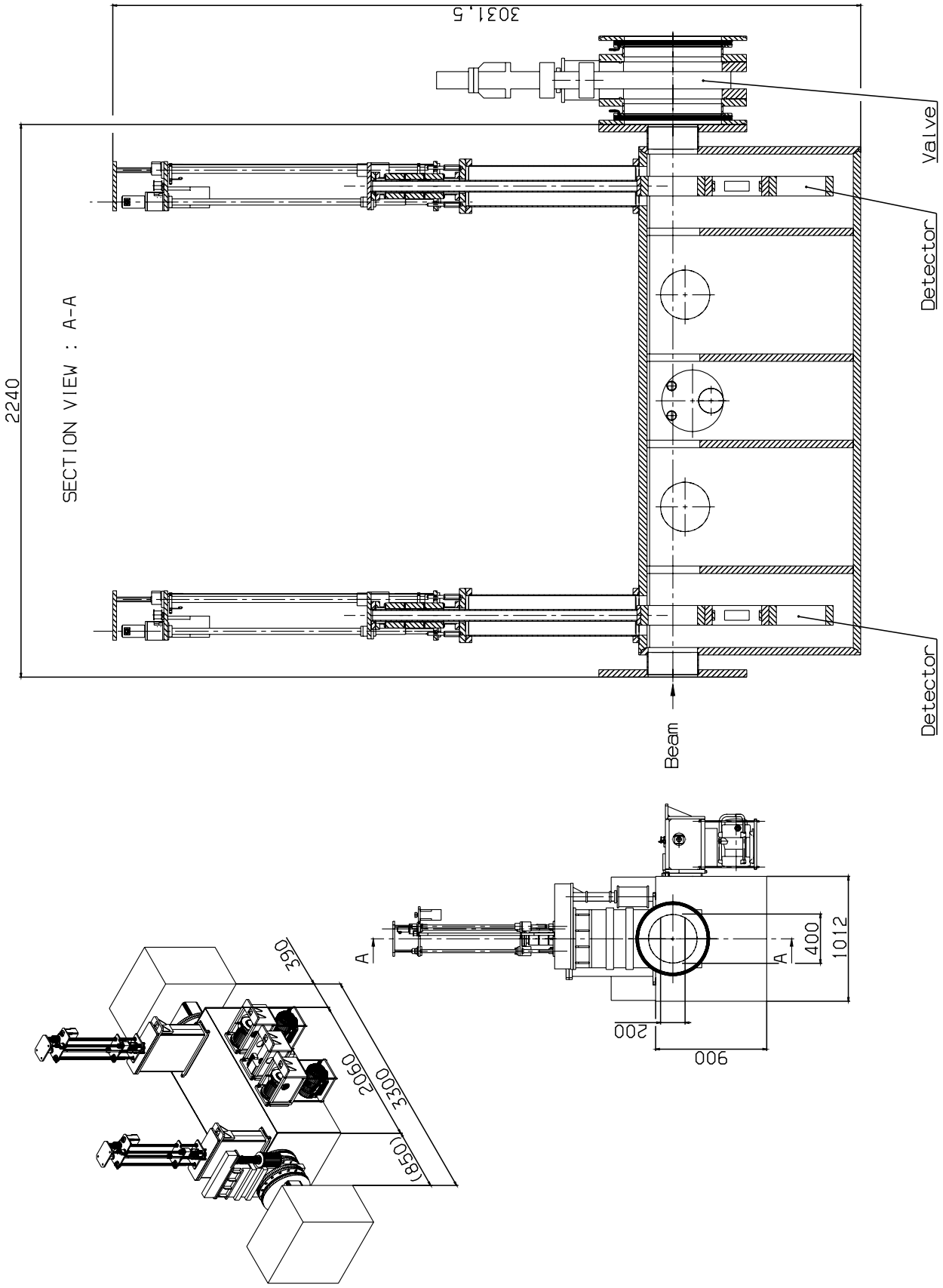

Figure 2.4-96*:* Diagnostic chamber including the setup at the PF3 focal plane.

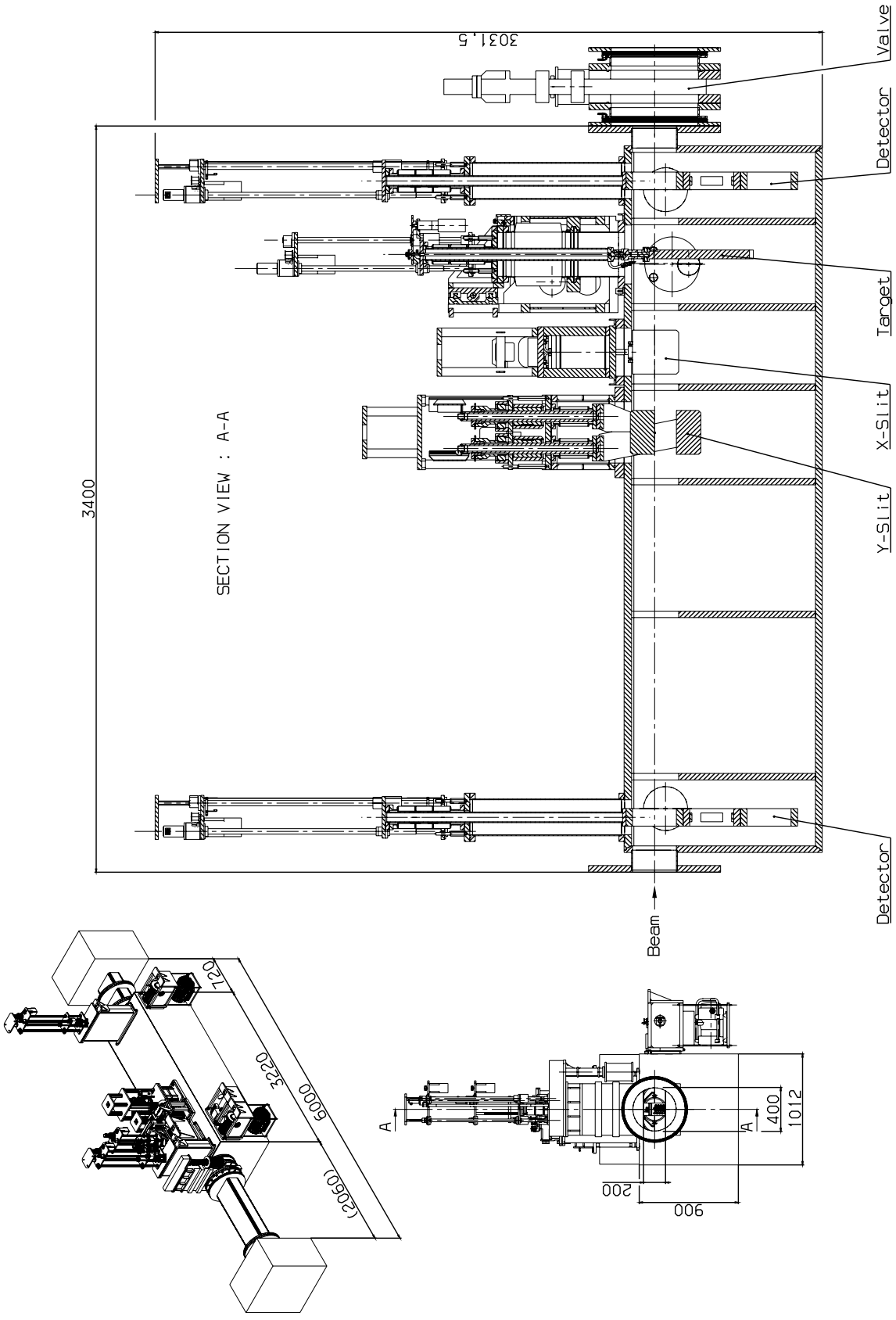

Figure 2.4-97*:* Diagnostic chamber including the setup at the PF4 focal plane (end plane of the Pre-Separator).

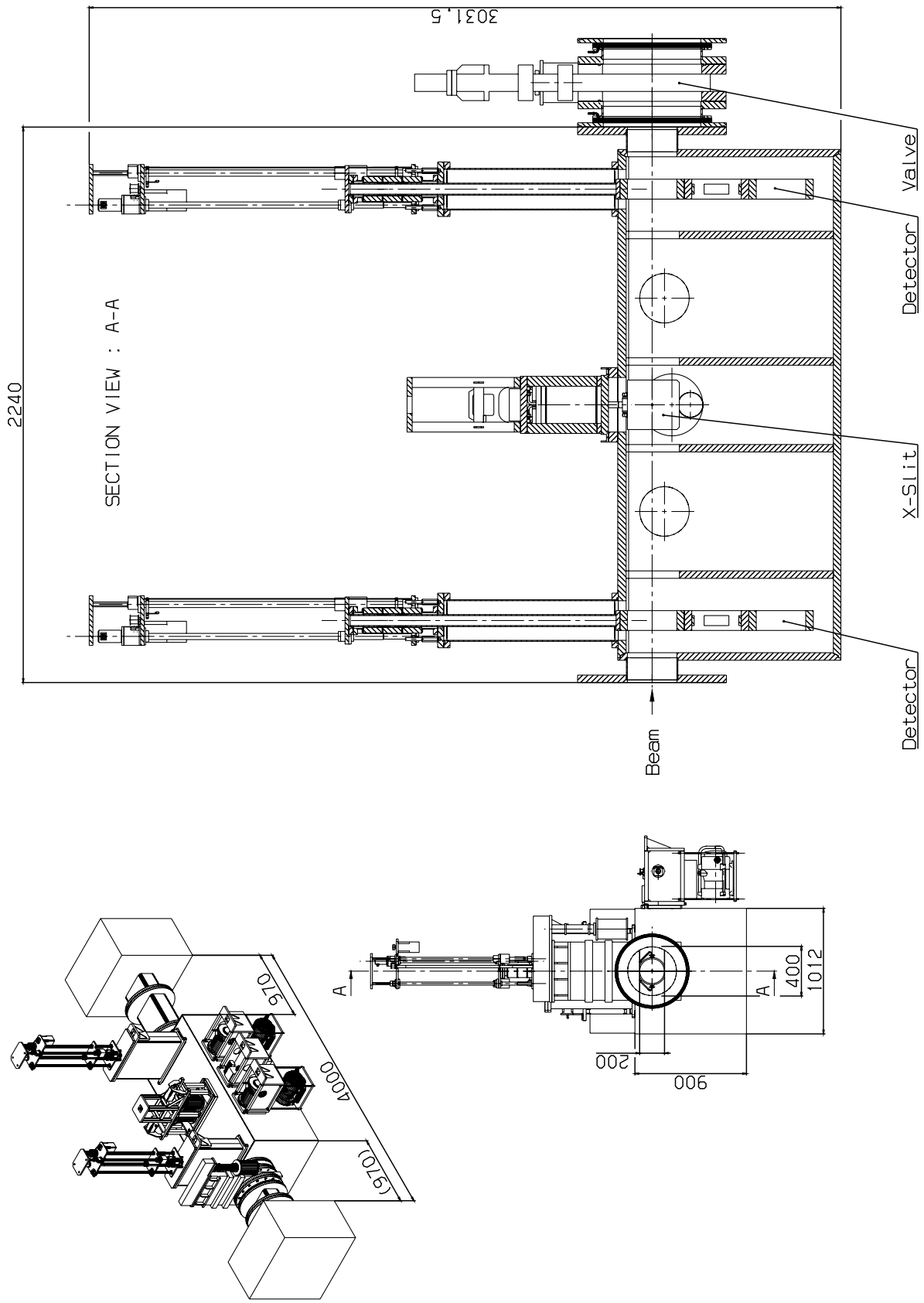

Figure 2.4-98*:* Diagnostic chamber including the setup at the MF1 focal plane.

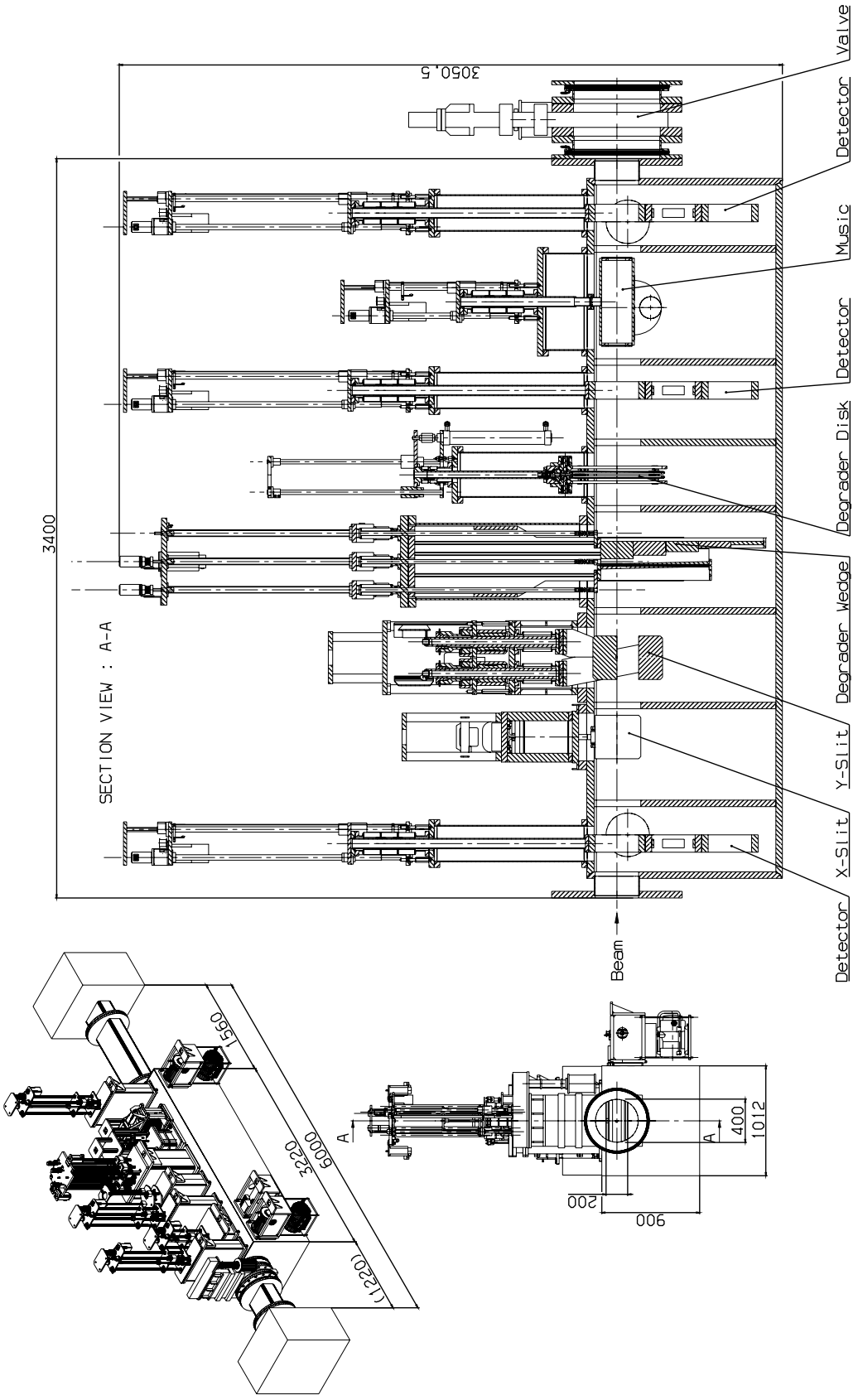

Figure 2.4-99*:* Diagnostic chamber including the setup at the MF2 focal plane (middle plane of the Main-Separator).

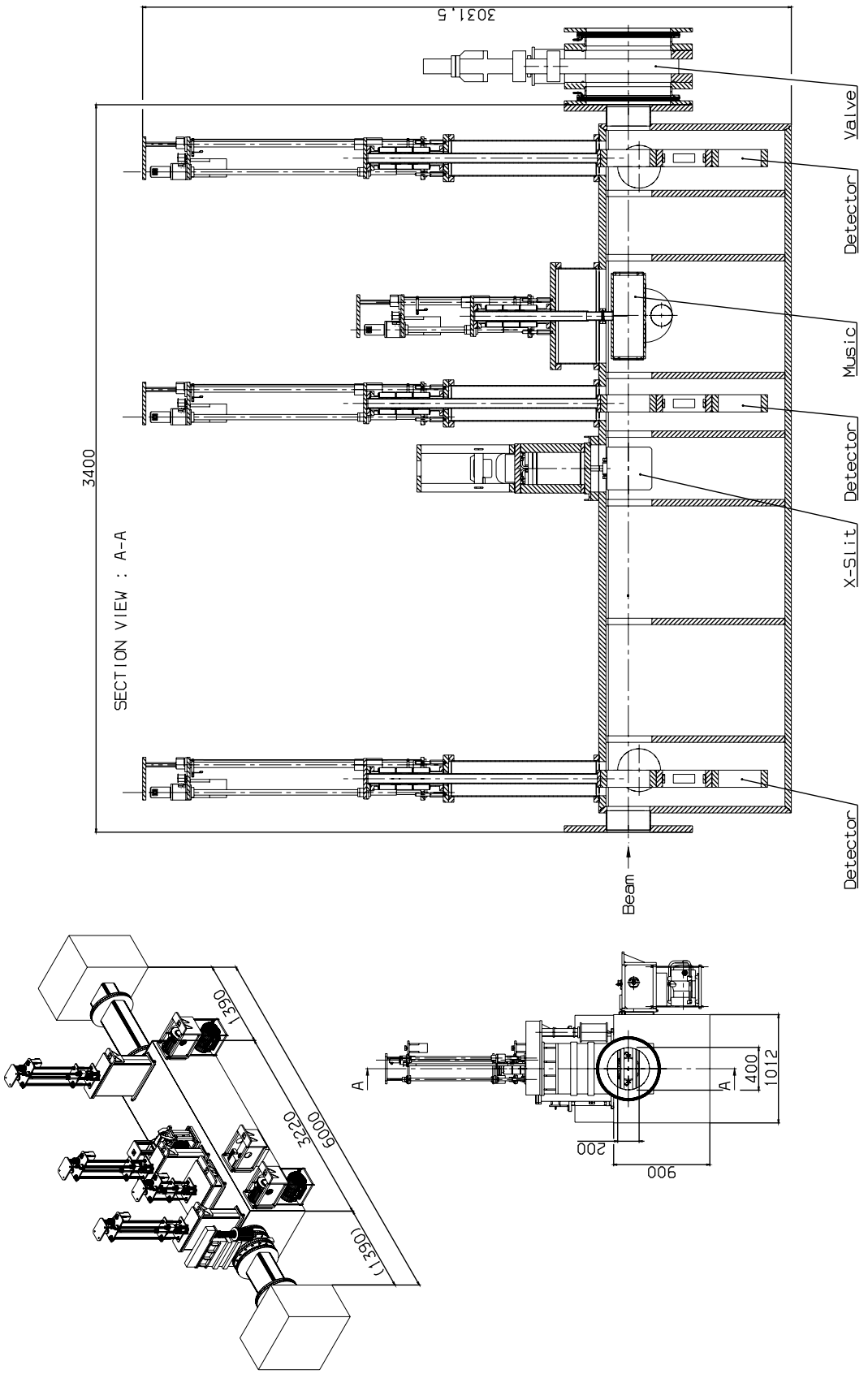

Figure 2.4-100: Diagnostic chamber including setup at the MF4 focal plane (end of the High-Energy-Branch).

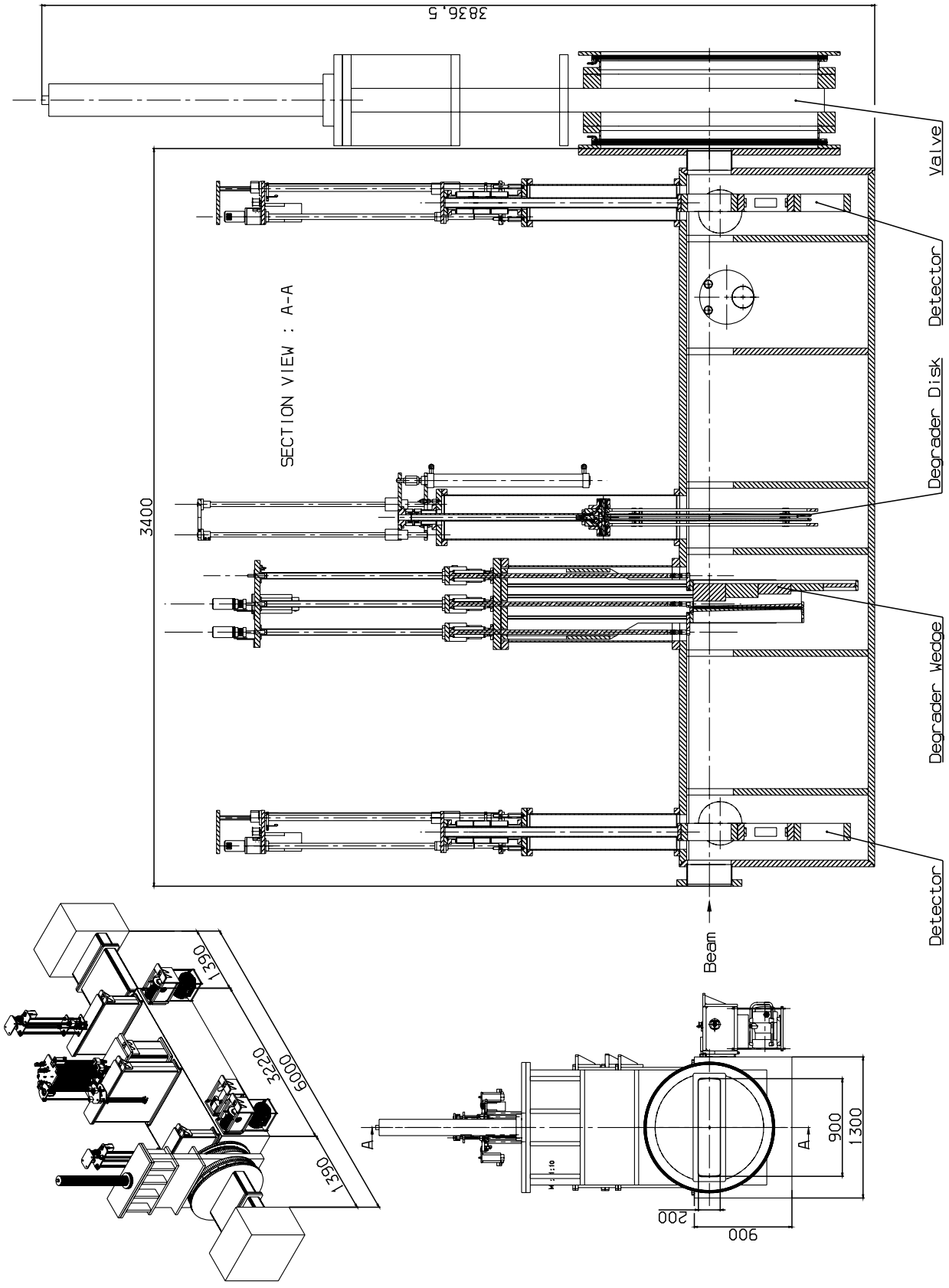

Figure 2.4-101*:* Diagnostic chamber including the setup at the MF9 focal plane (end of the Low-Energy-Branch).

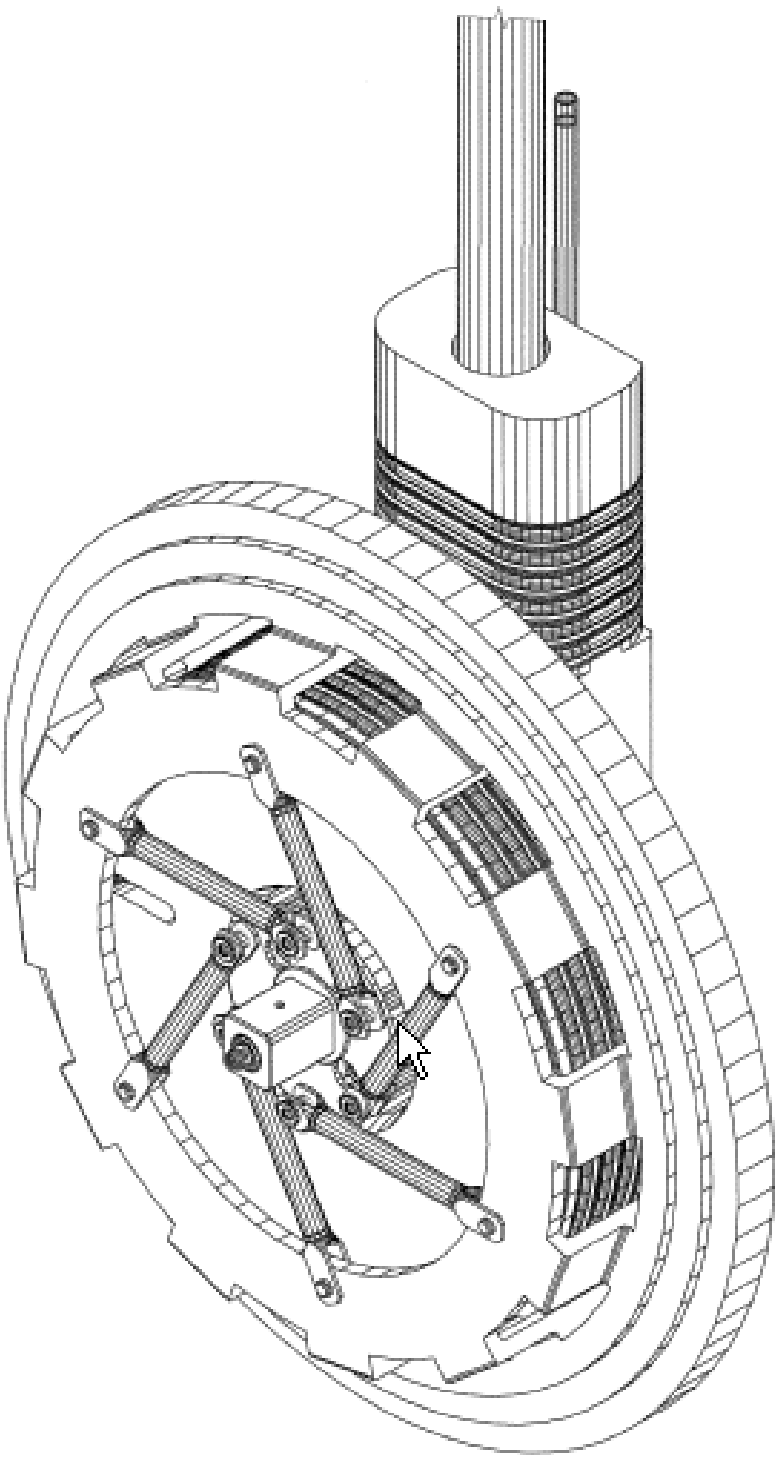

Figure 2.4-102*:* 3D view of the target wheel.

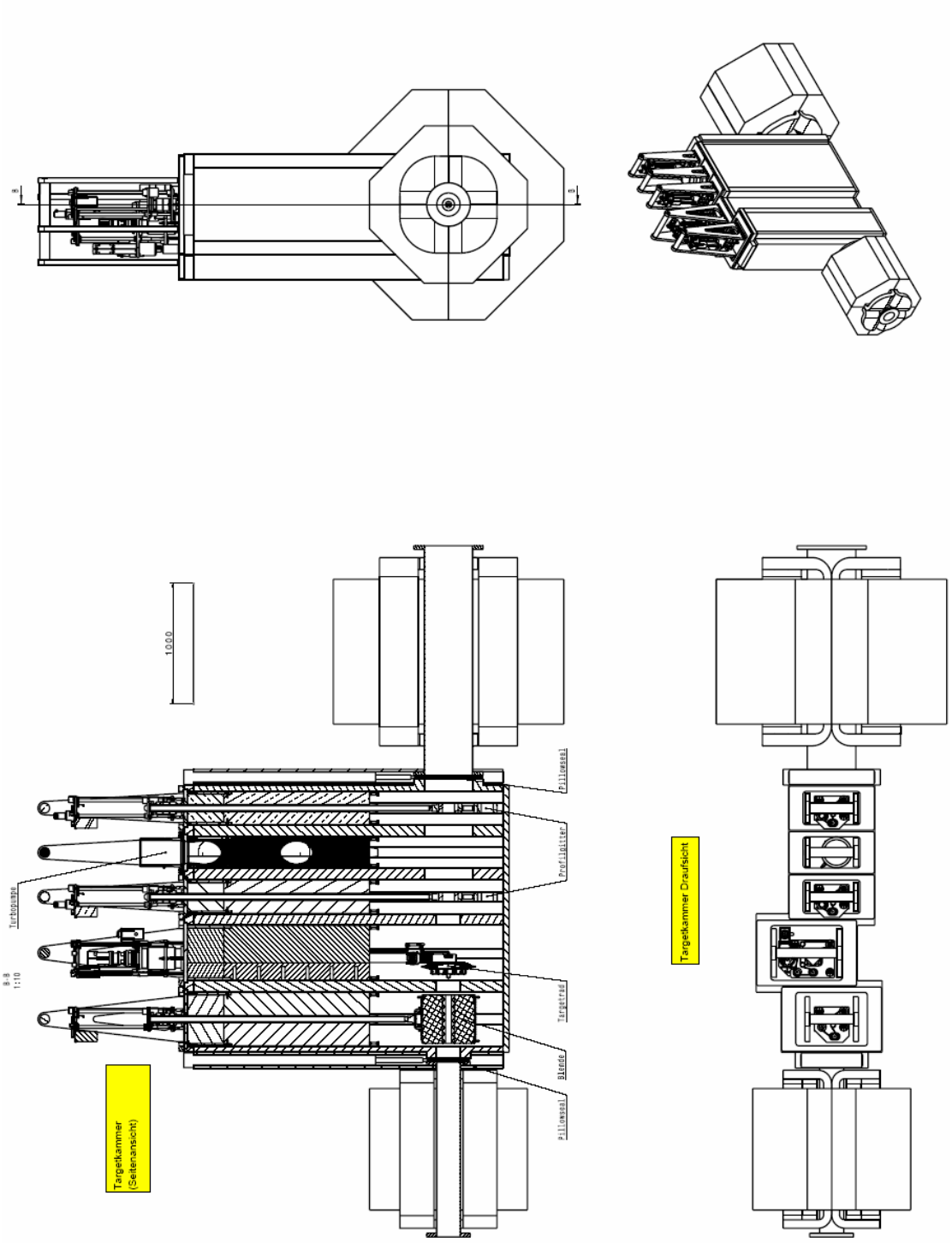

Figure 2.4-103*:* Schematic layout of the Super-FRS target box. Separate plugs are foreseen for the diagnostic detectors (beam position and intensity), the pumping station, the target-wheel assembly and the collimator.

2.4.8 Particles Sources

n/a

2.4.9 Electron Cooling

n/a

2.4.10 Stochastic Cooling

n/a

2.4.11 Experimental Devices

2.4.11.1 Beam Catcher

The beam catcher serves two purposes, firstly to absorb the main part of the primary beam energy and secondly to shield the subsequent parts of the separator from a high level of secondary radiation. The challenge is to solve the technical problems due to the specific energy deposition of the heavy ions up to uranium for fast and slow extraction modes as it is outlined in section 2.4.11.3. Most of the kinetic energy of the heavy ions has to be absorbed by the beam catcher system, whereas in the production target only about 10 % is lost. The beam energy of up to 58 kJ is deposited in one pulse of 50 ns for fast extracted uranium ions at 1.5 GeV/u.

The layout of the beam catcher system is determined by the goals to provide save and efficient operating conditions including possible maintenance. Furthermore, it requires a well defined operating range and interlock system. The choice of the relevant parameters is given below.

The maximum beam energy is limited to 1500 MeV/u for the heaviest ions at maximum intensity, whereas for light ions one can safely go up to 2700 MeV/u.
For the minimum operating energy one has to consider to stay in the favourable ratio of the atomic and nuclear interaction length, which considerably reduces the effective Bragg peak in the stopping power. This condition is relatively easy to achieve for the critical case of fast extraction due to the fixed operating domain of the collector ring CR, i.e. the stochastic cooling requires 740 MeV/u and the operation in the isochronous mode at about 780 MeV/u.
For the allowed energy range of slowly extracted beams one has only the restriction that the energy loss of the primary beam in the target may be sufficiently large that the beam is stopped in front of the first beam catcher.

The calculated energy deposition is presented in Figure 2.4-104 for different projectiles at 1 GeV/u. The reduction of the energy deposition due to the formation of lighter-Z fragments is clearly demonstrated. The Bragg peak of uranium ions still represents the maximum of the curve, whereas the Bragg peak of xenon is still visible but it is not the maximum of the curve any more. For the case of argon ions the Bragg peak is reduced even more by nuclear interaction. At the entrance of the beam catcher the energy deposition of uranium ions exceeds the one of lighter ions by far, but at larger penetration depth the situation is reversed due to the faster stopping of the higher charged ions. For light fragments and neutrons no high-power catcher is needed and a denser material for better shielding can be applied as a component of the beam catcher.

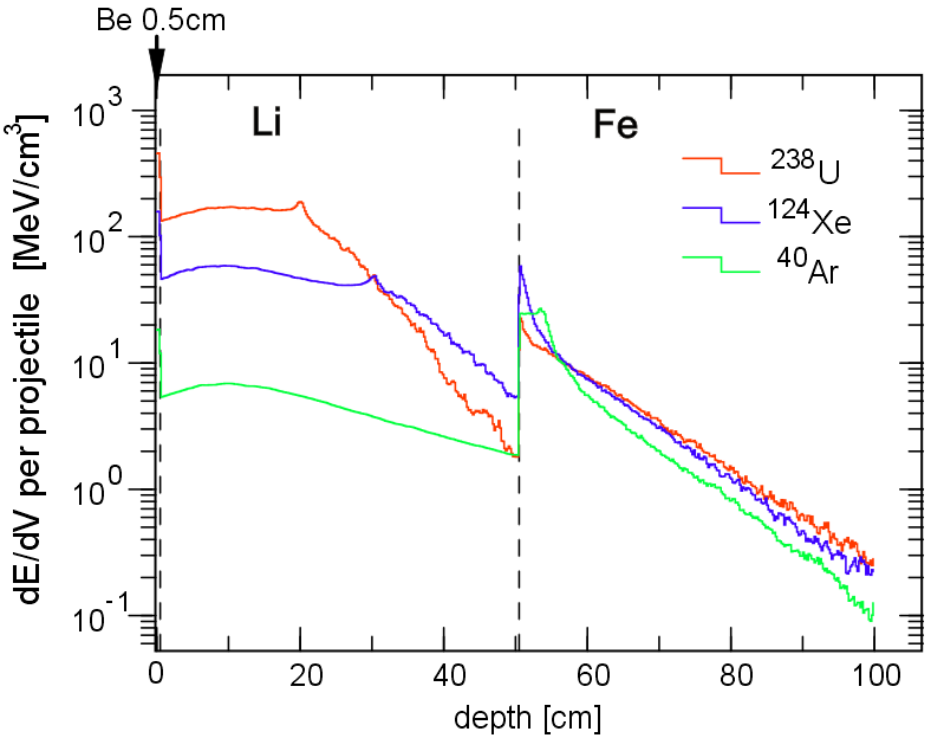

Figure 2.4-104*:* Deposited energy per 1000 MeV/u primary projectile and a 4 cm^2 two-dimensional Gaussian spot size for different ions, simulated with the PHITS code [5]. Here the high power part of the beam catcher consists of lithium in a container with a beryllium window and the second half consists of iron. The jump in the curves is due to the different densities of the materials.

2.4.11.1.1 Position of Beam Catchers

Dumping the primary beam within a magnetic separator requires special considerations. Depending on the magnetic rigidity (Bρ) of the selected fragments the primary beam may be deflected over a wide range of positions. This position in the first dispersive separator section can be characterized by the relative Bρ difference to the selected fragment beam, $\delta_p = B\rho_{prim} / B\rho_{frag} - 1$. The goal is to catch the primary beam behind the production target in beam catchers positioned outside of the magnetic elements at both sides of the optical axis depending if neutron-rich or neutron-deficient fragments are separated.

Detailed ion-optical calculations including nuclear and atomic interactions demonstrate that the beam catcher must cover a range from δ_p = -30 % to +30 % for heavy ion beams up to uranium and up to 50 % for very light ions (Z < 9). Finally the situation due to possible failures of the magnet power supplies must be covered by the beam catcher system. These requirements can be fulfilled by the special layout of the Pre-Separator consisting of split dipole magnets with subsequent beam catchers. Each catcher covers a certain range of δ_p , as illustrated in Figure 2.4-105.

The maximum width of the fragment beam at the catchers can reach ±15cm. The catchers are designed to have exactly this opening. The first two catchers (BC1 and BC2) have not to be movable, but BC3 must be able to act like a slit to catch the primary beam also in cases where it is less than 15cm way from the optical axis.

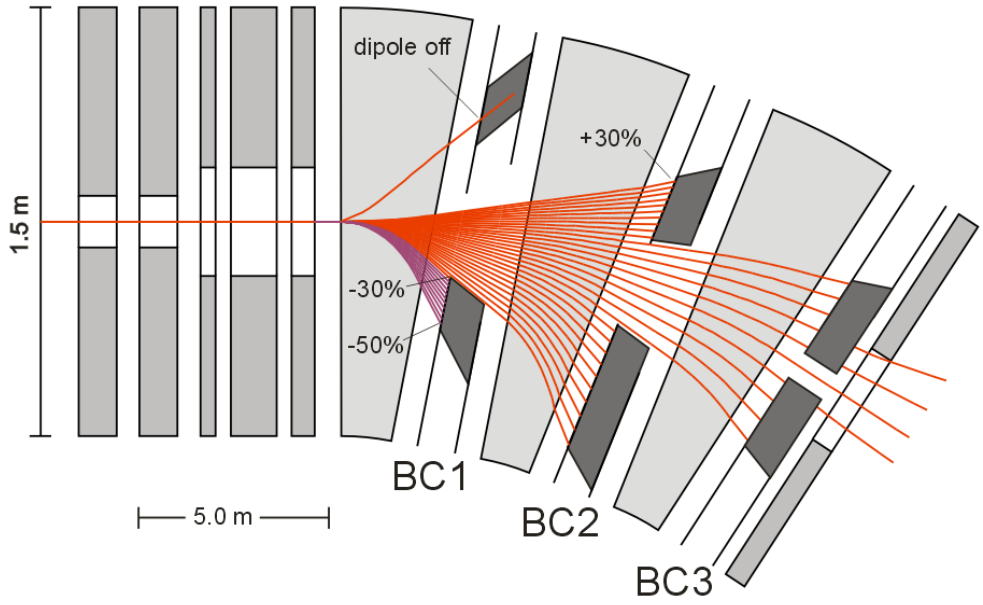

Figure 2.4-105*:* Trajectories of primary beams with different δp values in steps of 2 % calculated with the ion-optical program GICOSY [43]. The red rays represent possible separation scenarios for uranium beams and the purple rays hold for lighter ions with Z < 9 to produce neutron-rich fragments. Note, due to the different scale in longitudinal and transverse direction the angles are not conformally represented.

2.4.11.1.2 Separation of fragment beams

Many Monte Carlo simulations of the primary and fragment beam distributions using the code MOCADI [8] were performed to make sure that the beam-catcher system is universal for exotic nuclear beam experiments. A special challenge is to cope with heavy primary beams still carrying electrons after penetration through the target. An example is presented in Figure 2.4-106, for a ^{238}U beam after passing a 4 g/cm^2 lithium target at 1500 MeV/u. The Super-FRS is set to separate ^{132}Sn fission fragments and the primary beam still populates mainly 3 charge states, 92+, 91+ and 90+. In principle, an efficient separation scheme relies on a large Bρ difference between the primary beam and the fragment beam, but in this case the beam catcher will reduce also the transmission of the selected fragments.

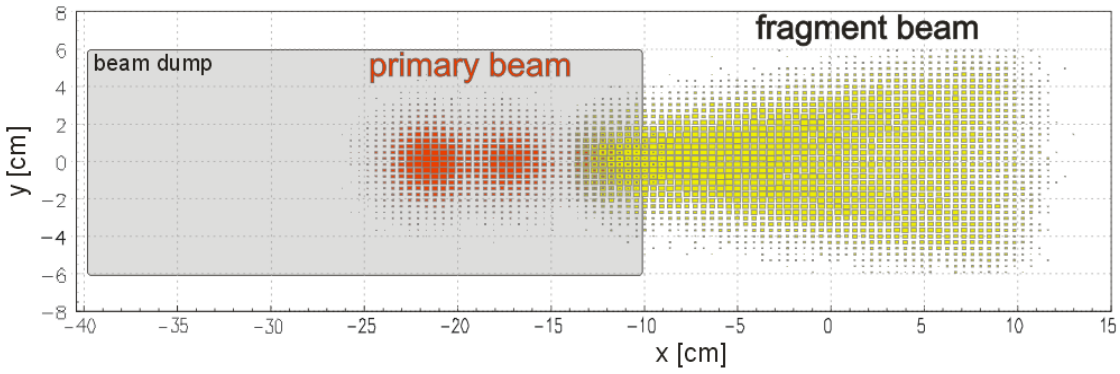

Figure 2.4-106*:* Calculated beam spot of a ^{238}U primary beam with three atomic charge states and of the fragment beam ^{132}Sn set. The beam catcher is moved in from the left hand side to intercept the primary beam.

Crucial for the layout of the beam catcher is the spot size of the primary beam which determines the maximum temperature. The two different extraction modes will be treated separately. At first we concentrate on the fast extraction as in this case no thermal conduction can distribute the heat and the danger of damaging or even melting the catcher is much higher.

The fast extracted primary beam is characterized by a much larger phase space volume (see section 2.4.1), which results in favourable large beam spots at the catcher. For the fast extraction mode with $\sigma_p/p = 0.25$ % but still keeping a small spot size of (1x2) mm^2 (1-σ) on the target and the same case as in Figure 2.4-106 the calculated projections of the beam size in horizontal (x) and vertical direction (y) are shown in Figure 2.4-107.

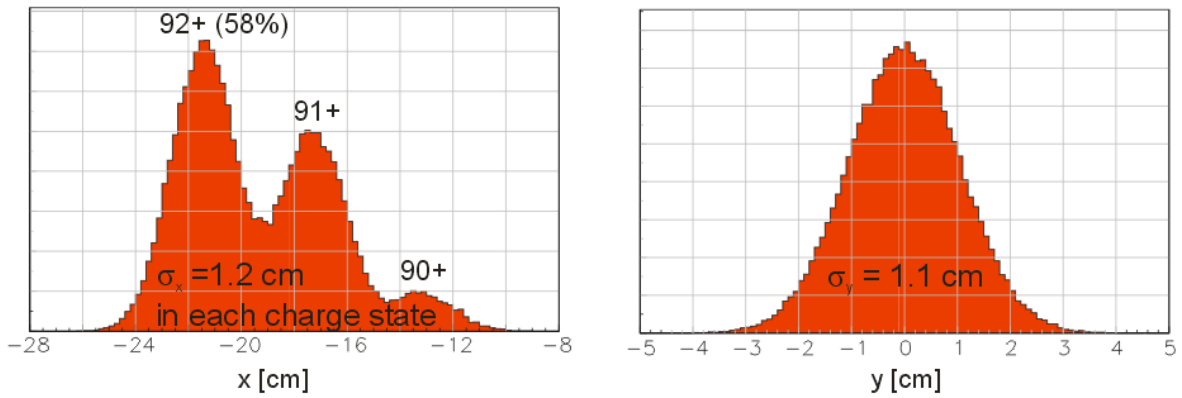

Figure 2.4-107*:* Spot size of the uranium primary beam on the beam catcher BC3 at PF1 in horizontal (left) and vertical (right) direction in fast extraction mode. The peaks are projections of the distributions in Figure 2.4-106.

A beam dumped at an earlier stage in the Pre-Separator has less dispersion, but this is compensated by less focusing and thus results in a similar spot size. In general, the spot size in the fast extraction regime can never become less than 1.0 cm^2 defined as a 1-σ level. It is even larger than the spot size at the target when it has been increased to ensure that the target survives. Starting with a spot size of (3x7) mm^2 (1-σ) at the target the resulting spot size on all three catchers is given in Figure 2.4-108 as function of the mean position where the primary beam may hit.

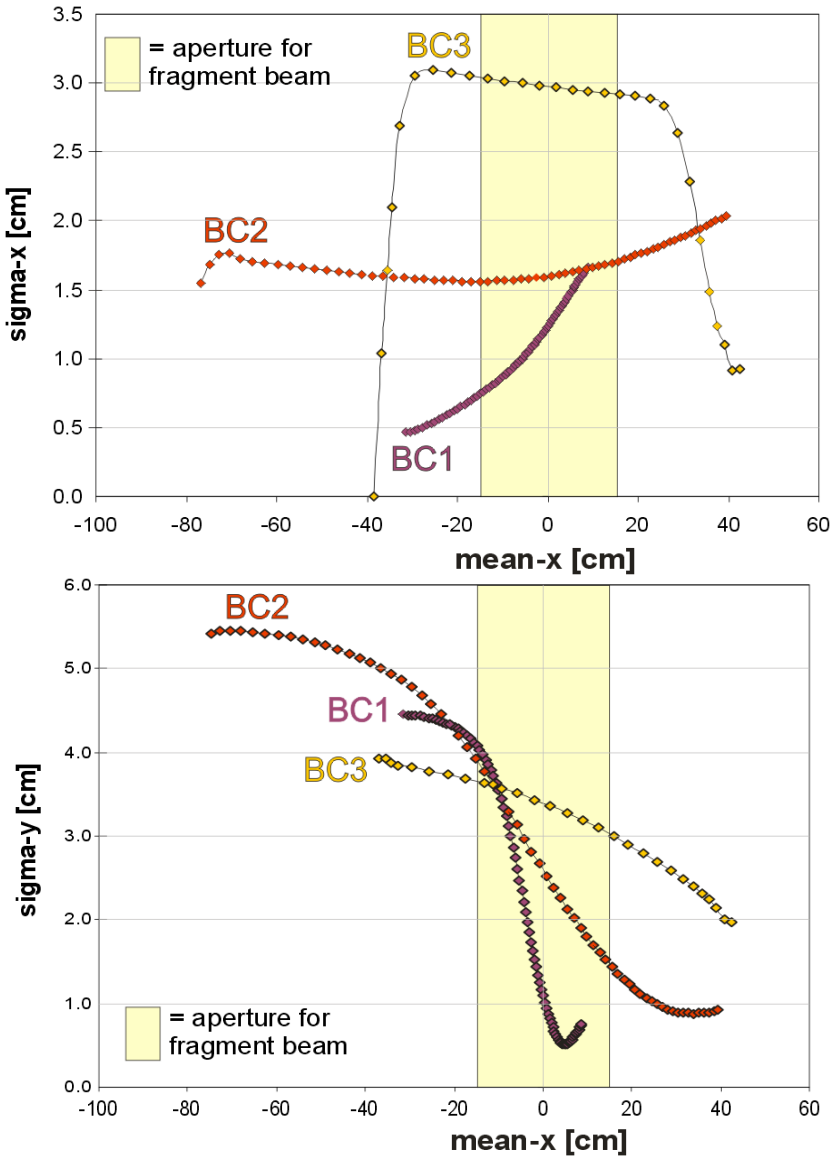

Figure 2.4-108*:* Spot size of a uranium primary beam in horizontal (x, upper panel) and vertical direction(y, lower panel) as a function of the mean position x on the catcher. Depending on the relative difference in magnetic rigidity different beam catchers behind the first (BC1), the second (BC2) or the third dipole (BC3) are hit. The simulation is for a beam in fast extraction mode with enlarged spot size of 3mm x 8mm (sigma) on a 4 g/cm^2 Li-target.

For slow extraction the initial emittance is much smaller but the nuclear and atomic interactions in the target still broaden the beam, resulting in a spot between 0.25 and 0.5 cm^2 at the beam catchers.

2.4.11.1.3 Choice of Beam Catcher Material

As already discussed the beam catcher serves two purposes, energy absorption and shielding, which require the use two different kinds of material. In the first part of the beam catcher, material with a low specific heat and low thermal expansion to avoid problems of melting and high pressure will be applied. In the second part material of higher density and Z will be used to achieve efficient radiation shielding in the limited space of the separator. All materials should be good heat conductors.

The entrance material should be low in mass number (A) to avoid too high temperatures. This can already be seen from the simple formula below for the temperature rise (ΔT) due to a number of particles (N) characterized by a stopping power $dE/d(\rho x)$, a beam spot area σ^2, and a molar heat capacity (C_{mol}), which for high temperatures becomes a constant defined by Avogadro's number (N_A)and Boltzmann's constant (k_B).

$$\Delta T = N \frac{dE/d(\rho x)\ A}{\sigma^2\ \ C_{mol}}\ ; \qquad C_{mol} = 3N_A k_B\ for\ high\ T$$

As $dE/d(\rho x)$ only moderately changes for different A and Z of the stopping materials, low A is clearly preferable.

Energy deposition in different materials

Besides the beam spot size the density of the deposited energy also depends on the amount of nuclear reactions of the primary beam. Simulations with the codes FLUKA [43,44] and PHITS [5] were performed to study the energy deposition taking into account both nuclear and atomic interactions and the contributions of the secondary beam. An example for 10^{12} Uranium at 740 MeV/u dumped in carbon with a round Gaussian beam spot with σ = 1 cm is shown in Figure 2.4-109. In this calculation the initial energy spread was assumed to be zero. Without fragmentation the ratio of the stopping power at the entrance and in the Bragg peak would be 6.9 [45]. However, nuclear reactions reduce this ratio to 3.1.

In Li and Be the nuclear reaction rate is higher compared to the energy-loss cross section. Therefore, the Bragg peak would be reduced by an even larger factor. Values are listed in
. The same conclusions hold for higher initial energies.

The density of energy deposition in the bulk material can also be reduced by geometrical shaping of the entrance of the beam catcher such that the range straggling is enhanced. In the example of Figure 2.4-109 the ratio of the peak to entrance energy deposition has been reduced to about 1.8 with an inclined surface of a slope of 0.1.

In Table 2.4-27 the specific energy deposition and the resulting temperature and pressure rise are compared for different materials. Lithium has the lowest mass number and therefore the temperature rise has the lowest value. Beryllium and graphite have a rather high Debye temperature and do not reach their full heat capacity at room temperature.

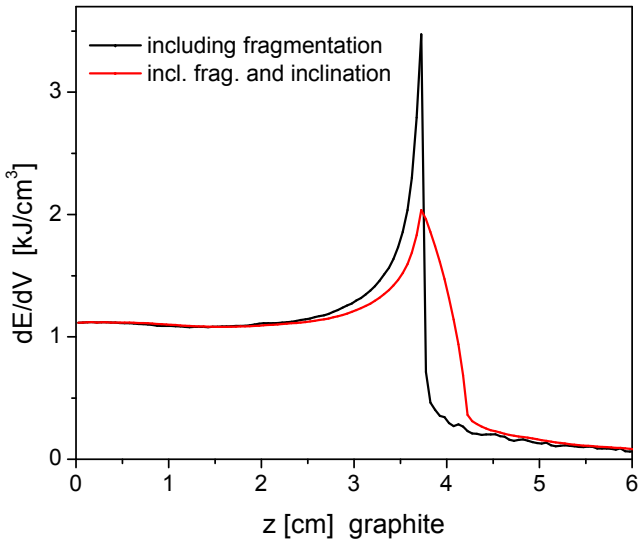

Figure 2.4-109*:* FLUKA [43] simulation of the energy deposition of a 740 MeV/u ^{238}U beam with intensity 10^{12} per spill in graphite (ρ = 1.84 g/cm^3) with a round Gaussian beam spot size with σ = 1 cm. The ratio of dE/dV at the entrance compared to the peak is only 3.1 compared to 6.9 [45] without nuclear reactions. An inclined entrance with slope of 0.1 further reduces this ratio to only 1.8**.**

Table 2.4-27*:* Specific energy deposition at an energy of 740 MeV/u at the entrance of the beam catcher,, maximum energy deposition in the Bragg peak including the fragmentation process, initial temperature (Ti), the resulting maximum temperature (ΔT) and pressure rise (ΔP) for one spill of a fast extracted uranium beam at a maximum energy density dumped on a spot size of σ_x*σ_y = 1.7cm^2 corresponding to the minimum spot size resulting from Figure 2.4-108. The specific heat, thermal expansion coefficient and bulk modulus for the calculation were taken from refs. [46].

Intensity per spill	Material	dE/d(ρx) [MeV/mg cm^2]	dE/d(ρx)$_{eff}$ [MeV/mg cm^2] in Bragg peak	T_i [K]	ΔT [K]	ΔP [MPa]
6x10^{11}	Li	18.0	36	490	88	230
6x10^{11}	Be	17.6	36	293	163	720
6x10^{11}	C (graphite[2])	19.4	59	773	279	25
10^{10}	Al	17.5	70	300	11.4	60
10^{10}	H_2O	22.1	46	300	1.7	6.6

The pressure rise of 720 MPa exceeds the yield strength of beryllium. Beryllium can therefore not be used. As a consequence this rules out a solution of liquid lithium with a beryllium entrance window. Lithium cannot be used in combination with carbon due to the chemical reactions. Only a windowless lithium beam catcher could in principle satisfy the requirements. Considering the low density of lithium of 0.54 g/cm^3 the catcher would be about 50 cm long, at least 20 cm wide resulting in a required flow of about 1 m^3/s of liquid lithium that would have to be pumped. Such a realization would entail many technical problems and limits.
The properties of diamond would be ideal for the beam catcher material but by far too expensive. However, the derivate graphite is also suitable. The temperature in graphite is tolerable, the pressure is low because of the low bulk modulus and suitable for a long-term operation (see Figure 2.4-110). Water would be evaporated in the hot spot of the beam and is therefore not

[2] Values based on SGL carbon group grade R 6650.

suited directly as a beam catcher but may be favourably used for cooling of the solid material. In this region without much direct beam hitting aluminium can also be used.

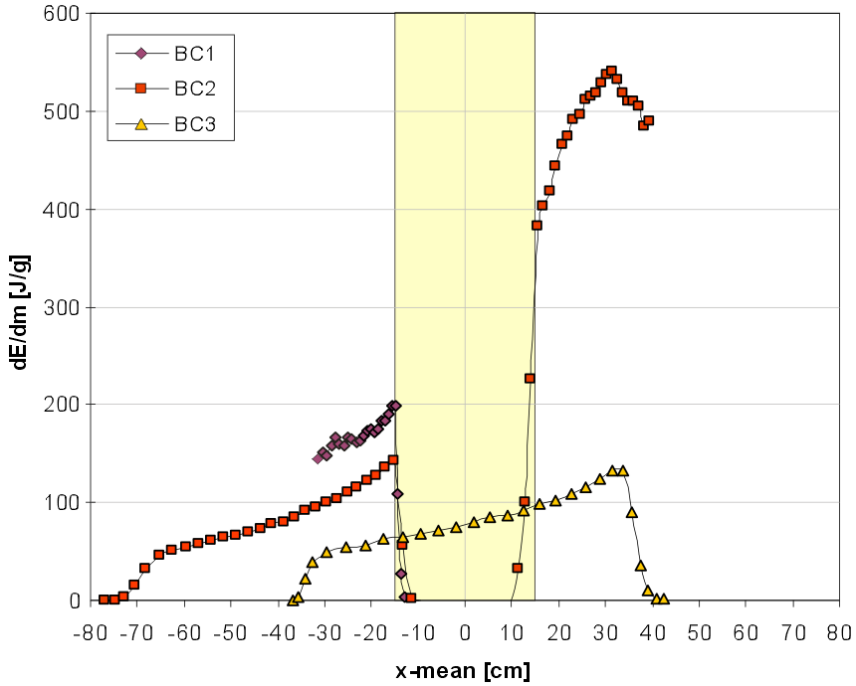

Figure 2.4-110*:* Energy density deposited by one intense pulse of $6x10^{11}$ uranium ions at 740 MeV/u in graphite as a function of position for all three beam catchers. The values correspond to the spot sizes shown before and the maximum of the effective energy deposition averaged over all fragments according to the FLUKA [43] calculation of Figure 2.4-109**. The yellow area indicates the fragment beam.**

The values for graphite listed above will be lower in a realistic running scenario where a target with 10-50 % reaction probability is usually applied. For the heaviest beams the population of several atomic charge states help to distribute the beam especially on beam catcher BC3, cf. Table 2.4-28. An additional improvement comes due to the wedge shaped entrance of the beam catcher. Under standart operating conditions the energy density deposited in one spill will be usually much smaller. Therefore, also Beryllium can be a suitable material for some of the catchers.

Table 2.4-28*:* Equilibrium charge-state distribution of uranium ions after a carbon target as a function of specific energy according to the GLOBAL and CHARGE predictions [47].

Energy [MeV/u]	92+ [%]	91+ [%]	90+ [%]	89+ [%]	88+ [%]
1500	77.7	20.8	1.5	<0.01	
1000	58.0	35.9	6.1	<0.1	
750	41.9	45.7	12.2	0.2	<0.01
500	21.8	49.5	27.7	0.9	~0.01
250	4.0	30.6	59.7	5.5	0.2

2.4.11.1.4 Design of the BeamCatcher

Graphite part

From the discussions above the preliminary design of the beam catcher looks as follows: The entrance part consists of graphite whereas the second part is made of iron. Figure 2.4-111 shows the graphite part with the attached heat sink. The position of the cooling pipes with water is indicated. They run inside the heat sink made of aluminium. Aluminium is chosen because of its good thermal conductivity and lower mass number compared to copper. Still it needs to be sufficiently far away from the main primary beam and may be hit only by far tails. Aluminium has also the advantage of relatively low activation compared to copper.
The V-shape helps to distribute the heat better especially in the Bragg peak region and increases the surface for better cooling. The iron part should be 60 cm long to sufficiently reduce the neutron radiation for the subsequent magnet coils. The transverse size varies between 70 cm and 20 cm depending on the individual catcher, see Figure 2.4-105.

After an initial heating phase the temperature reaches its equilibrium. The equilibrium distribution was calculated using the ANSYS code [48] for the geometry depicted above. This simulation was done assuming a turbulent flow of the water in several cooling tubes. The profile of the power deposited was roughly adjusted to the fast extraction scheme as shown in Figure 2.4-107 and Figure 2.4-113. A volume with a spot size of (9 x 4.5) cm^2 and a depth of 9.1 cm was heated homogenously with a total power of 23 kW corresponding to $6x10^{11}$ ^{238}U ions at 1500 MeV/u every 1.5 s. Figure 2.4-112 shows that the maximum temperature in a small spot in the centre of the beam catcher becomes only 950°C in case of a DC beam. The walls of the cooling tubes stay below 50°C.

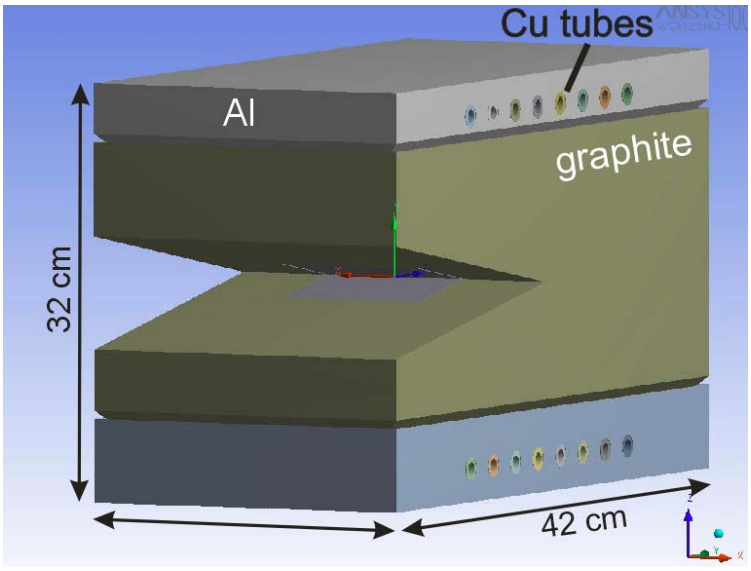

Figure 2.4-111*:* Construction of the beam catcher. The entrance part is made of graphite with a subsequent part of 60cm iron which is not shown. The cooling water runs in copper tubes inside of an aluminium block in close thermal contact to the graphite. The entrance is V-shaped to distribute the energy better and facilitate the cooling over a larger surface. A heavy ion beam has at least 20cm of graphite in its path.

The slow extraction mode would result in a smaller beam spot but a simple estimate of the heat diffusion time, following refs. [49,50], shows that the thermal diffusion time (t_D) can be fast enough to distribute the heat from a smaller volume, $t_D = \sigma^2 C_p \rho/(4\lambda)$. Here σ is the spot size, the specific heat $C_p = 1.83$ J kg^{-1} K^{-1} at 1100 K, density $\rho = 1.84$ g/cm^3 and the thermal conductivity $\lambda = 70$ W m^{-1} K^{-1}. For $\sigma = 0.5$ cm, t_D becomes 0.28 s. In case of 1 cm it would be $t_D =$ 1.1 s. This means that the temperature will not rise to values higher than in the fast extraction mode with a repetition rate of 1 s.
The simulations also show that it is important for a tolerable maximum temperature in the centre to have the cooling water close, but not too close to avoid boiling of the water on the walls of the hot tubes which would drastically reduce the heat transfer.
The thermal coupling from the graphite to the aluminium block needs further investigations. A liquid metal layer may be used. The heat transfer to the cooling tubes is increased by turbulent flow in special swirl tubes providing a steady turbulent flow [51]. A prototype must be built and heated with external heat sources.

The thermal expansion of the graphite will lead to mechanical stress. The analysis with the ANSYS code shows a maximum deformation in the center of up to 0.1mm. This corresponds to an equivalent von-Mises stress of 10-20 MPa. In the fast extraction mode on top of this value the pressure wave from the instantaneous heating must be added. Together these pressures stay still below a critical limit for cyclic stress of ~ 60 MPa. In the DC mode the mechanical stress stays below the critical limits for a full graphite/aluminium construction. Nevertheless the mounting should be done on a cold side which will not increase the stress too much. A large uncertainty is the additional swelling of the material due to radiation damage. To allow more deformation the graphite block can be divided in an upper and a lower half, cut into many slices. This detailed design work is still in progress. Special care has to be taken about tensile forces such as from rarefaction waves following the initial positive pressure wave. A simulation of the distribution and damping of such waves is ongoing.

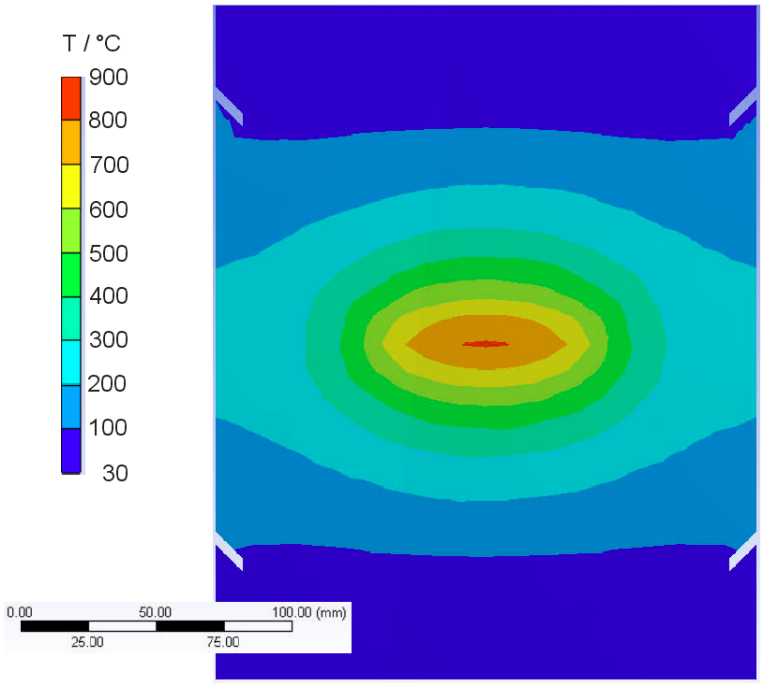

Figure 2.4-112*:* Calculated equilibrium temperature profile of the beam catcher for an irradiation with a DC beam depositing 23 kW on a spot size of (9 x 4.5) cm^2 up to a depth of 9.1 cm. Cut through the central hot region seen from the front.

Iron part

After a certain distance in graphite the deposited energy density becomes low enough to use iron as a beam catcher material. For example, after a penetration depth of 20 cm of graphite the deposited energy per volume in the iron drops below 10 MeV/cm^3 per incident ion for a 1500 MeV/u uranium beam, see Figure 2.4-113. For 10^{12} ions in one fast spill this causes a temperature rise of at most 0.5 K which corresponds to a pressure rise of smaller than 3 MPa. Most of the energy is deposited in the carbon part but still the total heating of the iron can reach a power of the order of 1 kW. This requires water cooling of the iron as well.

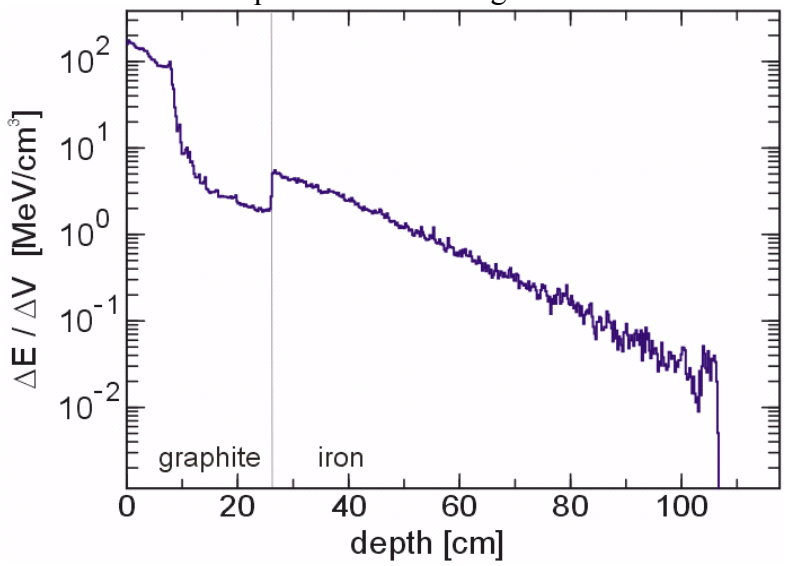

Figure 2.4-113*:* Energy deposition per volume in the carbon and iron part of the beam catcher along the primary beam direction by a 1.5 GeV/u ^{238}U beam calculated with PHITS [5]. For the sake of clarity the V-shaped opening of the beam catcher was replaced by a simple block of graphite.

There can be cases where not all high intensity components of the primary beam or fragments can be stopped in front of the degrader at PF2. This contribution should stay on a level of less than 1 % of the full intensity of the primary beam to cause no damage for the degrader. However, the subsequent superconducting magnets have to be protected. Depending on the position and the energy loss in the degrader the magnetic rigidity of this beam can vary a lot in the second half of the Pre-Separator. Figure 2.4-114 shows possible trajectories and corresponding options for the beam catcher locations. At least after the slit at PF4 the total intensity must be reduced to an equivalent of 10^9 uranium ions at 1 GeV/u. Like in the first half it is possible to find a setting of slits in which the beam is always dumped in a dedicated beam. Some of them need to be movable because they may otherwise restrict the fragment transmission. The construction of these beam catchers, however, is much simpler than in the first half of the Pre-Separator. Indeed they can be adopted from the present FRS slits.
From Figure 2.4-113 with the condition of 100 times less incoming beam intensity, it follows that the slits must have a thickness of about 30 cm iron. As these slits are not radiated very often higher density material (tungsten alloys) may also be used without suffering from activation problems.

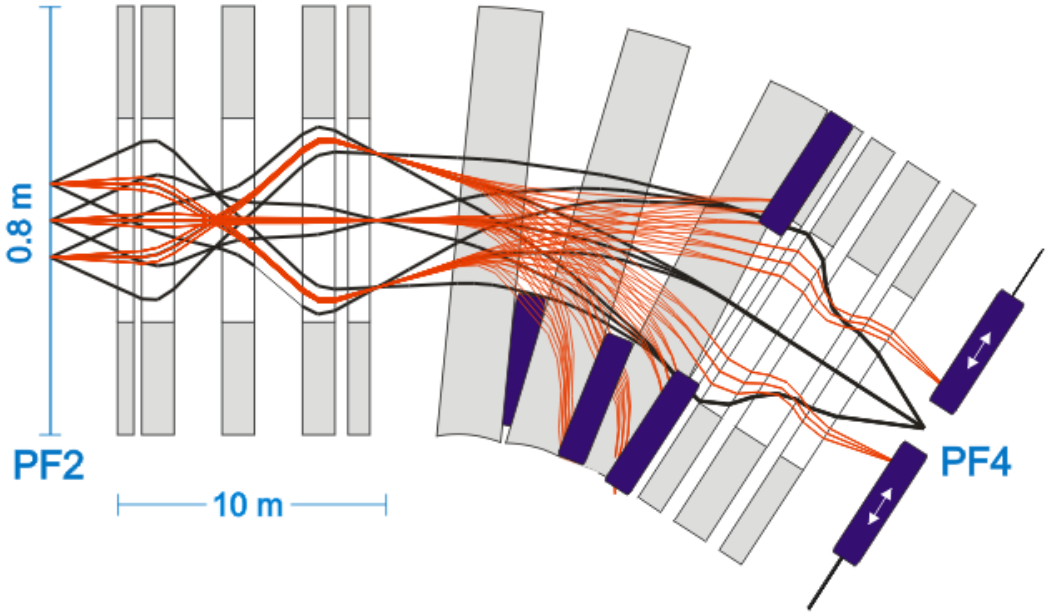

Figure 2.4-114*:* Location of beam catcher positions behind the degrader station at PF2. Trajectories of the fragment beam are shown in black and possible trajectories of the primary beam in red. As the primary beam loses in most cases more energy than the fragments the beam catchers are needed mainly on one side.

2.4.11.1.5 Radiation Damage

Radiation damage in the carbon part of the beam catcher is caused by three mechanisms:

- Elastic collisions of the primary beam, fragments or neutrons with the carbon atoms,
- for high linear energy deposition the heating by the electronic energy loss can cause microscopic material melting and track formation. This happens in graphite above a threshold of about dE/dx = 7.3 ± 1.5 keV/nm [52] and will therefore occur mainly in the Bragg peak close to the end of the range,
- spallation of the nuclides in the material and creation of other chemical elements.

The number of displacements per atom (DPA) resulting from elastic collisions was estimated with the PHITS code. The result is shown in Figure 2.4-115 as a function of the depth in the beam catcher for a total number of ions of 10^{20} uranium ions, corresponding to 116 days of

operation per year over 10 years with the full intensity and energy. A strong peak appears towards the end of the range in carbon near the maximum of nuclear energy loss. But as the range and beam position will vary in different experiments the number of DPAs will stay on average below 1.
The track formation imposes the strongest limit. First tests have shown that rather low rates of $10^{13}/cm^2$ of uranium ions at Bragg peak energies already lead to significant material modifications. At room temperature almost each ion will create a track in this energy regime, leading to swelling of the material by about 1% in volume and hardening of the material [53]. On the other hand at higher energies like at the entrance to the catcher the probability of track formation is reduced by a factor of 1000. Almost no amorphisation was observed in HOPG graphite for irradiation at a temperature above 800K [54].

Due to the still widely unknown processes of track creation and annealing we cannot predict the expected lifetime of the device. But it may become brittle very fast in the center whereas the outer structure can stay intact long enough.
The iron part is damaged mainly by fast neutrons. Here electronic energy loss plays no role. As shown in Figure 2.4-115 the number of DPAs stays below 1. This should allow operation over the whole lifetime of the Super-FRS.

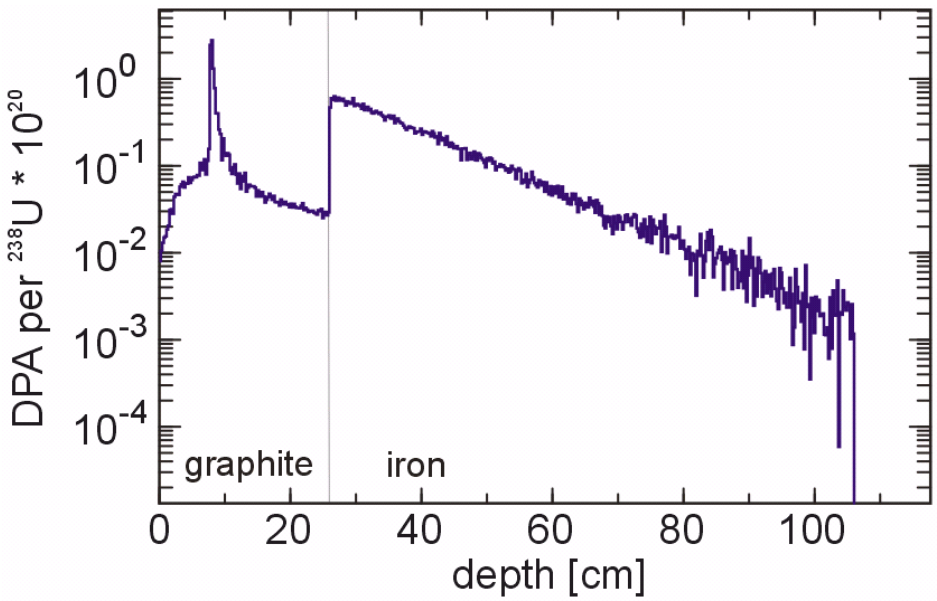

Figure 2.4-115*:* PHITS simulation of DPAs from elastic collision, all values stay below 1 DPA for the whole lifetime of the device even with full uranium beam intensity over 15 years with 77 days continuous operation in each year (10^{20} ions). The peak in carbon represents the end of the range near the maximum of nuclear stopping power. The initial spot size on the beam catcher was (2.5 x 1.1) cm^2.

From nuclear reactors it is well known that the material can also be modified by induced nuclear reactions. The amount of different elements created was calculated in a FLUKA [43] simulation of the beam catcher. Mainly helium is created in the graphite and the iron part. The ratio of atoms compared to carbon can reach 10^{-5} (10 appm) in the graphite and $3 \cdot 10^{-6}$ (3 appm) in the iron after an assumed total irradiation by 10^{20} uranium ions considering that not always exactly the same spot is hit on the same beam catcher. This may lead to swelling of the material. In iron many metals close in atomic number are produced which cause no additional damage.

2.4.11.1.6 Activation

The PSI graphite wheel can serve as a reference for production of radionuclides in graphite [55]. In agreement with the FLUKA calculation they show mainly the production of ^{7}Be and

^{3}H. The FLUKA calculation for 100 days of irradiation with 10^{12} Uranium at 1.5 GeV/u and a following waiting time of 2 days shows an activation of $2{\cdot}10^{12}$ Bq due to ^{7}Be and $9{\cdot}10^{10}$ Bq due to ^{3}H. The resulting dose rate from the ^{7}Be activity in 1 m distance is 15 mSv/h without shielding effects as defined in ref. [56], self-shielding by the carbon block reduces the value to 4 mSv/h. Even though most of the dose rate comes from ^{7}Be the gaseous long lived tritium has to be considered for handling. The activity from other nuclides is many orders of magnitude lower and mainly due to trace elements in the carbon [55]. The activation of the cooling water is similar to the activation of the carbon. Again mainly ^{7}Be is produced but the amount of water in the beam catcher is about a factor 10-100 less than carbon. In aluminium also long lived ^{22}Na is produced.
More serious is the iron part of the beam catcher where more long-lived heavy nuclides are produced. A FLUKA simulation of a scenario of 4 times 90 days irradiation followed by 120 days waiting was done for a 10^{12}/s uranium beam always hitting the same beam catcher after having passed the target. The resulting activity is summarized in Table 2.4-29. The conversion into ambient dose rate, H*(10), shows the strong value of 1.1 Sv/h 1 week after switching off the beam which is caused entirely by gamma radiation. This already includes the shielding by the thick iron block itself which blocks radiation from the inside with an absorption length depending on gamma energy [57]. A longer waiting time of 120 days would result in a dose rate of 290 mSv/h.

Table 2.4-29*:* Table of nuclides contributing to more than 95% of the activity in the 340 kg iron of a beam catcher, 3 or 120 days after switching off the beam in the scenario described in the text. Pure beta emitters are marked by (β).

nuclide	$T_{1/2}$ / days	Activity (3d)/ Bq	Activity (120d)/Bq
^{3}H	4498, β	$6.3\text{x}10^{11}$	$6.2\text{x}10^{11}$
^{7}Be	53.3	$4.4\text{x}10^{11}$	$9.6\text{x}10^{10}$
^{37}Ar	35.0, β	$6.3\text{x}10^{11}$	$6.2\text{x}10^{10}$
^{46}Sc	83.8	$9.2\text{x}10^{11}$	$3.5\text{x}10^{11}$
^{48}V	16.0	$4.2\text{x}10^{12}$	$2.7\text{x}10^{10}$
^{49}V	330	$3.8\text{x}10^{12}$	$2.0\text{x}10^{12}$
^{51}Cr	27.7	$1.3\text{x}10^{13}$	$6.9\text{x}10^{11}$
^{52}Mn	5.59	$3.3\text{x}10^{12}$	$1.7\text{x}10^{6}$
^{54}Mn	312	$1.2\text{x}10^{13}$	$9.0\text{x}10^{12}$
^{55}Fe	996, β	$1.1\text{x}10^{13}$	$9.9\text{x}10^{12}$
^{56}Co	77.3	$4.7\text{x}10^{11}$	$1.6\text{x}10^{11}$

2.4.11.1.7 Handling, Infrastructure

The dose rates mentioned above do not allow direct human access for maintenance. The plug system foreseen for the target will also be used for the beam catchers. The vacuum chamber at the exit of the dipole magnet needs to be very wide, cf. Figure 2.4-105. It is planned to build the vacuum chamber for the dipole magnet extended to incorporate the beam catcher. It also has to contain the iron shielding plug as usual vacuum seals can be used only on top of the plug. The whole setup of the three dipole magnets and the large vacuum chambers for the three beam catchers is shown in Figure 2.4-116.

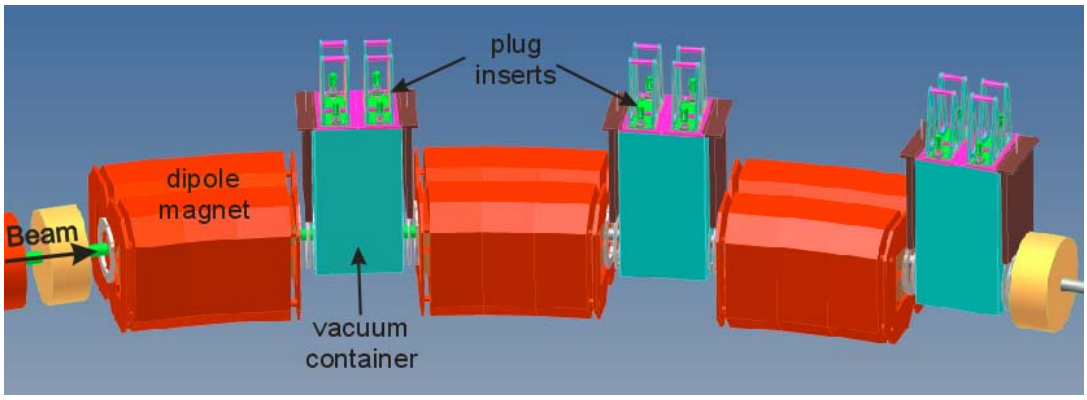

Figure 2.4-116*:* Layout of the beam catchers positioned behind each 11° dipole magnet of the Super-FRS.

A more detailed view of the plug and beam catchers is given in Figure 2.4-117. Pillow seals will be used at the entrance of the dipole magnet and behind the beam catcher where the aperture is small. Radiation shielding is provided by the iron plug inside the vacuum chamber or by surrounding concrete shielding. The beam catcher and a position sensitive detector are mounted moveable on a rail and the corresponding motors are located on top of the plug.

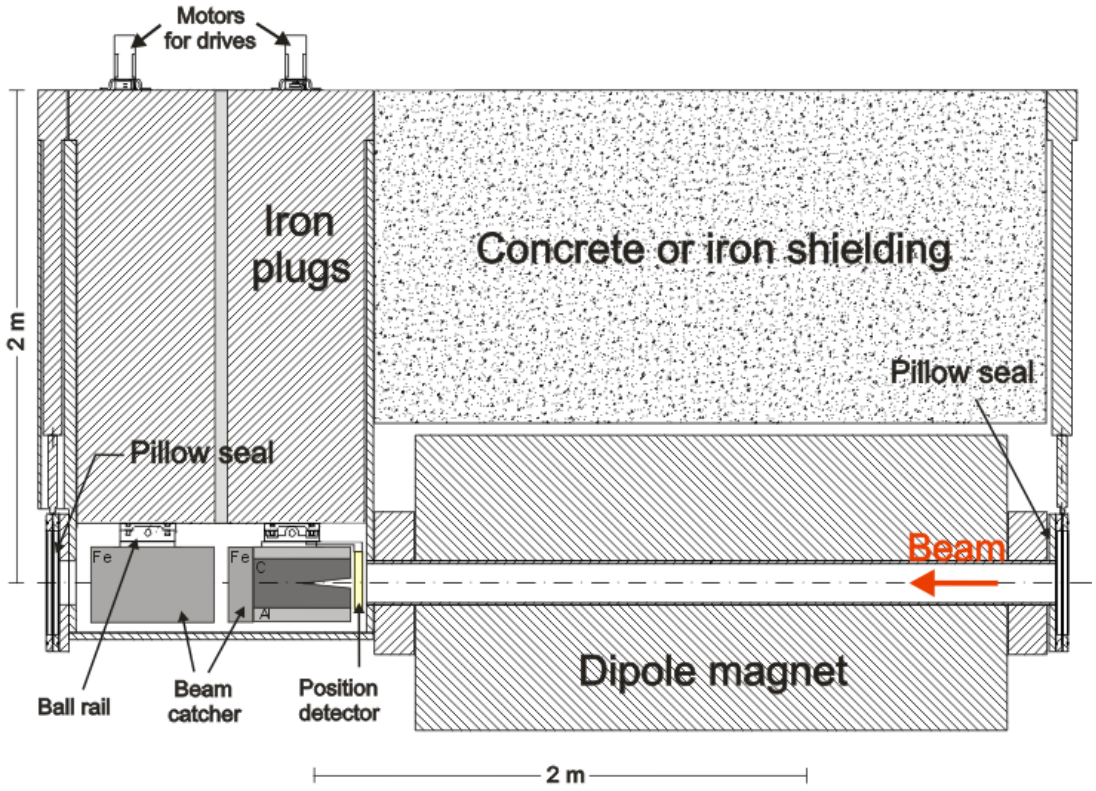

Figure 2.4-117*:* Scheme of the technical layout of the beam catcher. Cut through the beam catcher and the preceding dipole magnet.

For maintenance the beam catcher must be removed first into a shielding bottle and carried to a safe deposit. As the dose rate with an iron bottle of 30 cm thickness at the critical regions reaches up to 10 μSv/h on the outside, it must be kept in an area with controlled access. A modification or maintenance of the carbon or iron is possible with manipulators inside the hot cell.

With a total height of the whole plug of about 2.5 m and the largest beam catcher being 70 cm long and 45 cm wide the total weight of the shielding bottle including the iron plug inside is about 35 tons.
The cooling water must be kept in a closed circuit as it becomes activated. The heat exchanger capable of removing 60 kW and keeping the water at room temperature will be located at the top of the shielding plug in the maintenance tunnel. The water pipes lead through the plug. The water is not so much activated thus it is sufficient to place the heat exchanger behind an iron shielding of 10 cm thickness.

2.4.11.2 Degrader Systems and Ion-Catcher

The degrader systems are key components for the isotopically pure in-flight separation. Their effect and the ion-optical properties have been described in detail in ref. [58]. A newly implemented feature is the slowing-down, thermalization and post-acceleration of exotic nuclei employing a helium-filled stopping cell at the Low-Energy Branch. For this hybrid system, which will combine the advantages of the in-flight separation and isotope-separation on-line, a monoenergetic degrader system will be used. Existing techniques will be further developed and adapted to the performance of the Super-FRS. This concerns mainly the mechanical dimensions and thermal stress and radiation damage due to higher beam intensities. The numbers given in the following are based on calculations assuming the separation of exotic nuclei ranging from ^{11}Li up to ^{232}Rn. The range of specific kinetic energies and thicknesses is given in the following Table 2.4-30.

Table 2.4-30: Thickness of degrader system at the location PF2, MF2, MF11.

	Thickness in units of range	Energy range (MeV/u)
PF2	0.1 ... 0.5	1000 ... 1500
MF2	0.1 ... 0.5	500 ... 1000
MF11	0.1 ... 1.0	100 ... 500

Figure 2.4-118 shows the generic concept of the degrader systems to be used at the central focal of the pre- and main-separator, PF2 and MF2, respectively, and at the final focal plane MF11 of the energy buncher. The unit consists of several components fulfilling different purposes: a rotational stage with two wedge-shaped disks of opposite rotation, thus allowing to vary the thickness continuously along the dispersive direction (indicated by the angle α), and two wedges moving linearly in opposite direction thus causing a continuously varying homogeneous thickness (d). In addition to that, homogeneous or wedge shaped pieces of material can be added (not shown in the figure) in order to provide larger thicknesses and/or angles.

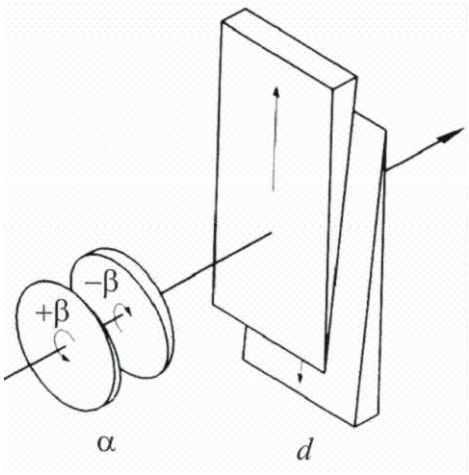

Figure 2.4-118*:* Schematic view of the degrader systems, which will be installed at the focal planes PF2, MF2, and MF11 of the Super-FRS. They consist of two rotating parts with wedge-shaped disks to generate the wedge-angle α and two linear drives equipped with rectangular wedges for the continuous thickness variation. Additional degrader plates may be added on an additional linear drive (not shown).

Detailed investigations [4,9,58,59] have been carried out to investigate the performance of a fragment separator employing a degrader system in dependence of the degrader material. These studies take into account nuclear absorption in the material, atomic processes like energy-loss straggling, small-angle scattering and charge-exchange, and the transport of the ions through the ion-optical system. Although for the lightest ions ($A < 20$) a very light degrader material would be preferred, the overall optimum choice yielding high transmission for all nuclei is a medium-heavy element, like e.g. aluminium. Because of practical reasons, also quartz will be investigated (see below).

The energy spread additionally imposed on the fragments when penetrating through the degrader is the limiting factor of the resolution for the subsequent magnetic rigidity analysis. Thus it needs to be minimized and adjusted to the ion-optical resolution. Energy-loss straggling is unavoidable and thus the ultimate limitation. Practically, the main limitation arises from inhomogeneities and imperfect alignment of the degraders. The real shape of the degraders should match as good as possible the ideal shape, thickness non uniformities arising from inhomogeneous material (density) and/or surface inhomogeneities must be minimized. The tables given below show the tolerable values such, that the inhomogeneities cause the same width at the final focus as does the energy-loss straggling. These tolerances are of the order of few ten micrometers in order to preserve the ion-optical resolution, so that the degrader plates and the mechanical holders and drives require very high precision.

Because of the strong requirements, quality control is an important issue. Although several different manufacturers promise to fulfil the specifications (shape tolerances, surface uniformity, density homogeneity), it has turned out that quality control needs to be done in-house. In the past years, the GSI target laboratory has developed tools to measure tolerances on a micrometer scale. The best results have been obtained with quartz material, which showed sub-micron surface tolerances and deviations from the ideal shape of very few microns only. Thus, from this point of view quartz is the preferred material. However, due to the manufacturing process, the minimum thickness is limited to values exceeding about 5 millimetres for each plate thus yielding at present only rather thick plates. In the near future we will explore other possibilities together with industry.

According to the specifications, the prototype system described in section 2.4.11.2.3 already reaches this precision. In an experiment we have tested Suprasil®-2 material (which is quartz-type material) and received the anticipated good results. The material is routinely manufactured with optical quality and exhibits a surface roughness of less than 10 nm, a

maximum shape deviation of less than 1 μm and a material inhomogeneity less than 10^{-4}. Thus an areal weight homogeneity better than 0.2 mg/cm^2 is reached. Together with the prototype stepper motors and linear drives, a minimum thickness variation of 200 μg/cm^2 per step is achieved.

Concerning the ion-beam interaction with the degrader material, thermal and radiation damage issues are to be considered. The degrader unit of the pre-separator will receive the strongest load, and the worst case is a maximum intensity of 10^{10} uranium ions per second (resp. spill). Our calculations show that aluminium material will be heated by 8 K when the beam spot size has the expected dimensions of 4 cm^2. With 45 MPa, the pressure stays well below the cyclic stress limit of 290 MPa. The thermal diffusion time is of the order of 250 ms, thus well below the cycle time of the synchrotron. This time decreases linearly with the beam spot area, so that also for slow extractions no problems are expected. However, the numbers show that under continuous running conditions water cooling of the degrader of the Pre-Separator is required. The conditions will be similar to those which are presently prevailing in the FRS target area. In the considered energy domain of several 100 MeV/u elastic collisions leading to displacements and thus to radiation damage are of minor importance. Nevertheless it will be necessary to study whether such effects (like swelling, formation of bubbles, etc.) may occur after high-dose irradiations. This is an issue for the ongoing and coming development program.

For the degrader systems R&D is needed in order to further develop the existing technologies, e.g. to develop vacuum-compatible high-precision linear and rotational drives for degrader with areas which are larger than the ones which are operational now. Also the manufacturing and quality control of quartz-type degraders of the required dimensions is required.

2.4.11.2.1 Degrader System in the Pre-Separator

Width (cm)	Height (cm)	Thickness (g/cm^2)	Wedge angle (mrad)	Tolerances (μm)
15	5	1-10	0-120	120

2.4.11.2.2 Degrader System in the Main-Separator

Width (cm)	Height (cm)	Thickness (g/cm^2)	Wedge angle (mrad)	Tolerances (μm)
30	6	0.5-10	0-80	60

2.4.11.2.3 Degrader System in Combination with the Energy Buncher

At the entrance of the Low-Energy-Branch a particular and novel application using degraders is realized, an energy buncher system. Its main components are a dispersive magnetic dipole stage and a monoenergetic degrader. It reduces the momentum spread of in-flight separated ion beams, usually of the order of several percent (± 3 % in the case of the Super-FRS), down to values comparable to slowly extracted primary beams. Thus this scheme will be used to compress ("cool") the longitudinal emittance on a nanosecond timescale. It opens a new window to physics experiments with exotic nuclei: the energy-buncher stage will provide slow (Ekin ~ 100...1 MeV/u) monoenergetic (δE ~ 1 MeV/u) beams and will allow stopping exotic nuclei in very thin implantation arrays (~ mg/cm2) or in helium-filled (gaseous or superfluid) stopping cells. From the latter, singly-charged ions of all elements can be extracted and post-accelerated to a few 10 keV for physics experiments (see section 2.4.11.2.4).

Adapted to the ion-optical parameters of the energy buncher, the calculated envelopes of the ion beams, and the properties during the slowing down, the following dimensions and tolerances have been calculated for the degrader system at focal plane MF11:

Width (cm)	Height (cm)	Thickness (g/cm^2)	Wedge angle (mrad)	Tolerances (μm)
60	20	0.5-20	0-120	140

Similar to the other focal planes, this unit will comprise wedges, disks, and homogeneous plates to yield the necessary flexibility. The large dimensions need special care. A prototype is under development to gain experience and to test under realistic conditions at the FRS the performance and possible radiation damage or modifications of the material. Figure 2.4-119shows the drawings and the first mechanical linear drives during assembly.

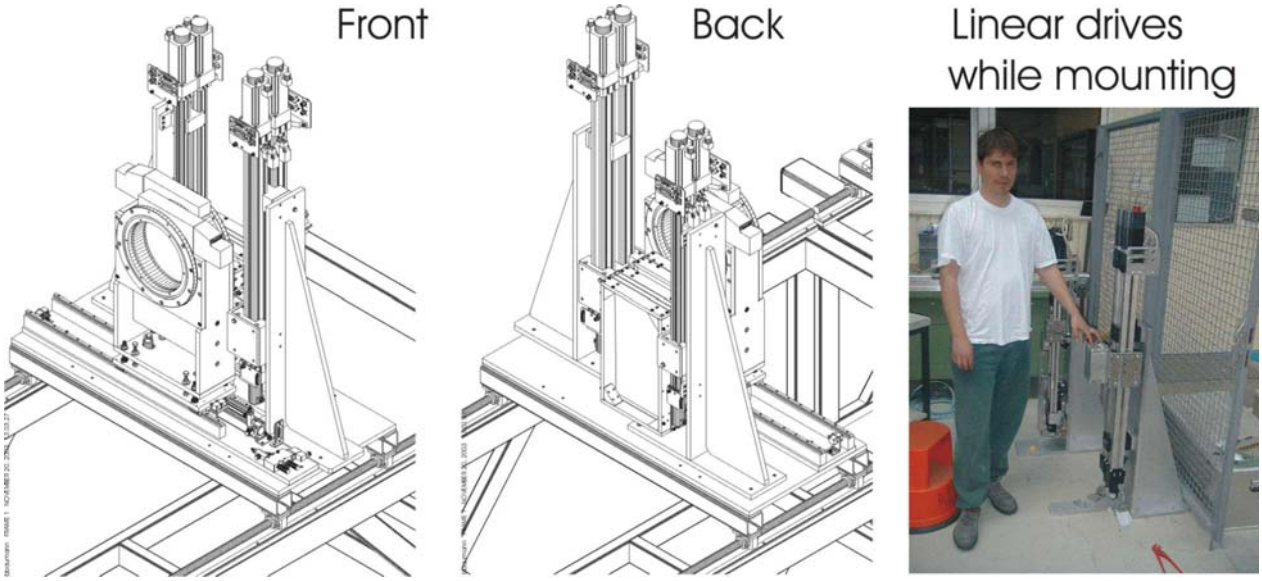

Figure 2.4-119*:* Drawings and first parts while mounting the prototype of the degrader for the energy buncher. This prototype will be used and tested for the FRS Ion Catcher setup.

2.4.11.2.4 Ion Catcher

This stopping unit and its related components (beam extraction, cooling, bunching, and distribution system) as well as results from their performance characterization are described in the Low-Energy-Branch Technical Report [60].
For the Super-FRS Ion Catcher there is an R&D program underway. Figure 2.4-120 shows the prototype of an ion-catcher and beam-distribution system, which has been setup and optimized off-line in collaboration with ANL Argonne, MSU, and Giessen University. The system has been commissioned in February 2005 and characterized with relativistic ^{58}Ni ions at the FRS [61], see Figure 2.4-121. During the on-line test, an overall efficiency of (1.8 ± 0.3) % has been achieved at a gas cell pressure of 100 mbar helium, which can be divided into a stopping efficiency of (5.0 ± 1.1) % and an extraction and transport efficiency of (35 ± 9) %. The overall efficiency is hence limited mostly by the stopping efficiency, which could be increased in the future by operating the stopping cell at higher pressures. From extraction time measurements of polyatomic ions formed in the gas cell extraction times of atomic ions of 20 ms to 50 ms can be derived. In these tests, only beam intensities of $2 \cdot 10^5$ ions per spill every ~ 8 s were used. However, on-line tests with a similar gas cell, operated at the MLL tandem accelerator at Munich, have shown the promising result that the overall efficiency of the stopping/extraction

system stays constant up to intensities of a few 10^8 ^{107}Ag-ions per second [62]. To circumvent problems with molecular contamination created in the gas cell in the future, a cryogenic stopping cell cooled with liquid nitrogen is under development in collaboration with KVI Groningen. This stopping cell will also allow reduced diffusion losses to the walls of the device.

As an alternative approach, groups of JYFL Jyväskylä and KVI Groningen are developing and investigating the possibility to stop and extract exotic nuclei in/from superfluid liquid helium[63]. Similar extraction times and efficiencies as in the case of gaseous helium are expected, but the approximately 800 times higher density (as compared to gaseous helium at standard temperature and pressure) will allow for a much more compact apparatus. After thermalization in superfluid helium, positive ions form "snowballs" – clusters of helium atoms that form around positive ions due to electrostriction. Applying electrical drag fields, the snowballs drift to the superfluid helium surface and escape to the vapour region with high efficiency. In the near future further tests with improved setups are planned: off-line tests at KVI and on-line tests at JYFL. These studies will be further pursued as part of the European DIRAC design study.

Figure 2.4-120*:* Off-line setup of a high-pressure helium-filled stopping system for relativistic heavy ions.

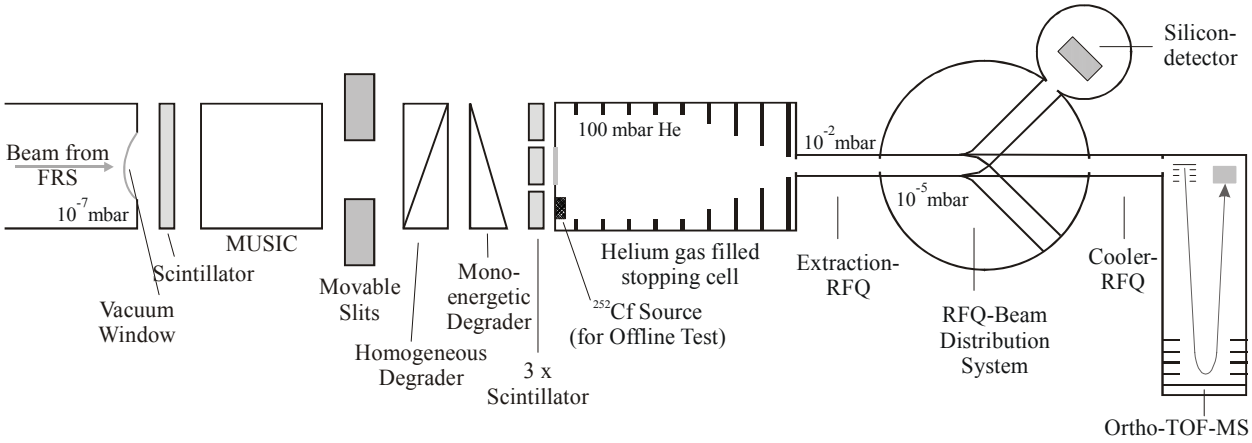

Figure 2.4-121*:* Schematic figure of the experimental setup of the Ion Catcher experiment behind the FRS. A multi-wire proportional chamber (MWPC) is used for beam tracking and ion rates are measured in a multiple sampling ionisation chamber (MUSIC). The ions are range-focused in the degrader system, consisting of a homogeneous and a monoenergetic degrader. Three scintillators in front of the gas cell are employed to measure the ratio of ions that do not enter the gas cell. Ions are stopped in the gas cell in helium at a pressure of 100 mbar and extracted, separated from the gas in an extraction RFQ, and guided in an RFQ-based beam distribution system alternatively to a silicon detector for counting radioactive ions or a time-of-flight mass spectrometer with orthogonal acceleration (Ortho-TOF-MS) for identification of the ions and extraction time measurement.

2.4.11.3 Production Targets

Similar to the present SIS18/FRS/ESR facility, both, slow and fast extraction from SIS100/300 will be used at Super-FRS: the former (with typical extraction times of a few seconds) for counter experiments at the experimental caves, the latter for experiments with radioactive secondary beams in the storage rings where short beam pulses with a length of typically $\tau \sim 50$ ns will be needed. The very high instantaneous power deposited in the target by fast-extracted beams (up to ~ 200 GW) could lead to destruction of the production target [64] by a single beam pulse. It is, therefore, essential to take special care in designing a target for fast extraction.

The key parameter for target technology is the specific power deposited by the primary beam and by the fragments produced in the target. Since only ions lighter than the projectile are formed in projectile fragmentation and fission, it is reasonable to consider only the parameters of the incident beams. The optimum target thickness will range from a few g/cm^2 up to about 8 g/cm^2 depending on the atomic number Z of the projectile and the selected energy. Table 2.4-31 lists typical specific energies deposited in graphite chosen as the target material by three benchmark beams, ^{40}Ar, ^{136}Xe and ^{238}U. All beam intensities are taken as 10^{12} ions/pulse, and the beam energies are 1 *A GeV*. The beam spot is assumed to be a two-dimensional Gaussian distribution with $\sigma_x = 1$ mm and $\sigma_y = 2$ mm.

Table 2.4-31*:* Typical beam parameters considered for planning production targets at the Super-FRS

Beam	Total beam energy *E* [kJ]	Graphite target thickness [g/cm^2]	Deposited energy *ΔE* [kJ]	Specific energy *ΔE/M* [kJ/g]
^{40}Ar	6.4	8.0	0.83	0.83
^{136}Xe	21.8	6.0	6.0	7.9
^{238}U	38.1	4.0	12.0	24

2.4.11.3.1 Target Design for Slow-Extraction

In slow extraction mode, the typical extraction time is 1 s, and, consequently, the energy values given in Table 2.4-32 can easily be converted into power with the same numerical values. The maximum beam power of 12 kW deposited by ^{238}U in the Super-FRS target can be compared to the values found in operating facilities (PSI, RIKEN/BigRIPS) or to those considered in planned facilities (GANIL/SPIRAL-II), see Table 2.4-32. The Super-FRS beam power in slow extraction is lower than in the above-mentioned facilities, and graphite should, therefore, be a good candidate for the target material.

Although graphite has one of the best thermal characteristics, the energy deposited by the uranium beam in a stationary target would lead to very high temperatures of about 10,000 K, which are well above the sublimation point. The solution that has therefore been chosen at PSI, RIKEN and SPIRAL-II involves a rotating-wheel concept, which allows to increase the volume in which the energy is deposited. The same concept will be used at the Super-FRS.

Table 2.4-32*:* Typical beam parameters for production targets of existing or planned secondary-beam facilities. All target concepts use rotating wheels and DC beams. For Super-FRS slowly extracted beams of a rate 1/s were assumed. Specific power values are calculated assuming that targets rotate with 60 rpm (500 rpm for BigRIPS).

Facility	Beam	Total beam power P [kW]	Graphite target thickness [g/cm^2]	Deposited power ΔP [kW]	Specific power $\Delta P/M$ [kW/g]
PSI	P	1000	10.8	54	0.18
RIKEN/BigRIPS	all ions	< 100	1	< 24	0.45
SPIRAL-II	D	200	~ 0.8	200	~ 0.25
Super-FRS	all ions	< 38	1 - 8	< 12	< 0.15

Calculations of an engineering model of the graphite target wheel

Concerning the engineering design of the Super-FRS target for slow extraction the solution developed and used at PSI [65] will be followed. A more detailed description of the rotating target wheel has been given in the final report of task 6 of the EU Design Study "DIRACsecondarybeams" [66].

The target is a graphite wheel with a diameter of 45 cm. Since it will be operated with a wide variety of incident-beam elements, the target thickness must be adjustable. This has been realized by subdividing the graphite ring into five concentric circles, each 16 mm wide, with thicknesses of 5.4, 13.5, 21.6, 32.4, and 43.2 mm, corresponding to 1, 2.5, 4, 6, and 8 g/cm^2, respectively. Following the PSI experience, the best choice for the graphite material is R6510P from SGL Carbon [67]. The most important property of this graphite is isotropic expansion during heating thus avoiding excessive radial amplitudes during target rotation. The target thickness can be changed by shifting the entire wheel assembly orthogonal to the beam direction. In the same way, the target can be removed entirely from the beam. The ^{238}U primary-beam spot is assumed to have a Gaussian shape with a width of 1 mm in horizontal (bending) direction and of 2 mm in vertical direction, leading to a specific energy deposition at 1 Hz rotation frequency of about 150 W/g.

The target is cooled only by thermal radiation from the surface without additional cooling. The advantage of operating graphite at elevated temperatures lies in the fact that, even though the thermal conductivity of graphite decreases with increasing radiation doses, the residual thermal conductivity after irradiation is higher if the irradiation occurs at high temperature. The

maximum operating temperature is given by a tolerable level of the sublimation rate of graphite (about 10 mg/g/year), and should not exceed 1800 K [65].

While the graphite rings have to be operated at high temperatures to facilitate thermal radiation, the spokes and bearings of the target wheel have to be kept at relatively low temperatures. This will lead to different thermal expansions and consequently to stress. To solve these problems, the graphite target ring is connected to another one by graphite spokes to allow thermal expansion. Minimum heat transfer to the axle is guaranteed by connecting this ring by thin hollow spokes made of INCONEL 600. The heat radiated from the graphite target is absorbed by water-cooled copper blocks to protect the bearings from the radiated heat.

These elements were taken into account for the following ANSYS calculations. Assuming that the target wheel rotates with a speed of 60 rpm, maximum temperatures of about 750 ^{o}C for the graphite wheel have been obtained (see Figure 2.4-122). The most critical parts in this arrangement are the bearings of the axle close to the shaft. It was investigated at PSI that temperatures of about 120 °C should not be exceeded. To assure this more detailed calculations have been done. The temperature distribution for the axle with bearings was calculated with the temperature distribution from the model above (see Figure 2.4-122). Temperatures of only 35 ^{o}C have been obtained (see Figure 2.4-123) so that the target wheel can be connected to the target drive without overheating the bearings.

The rotation of the wheel will be induced by an electrical motor running outside the vacuum; the torque will be transmitted via a magnetic coupling, steel drive shafts and a 90-degree gear. Important components are the ball bearings of the target wheel; at PSI these are made by GMN Co. [68] and consist of silver-coated rings and cages with MoS_2 lubrication and silicon nitride balls. They have been proven to run in vacuum during more than one year without failure [65].

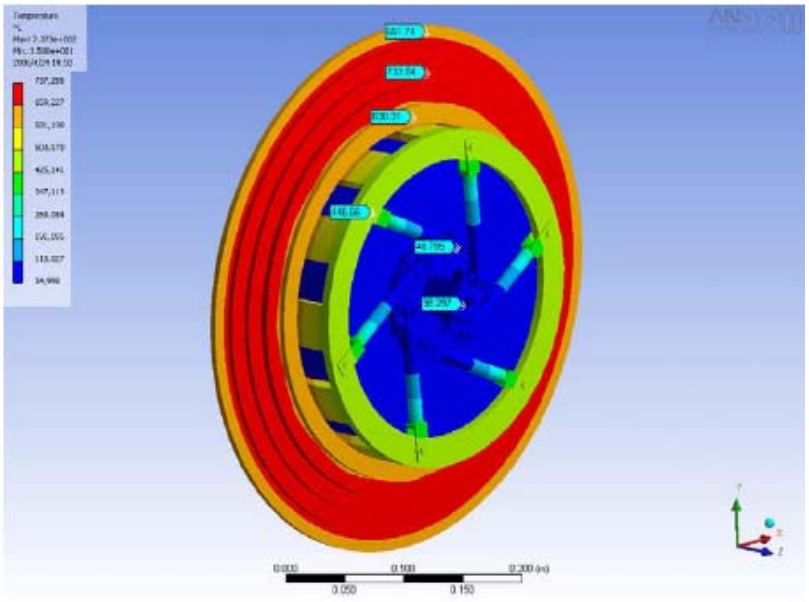

Figure 2.4-122*:* Surface temperature distribution of a graphite target mounted with spokes and shaft on an axle (rotating with 60 rpm around a water-cooled block) irradiated with a 238U beam (1 A GeV, 1012 ions/s, Gaussian beam profile with σx = 1 mm and σy = 2 mm) according to an ANSYS simulation.

Another important issue are the thermally-induced tensions in the graphite wheel, which were calculated with the ANSYS code and are shown below (see Figure 2.4-124, left side). Maximum stress values of less than 7 MPa have been obtained, which is well within the technical tension range for graphite of about 35-65 MPa. Higher stress values have been found for the

INCONEL spokes connecting the graphite parts with the hub of the target wheel. As the right-hand side of Figure 2.4-124 shows, the maximum stress amounts to about 200 MPa, again well below the listed tensile strength of INCONEL of about 600 MPa.

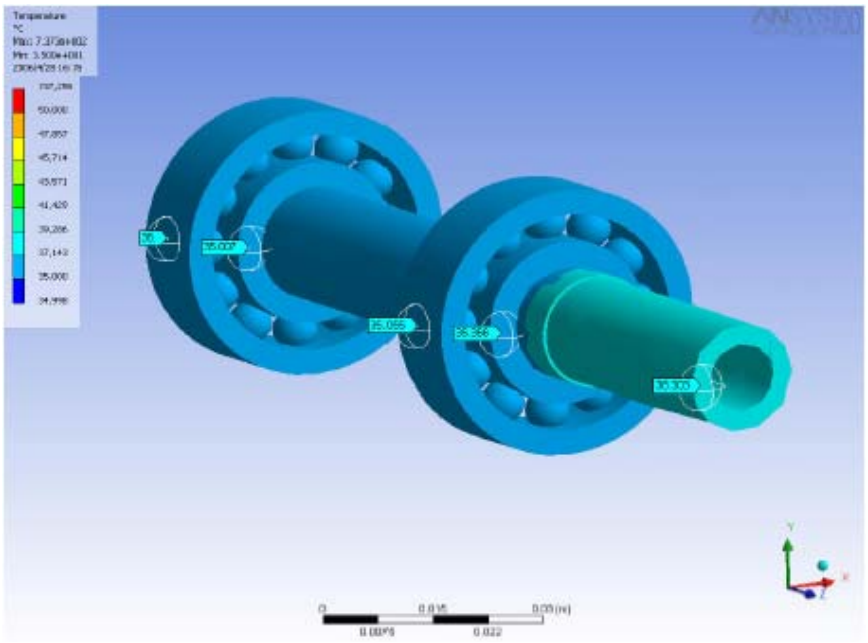

Figure 2.4-123*:* Temperature distribution of the axle and the bearings according to an ANSYS simulation.

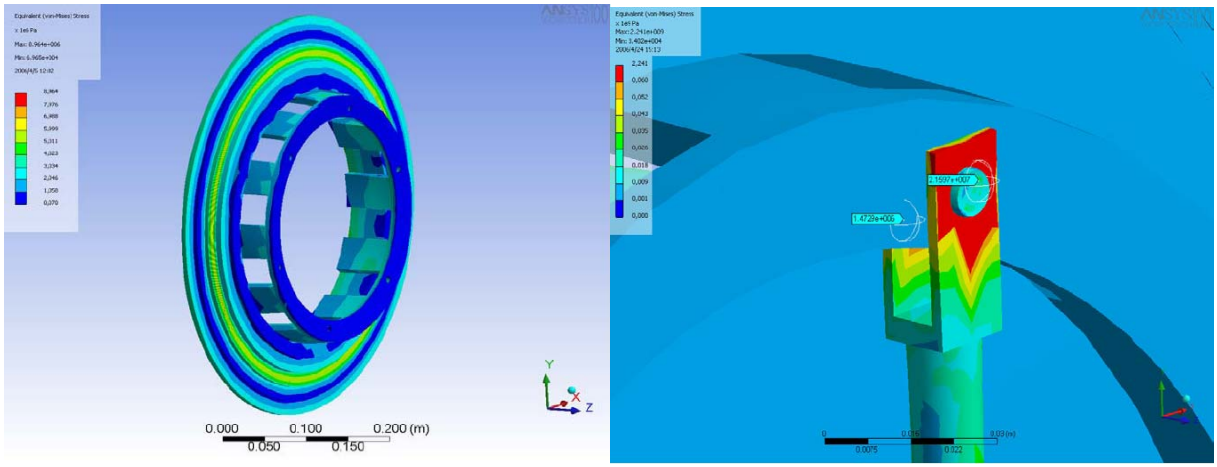

Figure 2.4-124*:* Left: Von-Mises-stress in the graphite wheel irradiated with a ^{238}U beam (same parameters as in Figure 2.4-122) according to an ANSYS simulation. Right: The same calculated for the connection between INCONEL spoke and graphite ring.

The need to strip heavy fragments after their creation in the target, such that the maximum yield of fully stripped fragments is obtained, requires a layer of a suitable stripper material (e.g. titanium) deposited on the downstream face of the target wheel. A technical solution that is compatible with the high temperatures of the graphite wheel is presently under discussion.

We do not yet know accurately how much radiation damage will affect the useful life time of the graphite target wheel. To get an estimate, we have tried to relate the radiation damage at high energies and in transmission mode to experimentally observed radiation damage at low energies (11 *A* MeV) where the specific energy loss is much higher and the ions are stopped in the graphite. For uranium ions, where the effect should be most pronounced, Tomut *et al.* [69]

have found a critical fluence value of about 10^{13} ^{238}U ions/cm^2 for low-energy uranium beams. At this critical fluence, the 3 nm-diameter tracks produced by uranium ions start to overlap, giving rise to the observed changes in graphite properties. According to Liu et al. [70] the track density at the high beam energies in the Super-FRS target are about a factor of 10^3 lower. Another factor of 10^3 can be gained from annealing of radiation damage at temperatures above 800 K [54]. Consequently, the track density resulting from one year of Super-FRS operation with ^{238}U (10^7 pulses with 10^{12} ions/s impinging on a wheel rotating with 1 Hz) is estimated to be 10^{11}/cm^2, well be below the critical limit given above.

In March 2008 the prototype of the graphite target wheel (Figure 2.4-125) has been delivered to GSI. It will first undergo thermal testing and will then be mounted at the present FRS target area for in-beam test operation.

Figure 2.4-125: Prototype of the graphite target wheel for Super-FRS delivered to GSI.

Target-area layout and infrastructure

Following the concepts realized at all current high-power target systems, the Super-FRS target-area elements (target assembly, pillow seals, diagnostic detectors etc.) consist of individual modules ("plugs") that combine the respective element with a tight local iron shielding. The plugs can be removed and inserted vertically by a crane (see Figure 2.4-126). They are inserted in a target box that is connected to the beam line via inflatable all-metal seals which do not require any clamping (so-called "pillow seals" [71]). In addition, all inserts together with their respective shielding are sealed from ambient air at working-platform level by organic-material seals that are operated manually during target service periods. The local shielding of each plug ensures that the neutron dose at platform level during beam-on periods is low enough to allow the use of polymer seals.

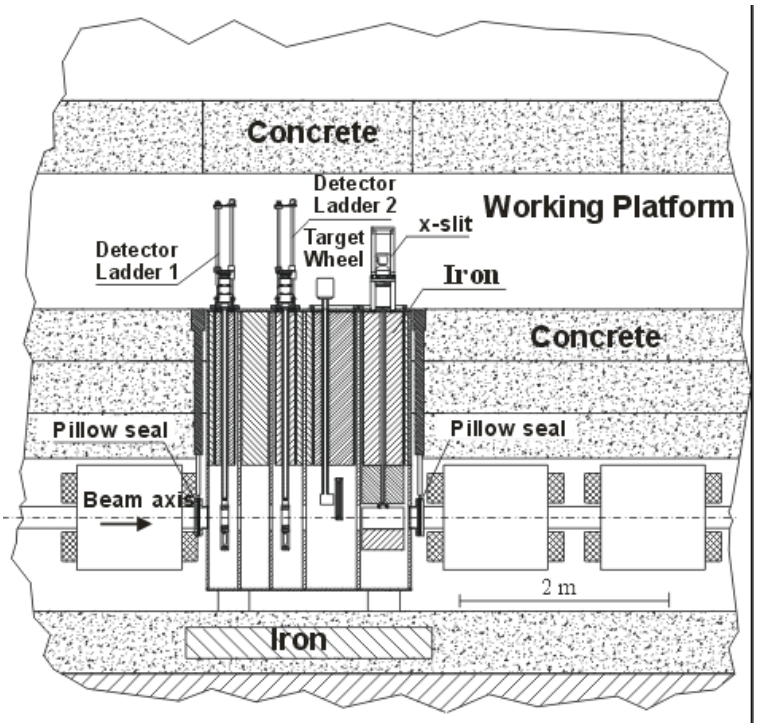

Figure 2.4-126*:* Schematic layout of the target area of the Super-FRS. A vertical plug system has been adapted which has proven to guarantee a safe and reliable operation at PSI in a very high radiation field. Routine maintenance at PSI is done about once per year.

The detailed design of the target box is shown in section 0.

2.4.11.3.2 Target Design for Fast-Extraction

The present planning for the Super-FRS target to be used with fast-extracted beams considers three options:

- For low specific beam powers, e.g. when using light ions or during the start-up phase of Super-FRS (where up to $2 \cdot 10^{10}$ ^{238}U ions/pulse are predicted), the use of the rotating graphite wheel with the same narrow focussing as used for slow extraction is foreseen also for fast extraction.
- For the highest power densities, as e.g. deposited by 10^{12} ^{238}U particles extracted within 50 ns, the beam spot on the graphite target has to be extended, causing moderate losses of transmission to the ring branch.
- Alternatively, a windowless liquid-metal jet may be considered. This latter idea follows plans for the previously planned RIA heavy-ion fragmentation facility in the USA [72] or those for high-intensity pulsed proton beams e.g. in a ν-factory [73]. In both of these cases, however, the instantaneous beam power is much lower than estimated for Super-FRS: RIA was supposed to run heavy ions in DC mode, whereas sub-μs-pulsed proton beams will be used to produce ν's. First calculations of a Super-FRS liquid-metal target for the fast-extraction scheme are reported in Refs. [74,75].

The above-mentioned options have uncertainties that need to be addressed in detail. It has e.g. to be investigated if many short beam pulses impinging on the graphite wheel lead to structural damage ("fatigue") in the graphite that could limit the life time of a target wheel.
Research and development for a liquid-metal jet target for the Super-FRS has been undertaken since February 2005 in the 6th framework program of the EU within the Design Study "DIRAC Secondary beams" [66]. Results obtained so far are presented below.

Fast-extracted beams on a graphite wheel target

In view of the complexity of the operation of a liquid-metal target, it is desirable to use the rotating-wheel target also for fast-extracted beams, as long as the critical parameters of graphite (temperature, pressure) are not exceeded. To judge the operability of a graphite wheel in fast-extraction mode, it is important to know the maxima (positive and negative) of the pressure waves that traverse the graphite target after the impact of a short ion pulse. For safe operation of the graphite wheel, the induced pressure should stay below the brittle-failure limit, which amounts to ~65 MPa for the selected graphite grade [76], while the induced temperature should stay below 1800 K, which is the maximum operating temperature given by a tolerable level of the sublimation rate of graphite (~ 10 mg/g/year) [65].

To obtain a rough estimate of the pressures induced in graphite by short ^{238}U pulses, experiments have been performed with the present SIS18 beams. Well focussed pulses were directed onto graphite cylinders of 10 mm length and 5-10 mm diameter and the elastic surface vibrations have been measured with a laser Doppler vibrometer (SIS Experiment S334 [77]). Table 2.4-33 lists typical specific energies deposited in graphite by ^{238}U of various energies and intensities, together with deduced or calculated pressures in the graphite. The first two rows printed in bold refer to the experimental situation of experiment S334 [77]. The other two rows are predictions for various SIS100 beam intensities. The beam spot on target is a round two-dimensional Gaussian distribution.

Table 2.4-33: Energy deposition in a graphite target by ^{238}U beams of various intensities per pulse.

Case	Beam intens. (1/pulse)	Beam energy (A MeV)	Sigma width [mm]	Specific energy $\Delta E/M$ [kJ/g]	Temp. rise ΔT [K]	Static pressure [MPa]	Dynamic pressure LS-DYNA [MPa]	Dynamic pressure FEAP [MPa]
1	**$5.48\cdot10^{8}$**	**350**	**0.38**	**0.25**	**170**	**9**	**4**	
2	**$2.40\cdot10^{9}$**	**350**	**0.38**	**1.0**	**650**	**31**	**25**	**17.5 [80]**
3	$5.0\cdot10^{10}$	1000	2.0	0.11	110	5.5		
4	$5.0\cdot10^{11}$	1000	4.9	0.96	580	30		

The simplest approach to calculate the quasi-static pressure jump inside the target is given by $p = 3\ K\ \alpha\ \Delta T$, where K is the bulk modulus, and α the linear expansion coefficient. ΔT is calculated from the specific energy deposit, $\Delta E/M$, divided by the heat capacity. Table 2.4-33 was calculated with K = 4.17 GPa and $\alpha = 4\cdot10^{-6}$ 1/K. The temperature rise listed in column 6 of Table 2.4-33 is always much lower than the operating limit, so that the limiting factor for target survival can be expected to be the tensile strength of graphite. Quasi-static pressures, p, are given in column 7. Columns 8 and 9 list dynamic pressures calculated with two different finite-elements models for solving non-linear dynamics, LS-DYNA [78], and FEAP [79,80]. In both cases, the pressure stays below the one calculated in the static approach. Moreover, all pressure values given in rows 1 and 2 stay below the limiting value given by the brittle-failure limit of ~65 MPa.

The conclusion from the above estimates is that for the SIS100 design intensity of $5 \cdot 10^{11}$ ^{238}U ions/pulse at 1 *A* GeV, and a moderately extended beam-spot size of σ_x= 4mm and σ_y = 6 mm the Super-FRS graphite target wheel can serve to perform experiments with high-power fast-extracted beams, too. Due to the enlarged beam-spot size, the simulated transmission of e.g. ^{132}Sn into the collector ring CR will be reduced from 27% for an ideal narrow beam spot (σ_y = 2 mm) to 17% for a beam spot with σ_y = 6 mm. For a certain group of ring-branch experiments, the worse ion-optical resolution due to the broader spot in x-direction can be compensated for by the resolution power of the rings.

Liquid-metal jet as a target for fast-extracted beams

The very high instantaneous power deposited by a well-focussed full-intensity uranium beam in fast extraction will lead to instantaneous destruction of solid materials. The safe use of a graphite wheel requires an expansion of the beam spot. An alternative solution may be a windowless liquid-metal target. Low-*Z* targets (Li, Na) are preferred, due to lower multiple scattering of radioactive nuclides, higher number of atoms per unit energy loss of the primary beam, and smaller range of long-lived radioactive products. Liquid Li has been chosen by ANL as a candidate [72], in view of its extremely high thermal range of more than 1100 K between melting and boiling, and its very low vapour pressure. A drawback is its low density of 0.5 g/cm^3, which leads to a wide target extension along beam direction.

Calculation of jet response to fast beam pulses

For the first test calculations, a jet made of liquid lithium was assumed. Two different theoretical approaches were taken. In the first approach [74], the response of a liquid-lithium jet to a high-intensity ^{238}U beam pulse of 50 ns length has been calculated with a 2-dimensional hydro-dynamical code, BIG-2 [81]. The benchmark Super-FRS beam, 10^{12} ^{238}U ions with 1 *A* GeV per 50 ns impinged on a 7 cm thick liquid Li target. The beam spot was assumed to be Gaussian with $\sigma_x = \sigma_y$ = 1 mm. In the present 2-dimensional calculation the high power density deposited in a column of liquid Li is predicted to lead to a fast vaporization of the Li contained in the volume traversed by the beam and to a shock wave that travels orthogonal to the beam direction.

The finite velocity of sound in Li makes sure that during the interaction the target density is unchanged, so that the probability of producing a fragment and its kinematical properties are unchanged. Typical parameters of Li in the beam trajectory according to the BIG-2 calculation are a temperature of 13,000 K, a pressure of 14 GPa, and an energy density of 42 kJ/g, see Figure 2.4-127 (left).

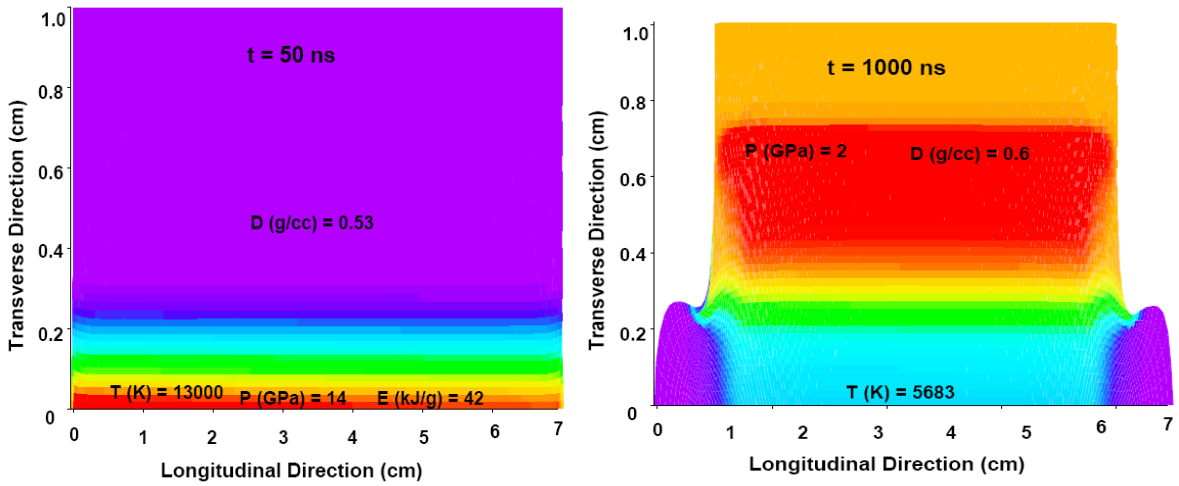

Figure 2.4-127*:* Calculated density of lithium - left: after the beam passage (after 50 ns) - right: 1μs after the passage of beam. Along the beam trajectory the vaporized Li explodes, shown by violet regions in the right figure. Orthogonal to the beam direction the shock front moves and within 1μs will travel by about 8 mm. For several positions in the Li jet, the values of temperature (T), pressure (P) and energy density (E) are also given in the plots [74].

The BIG-2 calculation predicts that the vaporized Li will explode in (positive and negative) beam direction with velocities of about 10 km/s, with the central density being reduced rapidly (Figure 2.4-127, right). Orthogonal to the beam direction, temperature and density are not much higher than normal, but a pressure wave travels outward with an initial velocity of about 1.5 km/s. After 1 μs the shock front has moved by about 8 mm.

The above conditions are, obviously, not suitable for a fragmentation target. They were just used as a benchmark to check if 3-dimensional hydro-dynamical calculations of the behaviour of the Li jet yield similar results, i.e. if the less time-consuming 2-dimensional calculations are realistic enough to use them to find suitable operating conditions for an actual Li-jet target. First 3-dimensional calculations were performed at LLNL, Livermore, USA, using the code ALE3D [82]. ALE3D is a three-dimensional finite-element code that utilizes Arbitrary Lagrangian-Eulerian techniques to simulate fluid dynamics and elastic-plastic response on an unstructured mesh. The code has a range of equation-of-states and constitutive descriptions that are appropriate for modelling hydrodynamic shock phenomena. The ALE3D numerical results for the scenario described above are very similar to the results from BIG-2.

Like in the case of the rotating graphite wheel it is of great interest to apply the conditions of the windowless liquid target with enlarged beam spots. Calculations with BIG-2 for 1 *A* GeV 10^{12} ^{238}U ions/50 ns with a spot area of $\sigma_x = 2$ mm and $\sigma_y = 12$ mm impinging on the liquid lithium target [64] demonstrate that after 1 μs the target remains liquid (density changes only by 0.04 g/cm^3) and is only marginally influenced by shock waves. In this case, where the specific energy deposition is 1.66 kJ/g, the Li temperature is predicted to rise by about 600 K, with a (compressional) pressure of about 900 MPa.

An alternate hydro-dynamical calculation for $5 \cdot 10^{10}$ ^{238}U ions with 1 *A* GeV impinging on a 7 cm thick liquid Li column was performed by A.Tauschwitz *et al.* [75]. The beam spot was assumed to have a Gaussian shape with $\sigma_x = 4$ mm and $\sigma_y = 8$ mm. A simple analytical linear Mie-Grueneisen equation of state was assumed. The particular feature of these calculations is that reflections of the pressure waves at the free surface of the Li column are taken into account. As a result, negative (tensile) pressures appear. If this tensile pressure exceeds the tensile

strength of liquid Li at the respective temperature, the jet is predicted to spall; i.e. a free surface develops within the fluid. Unfortunately, no data are available in the open literature for the tensile strength of liquid Li. Therefore, a formula given by Grady *et al.* [83] has been used in Ref. [75] to estimate a numerical value for this quantity. The resulting value is only 9 MPa, which would imply that in the scenario assumed above the jet would break after only 210 ns (Figure 2.4-128). A comparison of the kinetic energy of the spalled part of the liquid with the work for its detachment indicates that the material would move outward and break off from the jet.

It is obvious that further experimental and theoretical investigations are needed to make more reliable predictions for the operation limits of a liquid-Li jet. In particular, it is foreseen to measure the tensile strength of liquid lithium with the help of a laser Doppler vibrometer in an explosion chamber at IHED Moscow [84].

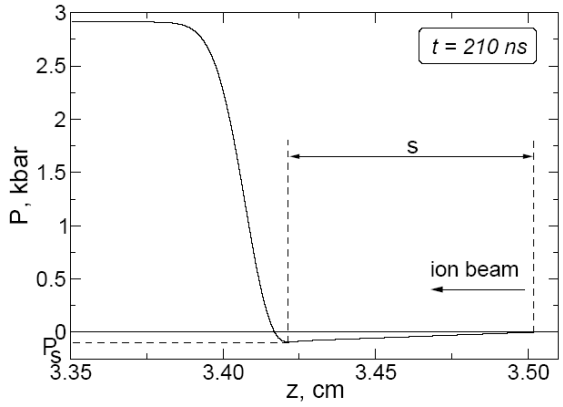

Figure 2.4-128*:* Calculated pressure profile on the axis of a 7cm liquid Li target after the penetration of $5x10^{11}$ 1 A GeV ^{238}U ions within 50 ns, at 210 ns after the beam interaction (according to Ref. [*75*]). The assumed Gaussian beam spot has σ_x = 4 mm and σ_y = 8 mm. At s = 8 mm from the point of impact of the beam, a negative pressure develops that exceeds the estimated spall strength of liquid Li of 9 MPa, leading to a destruction of the target.

Engineering design

Engineering aspects of a potential liquid-metal jet target have been studied in the framework of an EU-funded design study [66], with the goal to find a conceptual design of a suitable liquid-lithium jet and to build a prototype. The basic problems to be addressed are the following ones:

1. Is it possible to form a homogeneous liquid-Li flow with about 7 cm length in beam direction (corresponding to about 3.5 g/cm^2 of Li) and a width of about 1-2 cm?
2. Which technical components are required for the safe operation of a free-flowing jet of liquid lithium?

Before starting complicated and time-consuming liquid-metal experiments, first studies with a water jet should define the nozzle shape and some basic operation parameters (even though scaling of the hydrodynamic properties from water to liquid-Li is not possible). After that, liquid-Na experiments allow studying the technical aspects; for this metal long-term experience exists at FZ Karlsruhe. Moreover, a similarity analysis has shown that scaling from Na to Li is possible. As a last step, the technical aspects of operating a liquid-Li loop can be addressed. Therefore, the following strategy has been followed in this part of the Design Study [85]:

a) Investigate the jet flow patterns of a water jet as a function of nozzle shape, flow velocity and water-conditioning parameters.
b) Develop non-destructive methods to experimentally classify the jet shape, velocity field and surface properties.
c) Compare the measured jet properties with those calculated with continuous-fluid dynamics (CFD) calculations.
d) Optimize the jet parameters according to b) in numerical CFD models.
e) Set up a liquid-Na loop to provide an experimental set-up to determine the properties and operation conditions of a liquid-Na jet.
f) Optimize by CFD calculations the jet parameters for liquid Na and compare the predictions to measurements.
g) Repeat steps e) and f) for liquid lithium.

Up to now, the Design Study has completed more or less all steps a) to e). For step b) it was necessary to develop novel techniques to scan totally reflecting surfaces by the Double-Layer Projection (DLP) technique (Figure 2.4-129) shows the liquid-Na loop that will be used to complete step f) until the end of the Design Study. During the course of the study it has become clear, however, that the use of liquid lithium poses additional chemical problems, mostly related to reactions of Li with trace elements in the liquid (e.g. N), that have to be solved before the use of a free Li jet can be considered as a practical target at the Super-FRS.

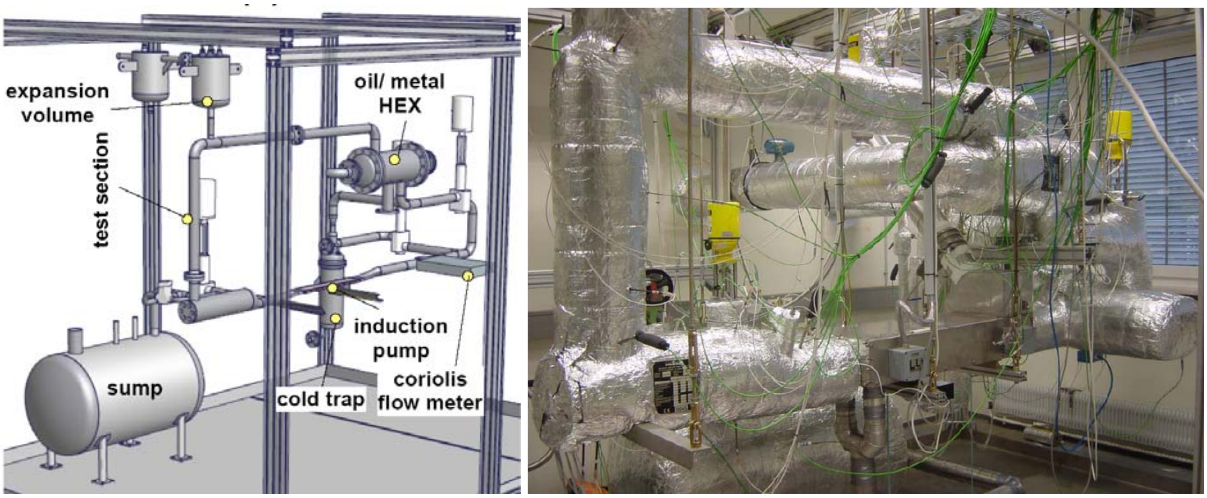

Figure 2.4-129*:* Left: Schematic diagram of the liquid-Na loop designed for testing a windowless Na jet. Right: Experimental liquid-Na set-up installed at the FZ Karlsruhe KALLA laboratory [*85*].

2.4.11.3.3 Conclusion

In summary, we can state that the target design for slow extraction is technically solved and fulfils all the requirements for experiments with exotic nuclei at the Super-FRS. Prototyping and test experiments at the present FRS have already started and will be continued.

For fast-extracted beams the design of a universal production target is still in progress. However, the rotating graphite wheel, ideally suited for slow-extraction, can also be used for fast extraction at the highest intensities under the condition that the separation power of the Super-FRS and the transmission are slightly reduced. Another option under investigation is the use of a liquid-Li target. Both 3-dimensional hydro-dynamical calculations and experimental investigations on the behaviour of a liquid-Li jet are underway. In particular, it has to be investigated if the low predicted spall strength of liquid Li can be verified experimentally.

2.4.12 Local Cryogenics

2.4.12.1 Cryogenics for Dipole Stages

There are 28 superconducting dipoles units in the Pre- and in the Main-Separator including the three branches (High-Energy-Branch, Low-Energy-Branch, and Ring-Branch) and in the experimental area of the Super-FRS (Magnetic Spectrometer and Energy-Buncher) as well. The superconducting dipole consists of a warm iron yoke and a warm bore. Only the upper and the lower coils are housed in one cryostat. According to the lattice design, always three dipole units of each dipole stage are always grouped together and will be supplied in parallel by one feedbox unit with liquid helium.

The flow scheme which is shown in Figure 2.4-130 demonstrates the following cooling concepts. Supercritical helium (5 K, 3.0 bar, pink line in the cryogenic transfer line) is expanded through the mass flow rate control valve, which works also as a J-T valve (FCV J-T) and its discharging pressure is variable between 1.2 bar and 1.5 bar (or even higher) as requested by the magnets. To re-condensate the flash gas produced by the control valve (FCV J-T), the discharging flow (dark blue) will be re-cooled through a heat exchanger in the so called subcooler. The heat exchanger is immersed in a liquid helium bath whose liquid level and temperature are adjusted by two pressure-control valves (PCV): a) one is on the circuit for collecting the return flow (light blue) from the magnet cryostats and b) another is on the circuit for the vapor return (yellow) from the subcooler. The helium flow at the outlet of the subcooler should contain only one-phase liquid helium that allows the helium supply to be equally distributed into three streams in parallel, each feeding one magnet cryostat. The liquid helium is transferred under the discharging pressure to each magnet cryostat via the so called jumper that makes the connection between the feedbox unit (subcooler and cryogenic transfer line) and the magnet cryostats.

Liquid helium is fed from the bottom of the coil container in the magnet cryostat and circulated through the flow channels around the coils. The heat load (steady state heat in-leaks, Joule heating of the instrumentation cables, SC wire junctions and AC loss during ramping, etc.) in the magnet cryostat may cause the evaporation of liquid helium. Therefore two-phase helium may be present in the return flow which comes out from the top on the coil container. A small fraction of such flow is used for cooling the resistive current leads whose cold ends are seated in the so called chimney helium vessel (light blue). The rest of the return flow (possibly two-phase helium) from one magnet cryostat merges with the other two streams before it enters into the subcooler.

The cooldown of the magnets can be carried out for individually groups. The cold helium gas is tuned in its flow rate by the cooldown control valve (violet) in a circuit which bypasses the subcooler. The control of the inlet temperature of the cooldown flow is also possible by mixing the cold helium with 300 K warm helium at required flow rates. The flow control valve (FCV) in the warm circuit that connects the helium vessel to the insulated quench gas collection/cooldown/warmup gas return line allows fine-tuning the cooldown flow through individual cold mass at request. Therefore the cooldown speed and the temperature gradient over the individual cold mass structures are controllable with respect to the specification. The warmup of the magnets can be done also on the base of a group by circulating the 300 K helium gas through both the 4 K and 50 K shield loops of the magnet cryostat.

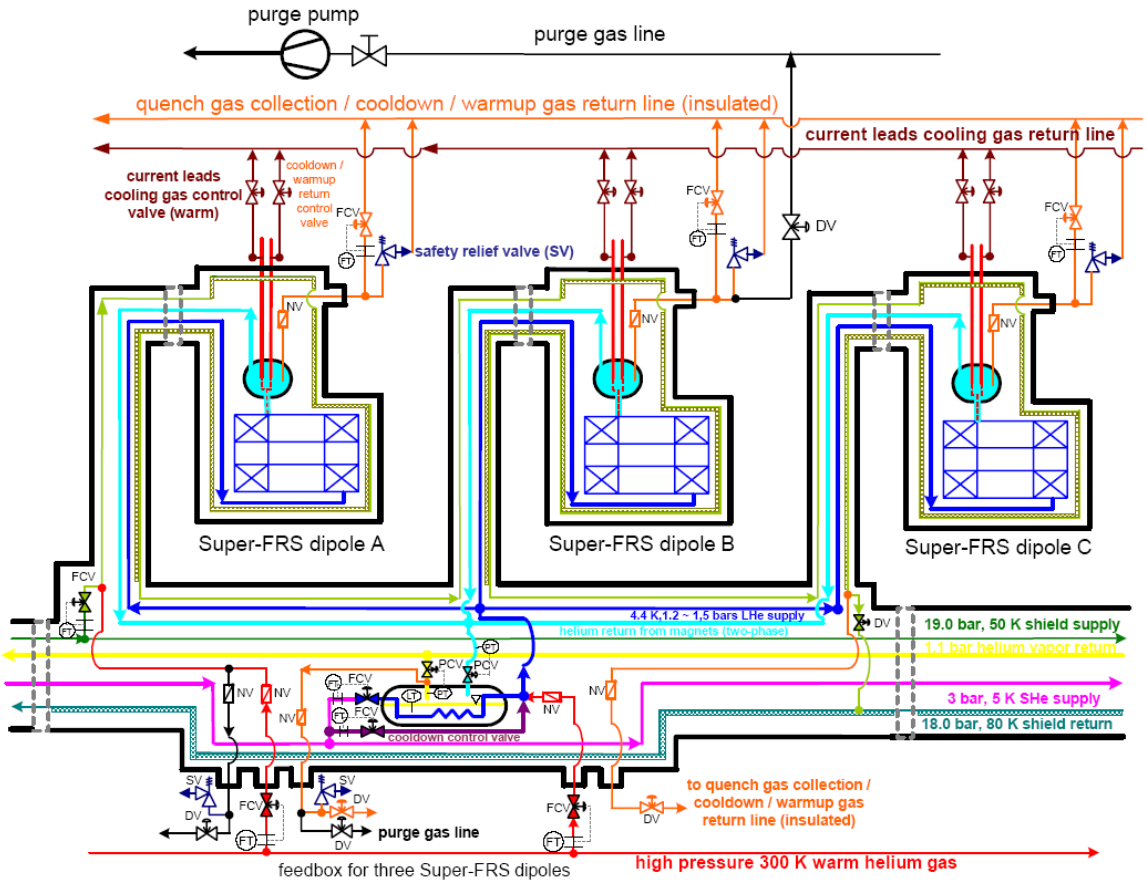

Figure 2.4-130: Flow scheme of three Super-FRS dipole units and one feedbox unit.

The 4 K helium vessel and coil container in each magnet cryostat are protected from the pressure increase in case of possible quenches by their own safety relief valves. Two additional safety valves are necessary, one for the subcooler protection and the other for the 50 K shield circuit protection. When a quench happens in any magnet of one group, the flow control valve (FCV J-T) located at the upstream of the 4 K flow process will be shut off and the two pressure control valves (PCV) at the downstream will be completely opened as the active action of the quench protection logic control. The protection measure is expected to ease the pressure buildup in the helium vessels. Nevertheless, as a passive action of the quench protection the safety relief valve will be opened once its set pressure is exceeded by the pressure peak resulting from the rapid energy dump in the liquid helium.

The 50 K to 80 K shield flow is connected in series for three dipole units in one group but in parallel with respect to the main transfer lines and to the other magnet groups. It is tuned in its flow rates by the flow control valve (light green) at the inlet and the on/off valve (DV) at the outlet. Therefore the cooldown / warmup / operation processes and commissioning/ maintenance / service / repairing of each magnet group are independent. Non-return check valves (NV) are used to reduce the potential risk of the thermoacoustic oscillations and the induced large heat in-leaks. Warm valves and piping are necessary for the purging process and the cooling gas return of the current leads.

In the feedbox unit there are in total seven headers which stretch over the full length of the feedbox unit. Three of them are the process tubing for the cryogenic circuit interconnections among the three dipole cryostats and the remaining four are the process tubing with general purpose of cryogenic fluid transfer. In fact, the feedbox unit has five interface connections of two types, three jumper interconnections to the magnet cryostats as type one and two cryogenic

transfer line interconnections as type two. Both types of interconnections are of 4-header inner configuration but with different dimensions. If the length of the feedbox unit is not a limitation from the manufacture point of view, it should be designed and fabricated as one standard module.

2.4.12.2 Cryogenics for Multiplets/Quadrupoles

In the Super-FRS there are 118 superconducting quadrupoles and hexapoles located in between every two groups of dipoles and in front of the Super-FRS target region. In the Main-Separator, usually five neighboring quadrupoles / hexapoles form a multiplet. This is installed in one single cryostat with a length up to 7 m and cooled in a liquid helium bath. The multiplet has a cold iron mass up to 37 tons. Therefore high cooling capacity is required to cool down such magnets. It is foreseen that one feedbox unit controls the liquid helium distribution for two multiplet cryostats. Figure 2.4-131 shows the flow scheme of two neighboring multiplets and the corresponding feedbox for the cryogenic supply. The feedbox unit is identical to the one for the dipole units except that only two jumpers are needed.

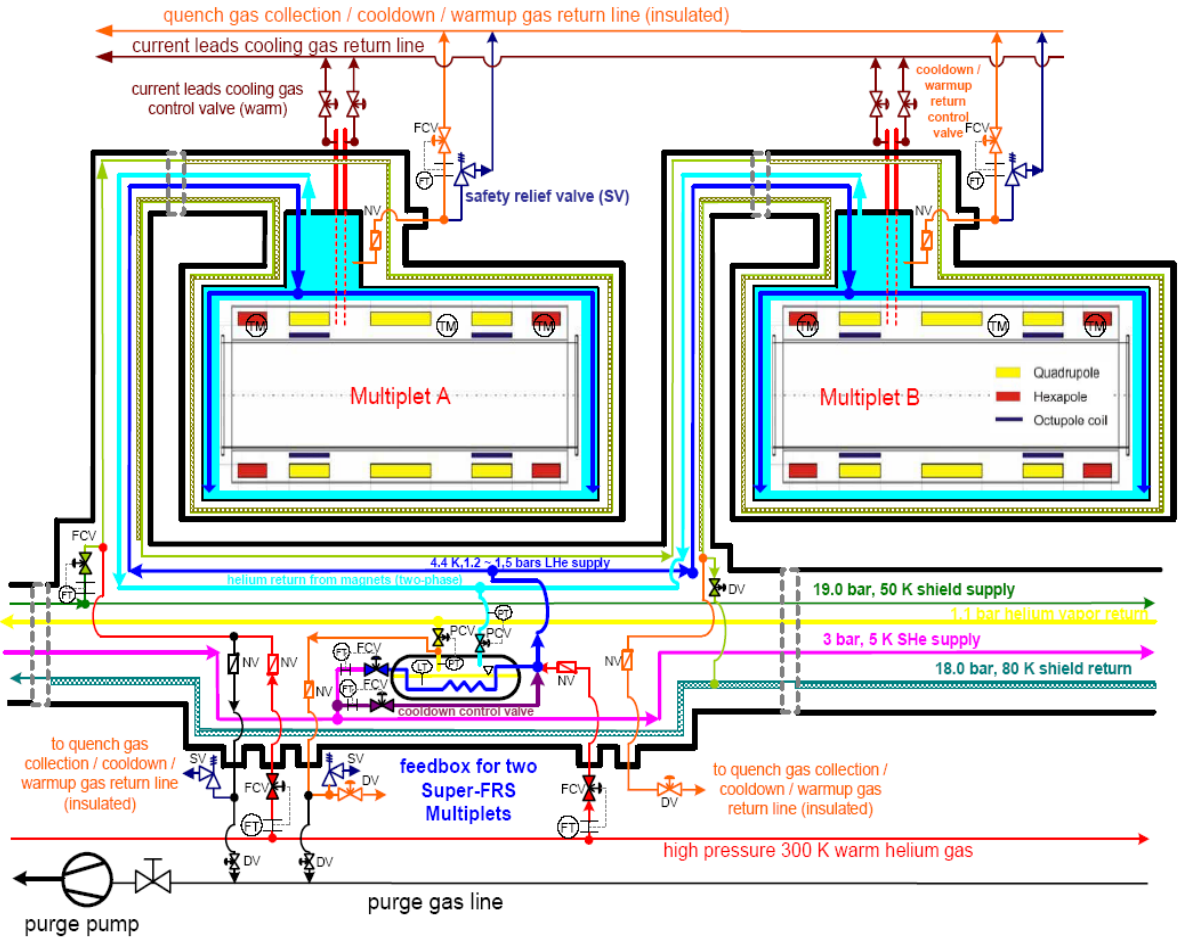

Figure 2.4-131: Flow scheme of two Super-FRS multiplets and one feedbox unit.

Since the weight of the cold mass in a multiplet is by a factor of 10 larger than in the dipole units, the cooldown time of the Super-FRS superconducting magnets is mainly determined by the time which is needed to cool down 23 multiplets and some 10 individually located quadrupoles and hexapoles; in total about 1100 tons cold mass. Experience from NSCL, MSU shows that the single A1900 dipole which has a similar size compared to the Super-FRS dipole could be cooled down to liquid helium temperature within one day. Therefore one needs to specify cooling capacity for the FAIR refrigerator CRYO1 in order to cool down about 1100 tons cold mass (about 100 tons for 28 dipoles included) in the Super-FRS within a reasonable

cooldown time. In fact, the total weight of 1100 tons cold mass in the Super-FRS is about one-fourth of the cold mass of 4600 tons of one LHC sector. The preliminary specification of cooling capacity for the FAIR refrigerator CRYO1 has been based on the specification of the LHC sector refrigerator (18 kW at 4.5 K).

The FAIR refrigerator CRYO1 is specified to provide cooling power of 3.5 kW at 4.5 K. This corresponds to a maximum helium mass flow rate of 235 g/s available at the cycle compressors. From 300 K to about 220 K, the cooling power of the refrigerator CRYO1 is specified to be about 110 kW at its maximum capacity which is mainly contributed by the LN2 pre-cooling in the first heat exchanger of the CRYO1 cold box. Figure 2.4-132 shows the assumed cooling power capacity change of the CRYO1 refrigerator over the refrigeration temperature from 300 K to 10 K which is based on the commissioning results of the LHC 18 kW refrigerator.

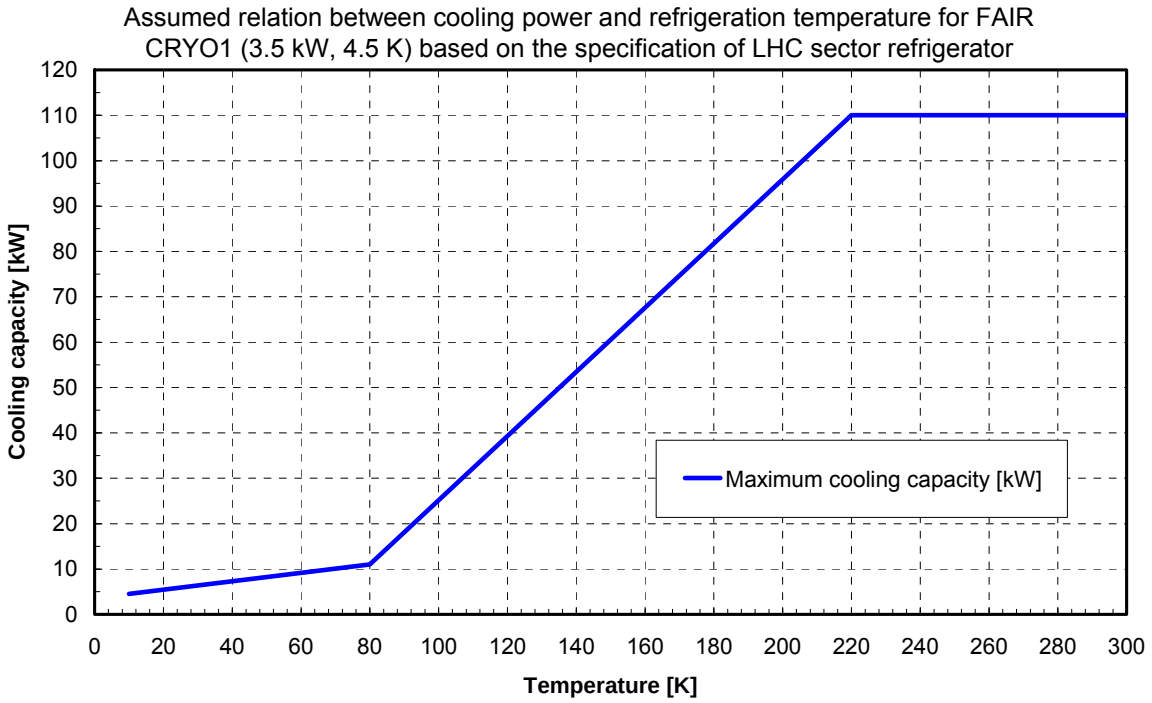

Figure 2.4-132*:* Specified cooling capacity of refrigerator CRYO1.

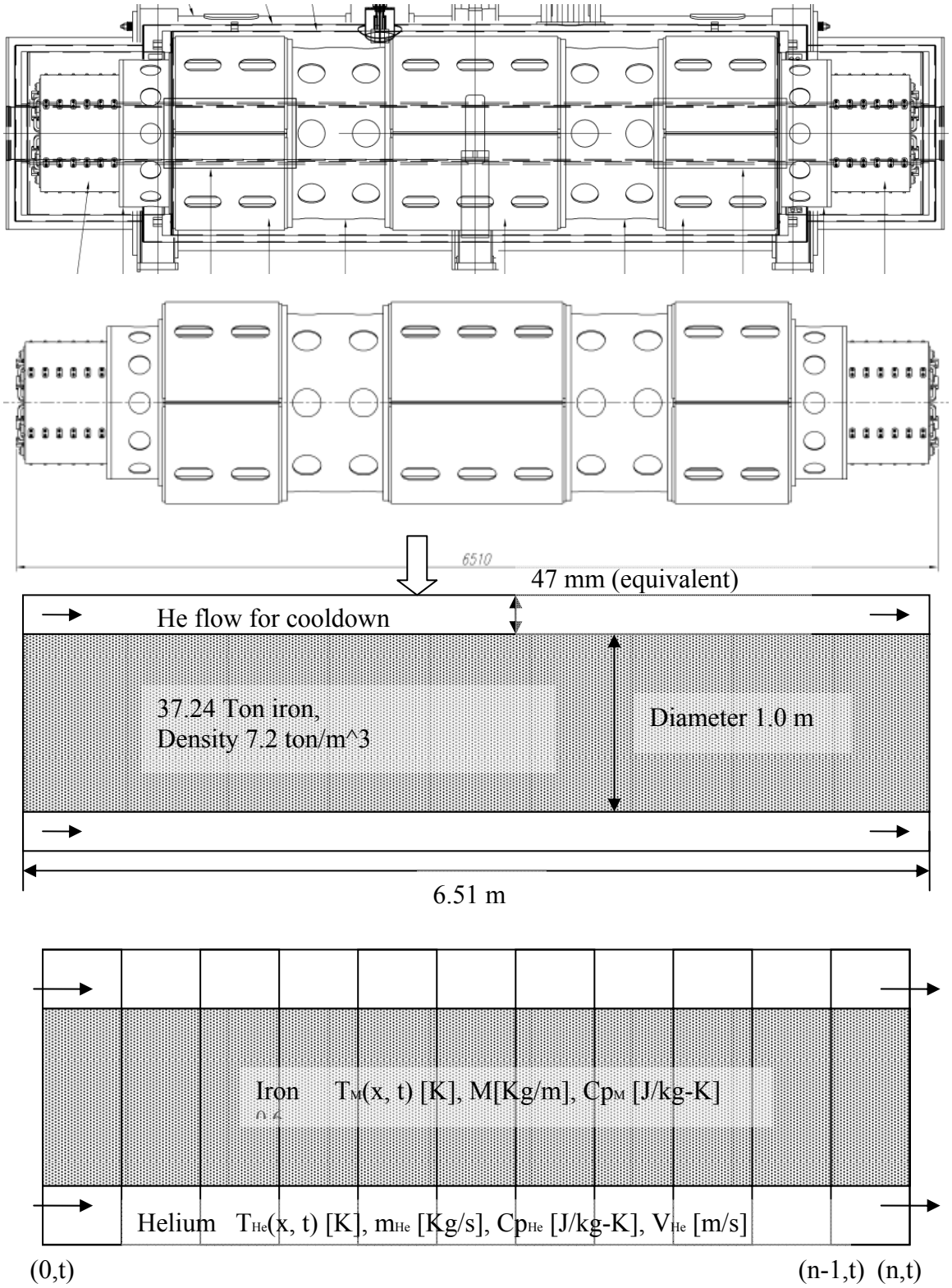

Figure 2.4-133: Schematic of cryogenic distribution for the Super-FRS.

With the cooling capacity specification of the FAIR refrigerator CRYO1, numerical simulation has been performed for one multiplet cooldown. Figure 2.4-133 shows the schematic model of the cold mass, mainly iron, and the surrounding helium flow for cooldown. The discrete spaces of the cold mass and helium flow for discrete derivative equations are shown as well. To simulate the practical cooldown process, two limitations have been set up. The first one is that the temperature difference along the cold mass should not be larger than 50 K at any cooldown

time. The second one is that the inlet temperature of helium gas is regulated by using one or two linear ramps at the starting phase until the maximum cooling capacity of the FAIR refrigerator CRYO1 is reached. The simulation results of the temperature profile in the cold mass over its length at different cooldown time can be seen in Figure 2.4-134. It is anticipated that two multiplets in one group as shown in Figure 2.4-131 could be cooled down to liquid helium temperature in parallel within about 5 days under the specified full cooling capacity of the FAIR refrigerator CRYO1.

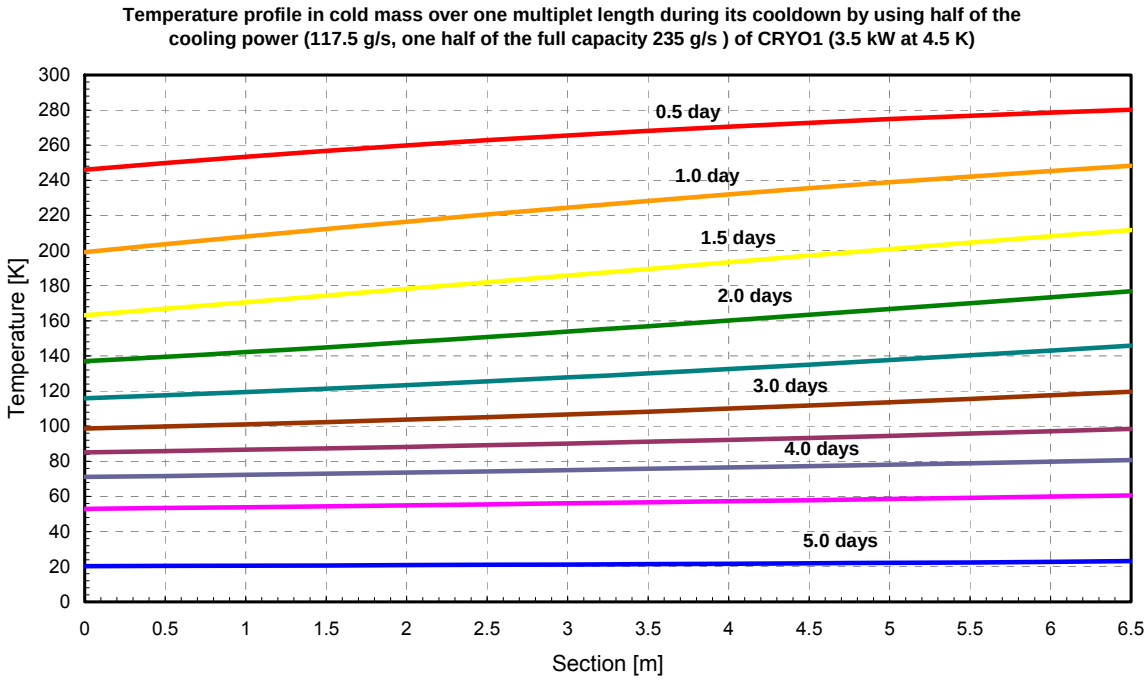

Figure 2.4-134*:* Temperature profile in cold mass of one multiplet for different cooldown times.

In order to know if the overall cooldown time of the whole Super-FRS SC magnets is influenced by the different ways of the multiplets' grouping, three grouping ways, i.e., a) 2 multiplets cooldown in parallel in one group (as shown in the Figure 2.4-131), b) 3 multiplets cooldown in parallel in one group, and c) 3 multiplets cooldown in series in one group, have been checked under different cooling powers of refrigerator CRYO1. Table 2.4-34 contains the results in terms of anticipated minimal cooldown time of the Super-FRS. For comparison, the predicted cooldown time of the standard cell and the one sector of LHC have also been listed in the table. One can see that the cooldown for 3 multiplets in parallel (14.5 days) takes about 10% more time than the cooldown in series (13 days) under the same cooling power conditions. The cooldown time for the individual components is highly dependent on the cooling power provided by the refrigerator, and the allowed temperature gradient over cold mass length, rather than the grouping and individuality. The overall cooldown time (about 60 to 70 days) of the whole Super-FRS is more or less determined by the specified cooling capacity of the FAIR refrigerator CRYO1.

Table 2.4-34: Rough estimate of the cooldown time for all Super-FRS magnets

Allocated Cooling Power [kW] for individual magnet group	Mass flow rate of gas helium during cooldown [g/s]	Cooldown speed at start [K/hour] (cooldown speed at lower temperature is determined by the cooling capacity)	Number of multiplets in one group	Cooldown time for one group (from 300 K to 10 K) [days]	Anticipated minimal cooldown time for Super-FRS SC magnets (from 300 K to 10 K) [days]
110 (full capacity)	235	3.5	2 in parallel	5	5 x 14 (groups) = 70
110 (full capacity)	235	3.5	3 in series	7	7 x 10 = 70
55 (half of the full capacity)	117.5	3.5	3 in series	13	13 x 5 = 65
55 (half of the full capacity)	117.5	3.5	3 in parallel	14.5	14.5 x 5 = 72.5
36.7(one third of the full capacity)	78	3.5	3 in series	20	20 x 3 = 60
21 (for each of the total 23 LHC standard cells)	28.6	DT < 75 K for each magnet	170 tons CM, 107m	11 (one LHC standard cell)	13 (whole LHC sector)

2.4.12.3 Cryogenics Distribution for SC Magnets in the Super-FRS

The schematic layout of the cryogenic distribution for all the superconducting dipoles, quadrupoles and multiplets in the Super-FRS and in front of the target region is shown in Figure 2.4-135. The cryogenic cooling power for the main part of the Super-FRS is supplied by the FAIR refrigerator CRYO1 (not shown) over the cryogenic transfer line through the connection tunnel. The cryogenic supply for the three multiplets in front of the Super-FRS target will be provided by the FAIR refrigerator CRYO2 (not shown) via a distribution box (planned to be located in building 4 and not shown) and the corresponding cryogenic transfer line in the 100 Tm HEBT tunnel. In overview, the cryogenic transfer line (thin light blue) and the feedbox units (thick orange) stretch over almost the whole lattice length along the magnets of Super-FRS including the three branches and the Magnetic-Spectrometer / Energy-Buncher in the Low-Energy experimental region. In the High-Energy experimental cave, the cryogenic supply is available for the R^3B equipment as required. In addition a certain length of the cryogenic transfer line is also foreseen for a later upgrade of the R^3B experiment.

Figure 2.4-135*:* Schematic of cryogenic distribution for the Super-FRS.

Figure 2.4-136 shows more details of the cryogenic distribution in the Pre- and Main-Separator. Following the three radiation resistive normal-conducting dipoles in the Pre-Separator there are 6 superconducting quadrupoles and 2 hexapole magnets which are located in a certain distance from each other. Therefore these magnets are housed in 8 cryostats individually. In a similar way to the dipole groups, every four of them before and after the symmetry mirror could be supplied in parallel by one feedbox unit with liquid helium. The feedbox unit is identical with the one used for dipole stage but has four jumpers. As described in the two previous sections, three dipole units in each dipole stage and two multiplets located on both side of the symmetry mirror position are fed in parallel by one feedbox unit individually. The feedbox units are connected by many short sections of cryogenic transfer line. The helium transfer is ended at the both sides of the target region by the functionality of two end-boxes. Such end-boxes should be integrated in the design of the last feedbox unit just before the helium transfer ends in order to save installation space.

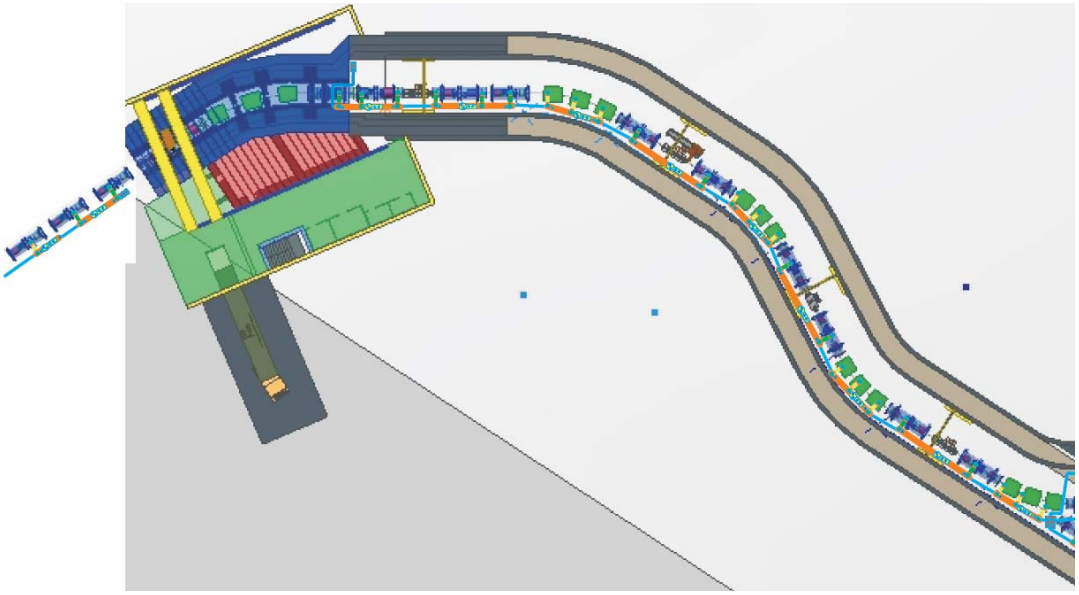

Figure 2.4-136*:* Zoom of the schematic of cryogenic distribution (line close to the shielding wall) in the Pre- and Main-Separator.

The zoom of the branching out of the Main-Separator to the individual experimental areas is shown in Figure 2.4-137, (a) panel. Like the beam optics, the cryogenic transfer is required to divide here into three branches. Therefore two helium distribution boxes are necessary to fulfill the requirement, one box (S1) may be located at the starting area of the Ring Branch and another box (S2) may be located in between the last multiplet and the R^3B detector in the High-Energy experimental cave. The helium distribution boxes S1 and S2 are required to carry out not only the function of making the helium flow separation but also the full control functionality to cope with the Super-FRS construction planning and different commissioning requests. In fact, the installation of the Ring Branch or the Low-Energy Branch may be planned to start after the complete finish of the High-Energy Branch including the R^3B experiment construction, and it may be required to start the cryogenic commissioning much earlier than the full installation of the Super-FRS is finished and to proceed by one branch after another according to the installation planning.

Figure 2.4-137 (panels (b) and (c)) show the flow schemes of these two distribution boxes S1 and S2, respectively. The cryogenic main supply from the FAIR refrigerator CRYO1 is planned to be connected via the distribution box S1 to the Super-FRS cryogenic installation. The design of the distribution box S1 allows the cryogenic commissioning and maintenance to be done for the Main-Separator, the Ring Branch and the High- and Low-Energy Branches in a fully independent way. The four on/off valves in the flow scheme of the distribution box S2 work as the interface between the Super-FRS installation and the R^3B experiment facilities in terms of cryogenic connection. The R^3B detector will be equipped with its own cryogenic installation with full functionality. In addition the distribution box S2 is designed to further isolate the cryogenic supply of the low energy branch from that of the High-Energy-Branch. By shutting off of all the valves to and from the low energy branch and the R^3B experiment in the distribution box S2, the cryogenic commissioning and maintenance could be done for the High-Energy-Branch only with the help of the two other temperature controlled valves (TCF). Because the distance between the last two multiplets in the High-Energy Branch is quite large (up to 20 m), two feedboxes are needed, i.e. one for each multiplet to control the cryogenic supply.

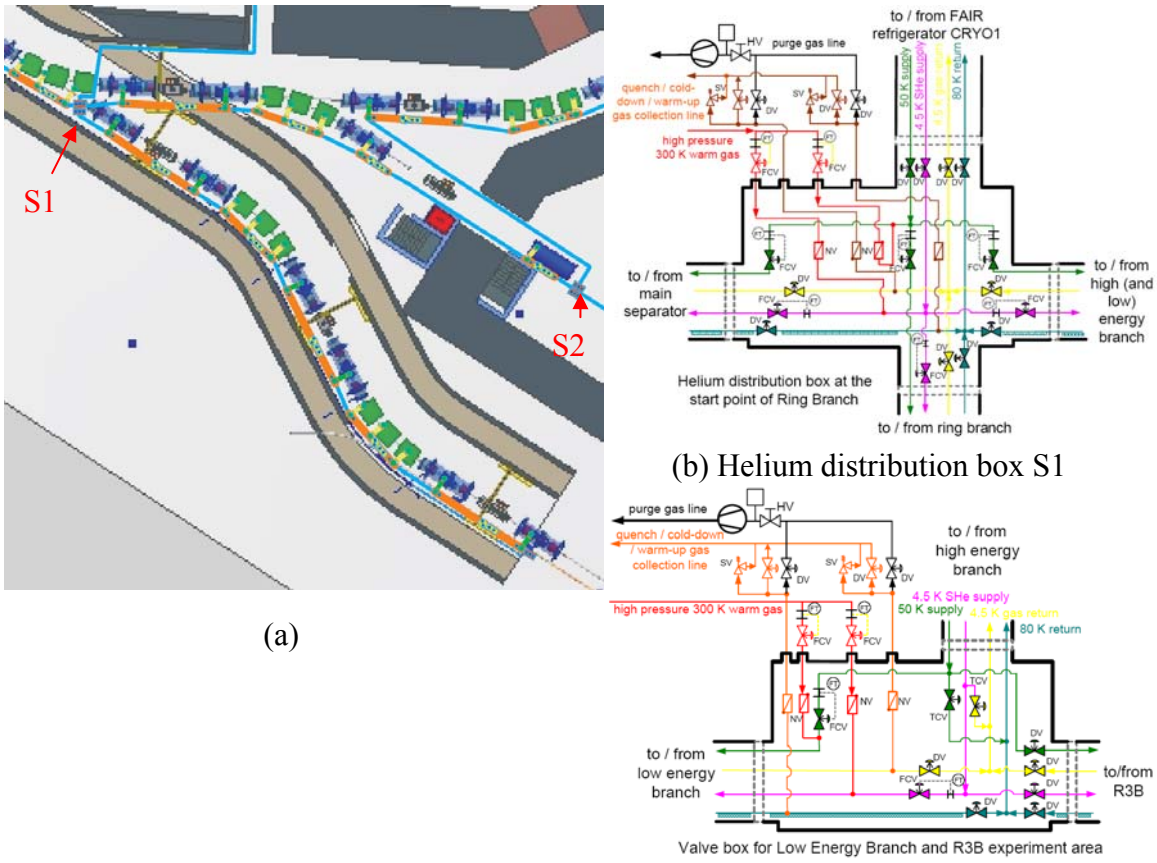

(a)

(b) Helium distribution box S1

(c) Helium distribution box S2

Figure 2.4-137: (a) Zoom of the schematic of cryogenic distribution in the region of three branches; (b) helium distribution box S1; (c) helium distribution box S2.

The zoom of the cryogenic distribution for the low energy experimental region is shown in Figure 2.4-138. In contrast to the normal dipole and multiplet grouping, one multiplet, one dipole and one quadrupole which are housed in three individual cryostats just in front of the energy buncher may need to be grouped together and supplied by one feedbox unit with liquid helium. Inconsistencies may happen due to the different hydrodynamic characteristics of the three components in one group. An alternative solution, for example helium supply in series instead of in parallel, must be considered. One point which should also be addressed is that a flexible cryogenic connection line may be needed for the jumpers between the feedbox and the magnets if these three components in one group are mounted on a rotatable platform according to the experimental requirement. A special case also occurs for the 5 quadrupoles and hexapoles in front of the DESPEC/stopping cell setups in the last part of Low-Energy experimental area.

Figure 2.4-138*:* Zoom of the schematic of cryogenic distribution for the low energy experimental area.

In summary, the main cryogenic facilities for the overall Super-FRS installation are listed in Table 2.4-35.

Table 2.4-35*:* Main cryogenic facilities for the Super-FRS

Main Components	Number / Length [m]
Feedbox without endbox integrated	22 (9 for dipoles+13 for multiplets)
Feedbox with endbox integrated	4 (for multiplets)
Helium distribution box	2 (S1 and S2)
Cryogenic transfer line in sections [m] (length of feedbox units and cryogenic transfer line from CRYO1 excluded)	~ 135 (~ 30 sections)
Warm helium/quench gas return piping [m]	~ 500
Instrumentation setups and warm gas control panes for feedboxes and helium distribution boxes	28 = 22 + 4 + 2

2.4.13 Accelerator Controls

This section gives a brief description of the FAIR accelerator control system (ACS). Taking into account the international distributed project structure and extraordinary technical complexity of the FAIR accelerators, a policy of strict standardization is essential. The same common accelerator control architecture, infrastructure, hardware and software base will be used for all FAIR machines. The main characteristics of the FAIR control system are described here. A more detailed description is in preparation.

The common FAIR accelerator control system will be defined, designed, implemented and commissioned as an in-kind contribution of Germany, under the responsibility of the Controls group at GSI. Architecture and interface definitions will be worked out in co-operation with partners and are obligatory and well enforced within the project such that all software and hardware developments must comply with the interface definitions specified. The ACS development will be supported and aided by partner specialists to implement device drivers, specific graphical user interface (GUI) applications and dedicated solutions within the defined general frameworks. Special measures have to be taken to impose project standards in order to achieve a coherent controls solution.

The FAIR facility will present unique challenges for the ACS which are well beyond the capacity of the existing system. From the very beginning, the design of the ACS has to consider all aspects of the expected functionality needed to operate the FAIR facility. The existing GSI control system will be modernized, with obsolete technology replaced, and will be integrated into the new FAIR control system. The ACS substantially builds on proven principles and solutions of the existing system and is based on a strictly modular design with well defined interfaces. In the design of the system, industrial and widely available commercial hardware and open software components will be used as much as possible. In addition, proven solutions and complete building blocks from other control systems (e.g. collaboration with CERN) will be used in order to reduce development effort. The ACS will be validated and tested already at the existing GSI machines in order to avoid parallel commissioning of a new control system and new FAIR machines.

2.4.13.1 General System architecture

The architecture of the common FAIR accelerator control system is illustrated in Figure 2.4-139. This architecture foresees three tiers:

- The **Presentation Tier** consists of applications for operators and end-users. Typically, these are GUI applications, but can also be web applications or command-line scripting tools.
- The **Business Tier** provides services to the control system. Services are provided both to presentation tier (e.g. name service, archive data) and to the resource tier. The services are responsible for managing almost orthogonal aspects of a control system across the entire facility. All applications reside upon this common layer to befit from the common software infrastructure.
- The **Resource Tier** is closest to the devices that the control system manages. Components of the resource tier map device-specific protocols (e.g. reading/writing of process variables, alarm detection, etc.) to the device-independent protocols standardized across the facility (abstraction). Also, some resource tier components might perform low-level closed-loop control of devices.

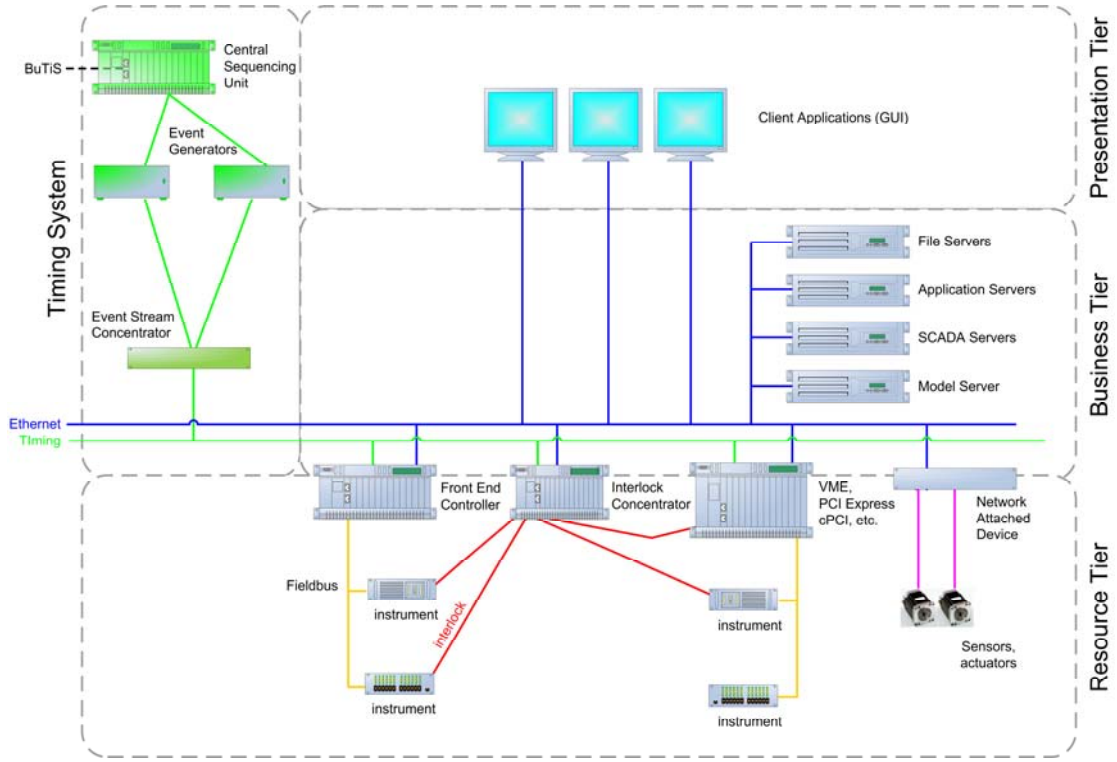

Figure 2.4-139*:* Architecture of the accelerator control system.

The FAIR control system will be implemented as an object-oriented decentralized distributed system. It will be based on a strictly modular design with well defined interfaces. This allows breaking down the project in interconnected work packages that can be implemented independently.

2.4.13.2 Hardware for Equipment Interfacing

The ACS will support several ways of connecting equipment of different types. However, the number of interfaces to the ACS must be kept limited as a large variety of different interfaces cannot be supported and maintained with limited personal resources.
At the resource tier, the various actuators, sensors and data acquisition devices are interfaced to the ACS through the following types of front-end controllers:

- VME, PCI and emerging PCI-express single board computers are dealing with high-performance real-time processing and data acquisitions. Such systems can employ a large variety of standardized and custom I/O modules (ADC, DAC, binary I/O, Counters, etc.). Typically, the accelerator timing systems, beam diagnostic systems, and interlocks are implemented in this technology.

- Most accelerator devices (e.g. all power supplies, rf-systems, kickers, etc.) are interfaced by a dedicated and cost-effective front-end controller (FEC) instead of being connected via a field-bus. This FEC is defined as the “FAIR standard controller”. It is a network node, connected to the timing network (wherever necessary), and provides local CPU-power for real-time control, fast data acquisition as well as any specific functionality needed (e.g. state-dependent tolerance band control). The FEC is a processor board with one operating system (e.g. Linux). Time critical functions are implemented in FPGA technology. A dedicated parallel bus is defined as an interface to electronics boards of devices. The FEC provides and features a device-implemented function generator (FG) for equipment that needs to be controlled by time-dependent

functions (ramps). The FG provides linear and quadratic interpolation at 1 MHz data rate between base points with 24 bit output resolution.

- Programmable Logic Controllers (PLCs) are increasingly used for controlling industrial equipment. This type of controller can be chosen when the process is not synchronized to accelerator timing and when sampling periods are longer than ~100 ms. Being highly reliable, cost effective and easy to program via standard high-level languages, PLCs are foreseen to manage and control vacuum components, machine cryogenics, rf monitoring, personal safety system, interlocks, etc.

2.4.13.3 Timing System

The FAIR facility involves a long chain of accelerators which need to be tightly synchronized. An important consideration in the design of the FAIR facility is a high degree of truly parallel operation of the different machines to facilitate the different research programs.

The primary task of the timing system is to trigger and synchronize equipment actions, timed according to the accelerator cycles, and to synchronize devices which have to operate simultaneously. The timing system must handle 20 ms cycles (present UNILAC) as well as machine cycles and manipulation phases in the order of several seconds for the synchrotrons and up to several hours for the storage rings. Careful analysis of machine requirements have resulted in a two staged timing solution: A general machine timing (GMT) system will be implemented as an event based system. It will provide concurrency of events by transmission time compensation, event resolution of at least 1 µs and event separation of follow-up events of better than 10 µs as well as absolute timestamps. For high-precision synchronization beyond the parameters of the GMT (e.g. distributed rf- and kicker-control, bunch-to-bucket transfers, time-of-flight measurements) a bunch timing system (BuTiS) will distribute high precision clock trains (100 kHz, 200 MHz) on carefully selected fibers, properly delayed and stabilized to compensate propagation delays to every BuTiS end-point and achieve a timing jitter of no more than 200 ps.

The GMT will broadcast centrally generated timing telegrams in a star topology. Distribution is based on Gigabit Ethernet transmission technology using fiber and Copper transmission lines. Transmission rate will be 1 MHz. A dedicated bi-directional timing network is used with active switches and fan-out modules to distribute the timing telegrams to an array of *event receivers* (EVR). Upstream signal propagation allows measuring the fiber and transmission delays with sub-microsecond precision. The emerging standard Precision Time Protocol (PTP) as defined in IEEE 1588 is foreseen to be used to synchronize distributed clocks in the timing network and compensate for transmission delays.

A key requirement of the FAIR control system is the need of an absolute timing reference to timestamp the accelerator data. UTC will be adopted as the standard of date and time for all FAIR accelerators as it is the basis for the worldwide system of civil time. The source of date and time for all FAIR accelerators will be a Global Positioning System (GPS) time receiver to which the GMT event transmission and the BuTiS clock trains will be synchronized and phase locked.

The outline of the GMT system is shown in Figure 2.4-140. For each of the FAIR machines a dedicated timing *event generator* (EVG) generates all timing signals utilizing internal counters, event sequencers and hardware inputs. The EGV broadcasts information about the beam to be handled next and is pre-loaded with an event table for cycles or beam manipulation phases. Alternative event tables are supported to handle abort of beams even during run-time of a cycle.

In addition to timing events other meta-information (e.g. accelerator cycle identifier, context and safe-beam flags) can be transmitted or broadcasted.

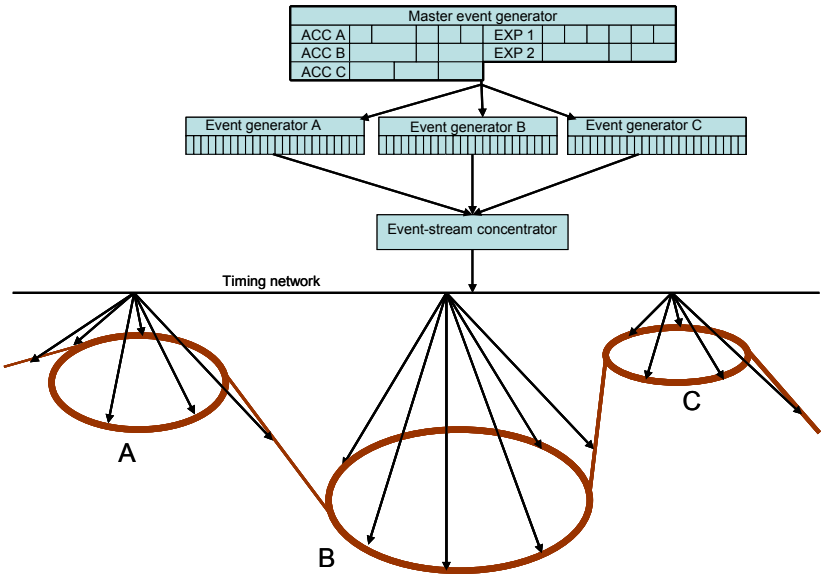

Figure 2.4-140*:* Structure and topology of the general machine timing (GMT).

A *master cycle sequencer* (MCS) will coordinate beams and cycles throughout the FAIR accelerators. It will orchestrate and synchronize every single machine EVG, establish a pattern of beams featuring a high level of truly parallel operation, take care of general restrictions, and will be able to handle alternative beam delivery scenarios in case of emergency or non-availability machines in the accelerator chain. The timing telegrams of all EVG and the MCS will be concentrated such that all information is available at any timing receiver in the facility.

Event receivers (EVR) decode the event stream and provide hardware outputs or software interrupts based on event information. The EVR has a synchronized local clock such that data can be time-stamped to the microsecond level. EVR shall be available in all relevant form factors such as VME, PMC, cPCI as well as an integrated module for the FAIR standard device controller. Propagation and transmission delays will be compensated in the EVR in order to achieve synchronous event reception all over the facility.

The upstream channel of the GMT system can be used to synchronously and deterministically exchange short telegrams between dedicated devices as is needed e.g. for bunch-to-bucket transfer. It is being investigated whether the upstream communication will be also used to gather interlock and safety-critical state information from the device level.

2.4.13.4 Networking

The FAIR controls network is a 1-Gb/s switched Ethernet network, with a backbone at 10-Gb/s. The number of nodes is about 2000. The chosen network design will provide enough flexibility for the number of nodes to be increased without difficulty if required.

Each node will be connected to a switch by a point-to-point link. The switches are connected to the site high-speed backbone though 10-Gb/s uplinks. To contain and control network traffic and impose cyber security, the technical accelerator network (ACCNET) will be separated from the campus general purpose network by using virtual LAN technology (VLAN network segregation). The technical network is connected with other network domains via dedicated net-

work routers. The traffic crossing two domains is restricted to a minimum by use of routing tables, and only mandatory traffic can pass such boundaries.

2.4.13.5 Computer Systems, FAIR Control Center

The upper layers of the FAIR control system (presentation tier) will be deployed on operation consoles and fixed displays, files and application servers to meet the requirements of the FAIR applications software.

The servers run a Linux operating system and are used to run the FAIR business-tier software, to host operational programs and also offer specific services. Emphasis will be put on the hardware reliability and availability issues by selecting multi-CPU architectures with redundant and hot-swappable power supplies, discs and fans. RAID techniques will be used to ensure data integrity and disaster recovery.

All FAIR machines including the existing injector chain machines are operated and controlled from a central FAIR Control Center (FCC). Some machines or facility parts including the Super-FRS have additional local control stations for commissioning, experimental runs or autonomous control. Whether there shall the possibility to remotely operate parts of the facility from outside the GSI/FAIR-site has not been discussed and decided yet.

The operator consoles in the FCC and local control stations will run the GUI applications and will be based on standard PC systems. They will also run a Linux operating system and will support multiple screens to display the data. The total number of operating consoles, screens and fixed displays to be deployed has not been evaluated at this time.

2.4.13.6 Front-End Software Architecture

The software running in the front-end equipment controllers (FECs) will be developed using an adequate front-end framework. This framework is a complete environment for specialists to design, develop, test and deploy real-time control software for the FECs and will also be the new standard for the GSI injector chain.

Taking up a proven principle of the present GSI control system, the front-end systems of the resource tier are split in two logical layers: *equipment control*, which implements the device connection and real-time equipment handling, and *device presentation* which models the equipment and implements the network access. Both functional layers can be physically implemented on the same hardware platform.

Devices are implemented as objects in the object-oriented software terminology. They provide access by services and applications via the controls network and will be modeled by similar patterns for all devices. This allows access through identical mechanisms for all devices. Devices are set, read or controlled by properties via the controls middleware.

Devices will support several beams at a given time (time multiplexing). The setting and configuration data for all beams reside in the equipment controllers. Because of this, no download from higher layers of the control system is needed between accelerator cycles, except for changes. Thus several sets of reference and actual data can be handled simultaneously, one for each of the beams configured in the accelerator facility. Switching the components settings to fit to the actual beam parameters is done in the equipment control sub layer, according to information which is distributed by the timing system.

2.4.13.7 Controls Middleware

The controls middleware is an ensemble of protocols, Application Programming Interfaces (API) and software frameworks, which allows seamless communication between the software entities of the ACS. Two conceptual models are supported: the *device access model* and the *messaging model*. The device access model is mainly used in the communication between the resource and business/presentation tier while the messaging model is mainly used within the business tier or between the business tier and applications running in the presentation tier.

The devices access model is implemented by using the CORBA protocol which provides a high level of abstraction. Complementary, the messaging model is based on the Java Message Service (JMS) as the messaging solution for Java based control applications.

2.4.13.8 Services and Application Software Architecture

Applications controlling the GSI/FAIR accelerator chain must handle a great variety of tasks such as visualization of data and significant computation, together with database and equipment access. These applications rely on several services such as security, transactions, and remote access and resource management. These requirements dictate a modular and distributed architecture with a clear separation between the user interfaces (GUI), the control core or service, the model, and the devices that are controlled.

In the general system architecture, the consoles of the presentation tier are responsible for GUI applications and translate the operator's actions into commands invocation in the business tier. The business tier, through its centralized shared processing power is in charge for providing services, coordination of the client applications, and accessing databases. It also ensures coherence of operator actions and enforces separation between presentation and application logic.

The business and presentation tier services and applications are based on the Spring framework. Spring, being an industrial standard defined by a set of specifications and APIs, is based on Java programming language. Components are the key technology to write modular object-oriented distributed applications.

The GUI applications will be based on a set of common control system services and generic components in order to avoid duplication of effort and solutions. All operational applications will use the provided interfaces which represent the "software view" of the ACS. The operational software development process relies on common development tools, guidelines and procedures for the design, implementation, testing, integration, deployment and change management.

By defining and implementing such a software development framework for services and GUI applications, the developers can concentrate on writing code for the accelerator controls components such as parameter management, setting generation, cycle handling, trim management; they do not have to write system level services.

2.4.13.9 Accelerator Settings and Management

The GSI/FAIR accelerators and beam lines will be set and manipulated as much as possible on the base of high level physical values. The generation and management of complex settings is a functionality provided by dedicated services in the business tier of the ACS. They are based on theoretical machine models and ion-optical simulation programs. Additionally, operators and machine specialists can apply small corrections (trims) to settings that need to be handled.

In order to obtain and preserve a comprehensive and coherent architecture for setting generation and management a modular framework will be provided. Every machine (linac, synchrotrons, storage rings, beam lines, etc.) will be represented by a *machine manager* (MM) service that provides an API to individual machine models. These might be implemented highly machine specific based on a set of make-rules which derive device specific settings from high level machine parameters. For the ring-machines (synchrotrons and storage rings) a generic model that can be highly customized is foreseen by the machine specialists.

In order to handle dependencies from other machines, organize and optimize the timing for cycle management of the FAIR complex a coordinating *beam manager* (BM) service will be implemented. The BM interfaces with all individual MM, accounts for maximum parallel operation, external constraints like dynamic cryogenic and energy load, and can be operated by the central cycle management application. This application allows editing cycles in the accelerator chain and will assist the user in finding an optimal sequence.

2.4.13.10 Industrial Controls

Some of the technical subsystems of the FAIR facility (e.g. machine cryogenics, vacuum system, facility monitoring) are not time-critical and highly industrial related. The control of these systems is foreseen to be realized based on a common industrial automation system (SCADA, supervisory control and data acquisition system) and integrated into the ACS. There are several advantages to this approach: A SCADA system is highly available and reliable and will run autonomously, decoupled from the ACS which is an important aspect for cryogenics and vacuum. Experience shows that industrial partners can be contracted to follow technical and functional specification to deliver turn-key solutions. Despite the autonomous controls, the industrial control system will however be fully integrated into the ACS by a gateway functionality.

The UNICOS framework (unified industrial control system) developed at CERN which is based on the commercial SCADA product PVSS2 is a strong candidate to be evaluated for use at FAIR. This framework provides components, methodology and tools to design, build and program industrial based control systems.

2.4.14 Survey and Alignment

2.4.14.1 General Considerations

This section describes common aspects of Survey and Alignment (S&A) that are significant for the accurate positioning of FAIR components in general. Surveying activities in support of any constructional work are not covered here and are not in scope of the S&A team.

2.4.14.1.1 Role of Survey and Alignment in FAIR: major tasks

The fundamental task of survey and alignment in the context of the construction of accelerators is the precise physical and geometrical positioning of machine elements, especially dipoles, quadrupoles, beam diagnostic devices, collimators etc. according to an exactly specified nominal position – the lattice – and the required alignment tolerances. An additional part of the scope of work is the metrological support to the physics experiments such as providing geodetic infrastructure in the experimental areas, aid on the installation of particle detectors and precise spatial measurement of such detectors.
It has to be emphasized that a precise alignment is needed not only for the first installation; but also the regular control of the actual position of the accelerator and the preservation of the nominal values over a long period is under the responsibility of the S&A team.

In order to be able to fulfil the given tasks, fundamental boundary conditions concerning building design, machine geometry or positioning tolerances – typically at some tenths of millimetre – have to be available at an early stage of planning, since the choice of measuring technology is substantially dependent on these parameters. Likewise, exerting an influence of S&A experts on design criteria in the areas of shielding, tunnel size, stay clear areas, cable routing, component supports and adjustment devices among others, is essential, to plan effective survey and alignment procedures.

2.4.14.1.2 Basic survey and alignment steps (installation phase)

Accelerator components need to be aligned to very tight tolerances. In order to perform these tasks, fundamental work packages are essential:

- Definition of appropriate coordinate systems
- Design, lay-out and installation of a primary network on the surface for the orientation of the connected machines (existing and planned) and increasing the accuracy of the tunnel network
- Network densification by transferring the primary net into the single machine buildings. These networks are the basis for the mark out of the ideal positions of the supports and accelerator components (accuracy ± 1-2 mm) and the pre-alignment.
- Precise three-dimensional reference network measurements including component positions for each individual machine (accuracy ± 0.1 mm)
- Relative alignment of neighbouring magnets, beam diagnostic devices and other components that have to be positioned to tight tolerances
- Precise three-dimensional measurement for quality control in order to detect failings in initial alignment or meanwhile occurred deformation

Independent of the methods that will be used to align any component, it has to be clear, that every component, which requires alignment, needs to be fiducialized before installing it into the ultimate FAIR facility (like e.g. the Super-FRS). The basic principles together with important preparatory work are described in section 2.4.14.2.

2.4.14.1.3 Concept development

Accelerator alignment is no ready-made service; concepts have to be individually developed or adapted to a certain machine, although some state-of-the-art procedures – known in accelerator community – can be used. The determination of requirements, development of special hard- and software, measuring methods and procedures as well as system tests, personnel planning (form a team, training) and last but not least the development of an appropriate data management system have to be taken into account while talking about survey and alignment. These developments are no specific R&D tasks, but need certain preliminary lead time.

2.4.14.1.4 Requirements on building structures: alignment point of view

The following section should give some indications of an appropriate building design, which has to allow the survey and alignment ability, and that must provide a good position stability of the accelerator.

It is recommended that each accelerator ring or functional separated section get its own stable foundation in order to obtain deformations - within one ring due to unavoidable movements of the underground - as small as possible. Machine lay-out should provide space for steering magnets at sensitive building crossings.

Generally, it was communicated to the responsible person of the civil engineer team that - within one ring as well as between the beam lines and the adjacent rings - lines of sight are to be kept free or to be created. These lines of sight enable to measure a reference network, which represents the basis for the adjustments of the individual components. That is, special openings, which can easily be opened and closed for measurement purposes, have to be taken into account within specified building design respectively within shielding concept. Details can only be specified after final machine lay-outs and building designs - and with this a coherent design of measurement network - are available.

In order to be able to perform high-precision measurements on accelerator components it is inevitable to have balanced climate conditions within the machine buildings during a measurement period; i.e., air turbulences, draft or strong temperature differences that affect optical measurement procedures have to be avoided within the working area; technical mechanisms are to be planned for these demands.

During design of gateway to the machines for installation, survey and alignment or maintenance in general, it has to be paid careful attention on an easy accessibility of the machine areas and a good approach to the individual components – in accordance with requirements of radiation protection.

The space required for the metrological infrastructure – besides storage room suitable places for test measurements and periodical calibration procedures are needed – were already communicated to the construction engineer.

The surface network, which is needed for the absolute orientation of the different machines in space and relative to each other as well as for the strengthening of the tunnel network, calls for the construction of vertical sight shafts and some concrete pillars. The number and position of shafts and pillars needed at FAIR site depend on a suitable net design. Appropriate simulation computations for the estimation of achievable accuracies are reasonable when geometry and position of the accelerators are finalized. As an example a very preliminary investigation yielded to a number of three sight shafts for the link between the surface and the SIS100-tunnel network (see Figure 2.4-141).

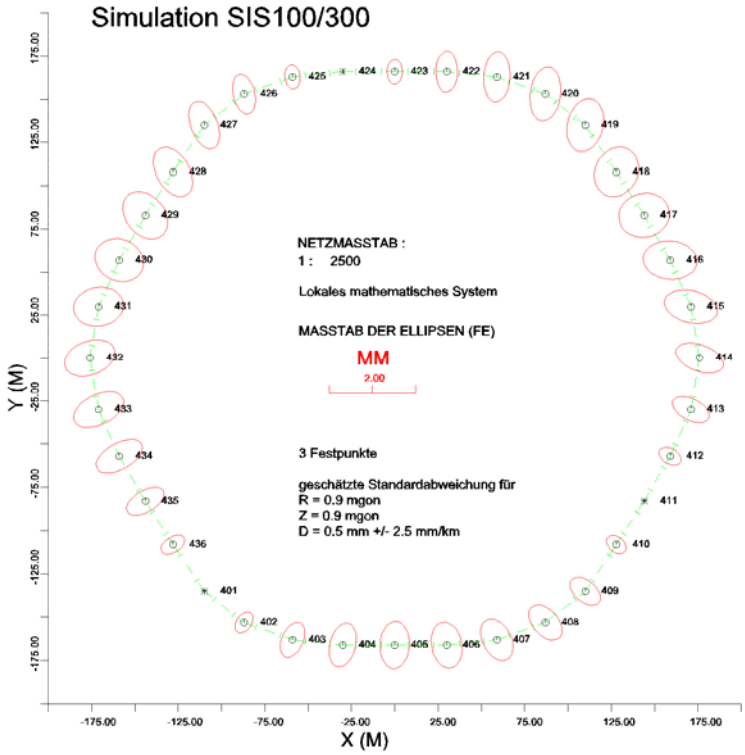

Figure 2.4-141: Preliminary result of tunnel network simulation (as example the SIS100 was chosen).

2.4.14.2 Work packages: description of basic principles

2.4.14.2.1 Fiducialization

Fiducialization is a term for relating the magnetic respectively mechanical axis of a component to reference marks – the fiducials – that can be seen or touched by instruments. These fiducials are used for positioning the accelerator components within the tunnel. Fiducialization is a two-step-process. Firstly the axis has to be determined; secondly the position of this axis has to be related to the external fiducials [86].
The results of any fiducialization should be 3D-coordinates x, y, z of the fiducials with respect to the magnetic axis and the field vector. This allows an explicit description of the six degrees of freedom – that is position and orientation in space – for every component.

During installation and maintenance of the existing GSI-machines extensive experiences in the field of fiducialization of resistive or conventional magnets and other components could be gained [87]. However, up to now there was no need or possibility to engage in superconducting magnets.

With the focus on fiducialization some differences in magnets have to be mentioned: the fiducials at warm magnets are usually located directly on the laminations. Once measured it is assumed that the fiducial marks do not change their position. The mechanical axis can easily be visualized by a mandrel as shown in Figure 2.4-142.

In contrast to the normal conducting magnets the sc-magnets are mostly enclosed in a cryostat. Therefore the yoke is not directly accessible when cooled down i.e. in normal working condition. The fiducials have to be placed on the cryostat, which has in fact no stable relationship to the magnet.

Figure 2.4-142*:* Existing Quadrupole with inserted mandrel.

A very close collaboration of magnetic and geometric measurement groups is essential to fulfil the requirements on giving realistic, precise values for the relation between axis and external reference marks. Additional information is necessary in order to be able to give reliable quantities for the accurate positioning of an invisible object – the magnetic axis. Therefore the dimensional control of the magnets to ensure the production tolerances has to be carried out as well as extensive analysis of possible movements of the magnet versus cryostat under different conditions. For instance quenches or the transport from measuring place into the tunnel can produce changes in position of yoke compared to the cryostat.
Due to the fact that the cryostat will need to provide stable supports for the fiducials, it was already recommended to attach great importance to the stability of the cryostat itself.

Fiducialization of superconducting magnets is a challenge, that needs careful preparatory work – some points are mentioned above –, which goes far beyond a single measurement to relate some points to each other.

2.4.14.2.2 Considerations on total error budget

Undoubtedly the process of fiducialization has to be at least as accurate as the positioning of the component to their nominal coordinates; actually much more accurate than that, due to the different sources of errors, which form the total error of a final magnet position within the tunnel [88].

Possible sources of error:

- ► Manufacturing
- ► Determination of the axis / "magnetic measurements"
- ► Relating axis to fiducials / "geometric measurements"
- ► Deformation of cryostat / deformation of correlated fiducials
- ► Displacement magnet versus cryostat due to transport
- ► Residuals after least square network adjustment
- ► Uncertainty of measurements during alignment procedure
- ► Movement of the floor (long / short term)
- ► etc.

⇒ Total error of final magnet position within the tunnel, which can be expressed as

$$s^2 = s_i^2 + s_j^2 + s_k^2 + s_l^2 + \ldots$$

This quadratic sum of all individual errors has to be taken into account when reflecting on positional tolerances, which are usually several times the r.m.s. again. Note that assumed errors of 0.1 (0.15 / 0.2 / ...) mm for all above mentioned error sources (which does not reflect the truth in either case) yield to a total error of 0.3 (0.4 / 0.6 / ...) mm.
The knowledge of a total error budget can help to derivate or re-evaluate reasonable tolerances.

2.4.14.2.3 Tolerances

A high degree of accuracy is required in the spatial positioning of accelerator components. Up to now for FAIR alignment tolerances are in no case finalized; thus accuracy of reference points, which will be needed in the entire ring tunnel etc. to create a survey network, is not defined yet; neither global nor relative uncertainty.
However, tolerances can be assumed to be in a range of some hundred microns, similar to the existing machine(s). This assumption leads to the choice of the measuring technology, whose accuracy of measurement – following a rough rule of thumb – has to be at least three to five times better than the given tolerance.

Up to now there are no indications of a demand for very high accuracies (10µm or similar) for any (experimental) setup. In this case fundamental changes in the so far traced measuring philosophy would be necessary.

2.4.14.2.4 Instrumentation

Measuring devices

State-of-the-art Laser Tracker, which is a mobile three-dimensional coordinate measurement machine, precision Total Stations and precise digital levels, will be the preferred instruments to fulfil the tasks of surveying and alignment in the majority of cases – both in initial installation phases and in regular periods of realignment.
The Laser Tracker is a dynamic measurement system which consists of a laser interferometer and a device for an absolute distance measurement, motor driven rotating mirrors with angle encoders to follow a corner cube reflector to the desired spot. The tracker gives 3D coordinates of a target in space with single point accuracy of ~27 µm (2sigma) at a distance of 2 m (~50µm @ 10m / ~110µm @30m). Due to its multiple use this kind of instrument will attend the entire project duration: from quality checks on components to test measurements at the magnet test facility, from fiducialization via reference network measurements within the tunnel to the alignment of magnets, detectors and other experiment installations.

Figure 2.4-143*:* Type of a Laser Tracker (left) and an Industrial Total Station (right).

At GSI a Laser Tracker is regularly applied since 1996 for fiducialization and in some cases for network measurement and alignment [89].
The measurements for the primary surface network and the transfer into the tunnel will partly require receiver of the satellite system GPS and an optical plummet. Due to the forest that has to be protected as far as possible, some problems will arise with GPS, thus classical triangulation/trilateration with Total Stations has to be performed, too.
In order to reach positioning accuracies in a range of few millimetres (3D, 1sigma) while using the Global Positioning System, it is inevitable to use several geodetic double frequency receivers simultaneously that carry out static measurements of a duration up to 20h; the data post-processing is necessary using e.g. the Bernese GPS software. A meanwhile well known 'real time kinematic' solution is not suitable to obtain the required high relative accuracies [90].

Figure 2.4-144*:* General design floor nest (left) and floor nest in-ground (right).

Again, the predetermination of measuring technology guides to the design of reference points in the tunnel floors and walls just like on the magnets and other components, which have to be aligned to very tight tolerances (fiducial points). No permanent instrument monuments (like pillars) will be installed within any tunnel. Each reference point will be shaped in a way, that removable targets with a diameter of 1.5 inch can be inserted with highest repeatability (e.g. ball mounted retroreflectors, etc. – see Figure 2.4-144 and Figure 2.4-145 © Metronom Automation GmbH).

Figure 2.4-145*:* Wall nest with 1.5" corner cube reflector (left) and Design drawing wall nests and component fiducials.

Test laboratory

Instrument testing should be an important part of the internal quality assurance program. Establishing an appropriate test laboratory to do performance checks, investigate test procedures, calibrate and maintain the definitely forthcoming manifold systems in the scope of metrology

should happen as early as possible. Conceptual work including formulation of a catalogue of requirements on laboratory design – especially climatic condition and building stability -, along with specification of inspection equipment and much more, is to be started soon.

Software

Suitable metrology software that provides running a number of different instrument - and hence - observation types, simulating point accuracies from expected observational uncertainties and, with this, planning a network layout, exists at GSI (PANDA, WinGeonet/Lego).
The already existing, long time utilised hard- and software modules (TASA) for network measurement, data analysis, online-alignment, data presentation and documentation etc., are based on the mainly use of Total Station [89]. This proved system was meanwhile adapted to newer techniques, thus a new data flow to LEGO adjustment module for combined Laser Tracker and Level measurements using TASA software package was realized.

2.4.14.2.5 Survey networks

Simulation

The design of survey networks, represented by fixed reference points within the different facilities, is a major task, which results in scheduling the most suitable number and position of the points and the quantity and kind of observations. The - still to be defined - required network accuracy in the various areas of the facility has to be achieved. Detailed simulation calculations yields to a prediction of global and relative uncertainties of all reference points including fiducial points on magnets etc.

Up to now no simulation was calculated for the subsystems, for which reliable, definite information concerning final size, detailed lattice, tunnel layout, location of the rings in relation to each other, design of buildings and much more are needed; whereas a first coarse estimation was made about the number of vertical shafts, needed to connect the surface network with the machine network in the SIS100/300 tunnel. From this follows a requirement of three connections, based on an assumption of a needed global accuracy of ±2 mm (1σ) for the SIS100/300 network of reference points.

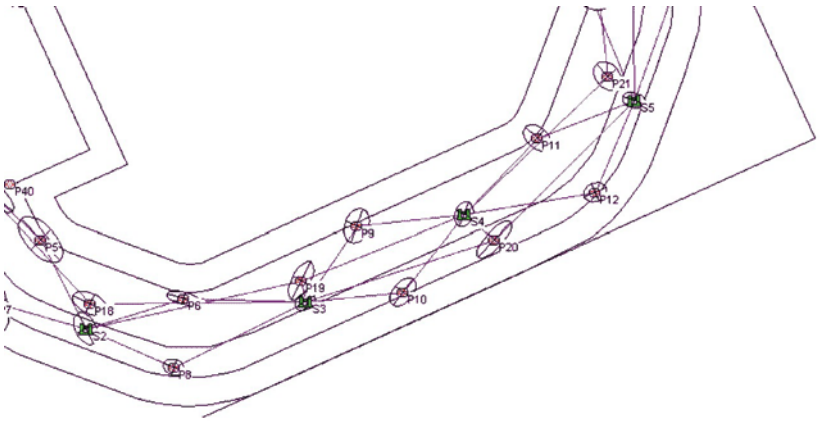

Figure 2.4-146*:* Sketch of a part of an exemplary network (exclusive components).

Free stationing

The actual survey and alignment plan relies on Laser Tracker combined with levelling, and in some cases combined with Total Station. Laser Tracker uses free stationing technique for orientation. Free stationing technique has no need for fixed instrument monuments. The measurement system can be set up very flexible, only visual contact to evenly spread points on the wall and floor is required. However, the number of necessary points – compared to a centred instrument setup – has to be higher; it has to be paid careful attention to the configuration of reference marks. This makes clear, that a robust, consolidated floor and side walls – at least during survey and alignment period - is imperative.

The principles of installing a three-dimensional net and the determination of the net parameters with the help of Laser Trackers are state of the art; they correspond to the proceeding of the international community in accelerator alignment.

2.4.14.2.6 Alignment – positioning of components

The precise, fast and correct alignment of machinery in three dimensions within the facility depends on the network configuration and quality as well as on suitable mechanics respectively the adjustment ability of a component at all.
With the knowledge of the position of the pre-aligned magnets et al with respect to the reference network points, adequate correction values can be calculated due to the comparison of actual coordinates with ideals. An online-alignment (absolute control of component movement) can be carried out by using a Laser Tracker.

Expected temperatures within the tunnel during operation, which will fundamentally differ from the values during installation and adjustment, have to be considered while computing the nominal values for the initial positioning of the components. Unequal behaviour of expansion of different used materials for components and related fiducials, supports, girders etc. must be taken into account. Furthermore, possible different temperature zones within a single machine during operation have to be considered: non-systematic positional changes or offsets between neighbouring components due to this influence must be compensated.

2.4.14.2.7 Physics experiments – metrological support

No conceptual work concerning alignment or other measurements of installations of any planned physics experiment has begun so far.

2.4.14.2.8 Monitoring

For a successful operation of particle accelerators the long-term as well as the short-term stability of the concrete floor supporting the beam components is crucial. Settlements have impact on the position of magnets and experiment setups. Excavation, increased traffic at construction site among other things can cause significant deformation at adjacent buildings. Due to the fact that the already existing machine is intended to remain operational while constructional works for FAIR will happen – respectively the accelerator of FAIR in its first stage is working while the next phase of civil construction takes place – a monitoring system becomes necessary. For this purpose, Hydrostatic Levelling Systems, which allow measurement of deformations in real-time with a very high accuracy (μm), can be used - like performed for example at JASRI / SPring-8 [91].
For the determination of long-term settlements within the existing buildings, surveys in approximately yearly intervals had been performed until year 2002. Critical areas within the different existing and planned buildings, which possibly need stationary monitoring systems in

the future in order to see short-term positional changes during construction work, are not yet identified.

2.4.14.3 Machine characteristics: impact on alignment procedures

The variety of the components of the HEBT, of the various storage rings or synchrotrons as well as of the Super-FRS must be aligned to the ideal beam axis with the help of 3D-measurements. The relevant positions of magnets etc. have to be determined with high accuracy. If it is assumed, to have no tighter requirements on component position accuracy than some hundred microns and no local peculiarities are obstructive, the basic survey and alignment strategy that is described above can be applied to all different machines, at least for the initial installation.

In spite of this statement and although important aspects are still not known, some unique characteristics of single machines are already obvious. In some of these cases it is sufficient to make special effort in constructional engineering, in design of magnets and supports or other mechanical components, in order to be able to maintain or to improve the alignment-ability of components. In other cases machine characteristics lead to a necessary substantial adaptation of survey and alignment methods – not for initial installation but especially for needed realignment activities after some time of operation.

2.4.14.3.1 Remote alignment system

FAIR will have some areas - especially the target and beam catcher area of Super-FRS - that will be hardly to reach or inaccessible for maintenance staff after some time of operation. This will be true even in shutdown periods due to an expected high level of radiation. Concerning future survey and realignment tasks these circumstances prohibit the use of well-established stationary monitoring systems or "classic" measurement instruments like Total Station or Laser Tracker. The basic necessity for using automated, remote systems for position control and realignment within these zones is therefore obvious.

A dedicated R&D project that was called **RALF** (**R**emote **AL**ignment on the **F**ly) dealt with the conceptual work on an approach for a high-precision survey and alignment system in inaccessible, high-radiation areas in order to preserve the survey ability in spite of limited access and in accordance with safety regulations and radiation protection requirements. The new measurement system has to meet following requirements:

- No access of human personnel
- Great demands on accuracy (some 1/10 mm)
- Very fast data acquisition
- Automated, remotely controlled adjustment of accelerator components
- Handling a nonlinear beamline with a length up to several decametre

The method will not be used as a permanent monitoring system but for regularly determination of the actual condition of the machine geometry.

Fundamental ideas of RALF are based on a photogrammetric solution: close-range photogrammetry is the only non-contact geodetic measurement technique that works without human impact on the object and accomplishes flexible measurement and monitoring tasks with highest accuracies.
The approach relies on a number of high-precision digital cameras that are installed on an automated guided vehicle system. Via tracks this device will be driven along the beamline in the activated area, which has to be surveyed. Appropriate fiducial points are mounted on the magnets / cryostats. In addition, photogrammetric tie-points and calibrated scale-bars are dis-

tributed in object space to guarantee a stable photogrammetric network. At least two adjacent components are captured in one shot, before the vehicle starts to move to the next stop for taking the following picture. After finishing data acquisition the camera system is lead out to a radiation-protected storage room to download the image data. A bundle adjustment provides correction values for the alignment of the accelerator components that is completed by remotely controlled adjustment devices. Another camera run is performed to check the quality of remote alignment [92].

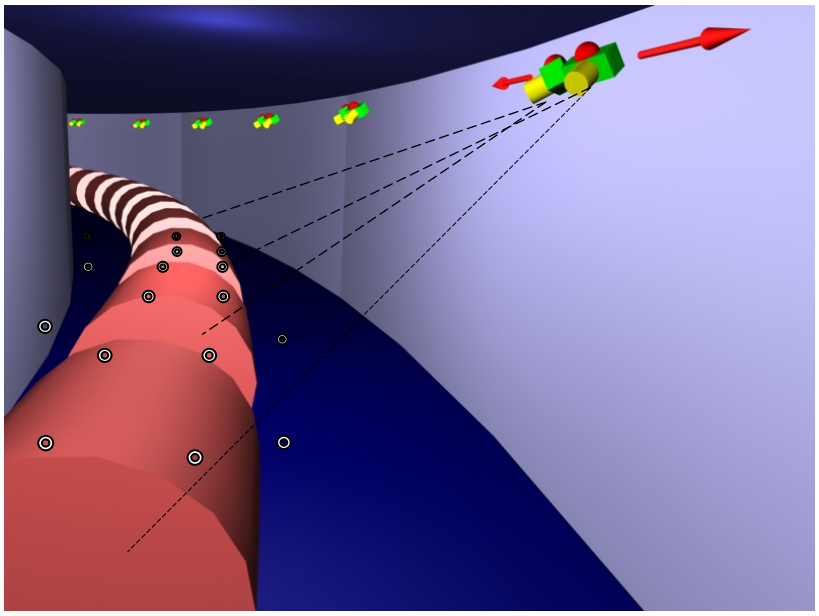

Figure 2.4-147*:* Schematic view of a possible configuration in an accelerator tunnel. The camera vehicle (green) carries two divergent digital cameras. By moving the vehicle along the tunnel (red arrows), any part of the magnets will be captured by two or more images. This results in an image bundle for the whole tunnel to be processed in a photogrammetric bundle adjustment.

Different digital cameras for industrial application have been tested at a photogrammetric test field, in order to analyze their geometric stability and the accuracy of image measurement. In the context of possible camera damages during operating time of RALF by *remaining* radiation after machine-shutdown, some experimental tests were performed at ambient conditions of gamma dose rates of up to 10 mSv/h, which can be expected at PF2 (pre-separator focus point 2 of Super-FRS). Although image analysis tools detected a slight influence, the tests showed no significant loss of image point accuracy.
Considerations to a photogrammetric network design, regarding stretched objects, have been carried out; extensive simulations were computed, which resulted in satisfactory, homogeneous object point accuracies in 3D (approx. 0,1 to 0,2 mm) [93].
Aspects of image analysis, camera vehicle and motion system, data transfer and power supply as well as adjustment devices appropriate to the environmental conditions were investigated. Fiducials of later on strongly shielded magnets and a measuring method to connect precisely the adjacent, accessible sections to the inaccessible areas were studied.
In order to verify the simulations, to test cameras, to try different types of targets and image analysis and to investigate the influence of different configurations of the bundle adjustment a test installation of RALF was done, which yielded excellent results. Thus the remote-controlled alignment system RALF is able to achieve a single point accuracy of below 0,1mm [94].

However, the crux of the problem will not be the metrological part but rather various practical aspects and constraints on the future accelerator facility that require more discussion with several departments (e.g. civil construction, radiation protection, beam physicists).

So, a storage room for the pausing measuring system (during operation of the accelerator) and an appropriate connecting path is needed, preferably far away from the target area. Otherwise a constant influence of neutron and gamma radiation on CCD / CMOS image sensors of cameras will lead to damage of the imagery (and thus to a loss of accuracy).
Space for the installation of a linear motion system must be predefined; the illumination of the areas to be surveyed has to be optimized accordingly; shielding of magnets must enable their metrological accessibility anyway. Last but not least adequate adjustment devices for remote-handling have to be designed.

Nonetheless, the concept of RALF is – owing to its fast data acquisition and thus its little need of access time to the machine - a promising alternative to traditional alignment methods as it is applicable at many accelerator areas of FAIR, not only in activated sections.

It has to be emphasized that implementation of an "S&A system in high-radiation environment" (RALF) into future activated areas has to take place during first installation of the machine, at least before starting operation, although initial alignment can be done by "classical" measurement systems.

2.4.14.3.2 Tilted planes

A previous proposal of the civil engineering team has suggested that the plane of the SIS100/300 ring-tunnel should be tilted by approximately 2%. From an accelerator alignment point of view, a sloped tunnel plane is controllable; however, any use of easy manageable spirit levels, plummets as well as systems like hydrostatic levelling systems (HLS) is stopped or complicated. The 'natural reference plane' for height measurements – the equipotential plane of earth – will be abandoned, hence every relatively modest installation must be assisted by real 3D-measurements. A tilted plane will increase error rates and costs due to a needed higher effort of personnel, time and equipment not only during initial installation but also during entire lifetime.

2.4.14.3.3 Re-using components

It should be mentioned, that – even if components of the existing machines will be re-used, which were already prepared for a precise, polar, three-dimensional alignment procedure – every magnet must be fiducialized again. Only this way an updated, modern survey and alignment concept can be implemented.

2.4.14.3.4 Assembling, support structures, chronological flow of construction work: influence on position accuracy

At present the beamline height of the Super-FRS is planned to be 2m above the floor. Together with a magnet height of additional ~1m (e.g. superferric dipole magnet), a working height for maintenance or alignment is reached, which is practicable but not very user-friendly. This has to be taken into account, when estimating time - and consequential costs - that is needed for any survey and alignment activity.
Furthermore, support frames and floor conditions have to be planned very carefully to avoid high lever arm effects. Small footprints compared to a high beamline level can cause big tangential deviations of the beam (respectively of the magnet) due to little deformations of the floor.

When two rings or a machine part and an experimental device will finally share the same building without any constructional separation, the installation of the last will definitely affect the position of the components of the first that will possibly be installed and initially aligned in

a previous phase. Both machines need of course all fundamental survey and alignment processes, but a realignment of the components that were set up sooner will be required when the installation of the elements of the other machine is finished. It is therefore recommended to survey additionally a common reference network for both, as a basis for the initial precise alignment of the last installed machine and the re-alignment of the components of the first. This fact must find its way into any time schedule.

2.4.14.4 Closing words

Generally it must be emphasized that survey and alignment tasks – that are predominantly service-oriented (i.e. personnel / expenditure of time) and less material intensive – bear significant dependencies to other work packages, which do not appear as obvious as they are actually. After machines were turned on, the survey and alignment has to be repeated at regular intervals, which distinguishes it from other construction and installation activities. It has to be kept in mind during design phase, that decisions in civil and mechanical engineering, magnet design as well as accelerator physics have great impact on labour-intensive alignment processes and thus on needed service- or shutdown time and finally costs. Efficient adjustment devices, reasonable alignment tolerances or tunnel width are named here representatively.

Furthermore, survey and alignment are 'driven' activities: most of the described tasks have to be seen as iterative or split processes. Hence, an 'exact' scheduling for S&A activities concerning flow of work, time needs and costs is only possible shortly before realisation. They are strongly dependent on design information, time of delivery or installation etc. A scenario such as installing the HEBT as a whole, carrying out network measurements and align all components one after another within one period is not realistic; it has to be assumed strongly, that in several areas multiple iterations of survey and alignment activities are required – independently of (respectively in addition to) different construction phases – in order to get an effective, exact positioning of all elements that is essential for high beam quality.

Planning and coordination of accelerator alignment tasks as well as performing the measurements itself need skilled people with consolidated knowledge. One problem in getting FAIR aligned may be, to find at the same time enough (internal and external) survey professionals, qualified in large-scale metrology. Even though it is planned to hire external service providers for temporary peaks, it should not be missed to form a core team very early, which is to be trained and sworn in, in order to be able to guarantee a high quality of positioning the FAIR components.

2.4.15 NUSTAR DAQ

The NUSTAR data acquisition (DAQ) concept tries to incorporate and deal with the changes that are related to the discontinuation of production and support of all CAMAC and FASTBUS modules, together with the much increasing number of channels in the different experiments. Dedicated front-end electronics boards are foreseen in most experiments for NUSTAR. The other main issue is to provide a maximum interoperability of the different setups of the NUSTAR facility for many parts of particular setups, detectors systems and their associated DAQ systems. An example is the in-ring instrumentation of the NESR that will be used in parallel by the EXL and ELISe collaborations. The same holds for the combination of Super-FRS instrumentation – R^3B setup, or gamma spectroscopy arrays in conjunction with reaction setups. As the communities overlap to a large extent it is favourable to come up with a combined DAQ framework that allows sharing expertise, thus saving manpower and running cost. The GSI MBS [95] system is an example for such a flexible DAQ scheme, that provides a generalized multi-processor environment, suitable for the readout, control and data storage of heterogeneous setups. The necessary extensions of the scheme have to be evaluated and integrated into the developing system by the NUSTAR DAQ group. A major part of this will be the integration of 'foreign' stand-alone DAQ systems or similarly the control and operation of various front-end electronics. System integration should be possible at different stages of the DAQ system.

(a) **"NUSTAR" DAQ systems:** It should be possible to couple different standalone "NUSTAR" DAQ systems, together in a simple way. Typically the individual DAQ systems are used to setup and debug detector groups or experiments. By foreseeing the necessary interconnects for triggers and control signals and by keeping the modularity of the system in mind while building local triggers and event buffer capabilities, such a scheme can be realized. The R^3B/CaveC setup together with the current FRS is an example where the necessary prerequisites are currently specified. Note, that different schemes of coupling might be used here: (i) the systems are synchronized with one common trigger (ii) the DAQ systems run standalone and are synchronized via timestamps (see section 2.4.15.1).

(b) **Front-end electronics (FEE):** For the common NUSTAR DAQ system, specific front-end electronics together with its digitization part is seen as part of the detector. This has the advantage that all analogue signal processing is done by the working groups with the most experience on the particular detector system. Only the control, trigger and data flow will be specified as interface description by the common NUSTAR DAQ system. This includes the necessary trigger types to be implemented, such as data, calibration and synchronization triggers together with a prescription how to lock the FEE to realize a clearly defined dead time of the total system. The timestamp-data interface has to be specified and slow control issues like version numbering, firmware revisions, software up/download from e.g. databases to particular FEE boards require R&D work. A first implementation for the digital interface that allows slow control and experiment data transfer from and to FEE boards already exists and is in use; the GTB-BUS a GSI development.

(c) **Inhomogeneous DAQ systems:** From our operating experience we know, that especially the large gamma arrays come with their own customized DAQ systems. As has been seen e.g. for the RISING [96] experiments at the FRS, a certain flexibility of the host (here the NUSTAR) DAQ system is mandatory to couple these systems together. The development and implementation of the TITRIS timestamp module together with

the time-ordered writing to mass storage within the MBS framework is an example for such integration efforts.

Implementation: As a first step it is planned to implement a standardized front-end electronics (e.g. for the R³B/CAVEC) for fast signals. It will consist of a taquila [41] front-end board that has been developed for the upgrade of the FOPI experiment at GSI. These boards can be used to record 16 channels of time-signals, amplitude- or charge-signals at a moderate channel cost of about 50-60€. As interface to the detector additional FEE (e.g. [97]) boards are used, that are used to amplify, shape and split the signals prior to their input the digitizer board. Such a system can be thought of being already a replacement for a full, e.g. NIM based pre-amplifier, discriminator and CAMAC/FASTBUS based digitizer chain. The taquila boards provide also a simple time stamp mechanism. We will study the behaviour of such a system within the next two years at the R³B/CAVEC setup using the LAND neutron-detector readout as reference implementation. Further R&D steps will be accomplished to come to a fully operable FEE environment. The FEE is digitally attached via the GTB bus to a VME based processor board [98] that can be used to control the FEE readout process and to perform online data reduction (see Figure 2.4-148).

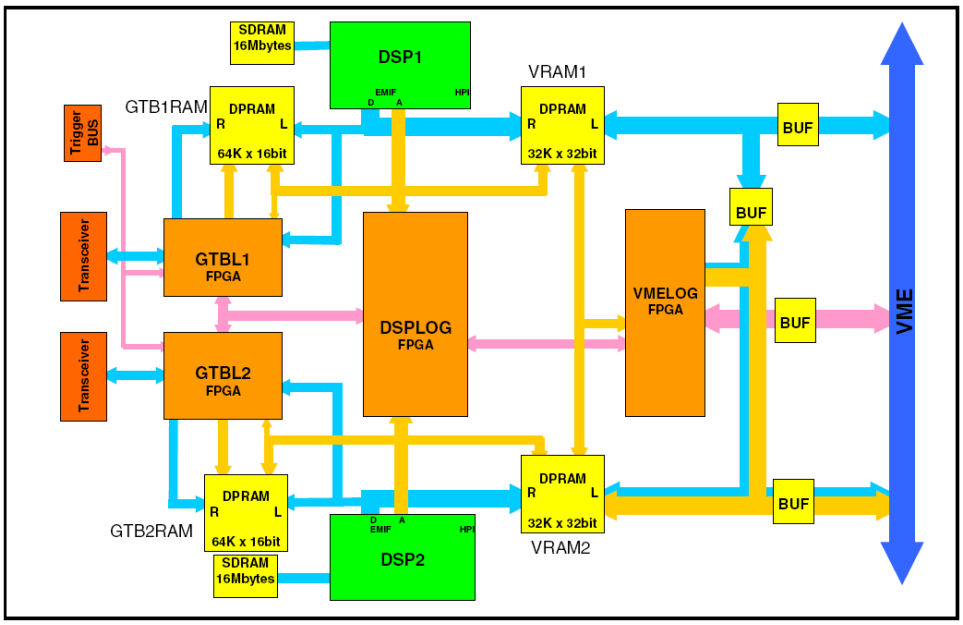

Figure 2.4-148: Block diagram of the VME based SAM3 processor board. Two TMS320C6711 digital signal processors running at 100 MHz are used. It is foreseen to provide this module's functionality within the framework of the NUSTAR DAQ system.

Requests: Apart from the R³B/FAIR experiment that will be the continuation of the R³B/CAVEC experiment the EXL community has already come up with detailed requests to the NUSTAR DAQ group. The EXL front-end electronics which includes the ADC will have its own Time stamp & slow control facilities. The slow control facilities will allow a level of hard and software debugging. The slow control will allow the modification of e.g. the sub-trigger, choice of pre-amplifiers and amplifiers, the shaping, the gain, discriminators, sampling, ADC functions, calibration and test sequences, cable redundancy, high voltage, and bias settings. The structure required to manage the above should, is requested from the NUSTAR DAQ system. Apart from the control aspects, also the data collection chain from the digitized data has to be implemented, where the expected data rates for both experiments are approaching the 100 MBytes/sec limit.

Controls: We foresee two kinds of data from the experiments: event-wise data that is taken with the physics and control triggers and what we call slow control data, like scaler readouts, beam profiles and so on. These data are of interest for the distributed slow control system throughout the NUSTAR facility and the accelerator. For this example, profile data may be taken to generate a feedback loop in order to perform automatic beam steering, whereas scaler data can provide information on the sanity of the particular setups. Of particular interest are fast control loops based on digital signal processing techniques, that can be already implemented in FPGA based front-end readout cards, coupled to slow control processes via e.g. a on board processor. The available processing power allows for an optimization of already single detector channels on-line so that the setup time can be drastically reduced. Such systems are currently tested for pile-up rejection and correction, pulse shape discrimination and intelligent adaptive triggering.

2.4.15.1 Time and trigger distribution systems

As can be seen from the above discussion one of the main infrastructures delivered by the NUSTAR DAQ framework will be a hierarchical time distribution system. Existing architectures for large scale time and trigger distribution systems are given e.g. by the TTC for LHC experiments [99], or the TCS [100,101] build for the COMPASS experiment, both at CERN. The Accelerator Division is currently working on a next generation timing system [102]. A Prototype system is available since mid 2007 and is being built by Work µ-wave GmbH. The activity was originally prompted by the requirement of the PHELIX experiment to synchronize a laser shot with the arriving pulse to a precision of 100 ps, thus the internal name "BuTiS" for 'Bunchphase Timing System'. This scope has of course widened, the objective is now to provide the timing reference for all FAIR accelerator components, and if there is interest, also the experiments. The currently available prototype system provides an absolute precision of 100 ps for the timestamps across the whole GSI site, and a timing jitter of well below 10 ps. The system is used as campus reference for standard frequencies (currently under evaluation are 200 MHz and 10 MHz) and standard time (UTC) which can be derived from a GPS based reference or a labelling of certain pulses via accelerator controls. In addition, auxiliary information channels are foreseen which will provide for example triggers for specific accelerator events.

Local time-stamps: A campus wide synchronisation method allows for common timestamps between different experiments. The common clock is not enough on its own for full synchronisation - one needs to be able to correlate particular clock edges with particular values of the timestamp counters in order to start from the same timestamp value everywhere. Existing local time distribution systems like e.g. the GSI TITRIS [103] modular, which is similar to the CENTRUM built by GANIL [104] and also the proposed AGATA GTS [105], have to be adapted to allow for the synchronization to the BuTiS clock with a defined phase. Different types of FEE will also provide their local clocks. One may consider the following scenarios:

a) Self-made timestamps, where a specification of the latency of the front-end trigger with respect to the timestamps is needed in order to be able to synchronize the particular data to the overall system. The latency can be automatically determined e.g. by using generated synchronization events from the host DAQ system to the particular timestamp generating system. Another question is how to couple local systems to BuTiS. One BuTiS receiver per local timestamping system might be too expensive it is a subject to further R&D whether an additional (experiment-wide) time distribution layer is desirable.
b) For the standardized NUSTAR DAQ one should consider to build a novel “Titris II” module in different form factors, to be used in VME crates or attached to the FEE, which can be coupled to the BuTiS system.

We can mainly base our studies on the already existing techniques, use of time-stamping followed by software filters and triggers which were developed for GREAT. Within GREAT these items are handled by the Metronome and its interface to the ADC cards. Within the next years we need to specify latencies for trigger decisions depending on the physics of the trigger, taking into account the limited pre-processing buffer depths, and their associated acceptance window. Here dedicated input from the different experiments is needed to come up with a generalized and flexible scheme.

2.4.15.2 Data collection and storage

Maximum data rates of 10-100 Mbytes/sec are estimated for the EXL and R³B setups. Thus the total data produced per day is in the order of 1-10 TBytes. This means, for the NUSTAR experiments we expect not more than 500TB/year of data. The requested band-width for data transfer is in accordance with the expected rates that can be transferred using standard network components.

The demand to run independent NUSTAR DAQ modules that can be combined in a flexible manner poses certain requirements to the transport layer in between the experiments and to the mass storage:

1. Standardized sub-event format; this is favourable in order to facilitate to event building from different data sources.
2. Flexible event builder combinations; one may consider to use different parts of the data stream at different locations to perform different tasks: mass storage; online analysis; slow control feedback.
3. Standardized event format; to be used for a common unpacking scheme for data analysis.

The NUSTAR DAQ system will provide the necessary data collection procedures for standard electronics module (e.g. VME) and collection from FE-boards that follow the conventions for the standardized digital interfaces (e.g. GTB). The necessary R&D work will be done in parallel to the various electronic developments in the NUSTAR community in close collaboration with the respective groups, co-ordinated by the DAQ responsible for the particular experiments.

2.4.15.3 Slow control and monitoring

The slow control requests for the NUSTAR DAQ system fall in two categories. First the sub-systems should provide certain information in order to be in the monitoring process of the total experiment specific combination of different DAQ systems at different locations. This functionality exceeds the implemented acquisition controls: a command dispatcher and log message facility, the sense, that also different online scalers providing dead-time and rates should be available. This implies also that there should be an extended way to be able to probe the actual configuration of the setup (this means an extended object with distances between the different parts of several 100 meters) including software revisions on the FE-boards and other related information. Probing means in this context, that the individual sub-systems provide information about the parameters and interlock conditions to be monitored. One may also think of status requests that return FPGA codes, hard- and software-revisions and related information.

The second category of slow control request is the information that will be provided by the experiment's DAQ and analysis stage by:

1. The accelerator; to allow e.g. automatic beam steering [106] as it is done at the CERN PSB to continuously adjust experiments settings without manual interference.
2. The general slow controls of the experiment or setup, allowing the definition of interlock and warning conditions.
3. Any other item not mentioned here that requires information of the experiments status extracted from the online data.

The advantage of such a scheme is that controls get their information from the different local systems so that the expertise is kept locally also.
The implementation of the above scheme will be an adaptive process, where tests of the method are and can be already done at existing setups, which will lead to a final design, also with the input of the locally existing controls group.

2.4.16 Cryogenics

2.4.16.1 Introduction

The double ring synchrotrons, parts of the beam transfer lines and the Super-FRS include about 930 superconducting (sc) magnets working at an operation temperature of about 4.4 K. The required temperature for the superconducting coils is achieved either by forced flow cooling with liquid helium or by using liquid helium baths. Figure 2.4-149 gives an overviev of the site.

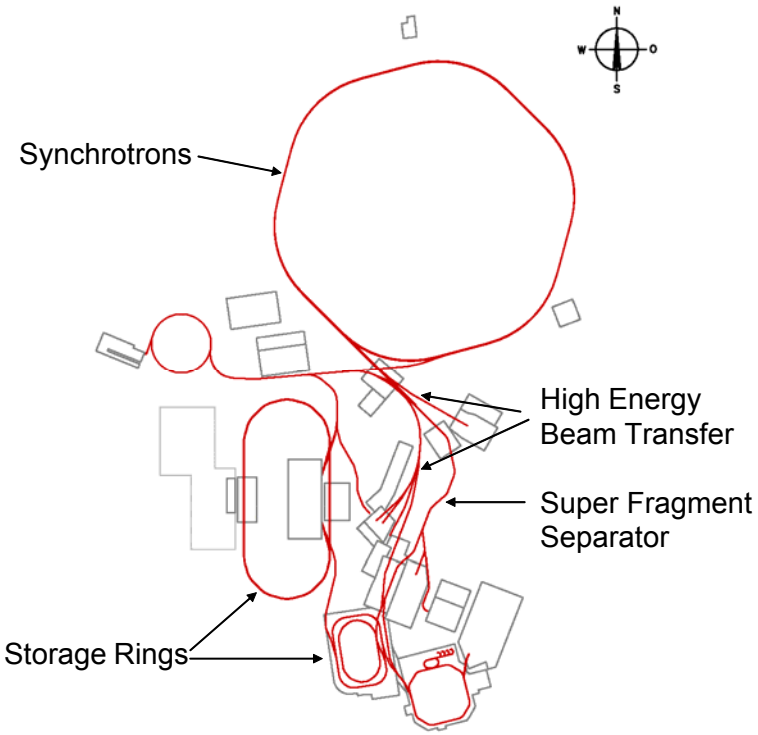

Figure 2.4-149: Overview of the FAIR site.

Liquid helium will be generated by two refrigerators with a cooling power of 34 kW at 4.4 K. It is distributed via vacuum insulated transfer lines to the feedboxes of the different helium users (e.g. synchrotrons, beam line, Super-FRS), which are located all over the site. Table 2.4-36 gives a list of the subprojects using superconducting magnets.

Additional helium cooling is required for the current leads, which connect the warm resistive power cables with the superconducting bus bars at 4 K. About 60 current leads will be installed for different nominal currents.

Table 2.4-36*:* Subprojects with cryogenic sections.

Subproject	Numbers of sc magnets
SIS 100	430
SIS 300	277
HEBT	36
Super-FRS	185
MTF	10*

*) The sc magnets that will be tested in the magnet test facility (MTF) belong to the subprojects listed above in the table.

The task of the cryogenic system is to provide the superconducting coils and the cryogenic installations with the required amount of liquid helium. In the next paragraphs the cryogenic system is described in detail consisting of

- the refrigerator,
- the distribution system,

2.4.16.2 The Refrigerator

Over the last forty years helium refrigeration technology enhanced toward higher reliability and efficiency and lower capital cost. All the major components of the FAIR helium refrigerators have been successfully demonstrated in similar systems [107]. With improved components within the refrigerators nowadays the main suppliers for Helium refrigerators offer plants up to 31 kW.

2.4.16.2.1 Basic Design

The cryogenic system of FAIR will consist of two main helium branches which will work independently in the beginning, but will be cold connected in the ongoing of the project. In addition there will be a cryogenic plant that supplies the series and string test facility also an independent small liquefier for liquid helium supply with transport dewars.

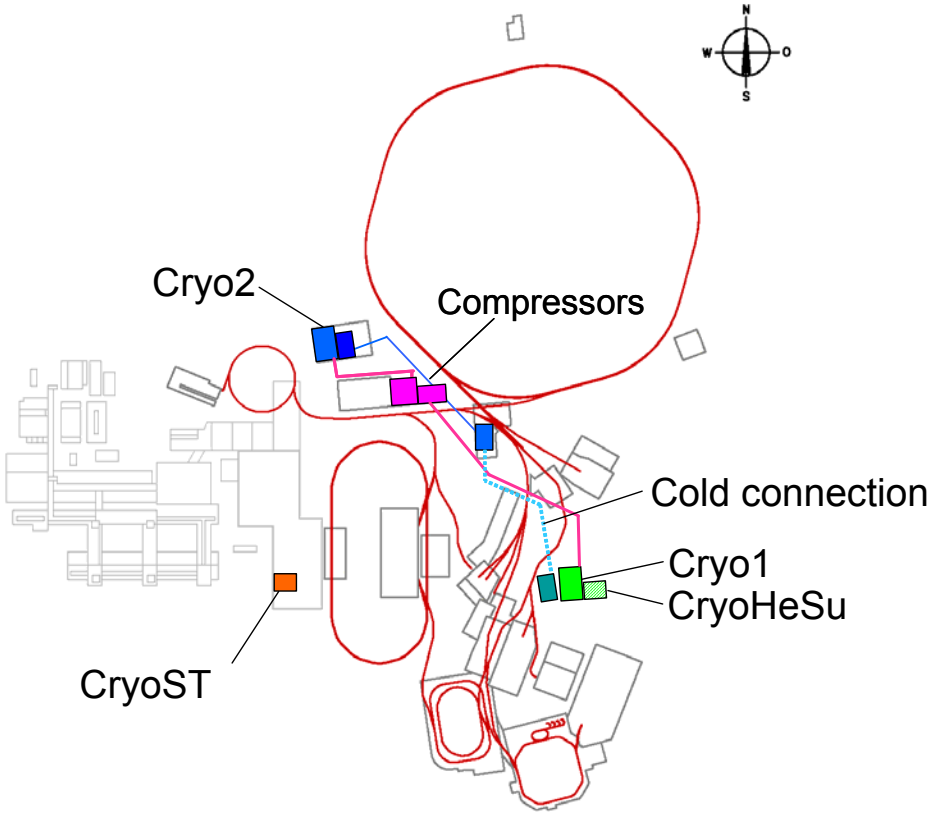

Figure 2.4-150: The two refrigerators and their locations in the project.

The first refrigerator, Cryo1, will have a nominal refrigerating capacity of approximately 4.2 kW. During normal operation of the new facility this plant will supply the Super-FRS and all equipment installed in the southern part of the FAIR facility. Cryo2 will supply the synchrotrons (SIS 100 and SIS 300) and parts of the HEBT. The series and string test facility will be supplied by CryoST (Cryo **S**eries **T**esting). For the high number of small experiments or single small consumers liquid helium will be provided in the central helium supply depot by a separate liquefier CryoHeSu (Cryo **He**lium **Su**pply).

The two refrigerators Cryo1 and Cryo2 will be interconnected by a cold connection to support one another as required. One plant will be sufficient to keep all the cold masses below 80 K during shutdowns.

Cryo1 and Cryo2 will share a common compressor station to increase reliability and to avoid two buildings with the very specially demands for a compressor building as noise and vibration protection, maintenance tolls (cranes, etc.), oil-resistant floor covering and groundwater protection.

2.4.16.2.2 Heat Load for the Refrigerators

For the design of the refrigerators the heat loads with the corresponding temperature levels are required. The nominal working temperature for both plants will be 4.4 K at 1.2 bar. The refrigerators will distribute high pressure liquid helium (3.0 bar, 4.6 K) to every user. Each user can operate the local cooling circuit with bath (Super-FRS) or forced flow cooling (two-phase for the SIS 100, one-phase for the SIS 300). The refrigerator supplies only liquid helium and receives low pressure gaseous helium in return. The return gas flow will be:

- at 4.4 K in case of the magnet cooling return line,
- at ambient temperature in case of current lead cooling.

Conventional current leads require that the refrigerator provides liquid helium and gets back gaseous helium at ambient temperature. This refrigeration service is called liquefaction.

The refrigerators will also supply a helium cooling stream from about 50 K for the cooling of thermal shields and for the cooling of high temperature superconductor (HTS) current leads. The return flow will have a temperature of 80 K.

Table 2.4-37 gives the sum of head loads for different consumers [108,109] splitted into the different refrigerators.

Table 2.4-37*:* Heat loads for FAIR (including safety factor).

Plant	Consumer	Heat load [kW]
Cryo1	Further Consumers	0.23
	Super-FRS	1.40
	Experiments	0.17
	SIS 100	1.0
		4.19
Cryo2		
	Further Consumers	1.91
	Experiments	0.180
	SIS 100	14.28
	SIS 300	3.72
		30.13
CryoST		
	Series- and String-tests	**2.50**
CryoHeSu		
	Liquid Supply	**0.10 (20-40lLHe/h)**

Only CryoHeSu is a pure liquefier. The other cryo-facilities have to share refrigeration power, liquefaction and shield cooling power. These numbers are given in Table 2.4-38.

Table 2.4-38*:* Split of liquefaction-, refrigeration- and shield cooling power in Watt at 4K.

	refrigeration / [W]		liquefaction / [W]	shield cooling / [W]
	static	dynamic		
Cryo 1	1.230	1.500	660 (5,7g/s @ 4K)	800
Cryo 2	12.000	1.4000	920 (84g/s @ 50K)	3230
CryoST	800	900	600	200

Based on these figures an overall refrigerating capacity of 37 kW is planned at a temperature of 4.4 K. The installed capacity contains a safety factor of 1.5 which has to be considered due to:

- required margin for the plant regulation,
- buffer to compensate performance decreases during operation,
- buffer to balance design risks on the experimental side.

In addition a redundant compressor will be added in order to increase the availability of the helium plant.

2.4.16.2.3 The Model Refrigerator

A model refrigerator has been designed to get information on component sizes, number of compressors, and flow rates in different operation modes. Provisional data on power con-

sumption for the specification of utility systems and approximate sizes of components for the building layouts are calculated.

Table 2.4-39: Process parameters of the refrigerator models including compressor parameters of the low pressure (LP) and high pressure (HP) levels, respectively.

		CRYO 1			CRYO 2		
Heat loads	**REF 1/2 / [W]**	**Mass flow**	**Supply**	**Return**	**Mass flow**	**Supply**	**Return**
3.0 or 4.4 K load	941				54 g/s	4.6 K 3 bar	4.4 K 1.19 bar
4.4 K load	2899 / 13362	169 g/s + 21 g/s	4.74 K 3 bar	4.4 K 1.19 bar	763 g/s + 2 g/s	4.6 K 3 bar	4.4 K 1.19 bar
50-80 K shield	13141 / 28874	85 g/s + 25 g/s	50 K 22 bar	80 K 18 bar	186 g/s + 73 g/s	50 K 22 bar	80 K 18 bar
Compressors							
LP I		397 g/s	307 K 0.94 bar	310 K 5.2 bar	886 g/s	307 K 0.94 bar	310 K 5.2 bar
LP II					249 g/s	307 K 0.94 bar	310 K 5.2 bar
HP		397 g/s	310 K 5.2 bar	310 K 23 bar	1135 g/s	310 K 5.2 bar	310 K 23 bar
Power Consumption			**app.**	**1600 kW**		**app.**	**4300 kW**

For the model refrigerator the calculated power consumption is about 5900 kW. Using a safety factor of 1.5 for the refrigeration loads a power consumption of 8.85 MW is expected for the FAIR refrigerators.

2.4.16.2.4 Compressor Stations

Central Compressor Station

The FAIR cryo system (Cryo 1 and Cryo 2) will have a central compressor station located in the building 17a. In this building 5 high- and 7 low pressure compressors will be installed, including one redundant compressor for each pressure level. Also the oil removal system and the gas management system will be installed there. An overhead crane allows all service and repair work at the compressors.

Compressor stations for CryoST and CryoHeSu

These Compressors should be placed near to the coldboxes.

2.4.16.2.5 Helium Storage

The FAIR system will contain 11 t of helium when in full operation. If the system (or part of it) is warmed up the helium inventory will be stored as gas or liquid (1 litre liquid helium at 4 K corresponds to approx. 700 litre gaseous helium at room temperature). In case of a quench of the superconducting magnets helium will be expulsed out of the quenching coils. This helium will be collected in a helium recovery system.
The FAIR helium system will have 7 gas storage tanks of 250 m³ each with a maximum storage pressure of 23 bars. These tanks will store 6 t of helium as a warm gas and will be located

outside the buildings. Helium, which is evaporated during shutdown periods, will be either pumped to the gas storage tanks or condensed and collected in dewars.
Two dewars for liquid helium will be installed with a storage volume of 20 m³. They contain about 5 t of helium. They are connected to the refrigerators by vacuum insulated lines. One liquid storage dewar will be placed at the location of each refrigerator cold box and would serve as a calorimeter/accumulator for the refrigeration/liquefaction acceptance tests.

The 5 t liquid storage capacity allows the accumulation of liquid helium in periods of low refrigeration demand. In case of peak loads (e.g. change of the operation modes) liquid helium can be provided from the liquid storage tanks.

2.4.16.3 The Helium Distribution System

The distribution of the cold helium from the two refrigerators to the individual consumers is organised via transfer lines and distribution boxes. The consumers are located at some distance from one another and are accessible only through radiation shielded tunnels. In Figure 2.4-151 the basic concept of the distribution system is shown.

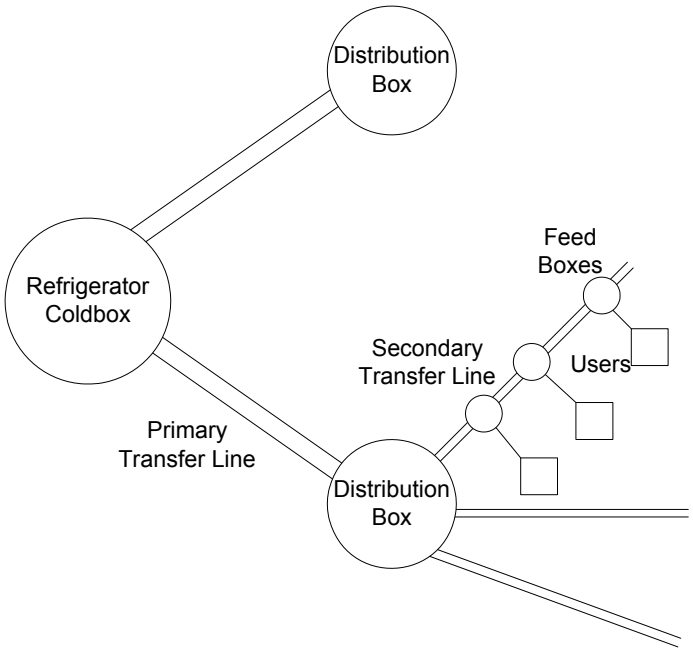

Figure 2.4-151*:* Schematic helium distribution system.

The primary transfer lines connect the refrigerator with the distribution boxes that supply the secondary transfer lines. From there helium flows to the feedboxes of the different sections. Figure 2.4-152 gives more details about the allocation of the users to the three distribution boxes and to the corresponding refrigerators. The expected mass flow rates for the different users are given as well. The upgrade version for the triangular mode of SIS100 is marked in green.

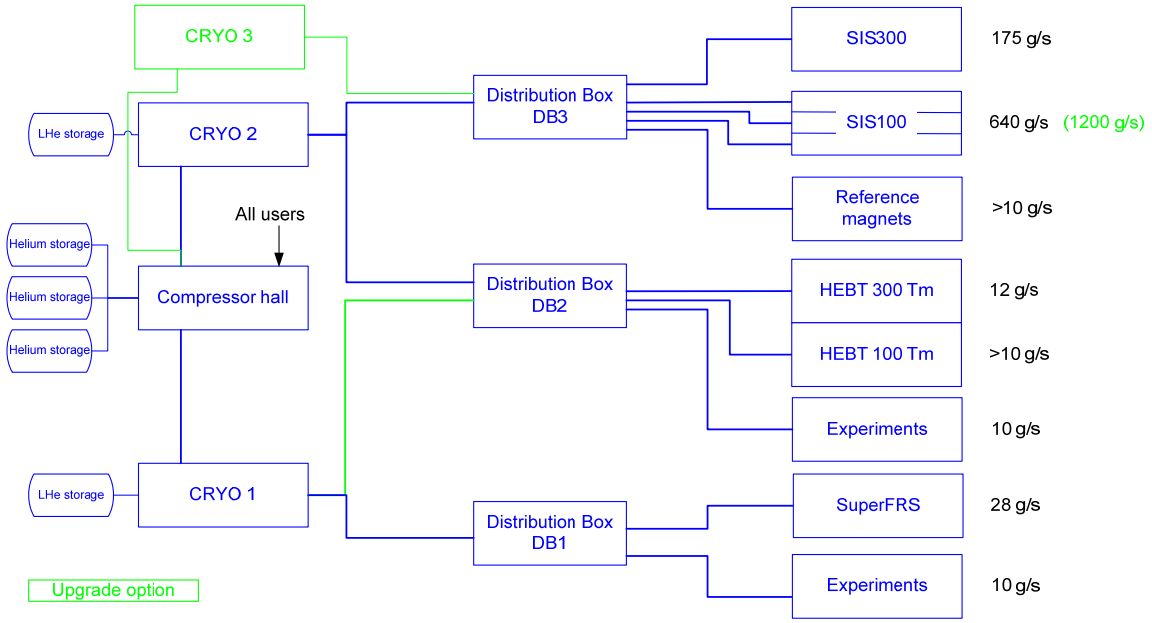

Figure 2.4-152*:* The 3 stages of the helium distribution system.

The transfer line vacuum jackets contain an actively cooled thermal shield and 5 individual lines (see Figure 2.4-153).

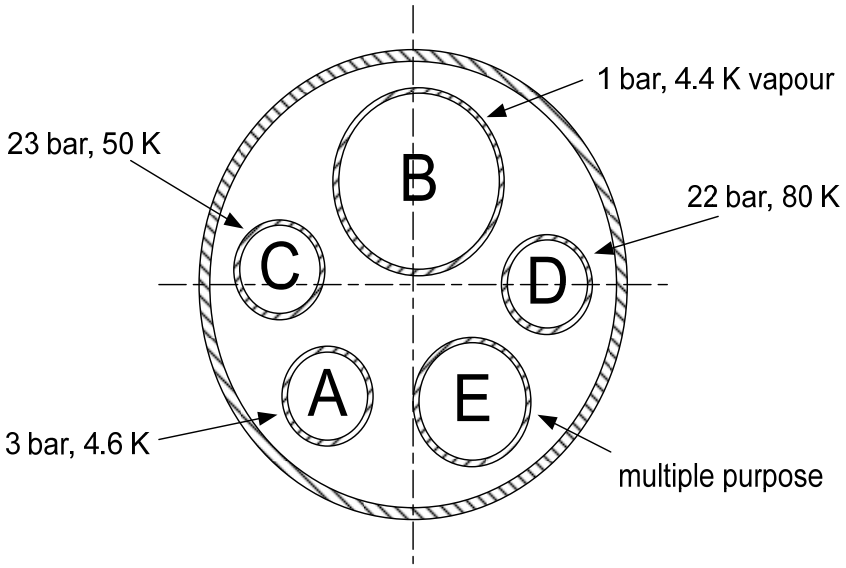

Figure 2.4-153*:* Cross section of a helium transfer line, thermal shield is not shown.

Line A and B are the feed and return lines of the cold helium flow. Single user cool down is supplied by line A as well. The varying temperature return flow flows through line E, the multi-purpose line. The return position at the low pressure side of the refrigerator depends on the helium temperature. Line E also serves to collect helium vented in the case of magnet quenches.

The size of the helium transfer lines can be determined from the calculated user heat loads and mass flows. Table 2.4-40 shows the diameters of two types of transfer lines, which will be used for the new facility as primary and secondary transfer lines.

Table 2.4-40*:* Diameters of helium transfer lines.

	Diameter of Lines [mm]					
Type (Tab. 12)	A	B	C	D	E	Outer
TL-1	40	80	40	40	50	380
TL-2	68	140	44	44	90	560

The basic helium distribution concept is that all helium coming from the refrigerator cold boxes is supplied via the transfer lines to a distribution box (cf. Figure 2.4-154) and then to the secondary transfer lines in the various tunnel sections.

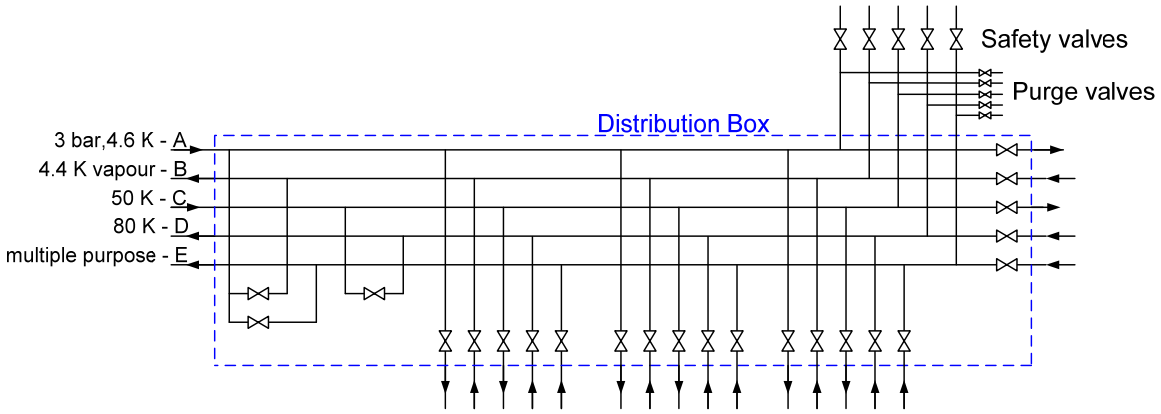

Figure 2.4-154*:* Flow sheet for a distribution box.

The installation of the transfer lines and the connections to the feedboxes require large manual labour cost. The lines will be delivered in sections of about 12 m length, threaded into the tunnel and transported to their respective installation location. That location must provide the working space for welding, x-ray, pressure and leak testing and, as necessary, repairs.

The FAIR system is installed in stages. The distribution system must be extended each time additional cryostats are installed. New sections may connect to sections already in operation. The connections of the helium and vacuum systems will be engineered in that way that implementation effort is minimized.

The total length of the primary helium transfer lines (TL) is approximately 850 m. The primary helium transfer line will connect the refrigerators (CRYO1 and CRYO2) to three distribution boxes (DB1 to DB3) for local distribution to the separate users. Details of the distribution system and the positioning of the distribution boxes are given in Figure 2.4-155. The refrigerator, the primary transfer lines and the distribution boxes are located outside the radiation areas to simplify the installation and operating service. Inside the radiation areas space will be required for the penetrating secondary transfer lines and the individual user feedboxes. The lengths of the different transfer lines are listed in Table 2.4-41.

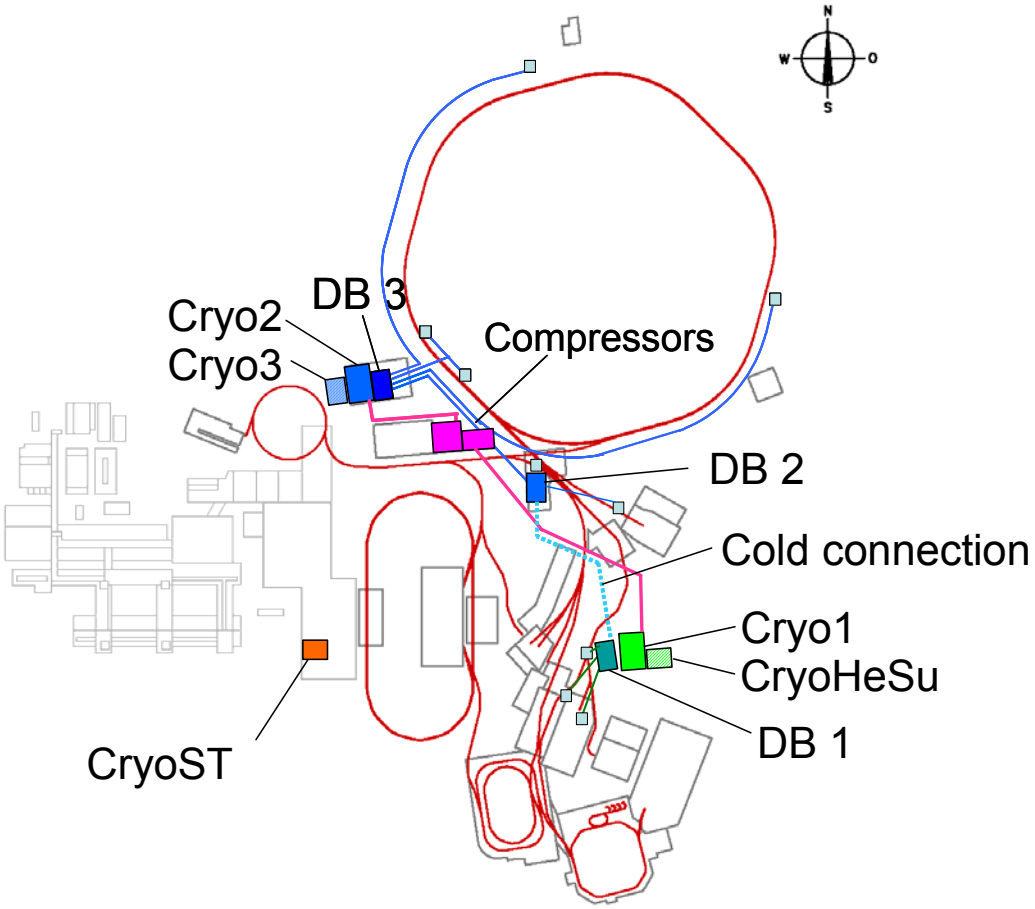

Figure 2.4-155*:* Helium transfer lines and distribution and feed boxes.

Table 2.4-41*:* Helium transfer lines and their lengths.

Helium Transfer Line	Length [m]	Type
CRYO1 to distribution box 1 (DB 1)	130	TL-1
CRYO1 to distribution box 2 (DB 2)	350	TL-1
DB 2 to SuperFRS	10	TL-1
CRYO2 to DB 2	180	TL-1
CRYO2 to DB 3	30	TL-2
DB 3 to Feedbox 1, SIS 100	110	TL-2
DB 3 to Feedbox 2, SIS 100	460	TL-2
DB 3 to Feedbox 3, SIS 100	460	TL-2
DB 3 to Feedbox , SIS 300	110	TL-1
DB 3 to HEBT	170	TL-2
SUM	2010	

2.4.16.3.1 Cold Electrical connections

As the current lead boxes will be placed near by the power supplies within the buildings 1, 2, 3 cold electrical connections between the current lead boxes and the local feed boxes at the synchrotron level are required. In Figure 2.4-156 the simplified flow diagram for the cooling of one current circuit is given. The local feed box will be supplied with supercritical helium from building 1. There the total helium flow will be subcooled. The flow is split up into the two main streams for the supply of two adjacent sectors and some smaller stream supplying the bus bars. The current lead boxes will be supplied with helium through the cold electrical connection. The same cable as for the magnets will be used as a bus bar within the cold connection. Every circuit

requires two cables. One cable will be fed with high pressure helium in the local feed box. Along the cable the helium will be throttled and partly evaporate. In current lead box the helium will cool the current leads. Than the helium stream is split into two streams. The liquid stream is fed through the second cable and will cool that bus bar. The vapour stream is merged with the vapour streams of the other circuits and fed through an additional tube in the cold connection. To allow this flow scheme an orifice will be build in at the inlet of the returning cable.
The cooling gas for the copper part of the current leads will supplied by the shielding line of the transfer line. The heat inleak of the transfer line will be in the range to supply a temperature below 55K.

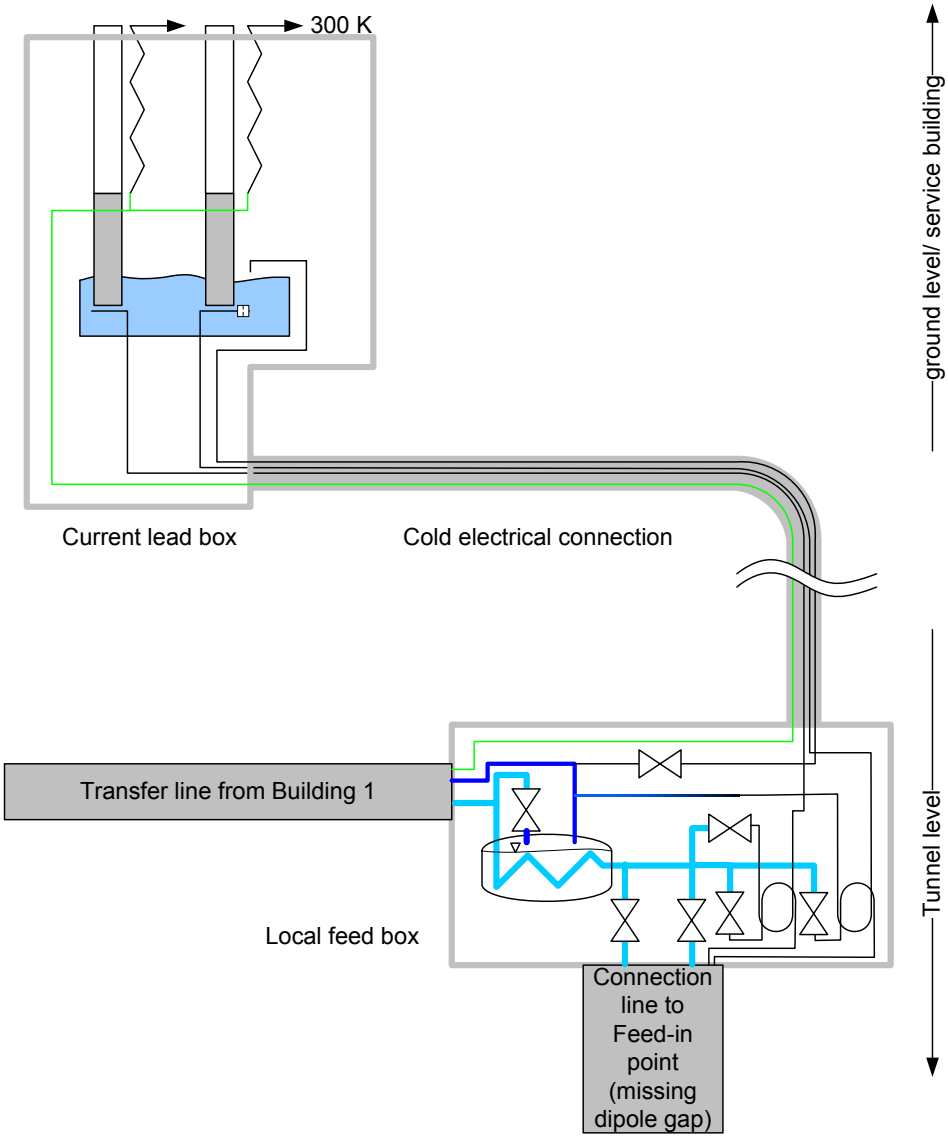

Figure 2.4-156: Schematic flow diagram for the 4K- flow of one exemplary current circuit and the 50 K flow required for shielding and the current leads.

The cold connection will be manufatured by winding several cables like a cord. Housed in a flexible transfer line to facilitate the laying of cold connection within the buildings.

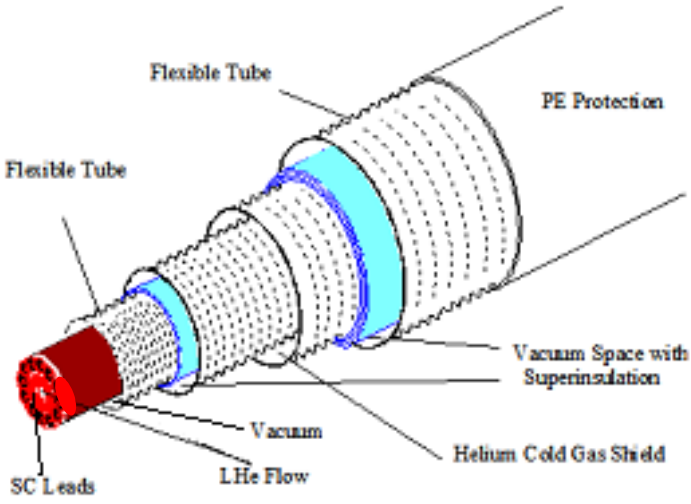

Figure 2.4-157*:* Flexible Transfer line housing bus bars [*110*].

The winding process is possible either with 7 cables or 19 cables. As an even number of cables is required for the electrical connection one of the cables will be replaced by a tube with equal outer diameter. The geometric data for both solutions are given in the following table:

Table 2.4-42*:* Geometric data of the cold electrical connection.

Number of electrical circuits		3	9
Number of cable		6	18
Number of tubes for returning gas		1	1
Outer diameter	[m]	0.143	0.163
Bending radius			
<= 3 bends	[m]	1.3	1.4
> 3 bends	[m]	1.8	1.9

The flexible connection will be supplied on a standard cable drum (4.2m diameter). The termination of the connection will look like given in Figure 2.4-158.

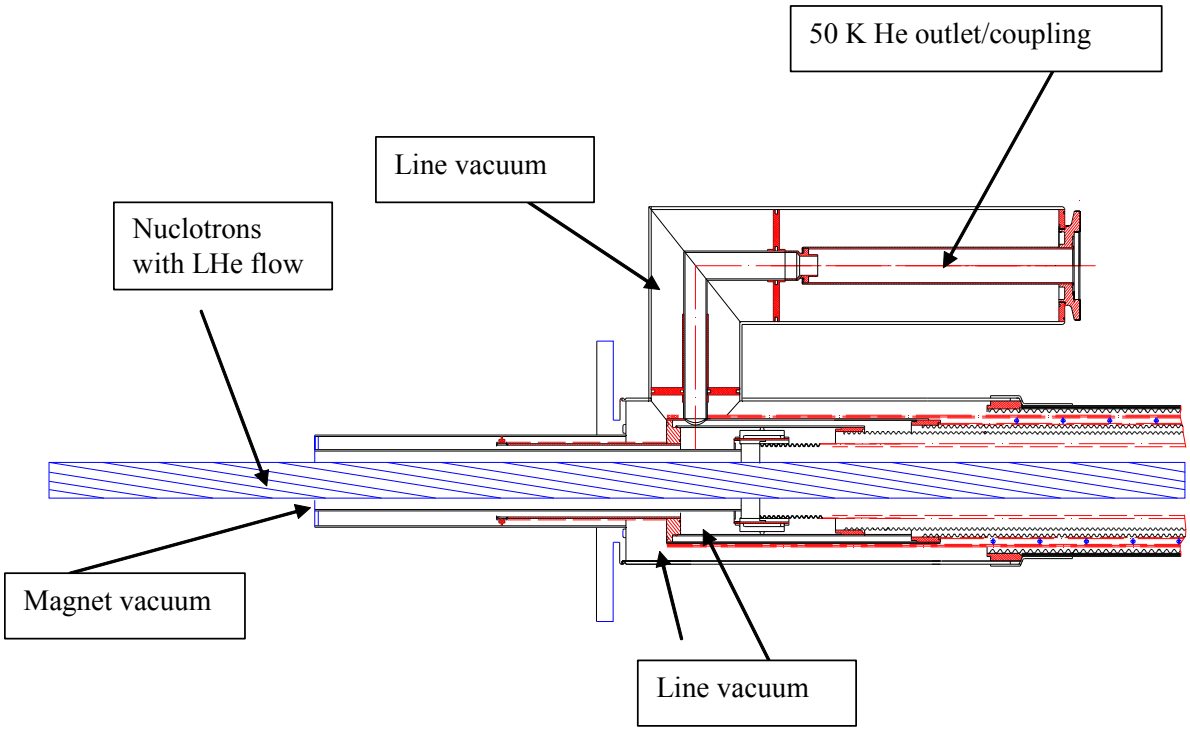

Figure 2.4-158*:* Possible termination of the cold electrical connection.

The heat load for the cold electrical connection consists of two main parts, heat conduction from the outside and AC losses in the cable. The heat conduction to the 4.4 K level will be of 80 mW/m for 7 cables and 100 mW/m for 19 cables. The heat inleak to the outer shielding gas with a temperature difference from room temperature to 50 K will be in the range of 1.2 W/m for 7 cables and 1.5 W/m for 19 cables.
These data are based on measurements on existing transfer lines with the same design principle.

2.4.17 Magnet testing

2.4.17.1 Introduction

The FAIR project needs a large number of magnets which have to be produced within a short period of time. To guarantee successful operation of all magnets after installation in the different facilities, a dedicated magnet test program is indispensable covering the following items:

1. quality assurance (production and testing),
2. training the magnets,
3. measurement of the magnetic field, field quality and magnetic axis in case of quadrupoles and higher order multipoles,
4. provide information for operating the magnets,
5. test the quench protection systems for the different machines.

The procedure for magnet testing and magnetic measurements is described below. Due to the relatively small number of magnets per series a well established cold-warm correlation for the field quality cannot be assumed in advance. Thus it is assumed that each superconducting magnet has to be trained and measured at operating temperature.
Measurements planned for each superconducting magnet are:

- warm magnetic measurements in industry,
- training of the magnet,
- power test at different ramp rates for pulsed magnets,
- integral loss measurement (voltage-current and calorimetric methods),
- magnetic measurements,
- insulation and electrical integrity tests,

For normal conducting magnets the following measurements have to be performed:

- geometry tests in industry
- warm magnetic measurement in industry
- insulation and electrical integrity tests in industry,
- pre-series and special magnet fully tested at the GSI lab

Table 2.4-43*:* Total number of normal and superconducting magnets for Super-FRS. All nc magnets are radiation resistant magnets.

Super-FRS Magnet types	no. of magnets
nc main magnets (dipoles):	3
nc main magnets (quadrupoles):	3
nc main magnets (sextupole):	3
nc correctors,steeres.	0
nc special magnets (septa, ...)	0
sc main magnets (dipoles and quadrupoles)	28
sc main magnets (dipoles and quadrupoles)	68
sc correctors (mulipole, steering, hexapole,..)	94

Magnetic measurements are performed to ensure the required field and field quality of each individual magnet. The quantities to be measured depend on the type of magnet:

- Dipole:
  - $\int Bdl$, the magnetic field B integrated over the magnet length l
  - field direction

    - field quality
- Quadrupole:
    - $\int Gdl$ with the magnetic field gradient G integrated over the magnet length l
    - axis
    - field direction
    - field quality
- Corrector magnets
    - $\int C_n dl$ with C_n the n^{th} harmonic integrated over the magnet length l
    - axis
    - field direction
    - field quality

Ramped magnets must be measured in AC and DC mode. The time delay until the field has stabilized has to be measured for pulsed magnets as well, i.e. magnets which must reach their excitation level during a short time period (in the order of a second).

2.4.17.2 Conventional Magnets

Preparative tests of normal conducting magnets, such as insulation test, cooling water flow, etc., are part of the factory acceptance tests (see section 2.4.17.2.1) of each individual magnet and are not considered as part of the site acceptance test. Thus magnetic measurement is the main measurement task to perform for normal conducting magnets. Special consideration is required if cold-warm transitions in the beamline are necessary (e.g. for injection and extraction of the synchrotrons). The measurement methods applied to the main magnet types are given in Table 2.4-44.

2.4.17.2.1 Factory Acceptance Tests

Samples for BH Curves
They have to be provided by the manufacturer. These will be used to assert that the properties of the steel match the specification. If possible, the manufacturer should also measure these samples.

Yoke Packing Factor
The dipoles and quadrupoles of this ring are made of laminated steel. Thus the packing factor has to be measured for the whole magnet or at least for all its individual packs.

Pole geometry
The field quality is mainly formed by the shape of the pole. Thus the shape of the pole itself as well as the position of one pole to the other(s) has to be measured.

Electrical Safety
The magnet producer will have to ensure the save electrical operation of the magnet. As part of this requirement the insulation of the coils and connections has to be tested up to a voltage V_{max} of (V_{max} = 2 V_{op} + 1000 V) with V_{op} the maximum operational voltage in the branch of the machine, where this magnet is to be connected. This test is typically conducted immersing the coil in water and filling the cooling channels of the coil with water at the maximum acceptable pressure level.

Interlock systems
The water flow and the water temperature through the magnets will be monitored by the machine safety system. Therefore flow and temperature interlocks have to be installed at the water inlet and outlet.

Magnetic Measurement of main magnets
Machine operation requires precise data of the field of the magnet for the main magnets. The magnetic field of dipoles and quadrupoles has to be measured at:

- injection field,
- mid field,
- maximum field,

for DC operation. If the magnets are also ramped quickly, measurements have to be performed which allow to estimate the field strength and the field quality for the whole operation cycle with sufficient accuracy.

For magnets with less stringent field quality requirements (e.g. correctors and steerer magnets whose field has only to be known in the range of a percent) it is sufficient to monitor the production randomly by measuring only one or few magnets (see also section 2.4.17.1). The different measurement methods foreseen for the different magnets are summarized in Table 2.4-44. The curvature of the used search coils for the dipoles is given in Table 2.4-45and the radius of the rotating coil is given in Table 2.4-46.

Matching Magnet Length
For machines with only a few dipoles and quadrupoles (e.g. 24 pieces) the length of the magnets has to be matched. For this purpose laminations are inserted at the end of the yoke. The field of the magnet has to be remeasured after this operation.

Table 2.4-44*:* Magnetic measurement method to apply for the different magnets.

a) dipoles

	field strength	field direction	field homogeneity	centre
CR NESR RESR Super-FRS	search coil	pole shoes	search coil	pole shoes

b) quadrupoles / correctors

	field strength	axis	field direction	field homogeneity
SIS 300 HESR SIS 100	rotating coil		pole shoes	rotating coil
CR NESR RESR Super-FRS	rotating coil		pole shoes	rotating coil

Table 2.4-45*:* Search coil curvature applied for measuring the main dipoles of the different facilities.

Facility	Curvature of the search coil [m]
Super FRS	12.5, 4.35
CR	8.125
NESR / RESR	8.125
HEBT	62.5, 4.35

Table 2.4-46*:* Radius of the rotating coil for the different machines for measuring quadrupoles and higher order correctors (to be adjustment after the magnet designs are fixed).

Facility	Radius of the rotating coil [mm]
Super FRS	180 (multiplet system)
CR	70, 156
NESR / RESR	90, 128
HEBT	52,5, 65, 156

Fiduzialisation
General considerations concerning the fiduzialisation are given in section 2.4.14.2.1.

2.4.17.2.2 Site Acceptance Tests

Only each first main magnet will be measured magnetically at GSI. The same measurements as described in 2.4.17.2.1 will be performed. Additionally the end field will be mapped for the main magnets.

2.4.17.2.3 Schedule

For the Site Acceptance Test, 1 month has to be foreseen for main dipoles or quadrupoles if their weight is less than 16 tons, or if the magnet can be disassembled in two pieces, 2 times 16 tons. Special magnets will require 2 month if still less than 16 tons or 2 times 16 tons. Testing any other magnet will last more than 2 month as it can not be tested in the prototype test facility. These will be tested at, or near the location, of final installation.

2.4.17.3 Superconducting Magnets

Many different tasks are required for all superconducting magnets to ensure their quality and performance. These tests are partly done in industry during the production (and not exhaustively documented here) and partly at the GSI lab. The measuring tasks are listed in chronological order in Table 2.4-47.

Table 2.4-47*:* Main magnet tests in Industry and at the FAIR lab.

Industry Factory Acceptance Tests	production	electrical tests, insulation tests	
		geometry, Young's modulus of the coil	
		magnetic measurements	collared coil yoked magnet
	acceptance	vacuum tests hydraulic measurements	
GSI lab. Site Acceptance Tests	acceptance	electrical tests, insulation tests, instrumentation tests	
		geometry	
		magnetic measurements at warm	
		vacuum test	
	integrity	electrical tests, insulation tests, instrumentation tests at operating temperature	
	quality check	power tests (training and quench behaviour)	
		loss measurements	
		magnetic measurements under operating conditions	

2.4.17.3.1 Factory Acceptance Tests

The Factory Acceptance Tests (FAT) as the final production acceptance test includes tests of all final components and tests of the final assembly (product). Some of these tests are carried out during manufacturing. For the FAT the appropriate test protocols must be provided by the contractor and then they have to be checked by the staff responsible for Quality Assurance (FAIR site) and approved or rejected. If a tested magnet fulfils all criteria of FAT it can be shipped to GSI.

The value, parameters, conditions and compatibility of the FAT tests will be specified during Preliminary Design Review unless they are previously specified in the Technical Specification.

As an example of a FAT with reference to the components is shown below:

1. Cable and Coil Tests:

- The most important dimensions of the coil are measured during the manufacturing process.
- The CuNi tube for the cable must be certified for its tightness by the manufacturer. Otherwise a helium leakage test will be performed prior to the coil winding. After coil winding the coil will be tested for helium tightness.
- Insulations tests (after coil winding, assembling with the yoke, assembling with the cryostat).
- Continuity test after each steps involve instrumentation
- The mass-flow through the cooling channel is measured with fixed input pressure > 1 bar and output pressure ~ 1 bar.

2. Yoke Tests:

- The most important dimensions of the yoke are measured during the manufacturing process.
- Measurement of magnetic permeability of the yoke material

3. Cryostat Tests:

- The most important dimensions of the cryostat are measured during the manufacturing process. After assembly of the cryostat the leakage is measured to assure that the required insulation vacuum can be achieved.
- Geometry of the magnet inside the cryostat.

4. Instrumentation and Sensor Tests:

- The internal resistance and insulation versus ground is measured.
- Voltage taps: a measurement of the contact to the coil and to the sensors is performed.

5. Vacuum chamber Tests:

The vacuum chamber test is described in related chapter.

6. Magnet Tests:

- Continuity Test of all type of taps (voltage, current, temperature sensors), resistance and inductance tests.
- Insulation Test – min. twice the operation voltage plus 500V during 2 min. between coil and ground .
- Shorts between wires in the coil – e.g. high voltage discharge test and comparison with the results of the manufacturing stage.
- Vacuum Test of the cryostat – the results has to show a leak rate better than 10^{-8}mbar/s.
- Vacuum Test of the helium process lines – the results has to show a leak rate better than 10^{-8}mbar/s.
- Pressure Test of the helium process volume has be checked with a pressure 1.4 times higher than the design pressure.
- Quench Heater Test – some of the SIS100 (6) quadrupoles are equipped with a quench heaters; the quench heaters have to be powered and the proper current and voltage curves have to be achieved.
- Warm Magnetic Measurement – is described below
- Vacuum Chamber Test – is described in related chapter,
- Geometry Test – is described in related chapter.

Warm Magnetic Measurement

Apart from insulation, electrical and geometric tests, magnetic measurements allow to monitor the quality of the production. The field quality of iron dominated magnets is mainly determined by the shape of the iron pole, thus the field quality can only be tested when operating at nominal conditions. Thus only the geometry of the iron is controlled during the production. Additionally a check of the coil has to be foreseen before assembling them with the iron yoke.

2.4.17.3.2 Site Acceptance Tests

The Site Acceptance Tests (SAT), as the final acceptance test, includes results of FAT and all tests done at GSI and the final evaluation of the test results.

The value, parameters, conditions and compatibility of the SAT tests will be specified during the Final Design Review unless they have been previously specified in the Technical Specification.

The SAT includes 3 main stages which shall assure the quality of the magnet. The magnet can be rejected after each stage of the SAT procedure and sent back to the manufacturer for reparation or replacement.

Stage 1 - Reception Tests

After delivery each individual superconducting magnet has to pass a reception test at warm. In principle all reception tests have to confirm the FAT tests. If the magnet does not fulfil the criteria of the Reception Tests, it will be tested at Operation Temperature and will be sent back to the manufacturer for reparation.

As an example the following reception test is shown below:

1. Electrical Tests:

- Insulation Tests.
- Resistance and Inductance Tests.
- Continuity and Instrumentation Tests.

2. Vacuum leakage and pressure tests

- Vacuum Test of the cryostat – the results has to show a leak rate better than 10^{-8}mbar/s.
- Vacuum Test of the helium process lines – the results has to show a leak rate better than 10^{-8}mbar/s.
- Pressure Test of the helium process volume has be checked with a pressure 1.4 times higher than the design pressure.

3. Geometry tests

For cryostated magnets the geometry of the bore and the position of reference surfaces on the cold mass are measured with respect to the fiducials of the cryostat.

Stage 2 - Tests at Operation Temperature

All magnets have to be tested in operating conditions to warrant the full functionality, as testing is considered cheaper than identifying a troublemaker in the ring and having it repaired.
During the tests all safety parameters and requirements have to be checked and fulfilled not to risk to loose a magnet during the power test (e. g. a coil to coil short burning the conductors of the magnet).
After all tests at operating temperature have been performed, the preliminary evaluation of the test results has to be done.
The main steps of the tests performed at the operating temperature are outlined in the following:

1. Tests before Cooling Down

- Insulation Tests.
- Vacuum and Leakage Tests
- Check of purity of the helium process gas
- Resistance and Inductance Tests.
- Continuity and Instrumentation Tests.

2. Tests before Power Test at cold

- Insulation Tests.
- Vacuum and Leakage Tests
- Continuity and Instrumentation Tests.

3. Power Test

- Training the magnet up to the nominal current - First Thermal Cycle Criterion
- 'Fast' excitation and de-excitation
- Training during the second thermal-cycle if the First Thermal Cycle Criterion is not fulfilled - Second Thermal Cycle Criterion
- measurement of the resistance of all joints in the magnet
- Temperature margin
- AC and DC losses measurements
- Vacuum and Leakage Tests during all measurements

4. Cold Magnetic Measurements

- $\int Bdl$, $\int Gdl$, harmonics, axis
- Field at DC at least at injection, maximum field and at the geometrical middle
- For ramped magnets (SIS 100 / SIS 300) also the AC components

5. Tests after Power Test at cold

- Insulation Tests.
- Continuity and Instrumentation Tests.

6. Test after Warming Up

- Insulation Tests.
- Resistance and Inductance Tests.
- Continuity and Instrumentation Tests.

Stage 3 - Final Evaluation Board

All results of the tests have to be presented to the "Final Evaluation Board". This board will finally accept or reject a magnet based on the fulfilment of machine requirements by the magnet performance. This board can request to further test magnets not performing within the specifications. This investigation will require special diagnostic and measurement methods like Time Domain Reflectometry, High Voltage Discharge, and Partial Discharge.
Further a set of expected signals has to be built along with an electrical model of each individual magnet (only practicable for magnets built in series).

Power Test
After the magnet has been cooled down and the integrity of its instrumentation is checked, the magnet current is ramped up until it either reaches the ultimate current or a portion of the superconductor becomes normal conducting (called quench). In the first case the magnet is successfully trained. In the later case the magnetic energy is transformed into thermal energy. Then the magnet needs to be cooled down again and the procedure has to be repeated until the ulti-

mate current is reached. Pulsed magnets need to be checked additionally if they can be ramped without quenching.
The First and Second Run Criterion are to be applied for power test. The First Run Criterion (FRC) states that magnet has to reach the nominal current (as a pulse and quasi DC) before certain numbers of quench (will be specified after pre-series magnet testing, for example 4). If the magnet does not fulfil FRC is should be submitted to a Second Thermal Cycle. For such magnets the Second Run Criterion (SRC) has to be applied. The SRC states that the level of the first quench during 2^{nd} run has to be above the first quench during the 1^{st} run and the magnet has to reach the nominal current (as a pulse and quasi DC) before certain numbers of quench (will be specified after pre-series magnet testing).

Electrical Tests
The integrity of the magnet instrumentation (voltage taps, thermometers) and electrical insulation has to be checked regularly to guarantee safety operation. These are typically performed after magnet reception, installing the magnet on the test bench, cool down, magnet training and warm up.
The Insulation Test of each electrical circuit versus ground and between independent electrical circuits has to be performed if there is a mechanical contact between them. An insulation test has to be performed after each step which can affect the insulation quality; at least after completion of each stage. General measurement method is the high voltage DC test.
The Resistance and Inductance Tests have to be performed after each step which changes the electrical configuration of the circuit and after any action which can affect the insulation of the circuit. General measurement methods are DC resistance measurement, AC impedance measurement, and high voltage discharge test
The Continuity and Instrumentation Tests has to be performed after each step which can affect the mechanical and electrical integrity of the electrical circuit (magnet and sensors). Especially the instrumentation has to be checked after each step involving mechanical or thermal contraction. The DC resistance measurements (or voltage drop) on the circuit allow detecting possible broken connections (instrumentation).
The Quench Heaters Tests has to be performed for all magnets equipped with quench heaters. Some of the SIS100 quadrupole (6) are equipped with quench heaters.
Quench heaters have to be powered after each action which can affect the integrity of its circuits (after QH installation, cryostating and installation on the test bench). The voltage and current of the Quench Heater Test must correspond to defined patterns. These guarantee proper QH performance and assert that the QH will release sufficient amount of energy to warm up the magnet during the quench.

Vacuum and Leakage Tests
The leakage of the cryostat has to be tested and has to show a leak rate better than 10^{-8} mbar/s. Also all helium process lines should have a leak rate better than 10^{-8} mbar/s. The helium process volumes will be checked with a pressure 1.4 times higher than the design pressure.

Cold Magnetic Measurements
Cold magnetic measurements are performed with the magnet at operating (cryogenic) temperatures while the measuring equipment is working at room temperature. Anti-cryostats are inserted in magnets with a cold bore (the SIS 100, SIS 300 and HESR magnets), wherein the measurement equipment is placed. The use of a non-metallic anti-cryostat is preferred over a metallic warm bore (e.g. used for LHC series measurements) to avoid additional eddy current losses in fast-ramped magnets, which also affect the quality of the measurement. For other magnet types only the coils are housed in a cryostat, the iron of the pole shoes and the bore is at

room temperature. The quantities to be measured are listed in section 2.4.17.1. However, in addition the time dependence of the multipoles has to be measured.

The cold magnetic measurements are performed by operating the magnet at 4 K while the measuring equipment is working at room temperature. Four methods were selected for the various superconducting magnet types [111]:

- Mole based approach for magnets operated at cryogenic temperatures: A mole is a rotating coil probe based magnetometer, where the main auxiliary components (the motor, the inclinometer and the angular encoder) form an entity (see Figure 2.4-159) able to operate in high magnetic field.
- Search coils for bent dipole magnets, or magnets with warm iron and a warm bore (Super- FRS dipoles).
- Rotating coils for quadrupole and corrector magnets with a warm bore: These instruments differ from the mole as only the coil probe itself is exposed to the magnetic field.
- Stretched wire measurement for quadrupole or corrector magnet types, which are fabricated in small numbers. The stretched wire is versatile equipment and can cover the whole aperture of nearly any magnet (see Figure 2.4-1).

Thus the Super-FRS dipole magnets will be measured using search coils providing data about the main field strength and the field homogeneity. The axis and angle will be provided by the pole shoes. The quadrupoles and correctors will be measured using rotating coils (see also Table 2.4-48). Both methods have been applied frequently at GSI in the past [112,113]. If the rotating coil cannot cover the whole field region due to the pole shoes, an additional stretched wire measurement can assert the quality there. The SIS 100 and SIS 300 magnets are supposed to be measured using the mole (see also Figure 2.4-159 and Figure 2.4-161). The latter types are of cylindrical aperture and thus the advantages of a rotating coil based method are evident. Considering the overall length of a magnet mounted in its cryostat on a test bench, which will be in the order of about 6 m, the mole based approach is favoured over the pure rotating coil approach here [111].
The mole will be placed sequentially at different lateral positions to cover the whole area, and the field quality can be derived from these measurements [114].
Although search coils seem to be more appropriate for the rectangular apertures of SIS100 dipoles, the use of the modular mole ready for testing the other superconducting magnets is preferred as it can also measure the field direction of the main field and the higher order multipoles of the dipole. Different lateral measurement will then need to be combined to a single set of harmonics [115,116]. A dedicated search coil will be used to cross-check the integral dipole strength measured by the mole.

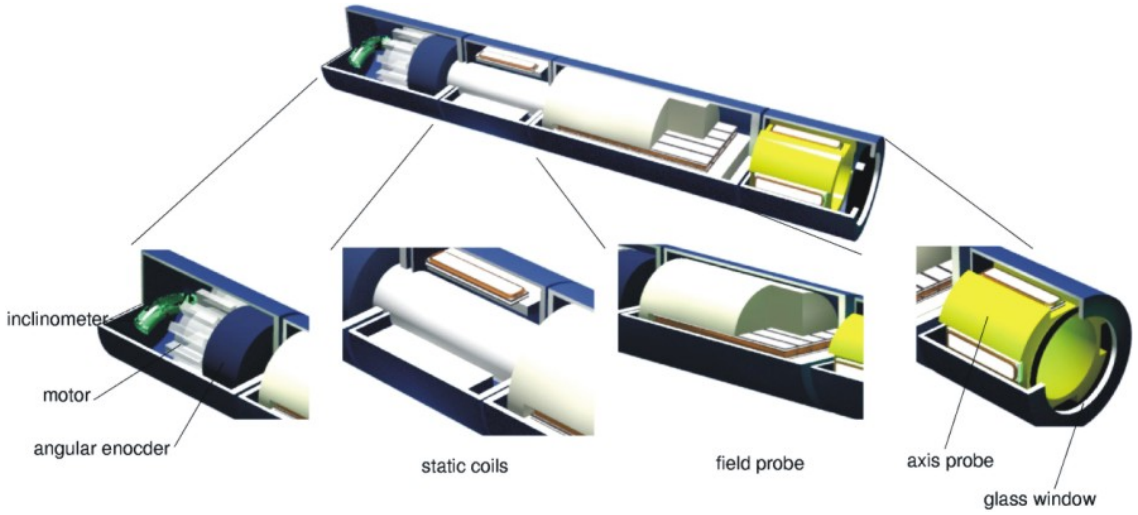

Figure 2.4-159*:* Sketch of the modular magnetic measurement system. This system is based on a "mole". On top a measurement device as used for a standard measurement is shown. It consists of a driving unit, a field probe, and a probe for searching the axis. The driving unit contains the motor, the angular encoder, and the inclinometer. The field and axis probes contain the field and axis coils, respectively. On the right side the glass window completes the device. In the mid of the coil a retro-reflector is mounted. The dynamic effects of the field are measured ramp by ramp.

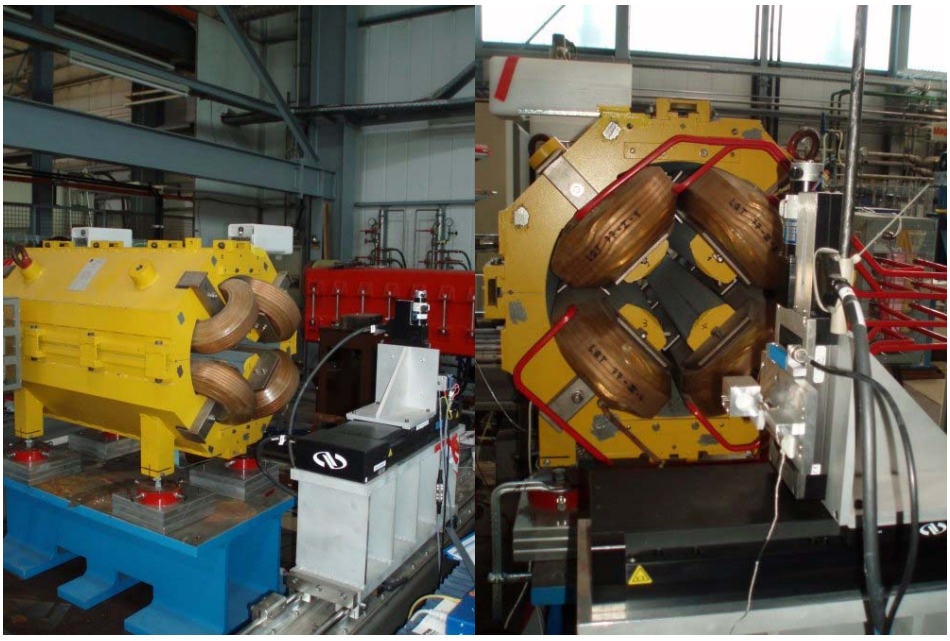

Figure 2.4-160*:* Photograph of the single stretched wire system (Courtesy of F. Klos). One can see the two stages (left side: front, right side: back) set up to measure a conventional quadrupole.

Table 2.4-48*:* Magnetic measurement systems applied to the magnets of the various machines at operating conditions.

a) dipoles

	field strength	field direction	field homogeneity	centre
SIS 300				
			mole	
SIS 100				
Super-FRS	search coil	pole shoes	search coil	pole shoes

b) quadrupoles

	field strength	axis	field direction	field homogeneity
SIS 300				
			mole	
SIS 100				
Super-FRS multiplets		adapted rotating coil system		

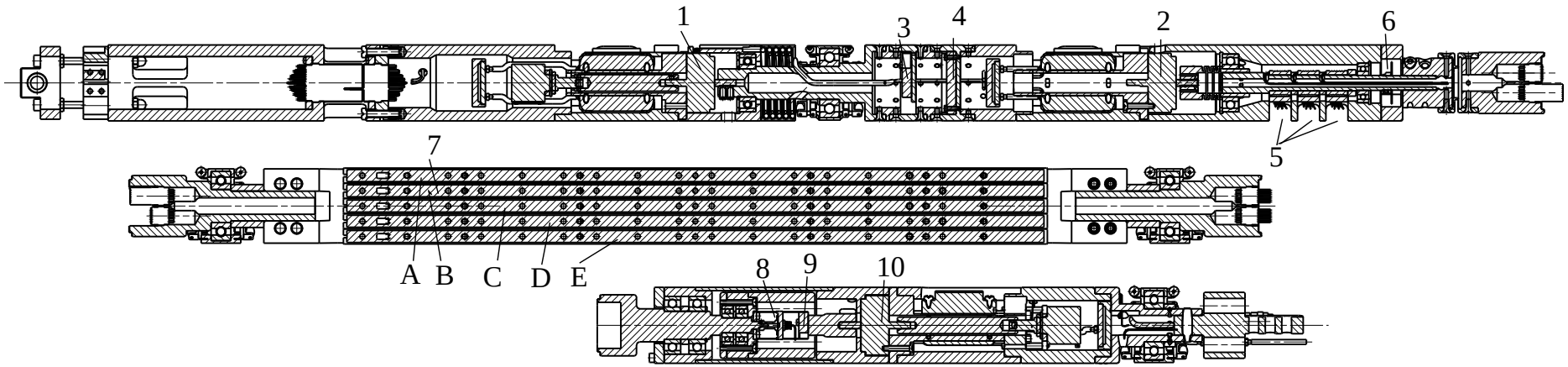

Figure 2.4-161*:* The different modules of the mole. On top is the motor unit, followed by the field coil probe and the precision encoder unit. The levelling piezo motor 1, the coil rotation piezo motor 2, the inclinometers 3 and 4, the slip rings 5, the angular encoder with 512 marks 6, the coil probes 7, the angular encoder with 7500 counts 8, its inclinometer 9 and levelling motor 10. A ... E the different coils of the probe.

The field properties listed in section 2.4.17.1 have to be measured for all superconducting magnets. Besides this the dynamic behaviour of the magnetic field of all fast-ramped superconducting magnets during ramping must be measured. These so-called dynamic measurements will be carried out ramp by ramp, i.e. the coil will be placed at a certain angular position and the magnet will be ramped up and down and the induced signal will be measured. Then the coil will step to the next angular position and the measurement will be repeated, and so on. After the loop is finished, all multipoles can be computed from these data. In this case the power converter's reproducibility must be good enough to guarantee the necessary accuracy for this measurement procedure [117]. Therefore the static reference coil of the mole (see Figure 2.4-159) is used to check the power converter's ramp-to-ramp reproducibility. As an alternative method a probe with many coils (in the order of 16) mounted on a cylindrical surface can be fabricated [118,119]. The different required systems are given in Table 2.4-49 and Table 2.4-50.

Table 2.4-49*:* Magnetic measurement systems for the different machines for measuring the main dipoles.

machine	system	main dimension	comments
Super FRS	search coil	curvature: 12.5 m	separator magnets
	search coil	curvature: 4.35 m	Energy Buncher magnets
SIS 100	mole	coil radius 22.5 mm	
	search coil	curvature 52.5 m	for cross checks of the integral length and angle
	single stretched wire		only applicable if rectangular anticryostat will be available
SIS 300	mole	coil radius 30 mm	
	search coil	curvature 52.5 m	for cross checks of the integral length

Table 2.4-50*:* Magnetic measurement systems for the different machines for measuring the quadrupoles and higher order multipoles.

machine	system	coil radius [mm]	comments
Super FRS	adapted rotating coil	175	
	single stretched wire		for cross checks of angle, axis, integral gradient
SIS 100	mole	coil radius 22.5	
	single stretched wire		for cross checks of angle, axis, integral gradient
SIS 300	mole	coil radius 30	
	single stretched wire		for cross checks of angle, axis, integral gradient

2.4.17.3.3 Test Facility for Superconducting Magnets

The series production of the superconducting magnets of Super-FRS, SIS100, SIS300 will be performed in the "Series Test Facility" next to the string tests for SIS100 and SIS 300. Additionally, Super-FRS magnets not conforming to the specifications will be investigated there.
The Series Test Facility is present in Figure 2.4-162. It consists of 1 special test bench for the "String Test", 2 test benches for Super-FRS magnets and 4 test benches for SIS100 and SIS300 magnets. The assumption is that SIS300 magnet will be tested (and produced) after SIS100 magnets. The test benches first used for SIS 100 magnets need to be modified for testing SIS300 magnets [120].
The already existing "Prototype Test Facility" will be dedicated to investigations of the non-conforming SIS100 and SIS300 magnets, and corrector testing. This facility has to be reconstructed and reorganized for this task [121].
Non-conformant magnets requiring an extended test will be tested at the PTF. In that case each magnet has to be dismounted from the test bench and rein-stalled in the PTF, which is time consuming.

The following space and logistics are required for the Series Test Facility:

- test hall 3800m^2,
- minimum 1000m^2 outside storage area close to test hall,
- 300m^2 for additional constructions or additional buildings for power transformers and compressor,
- 50 tons crane for Super-FRS triplets,
- mobile crane for outside storage area,

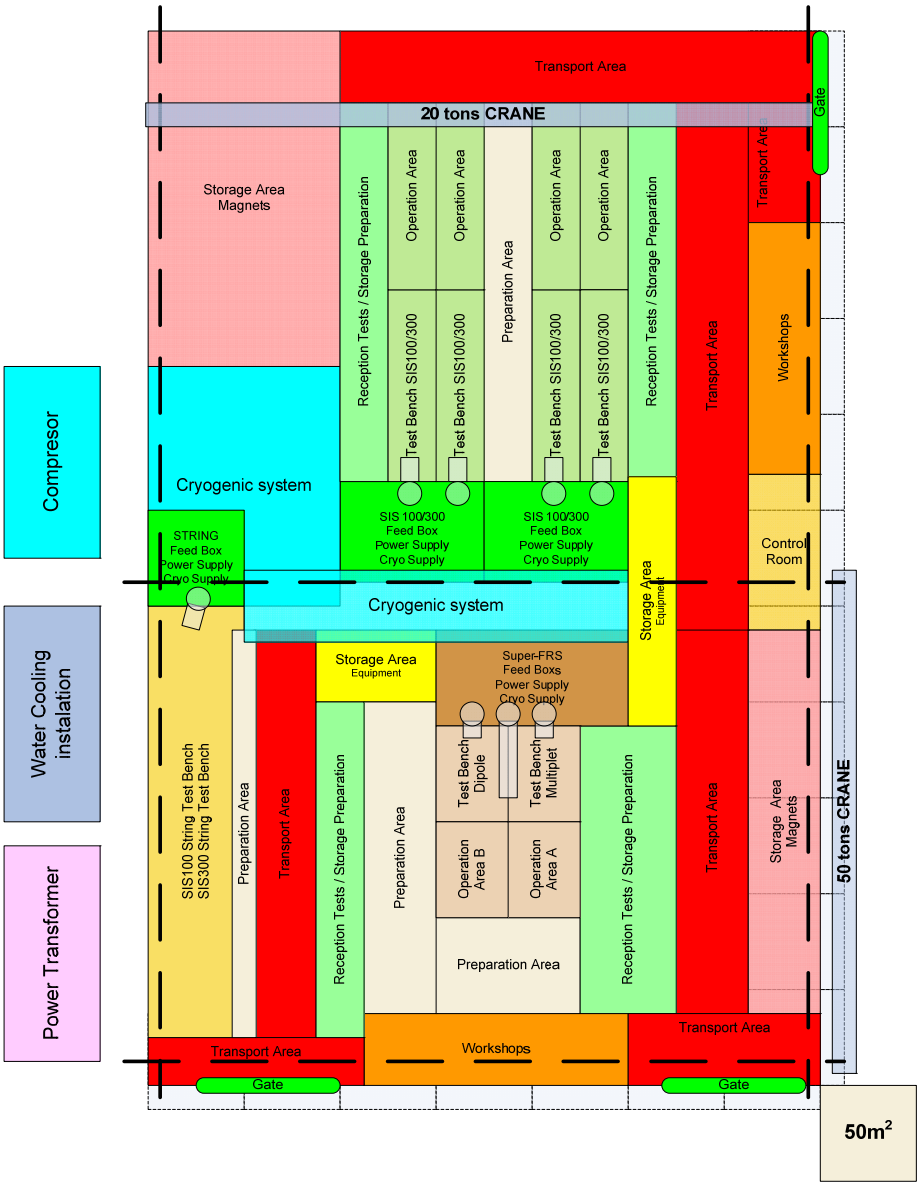

Figure 2.4-162*:* Schematic view of the test facility: benches for single magnets and for string tests.

Cryogenic Supply

All test benches for superconducting magnets will be supplied with helium by a refrigerator named "CryoST" as described in section 2.4.16.2.1.

- *Refrigerator*
  - The refrigerator capacity and cold helium piping to the magnet feedboxes will be provided by the cryogenics group. The test benches will be supplied with a 4 K (3 bar) and a 50 K supply line, and with a 4 K (≤1 bar to allow Temperatures ≤ 4 K, if necessary), an 80 K and a 300 K return line.
  - We assume that a refrigeration power of about 1700 W@4.4 K and 2000 W@50-80 K are required for standard operation of the test facility.
  - A liquefaction power of 5 g/s liquid helium is required for cooling the current leads.

- *Transfer lines*
    - To supply the magnet feedboxes with helium @ 4K, 3 m flexible, vacuum insulated, double coaxial lines for forward and return flow are necessary for each feed box.
    - To supply shield cooling @ 50K, two 3 m flexible, vacuum insulated, single coaxial lines are necessary for each feed box, and
    - a fixed multiple distribution line

- *Feedboxes* – each box contains the following components:
    - support for an anti-cryostat
    - cold Coriolis mass flow meters (max. 5g/s for SIS100; max. 200g/s for SIS300)
    - current leads for main magnets and correctors
    - helium supply (forward and return)
    - 4 temperature and 4 pressure sensors
    - temperature control units for the current leads and for the anti-cryostat
    - The feedboxes for the SIS100-type magnets have to be equipped with a Joule-Thomson expansion valve to produce two-phase helium.

Power Converters
For magnetic measurements of Super-FRS dipole and multiplet magnets a switch mode power converter with a rated load current of 1000A and a maximum load voltage of 400V will be installed. These will have to provide a current stablity of better than 10^{-4}. A switch mode power converter with a rated load current of 500A and a maximum load voltage of 400V will be foreseen to measure Super-FRS correctors.

Quench Detection and Magnet Protection

Although most single magnets (except SIS300 dipole and quadrupole) are self-protecting, a protection system allows minimizing the recovery time (necessary for cool down) after a quench occurred due to the possibility of energy extraction. The voltage taps are isolated wires soldered to the magnet cable. Voltage differences between two symmetric coil parts of the magnet are measured. In addition an unbalanced current through a centre tap is measured. The scheme of functionality is shown in Figure 2.4-163. The main components are the separated voltage detection, the security matrix for safety actions and triggering the data acquisition, and a data acquisition system for storage. The security matrix triggers the following safety actions:

- switch off the power converter which will switch a dump resistor into the coil circuit for energy extraction
- open the active quench valve in the feedbox
- activate the quench heaters for magnets, if applicable (6 quadrupoles)

The planned test facility is based on the setup of a Prototype Test Facility which is ready for operation since 2006 [121]. Due to large number of magnets a fully automated operation of the whole test facility is necessary to achieve the required throughput.

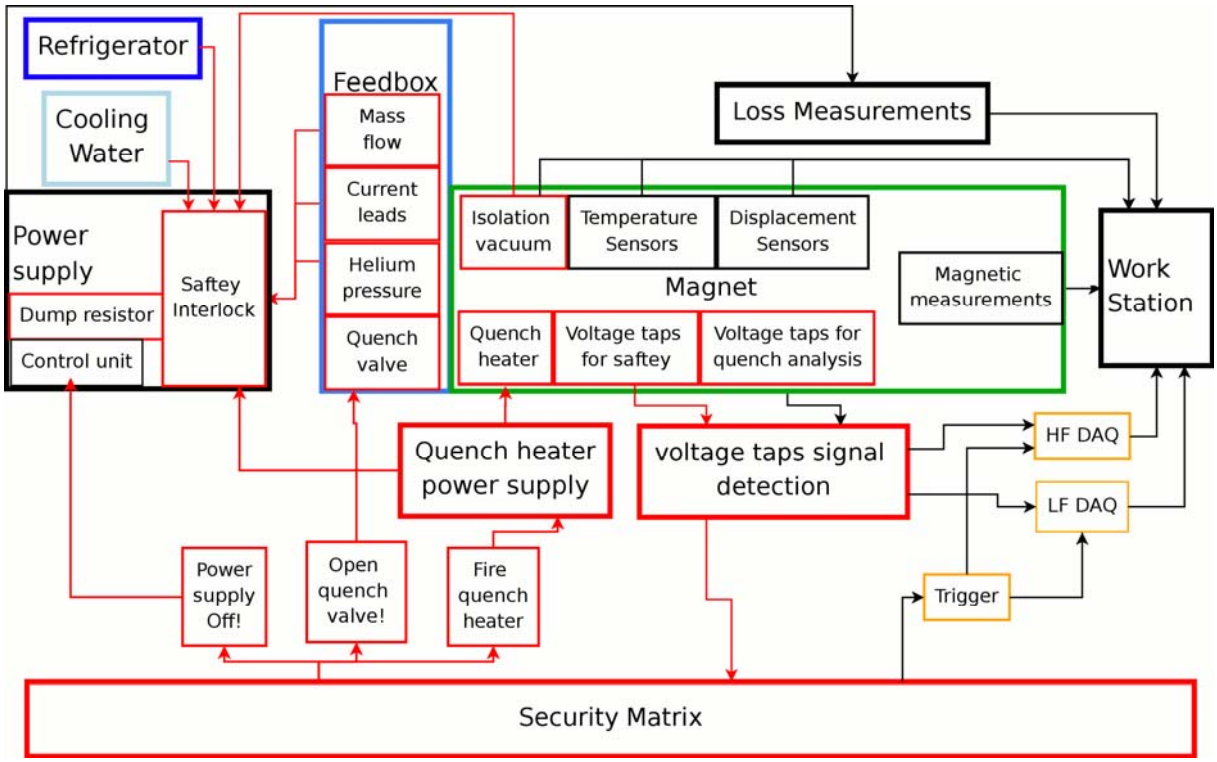

Figure 2.4-163*:* Scheme of the functionality of the series test facility for superconducting magnets. The blue parts show cooling sources. Security related devices and communication channels are given in red. Arrows show the flow of various signals. On the left the cryogenic supply, cooling water and electrical power supply are shown. The power supply provides a safety interlock, a dump resistor and its control unit. The feedbox is equipped with various equipments: current leads, quench valves, mass flow meters, and helium pressure sensors. The isolation vacuum of the cryostat is monitored. The magnet is equipped with temperature sensors and displacement sensors. Voltage taps allow supervising the voltage drop on the magnet coils. Dedicated electronics treat the signal of these taps and generates triggers in case a quench has occurred (security matrix). These triggers shut down the power supply, open the quench valves and fire the magnet's quench heaters (only in case of SIS 300 magnets). The data acquisition systems allow studying the origin of the quench. Loss measurements are performed using digital volt meters. Abbreviations: DAQ: data acquisition, HF: high frequency, LF: low frequency.

2.4.17.3.4 String Tests

There will be no string test for the Super-FRS.

2.4.17.3.5 Schedule

The previous sections listed the different tasks and the various devices to conduct the different measurements. Table 2.4-51 lists the number of magnets per type and summarizes them for the various stages.

Table 2.4-51*:* Number of superconducting magnet per type. The number of dipoles, quadrupoles and other magnets are listed per type. The type is named after the machine the magnet is used for.

	Dipole unit	Quadrupole unit	Correctors	Steering Magnet	Chromaticity Hexapole	Resonance Hexapole	Septa
cos θ							
SIS 300	67	102	12***	78****	24	12	1
Superferric							
SIS 100	109	86*	12***	84****	48	-	-
Super-FRS	28	28**	32	12	36	-	-
total	204	216	56	174	108	12	1

* SIS100 Doublet Quadrupole
** Super-FRS Triplet
*** Error compensation multipole corrector - quadrupole, hexapole and octupole nested.
**** Horizontal and vertical dipole nested.

Expected measurement time required for the different tasks

All estimates concerning the installation, cool-down, measurement, and warm-up periods are presently based on the experiences of other laboratories, i.e. series tests of HERA (DESY) and of LHC (CERN), on the experience of our collaboration partners and miniTAC expert meeting organized in May 2007 at GSI [122,123,124,125].

To estimate the time required for the tests the following assumption were made:

- total testing time is 47 weeks per year,
- shut-down time is 4 weeks for reparation and 1 week of the end year holiday,
- efficiency of each double test bench is 75%,
- cryogenic and test operators will work in 3 shifts and 7 days,
- preparation and installation team will work in 2 shifts and 7 days – this can cause 8 hours of delay during installation and disconnection (see Table 2.4-52),
- 2 test benches for Super-FRS and 4 test benches for SIS100/SIS300
- no additional delay due to logistic problems – sufficient storage and preparation areas, and proper cranes,
- all test benches are ready on time for testing (preparation period is around 1 year and in addition the commissioning period is around 2 years for the Series Test Facility),
- corrector are powered – some fraction of correctors will be tested magnetically during series test of magnets
- all correctors have to be tested separately before installation into the superconducting unit (powering and magnetic measurements); proper power supply will be installed to assure high quality of magnetic measurement (no switching mode power supply),
- test benches of SIS100 are upgraded for testing SIS300 after SIS100 testing campaign is finish,
- the series production will start after finishing the string test and approval of all design
- string SIS300 will be built after the SIS100 string test is finished

The final time estimate is based on the remarks from experts. Because the time required for the series productions for FAIR are relatively short in comparison with CERN series productions, the testing time is increased by 50% with respect to the minimum required time for testing [126].
The assumed total measuring periods per magnet (including installation, pumping, cool-down, training, measurements, warm-up, and removal, see also Table 2.4-52) are the following:

- Super-FRS – Dipole Unit ~ 290h
- Super-FRS – Triplet Unit ~ 790h
- SIS100 – Dipole Unit ~ 210h
- SIS100 – Quadrupole Doublet Unit ~ 260h
- SIS300 – Dipole Unit ~ 210h
- SIS300 – Quadrupole Unit ~ 230h

Based on Table 2.4-51 and Table 2.4-52 the total testing times are estimated to following periods:

- Super-FRS (2 test benches, 24h/7days, 56 units) – 2.6 years
- SIS100 (4 test benches, 24h/7days, 198 units) – 2.0 years
- SIS300 (4 test benches, 24h/7days, 169 units) – 1.6 years

Table 2.4-52: Estimated testing time for each type of superconducting magnets.

	SIS100		Super-FRS		SIS300	
	Dipole Unit	Quadrupole Doublet Unit	Dipole Unit	Triplet Unit	Dipole Unit	Quadrupole Unit
Task	[h]	[h]	[h]	[h]	[h]	[h]
Delivery & Installation	24	29	40	34	24	30
Max. Delay	8	8	8	8	8	8
Pumping	30	33	33	45	30	30
Cool down 300K – 4K	45	45	60	300	45	45
Training & Testing	20	29	39	56	20	27
Magnetic Measurement	30	60	30	90	30	30
Warm-up	38	38	47	229	38	38
Max. Delay	8	8	8	8	8	8
Removal	11	13	26	22	11	13
Expected Testing Time	214	263	291	792	214	229

The testing time can be optimized by a larger number of test benches, increased number of personnel and more effective cryogenic system (if designed cooling scheme of the magnet allows faster cooling). The Figure 2.4-164 presents the time schedule for testing.

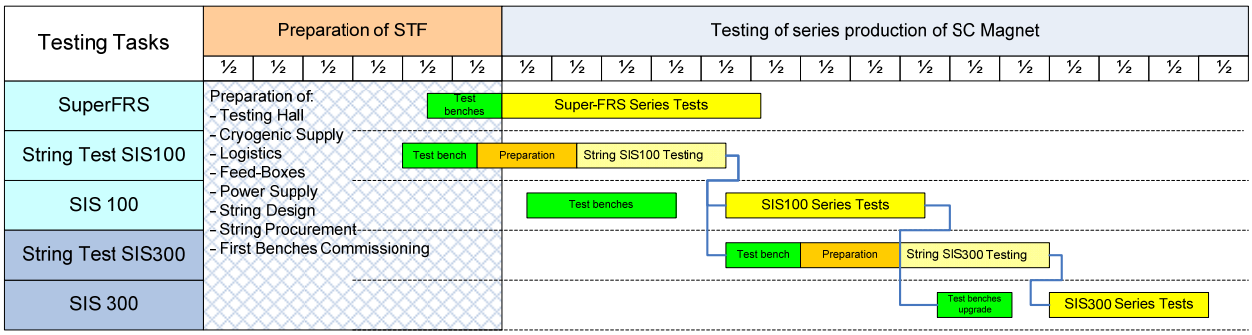

Figure 2.4-164: Expected schedule for testing of superconducting magnets.

2.4.17.4 Reference Magnets

There will be no reference magnets for Super-FRS.

2.4.18 Safety

2.4.18.1 Interlock system

The general procedure for high intensity beam operation is to adjust the beam at lower intensity and verify with detectors. The magnet setting is saved as a reference. The effective thickness of the target and other material in the beam line is also defined. For high intensity operation some diagnostic detectors must be removed but the conditions of SIS100/300, targets, magnets and the first degrader must stay the same. The interlock system must prevent damage and consequent delay for repairing.

2.4.18.2 Radiation environment (radiation protection)

2.4.18.2.1 General radiation protection measures

In areas open for access to technical or scientific personnel or to the general public, radiation dose limits given by the Radiation Protection Ordinance, must not be exceeded. Assuming a worst case scenario the additional annual dose for the population, arising from the operation of all facilities at the GSI site, must be less than 1 mSv, in addition the effective dose resulting from the release of radioactivity to the environment has to be smaller than 0.3 mSv/year. According to the limits of the German Radiation Protection Ordinance the dose rate should be less than 0.5 μSv/h on GSI ground and less than $\approx 8 \cdot 10^{-8}$ Sv/h outside the facility.

2.4.18.2.2 Shielding against direct radiation

The shielding of the Super-FRS has been calculated in two parts. The first part of the Pre-Separator with very strong radiation was simulated with the heavy ion transport code FLUKA [43,44].

In the production target up to 50% of the primary beam can react. But even these ions emerge from the target and the primary beam and most fragments are dumped inside the first part of the Pre-Separator, mainly in the beam catchers. For the realistic FLUKA simulation different scenarios where considered in which the beam after having passed the production target hits each beam catcher. Hitting mainly one catcher represents the worst case scenario for the nearby shielding. The cross section of the shielding around one of the beam catchers is depicted in Figure 2.4-165. A similar cross section is required in the whole first part of the Pre-Separator where the primary beam may be dumped. The effective dose rates resulting mainly from fast neutrons were calculated according to Ferrari and Pelliccioni [127].

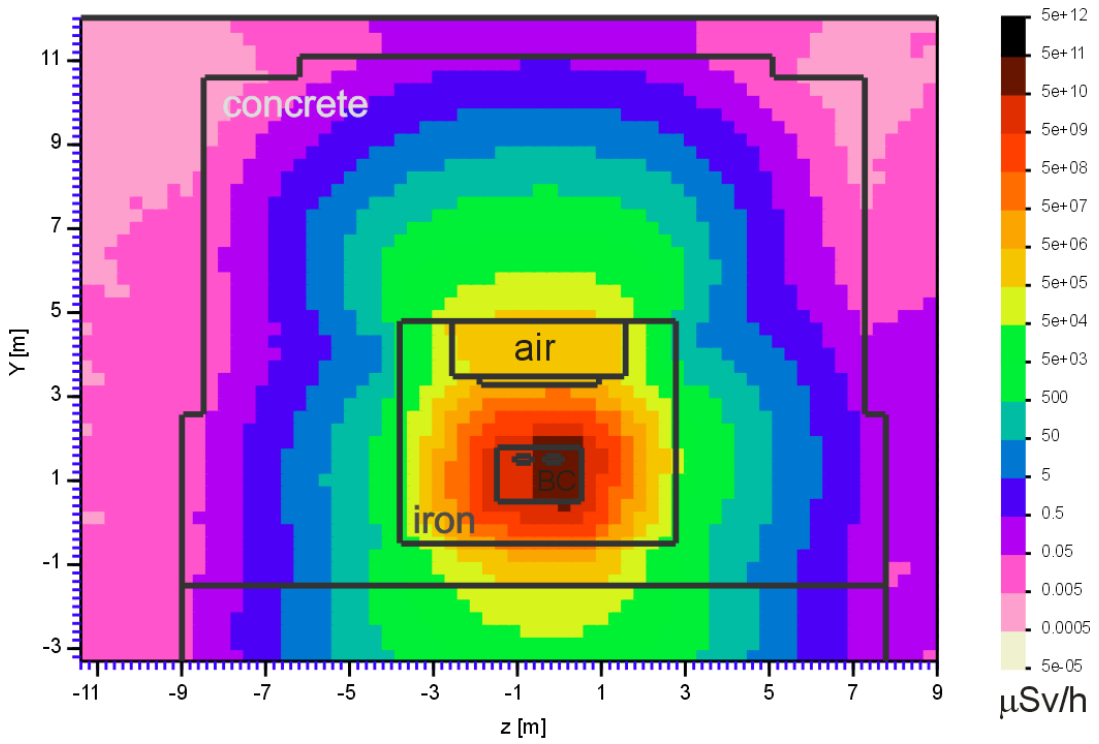

Figure 2.4-165*:* Cross section of the radiation shielding in the first part of the Pre-Separator. The result of a FLUKA simulation of the whole area shows the dose rate during highest intensity primary beam operation with 10^{12} ^{238}U/s hitting one of the beam catchers after having passed the production target. The reduction of fast neutrons by the inner iron and outer concrete shielding reduces the effective dose rates to a level below 0.5 µSv/h.

For the rest of the Super-FRS tunnel an analytical model has been developed. It is based on the measurements of double differential neutron yields originated from a 1 GeV/u uranium beam hitting a thick iron target, dose values can be estimated via the following formula:

$$H(r,\vartheta) = H_0(\vartheta) \cdot I \cdot \frac{1}{r^2} \cdot e^{-\frac{d \cdot \rho}{\lambda(\vartheta)}}$$

The dose (rate) $H(r,\vartheta)$ is derived from the angular dependent constants $H_0(\vartheta)$ and $\lambda(\vartheta)$, the density ρ of the shielding material with the thickness d and the ion rate I. The constants $H_0(\vartheta)$ and $\lambda(\vartheta)$ have been determined by Agosteo et al. [128] by fitting the results of a Monte-Carlo calculation using the measured neutron spectra mentioned above [129].
Three representative modes of the Super-FRS were investigated to cover the large variety of settings in the experimental operating:

- separation of a fragment with similar magnetic rigidity compared to the primary beam, e.g. ^{132}Sn by projectile fission of ^{238}U,
- separation of a very neutron rich fragment ^{11}Li by fragmentation of ^{18}O,
- separation a very neutron deficient fragment ^{100}Sn by fragmentation of ^{124}Xe.

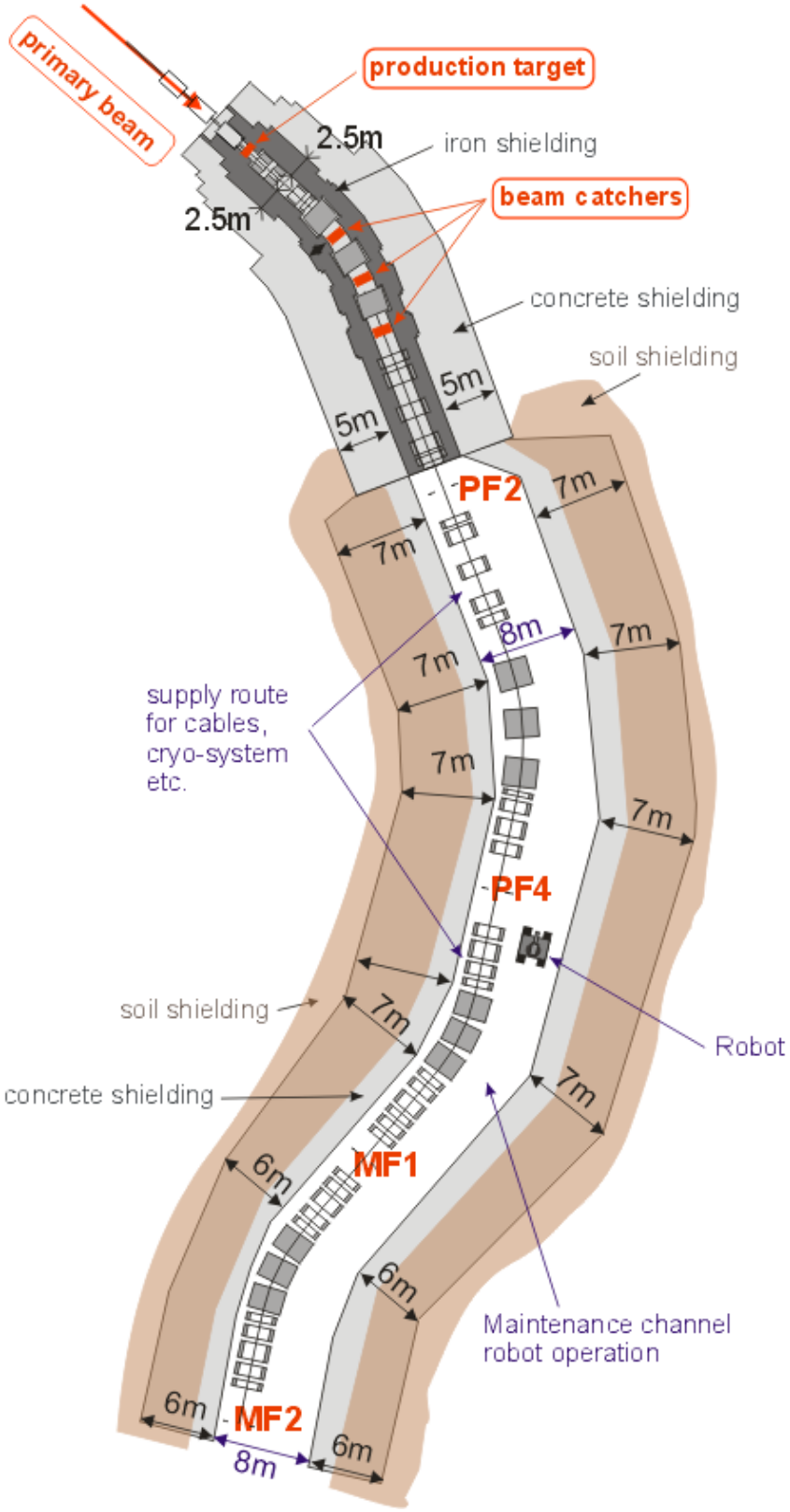

Figure 2.4-166*:* Schematic layout of the Super-FRS with beam line and shielding measures. The area from the target up to the intermediate focal plane PF2 of the Pre-Separator is shielded with iron in order to provide a compact radiation protection in the target building. The concrete in the Main-Separator can be partially replaced by soil taking into account an about 20% smaller absorption of the soil.

The distributions of the losses of fragment beams have been calculated with the fragmentation model of ABRABLA [130] and the simulation code for fragment separators Lieschen [131]. Figure 2.4-166 shows the calculated thicknesses of the concrete walls along the Super-FRS.

The thicknesses reach from ~7.0 m downstream of the target PF2 down to 6 m at the middle focal plane MF2 of the main separator. In the close vicinity of the target a compact iron shielding will be used to replace the concrete. Further on concrete will be partially replaced by soil taking into account the somewhat larger absorption length.

2.4.18.2.3 Shielding of magnets behind the target and beam catcher

The inevitable nuclear interaction in the target and the beam catcher requires special considerations on the damage of the magnetic elements. In addition also the heating due to radiation is a critical issue for the operation of superconducting magnets.

The following magnet sections deserve special investigations:

- The first quadrupole behind the target,
- The dipole magnets in the 1st Pre-Separator stage,
- The first hexapole magnet behind PF1.

The deposited energy in the coils of these magnets is calculated in the following by PHITS [5] simulations.

Quadrupole magnets behind the target

The radiation field behind the target is mainly caused by the fragments emitted in wide angles outside the acceptance of the Pre-Separator and by light secondary particles like protons and neutrons. Therefore, we have foreseen to install a (40 x 40 x 40) cm^3 iron shielding block in front of the first quadrupole magnet which stops the lighter ions and neutrons. This iron block should have an aperture just small enough to let the intense heavy ions pass. The light particles cannot be completely shielded by this iron block, therefore a detailed investigation was performed with the computer code PHITS [5]. The assumed geometry is depicted in Figure 2.4-167 and the case for 10^{12} ^{238}U ions at 1500 MeV/u impinging on a 4 g/cm^2 carbon target is simulated.

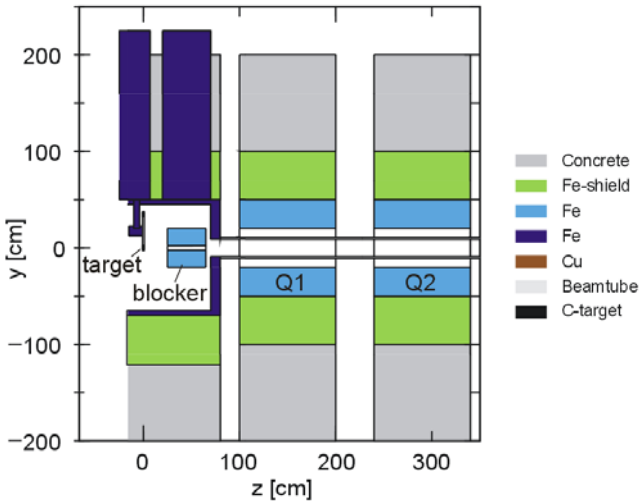

Figure 2.4-167*:* An iron beam block behind the target wheel shields the subsequent quadrupole magnets Q1 and Q2.

Figure 2.4-168 shows the heating of the iron block per incident uranium ion. The total power deposited can reach 2 kW which would exceed the performance of a practical cryogenic system. Critical are the coils of the subsequent magnets especially in case of superconducting magnets. The heating must stay below a quench limit of about 1 mJ/g. In the simulation a pure copper conductor was used because the Nb/Ti part is only a small fraction. A detailed plot of the deposited energy at the entrance of the quadrupole magnets is given in Figure 2.4-169. Note that 1 MeV/cm^3 per incident ion corresponds to 18 mJ/g for 10^{12} ions in copper.

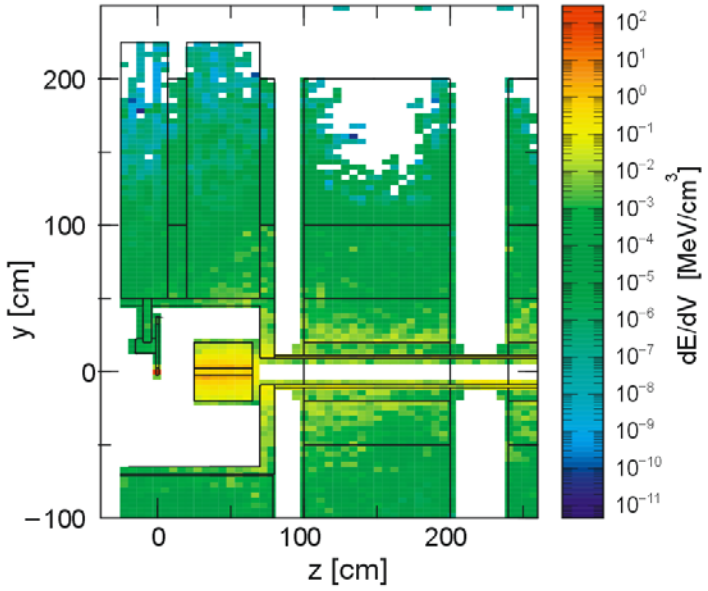

Figure 2.4-168: **Calculated (PHITS code [5])** energy deposition per primary 1.5 GeV/u uranium ion impinging on the 4 g/cm2 C target. The primary beam and fragments pass through the gap in the shielding block.

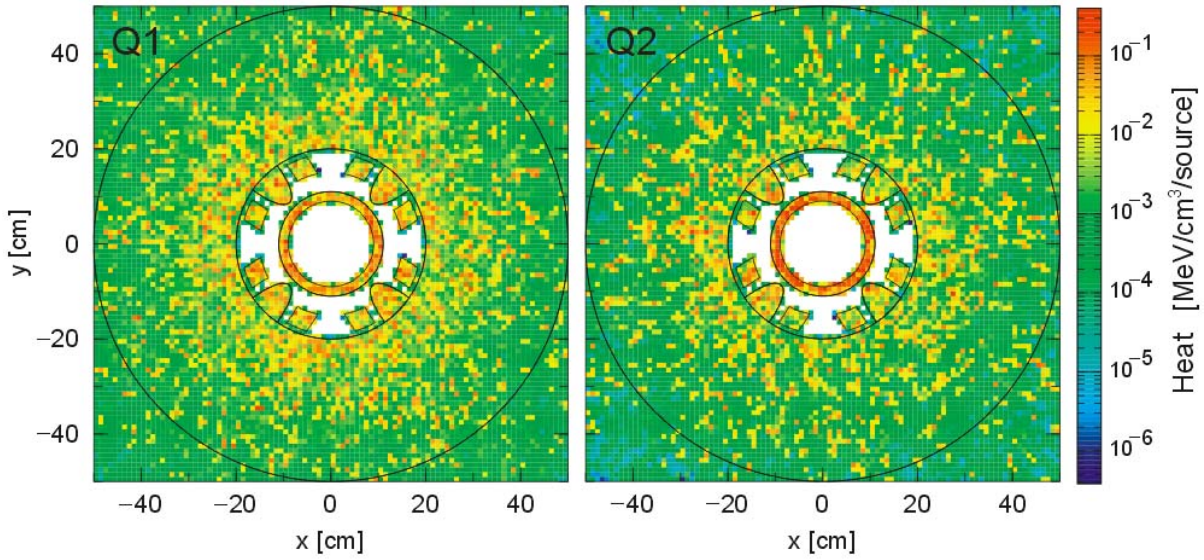

Figure 2.4-169: **Calculated (PHITS code [5]) energy d**eposition per primary uranium ion at the entrance of the first (left) and second (right) quadrupole magnet behind the 4 g/cm^2 carbon target.

The maximal energy density deposited by one spill in a part of the coil of the first quadrupole magnet is 0.0256 MeV/cm^3 per incident ion or 0.46 mJ/g for 10^{12} ions. The calculation was performed for the case of a 1500 MeV/u uranium beam impinging on a 4 g/cm^2 target. This

value is below the quench limit but the total power deposited exceeds the practical limit for a cryo system.

Hexapole behind the beam catcher at PF1:

At the beam catcher positions at BC1, BC2 and PF1 the full primary beam can be dumped. Much thicker shielding is therefore required than in the target area. The simulation using PHITS showed that 80 cm of iron is suited to suppress the neutron flux sufficiently. The geometry investigated is shown in Figure 2.4-170. Here, the graphite part had an inclined surface to increase the range straggling and thus the energy-loss density in the bulk material is substantially reduced. Critical for the exposure are the coils of the following hexapole magnet.

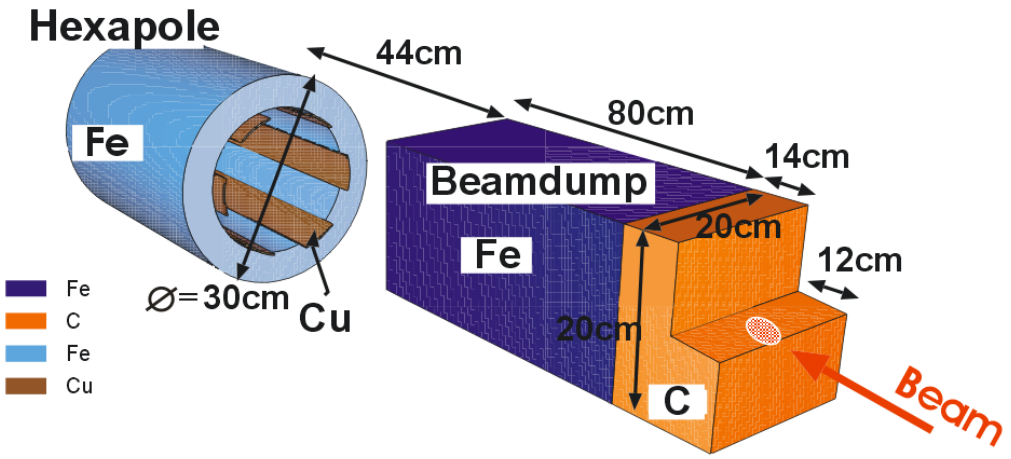

Figure 2.4-170*:* Geometry of the beam catcher in front of the hexapole magnet at PF1 used in the PHITS calculation.

In a side view the flux of protons and neutrons is shown in Figure 2.4-171 and Figure 2.4-172. Whereas the uranium ions are stopped in the graphite, an intense beam of protons deeply penetrates into the iron. Outside of the beam catcher the radiation is dominated by neutrons scattered in a wide distribution onto the hexapole magnet.

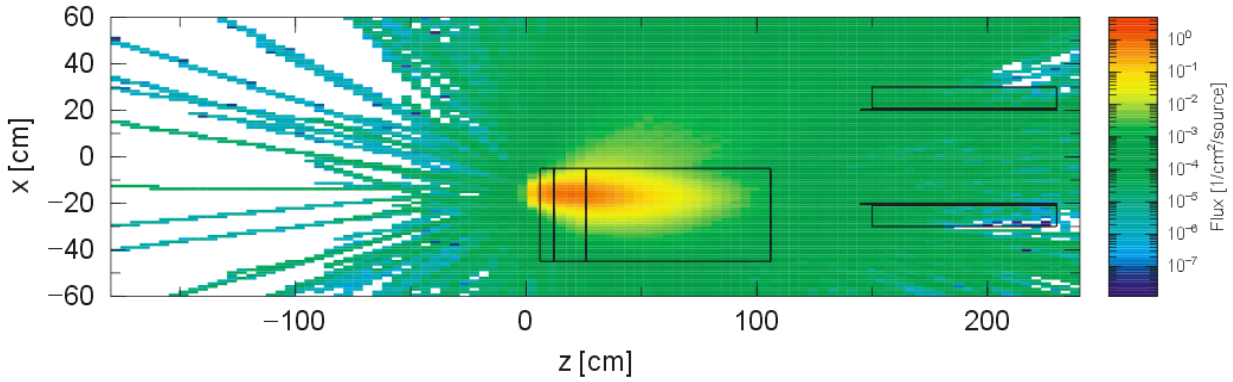

Figure 2.4-171*:* **Calculated (PHITS code [5])** fluence of protons per incident ^{238}U ion at 1500 MeV/u in the beam catcher area at PF1.

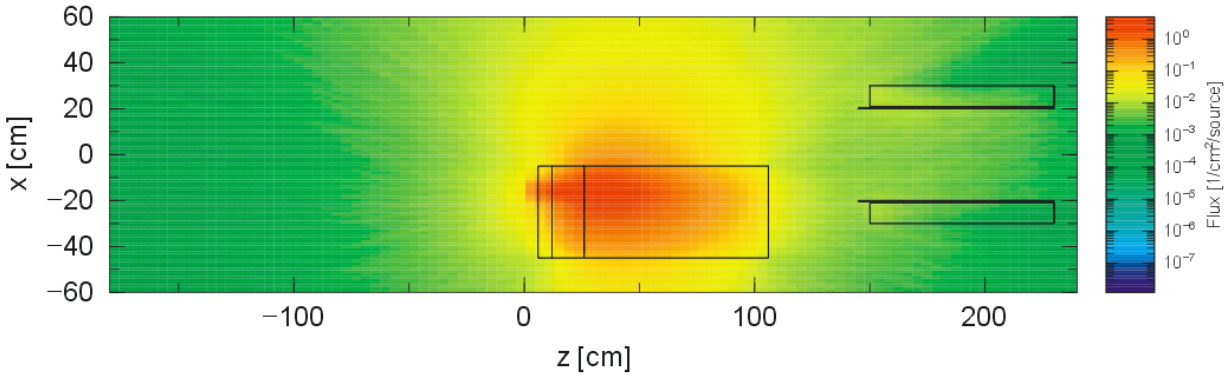

Figure 2.4-172: **Calculated (PHITS code [5]) f**Fluence of neutrons per incident ^{238}U ion at 1500 MeV/u in the beam catcher area at PF1.

The maximum deposited energy density in the coil in the direction of the incident primary beam of 0.045 MeV/cm^3 corresponds to 0.81 mJ/g for 10^{12} uranium ions.

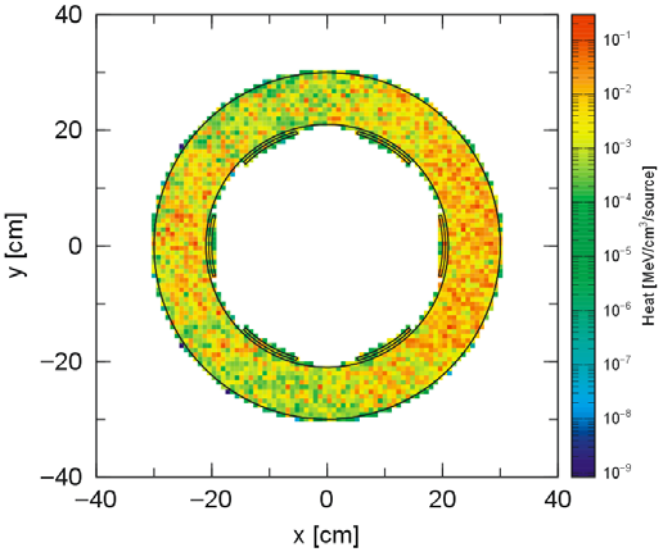

Figure 2.4-173: **Calculated (PHITS code [5])** energy deposition in the hexapole magnet behind PF1. The outer thick ring represents the iron part and the six small layers the coils of the hexapole magnet.

The results for the beam catchers between the dipole magnets (BC1 and BC2) are similar to the ones at PF1 as the same thickness of the beam catcher can be used. The situation for the dipole magnet is in general less critical because the coils are not positioned in the same plane as the beam.

2.4.18.2.4 Activation of beam line parts

Many parts of the Super-FRS can be activated, especially in the Pre-Separator up to PF1. In the FLUKA simulation a cycle of four times irradiation at highest uranium intensity of 90 days with subsequent cooling time of 120 days was investigated. In the first part of the calculation the nuclides were produced and in the second part the radiation from activation is shielded by the matter in the same realistic geometry. From the radiation reaching the outside of the material blocks the effective dose rates from activation were calculated according to the dose conversion coefficients of the INPC [132].

Figure 2.4-174 shows the resulting dose rates in a vertical cross section around the beam catcher. As already described the iron part of the beam catcher is activated most. As only a

small part of the beam reacts in the target the neutron flux above the target is much lower than at corresponding positions above the catcher and so is the activation.

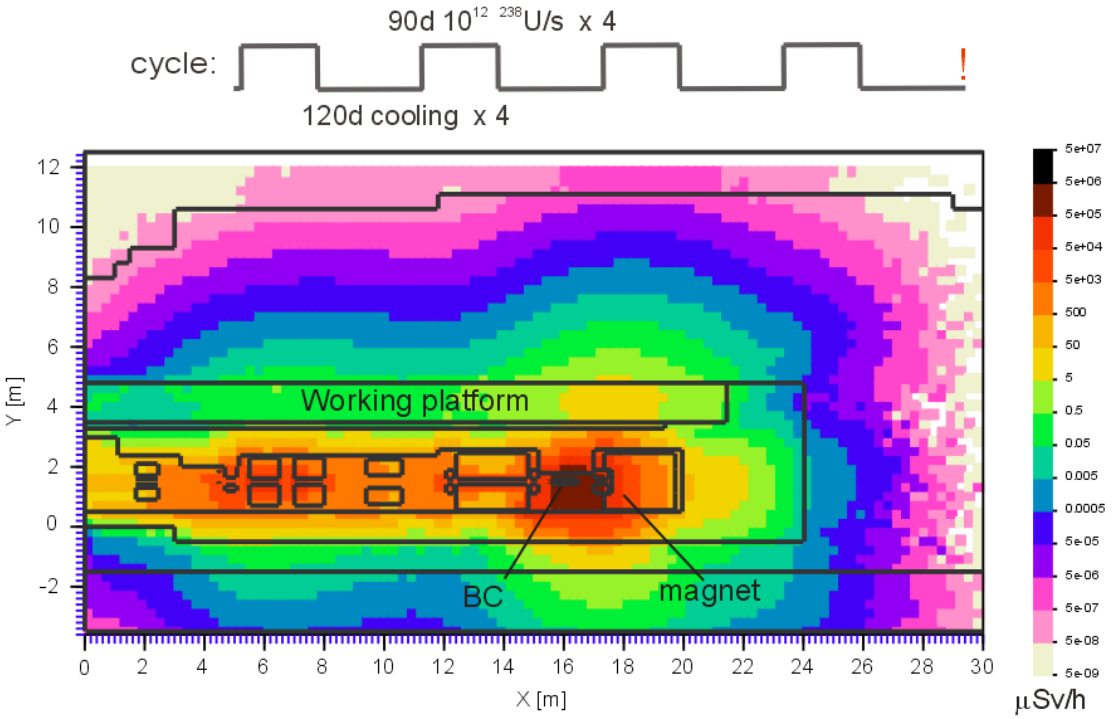

Figure 2.4-174*:* Cut through the area around the beam catcher BC1 where the primary beam is dumped after having passed the target. FLUKA simulation of the effective dose rate from activation after a cycle of four times irradiation at highest intensity of 90 days with subsequent cooling time of 120 days is shown. Whereas at the beam catcher the dose rate goes up to 5 Sv/h the level on the working platform reaches about 10 µSv/h at maximum.

For the important part of the working platform the older simulation using PHITS [5] shows consistent results: In the concrete close to the maintenances channel on top of the target or beam catcher ^{7}Be, ^{22}Na and ^{24}Na are the most important nuclides for activation. After continuous irradiation over 100 days with 1500 MeV/u 10^{12}/s uranium ions and one day of waiting the activity here reaches 160 Bq/cm^3. As the strongest contribution ^{24}Na is rather short lived ($T_{1/2}$ = 15 h) this value is reduced after 7 days to 30 Bq/cm^3. The corresponding integrated dose rates at a distance of 50 cm above the concrete are 8 µSv/h or 2 µSv/h, respectively. The values are slightly lower as the floor was considered to be concrete and not iron.
At PSI maintenance is carried out at the corresponding position with dose rates up to 100 µSv/h. As a conclusion the maintenance channel on top of the beam line from target to PF1 is accessible even after very long irradiation after a few days usually after one day of waiting. This is a reasonable time scale as anyway the concrete shielding on top has to be removed first. It also means that a plug with shielding as long as 200 cm is sufficient.
The highly activated parts like beam catcher and target including the shielding plug can then be pulled into a shielding bottle like the one shown in Figure 2.4-176 used at a corresponding position at PSI. While the concrete shielding is removed the hall has to be an area of controlled access for radiation protection. But as the radiation level is rather low it is also clear that with the help of the shielding bottle the radiation level outside the hall cannot exceed the limit of 0.08 µSv/h explained above. A hot cell is foreseen to store activated components, inside manipulators will be used to exchange parts, for example to mount a new target wheel.

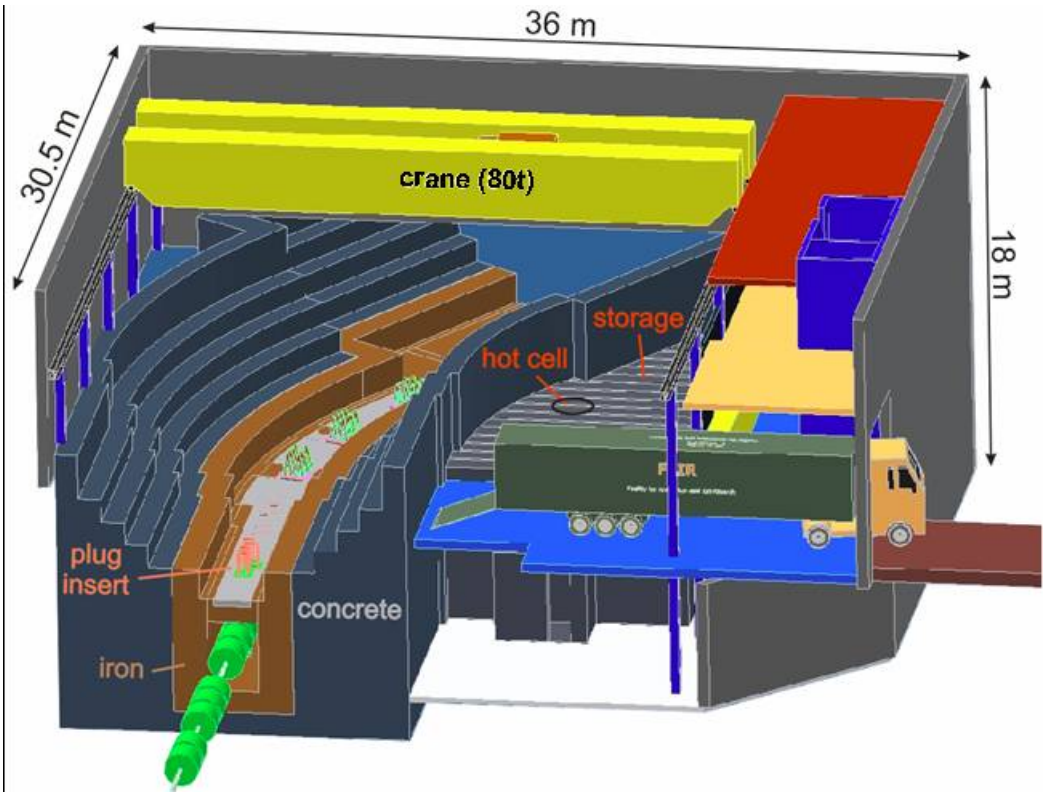

Figure 2.4-175*:* Layout of the Super-FRS target building. The top part of the concrete shielding can be removed to access the working platform. Heavy devices can be transported by crane to the nearby hot cell, storage places or directly onto a truck which can drive into the hall.

A typical value to still allow hands-on maintenance is 1 W/m for the beam power deposited by a 1 GeV proton beam along the beam line [133]. This value can be scaled to a heavy ion beam considering the shorter range and nuclear fragmentation [134]. As already described in section 2.4.11.1 the beam catcher will be the most activated part as it catches almost the full beam power of 40 kW. At 1 GeV/u the factor for comparing protons with uranium ions is still 0.2, which means an equivalent of 10 kW/m proton beam at the beam catcher, which forbids maintenance by people but robots can be used.

Figure 2.4-176*:* Radiation shielding bottle at PSI [65] to move activated parts to a hot cell. The whole plug is pulled into the bottle which is then transported with a crane.

The activation of the preceding and following dipole magnet is also shown in Figure 2.4-174. The activation there is much lower than that of the iron in the beam catcher. Still human access is not possible. But all cable connections can be removed from the working platform and the magnet separated into at least two pieces can be hooked to the crane and moved. This case presents the worst case accident for the machine; however, all devices are designed not to fail during their lifetime. Still this case can be managed when declaring the entire target hall a closed area and installing additional shielding where to store the magnet pieces.
The values are much reduced in the Main-Separator. A factor 1000 times lower beam intensity and more distributed beam catcher lead to about 1 W/m. Still, allowing 10^9 Uranium ions at 1 GeV/u to pass through the whole Main-Separator is equivalent to the uranium primary beam rate nowadays at the FRS ($2 \cdot 10^9$/spill as in 2004) even about a factor 5 higher due to the higher repetition rate. The FRS target area cannot be accessed directly during experiments and stays as an area with controlled access most of the time.

2.4.18.2.5 Activation of air

Activation of air can lead to exposition of personnel if areas with previous beam operation have to be entered. This exposition can be substantially reduced by applying a ventilation system in areas under consideration. However the outlet air of these areas may again lead to exposition of population and personnel. Hadronic or heavy ion beams in the energy range of 1 GeV/u pro-

duce a variety of radioactive isotopes while passing through air. Short-lived positron emitters like ^{11}C, ^{13}N, ^{14}O and ^{15}O are being produced due to spallation reactions. ^{7}Be and ^{32}P which have lifetimes in the order of weeks, play an important role in activation of air.
Longer lived beta-emitters like ^{3}H and ^{14}C are expected to be produced as well in substantial quantities. Finally, ^{41}Ar can be produced by capturing thermal or slow neutrons by the noble gas argon. It is important to reduce the path length of the neutrons in the air to reduce the activation process in air. A fully encapsulated target area is planned to effectively reduce the activation of air, (see Figure 2.4-166).

2.4.18.2.6 Activation of soil

Roughly 70 neutrons with energies larger than 100 MeV are being produced when a uranium particle with the energy of 1 GeV/u is completely stopped in a thick iron target. These neutrons may also lead to activation of soil when there is no sufficient shielding below the target area. ^{22}Na, ^{54}Mn, and depending on the composition of the soil ^{60}Co and other trace elements are of greatest relevance in terms of polluting the ground water.

2.4.19 Super-FRS Collaboration

All participating institutes working at the different branches of the Super-FRS have indicated that they will actively contribute in the design, construction and commissioning phases of the Super-FRS and its experimental setups. Only in discussions with these users we will find the optimal parameters for the construction and operating. Many technical contributions will come also from the GSI infrastructure and accelerator groups as successfully practiced with the FRS project. The specially listed institutes have indicated to contribute on specific subprojects, see NUSTAR LOIs).

GSI Darmstadt, D-64291 Darmstadt, Germany

Justus-Liebig Universität Gießen, D-35390 Gießen, Germany

Institute of Analytical Instrumentation, RAS, 198103 St. Petersburg, Russia

St. Petersburg State Technical University, 195251 St. Petersburg, Russia

Michigan State University, East Lansing, MI 48824, USA

Riken, 2-1 Hirosawa, Wako, Saitama 351-0198, Japan

Budker Institute of Nuclear Physics, RU630090 Novosibirsk, Russia

Argonne National Laboratory, Argonne, IL 60439, USA

Comenius University Bratislava, Sk-84248 Bratislava, Slovakia

Fachhochschule Mainz, D-55099 Mainz, Germany

Forschungszentrum Karlsruhe, D-76344 Eggenstein-Leopoldshafen, Germany

CEA, Saclay, F-91191 Gif-sur Yvette, France

University of Surrey, Guildford, GU2 5XH, UK

Paul Scherrer Institut, CH-5232 Villigen PSI, Schweiz

Technische Universität München, D-85748 Garching, Germany

Universidade de Santiago de Compostela, E-15706 Santiago de Compostela, Spain

Technische Universität Darmstadt, D-64289 Darmstadt, Germany

Johannes Gutenberg Universität, D-55099 Mainz, Germany

References

[1] J. Hubele et al., Z. Phys. **A340** (1991) 263;

[2] T. Blaich et al., Nucl. Instr. and Meth. **A314** (1992) 136.

[3] H. Geissel et al., Nucl. Instr. and Meth. B204 (2003) 71.

[4] H. Geissel et al., Nucl. Instr. and Meth. B247 (2006) 368.

[5] H. Iwase, K. Niita and T. Nakamura, J. Nucl. Sci. Tech. 39 (2002) 1142.

[6] K. L. Brown, SLAC 91, 1977.

[7] H. Wollnik, B. Hartmann and M. Berz, AIP Conference Proceedings 177 (1988) 74.

[8] N. Iwasa et al., Nucl. Instr. Meth. B126 (1997) 284.

[9] H. Geissel et al., Nucl. Instr. and Meth. A282 (1989) 247.

[10] D. J. Morrissey et al., Nucl. Instr. and Meth. B126 (1997) 316.

[11] T. Kubo, Nucl. Instr. and Meth. B204 (2003) 97.

[12] B. Sherrill, Nucl. Instr. and Meth. B204 (2003) 765.

[13] A. Zeller, private communication.

[14] M. Sawan et al., Fusion Technology 10 (1986) 741.

[15] R. Reed and D. Evans, "Insulation systems for the Muon Colliders", unpublished report (2000).

[16] A. Harvey and S. A. Walker, IEEE Trans. on Nucl. Sci. 16 (1969) 611.

[17] Opera-2D and Opera-3D/TOSCA, Vector-Field, Ltd, Oxford, England.

[18] A. F. Zeller, J. C. DeKamp, D. Johnson, Adv. in Cryog. Eng. 43 (1998) 245.

[19] K. Kusaka, T. Kubo and M. Mizoi, IEEE Trans. on Appl. Supercond. 14 (2004) 310.

[20] M. N. Wilson, "Superconducting Magnets", Clarendon Press, Oxford, 1983.

[21] B. Weckenmann, M. Kauschke, private communication, January 2008.

[22] P. Forck and A. Peters, AIP Conference Proceedings 773 (2004) 179.

[23] E. Berderman et al., Diamond and Related Materials 10 (2001) 1770.

[24] W. Adam et al., Eur. Phys. J. C33 (2004) s1014.

[25] M.J. French et al., Nucl. Instr. and Meth. A466 (2001) 359.

[26] http://www.gsi.de/informationen/wti/ee/elekt_entwicklung/TRB.html

[27] The RD42 Collaboration, Status Report 1999, CERN/LHCC 2000-011.

[28] E. Berdermann et al., Nucl. Phys. (Proc. Suppl.) B78 (1999) 533.

[29] R. Anne et al., GSI Report 1990-1 (1990) 257.

[30] H. Stelzer, Nucl. Instr. and Meth. A310 (1991) 103.

[31] A.S. Brogna et al, Nucl. Inst. and Meth. A568 (2006) 301.

[32] P. Forck, "Lecture Notes on Beam Instrumentation and Diagnostics", JUAS 2003, p. 77.

[33] H. Reeg and N. Schneider, "Current Transformers for GSI's keV/u to GeV/u ion beams – an overview", DIPAC 2001 Proceedings - ESRF, Grenoble.

[34] A. Peters et al., AIP Conference Proceedings 451 (1998) 163.

[35] B. Jurado, K.-H. Schmidt and K.-H. Behr, Nucl. Instr. and Meth. A483 (2002) 603.

[36] NoRHDia is an I3HP-Joint Research Activity, supported by the European Commission.

[37] P. Adrich et al., GSI Report 2003-1 (2003) 13; GSI Report 2004-1 (2004) 26.

[38] H. Folger, private communication.

[39] M. Pfützner et al., Nucl. Instr. and Meth. B86 (1994) 213.

[40] K. Kimura et al., Nucl. Instr. and Meth. A538 (2005) 608.

[41] K. Koch et al., IEEE Trans. on Nucl. Sci. 52 (2005) 745.

[42] Proceedings of the IEEE Nuclear Science Symposium '07, IEEE NSS-MIC-07, November 3-11, 2007, Honolulu, Hawaii, USA, in preparation; http://www.gsi.de/documents/DOC-2007-Nov-47.html

[43] "FLUKA: a multi-particle transport code", A. Fassò, A. Ferrari, J. Ranft and P.R. Sala, CERN-2005-10 (2005), INFN\TC-05\11, SLAC-R-773.

[44] "The physics models of FLUKA: status and recent developments", A. Fassò, et al., Computing in High Energy and Nuclear Physics 2003 Conference (CHEP2003), La Jolla, CA, USA, March 24-28, 2003; arXiv:hep-ph/0306267.

[45] http://www-linux.gsi.de/~weick/atima or as described as LS theory in; H. Geissel et al. Nucl. Instr. and Meth. in Phys. Res. B195 (2002) 3.

[46] International Nuclear Safety Center, Materials and Properties Database, "Recommended Graphite, Enthalpy Increments and Heat Capacities", Argonne Nat. Lab./US-DOE Internet documentation; http://www.ra.anl.gov/INSP/maturo

[47] C. Scheidenberger et al., Nucl. Instr. and Meth. B142 (1998) 441.

[48] ANSYS users manual, version 8.1, SAS IP, Inc. (2004).

[49] W. Kalbreier, W. Middelkoop and P. Sievers, CERN LAB II/BT/74-1, Geneva 1974.

[50] A. Abramov et al. "Advanced Conceptual Design of the NuMI Hadron Beam Absorber Core", NuMI-B-652, IHEP Protvino (2000); http://beamdocs.fnal.gov/DocDB/0006/000673/001/numib652.pdf

[51] J. Boscary et al., Fusion Engineering Design 43 (1998) 147.

[52] J. Liu et al., Phys. Rev. B64 (2001) 184115.

[53] M. Tomut et al., Proceedings of the third high power targetry workshop, Bad Zurzach 2007, PSI-Report in print., http://asq.web.psi.ch/hptrgts/

[54] J. Liu et al., Nucl. Instr. and Meth. B 245 (2006) 126.

[55] M. Argentini and R. Weinreich, "Measurement of radionuclide contents in activated graphite", PSI annual report 2000.

[56] N. Petoussi et al., "Dose distributions in the ICRU sphere for monoenergetic photons and electrons and for ca. 800 radionuclides", GSF-Bericht 7/93, GSF - Forschungszentrum für Umwelt und Gesundheit (1993).

[57] A. L. Conner, H. F. Atword and E. H. Plassmann, Phys. Rev. A3 (1970) 539.

[58] T. Schwab, GSI-Report 1991-10, Doctoral Thesis, University of Giessen (1990).

[59] J. Weckenmann et al., GSI Report 1990-13 (1990).

[60] LEB Technical Report, http://www-linux.gsi.de/~wwwnusta/tech_report/03-leb.pdf

[61] M. Petrick et al., Nucl. Instr. and Meth. B, submitted for publication.

[62] J.B. Neumayr et al., Nucl. Instr. and Meth. B244 (2006) 489.

[63] W. X. Huang et al., Europhys. Lett. 63 (5) (2003) 687-693.
[64] N. A. Tahir et al., Phys. Rev. E63 (2001) 036407-1.

[65] G. Heidenreich, AIP Conference Proceedings 642 (2002) 122.

[66] EU 6th Framework Program Design Study "DIRACsecondarybeams", Contract 515873.

[67] http://www.sglcarbon.com/gs/profile/structure

[68] Paul Müller Industrie Gmbh, Nürnberg, Germany; http://www.gmn.de

[69] M. Tomut et al., Proc. 3rd High-Power Targetry Workshop, 10.-14.09.2007, Bad Zurzach (Switzerland).

[70] J. Liu et al., Phys. Rev. B 64 (2001) 184115.

[71] Prophysik AG, Industriestrasse 416, 9491 Ruggell, Liechtenstein, E-Mail: prophysik@supra.net, tel: +4233771570, fax: +4233771575.

[72] J. A. Nolen et al., Nucl. Instr. and Meth. B 204 (2003) 293.

[73] A. Fabich and J. Lettry, Nucl. Instr. and Meth. A 503 (2003) 336;
A. Fabich, Ph.D Thesis, 2002, TU Wien; CERN, CERN-THESIS-2002-038.

[74] N. A. Tahir et al., J. Phys D: Appl. Phys. 38 (2005) 1828.

[75] An. Tauschwitz et al., Nucl. Instr. Meth. A, in print.

[76] R.Chavan, Analysis of Tokamak central column tiles, INT 195/99.

[77] R. Wilfinger et al., “Study of thermal stress waves induced by relativistic heavy ions beams in graphite ”, experimental proposal S334 at GSI.

[78] http://www.cadfem.de/LS-DYNA.2536.0.html

[79] http://www.ce.berkeley.edu/~rlt/feap/

[80] C. Plate and R. Mueller (TU Darmstadt), private communication.

[81] F. E. Fortov et al., Nucl. Sci. Eng. 123 (1996) 169.

[82] http://www.llnl.gov/CAFDA/ALE3D/ale3d.html

[83] D.E. Grady, J. Mech. Phys. Solids 36 (1988) 353.

[84] V. Efremov et al., "Feasibility of a liquid-Li jet target at FAIR/Super-FRS: Tensile strength of liquid lithium" (unpublished).

[85] http://www.iket.fzk.de/gsi/

[86] R. E. Ruland, "Setting reference targets", in Proc. CAS – CERN Accelerator School: Measurement and Alignment of Accelerator and Detector Magnets, Anacapri, Italy, 1997.

[87] I. Pschorn, H. Paluszek, "Implementation and first results of the survey and alignment of accelerator facilities at GSI using the TASA system", in Proc. IWAA1997 – 5th Int. workshop on accelerator alignment, Argonne, USA, 1997.

[88] W. Scandale, "From tolerance to alignment", in Proc. 2001 LHC days, Villars-sur-Ollon, Switzerland, 2001.

[89] I. Pschorn, "Combined techniques for network measurements at accelerator facilities", in Proc. IWAA1999 – 6th Int. workshop on accelerator alignment, Grenoble, France, 1999.

[90] S. Leinen, private communication.

[91] C. Zhang, K. Fukami, S. Matsui, "From the HLS measurement for ground movement at the SPring-8", in Proc. IWAA2004 – 8th Int. workshop on accelerator alignment, Geneva, Switzerland, 2004.

[92] I. Pschorn, A. Marbs, "A high-precision survey and alignment system in inaccessible, high-radiation areas of FAIR: Fundamental ideas", in Proc. IWAA2004 – 8th Int. workshop on accelerator alignment, Geneva, Switzerland, 2004.

[93] A. Marbs, F. Boochs and I. Pschorn, "A photogrammetric alignment approach at high-radiation areas of FAIR", in Proc. IWAA2006, SLAC, Stanford, Sep. 2006.

[94] A. Marbs, Final report on the research project of RALF (EU-FP6 funded), August 2005, unpublished.

[95] H. G. Essel et al., IEEE Trans. on Nucl. Sci. 43 (1996) 132;
H. G. Essel and N. Kurz, IEEE Trans. on Nucl. Sci. 47 (2000) 337.

[96] J. Hoffmann and N. Kurz, GSI Report 2003-1 (2003) 224.

[97] FOPI-Collaboration, GSI Report 1999-1 (1999) 177;
A. Schüttauf et al., GSI Report 2004-1 (2004) 231.

[98] J. Hoffmann and W. Ott, GSI Report 2003-1 (2003) 211.

[99] http://ttc.web.cern.ch/TTC/intro.html

[100] I. Konorov et al., IEEE 2001 Nucl. Sci. Symposium Conference Record, Vol.1 (2001) 98.

[101] L. Schmitt et al., IEEE Trans. on Nucl. Sci. 51 (2004) 439.

[102] P. Moritz, private Communication.

[103] GSI MBS V.43 release notes,
http://www-linux.gsi.de/~mbs/v43/manual/gm_mbs_r.pdf

[104] CENTRUM specifications,
http://nnsa.dl.ac.uk/documents/edoc421/edoc421.pdf

[105] Global Trigger and Synchronization system (GTS),
http://agata.pd.infn.it/documents/week9152003/MarcoBellato.pdf

[106] A. Jansson and M. Lindroos, "Intelligent' Automatic Beam Steering and Shaping", CERN/PS 2000-019, Proceedings of EPAC 2000 conference.

[107] Quack, H.: Cryogenic Systems for Large Research Projects, Proceedings of the 17th Intern. Conf. on Magnet Technology, Geneva, 24 - 28 Sep 2001.

[108] M. Kauschke: Lastenentwicklung in der Kryoversorgung, November 2007.

[109] B. Weckenmann: heat loads 0108, MS Excel sheet; January 2008.

[110] K. Schippl: Cryogenic Bus Bar for SIS100 Magnets, November 2007.

[111] P. Schnizer et al., "On the way to a measurement plan for GSI", Technical Note, Mar. 2004.

[112] G. Moritz, et al., IEEE Trans. on Magnetics, 24 (1988) 942.

[113] G. Moritz, Mechanical Equipment. In S. Turner, editor, CAS Magnetic Measurement and Alignment, pages 251–272. CERN, Aug. 1998.

[114] A. Jain, "Magnetic field measurements and mapping techniques", Lecture in Academic Training program at CERN,
http://agenda.cern.ch/fullAgenda.php?ida=a032529

[115] P. Schnizer et al., "Magnetic Field Analysis Magnetic field analysis for superferric accelerator magnets using elliptic multipoles and its advantages", accepted for publication in IEEE Trans. on Applied Superconductivity.

[116] P. Schnizer et al., "Field Representation for Elliptic Apertures", Technical Report, GSI, Jan. 2008.

[117] P. Schnizer et al., "A mole for measuring pulsed superconducting magnets", accepted for publication in IEEE Trans. on Applied Superconductivity.

[118] A. Jain, "Field Quality Measurements at High Ramp Rates in a Prototype Dipole for the FAIR Project", Presented at 20th Biennial Conference on Magnet Technology, Philadephia, Aug. 2007.

[119] J. DiMarco et al., "A Fast-Sampling, Fixed Coil Array for Measuring the AC Field of Fermilab Booster Corrector Magnets", Presented at 20th Biennial Conference on Magnet Technology, Philadelphia, Aug. 2007.

[120] A. Stafiniak, "Superconducting Test Facility for FAIR project - status January 2008", Internal Note 2008, GSI, MT-INT-AS-2008-001.

[121] A. Stafiniak et al., "Commissioning of the Prototype Test Facility for Rapidly-Cycling Superconducting Magnets for FAIR", MT20, 2007.

[122] R. Meinke, "Methods of Production Measurements of Superconducting Magnets", Technical Note DESY HERA 90-06.

[123] L. Bottura et al., "A Strategy for Series Magnetic Measurements of the LHC Superconducting Magnets", Technical Note LHC-MTA-IN-2001-162 2001-05-23.

[124] V. Chohan et al., "Testing of the LHC magnets in cryogenic conditions", 9th European Particle Accelerator Conference (EPAC'04) 5-9 July 2004, Lucerne, Switzerland.

[125] A. Siemko, "Cold Tests: Magnet Powering Aspects", Chamonix XII LHC Performance Workshop March 2003, EDMS No 375875.

[126] A. Stafiniak, "Testing Time for FAIR Superconducting Magnets - status January 2008", Internal Note 2008, GSI, MT-INT-AS-2008-001.

[127] A. Ferrari and M. Pelliccioni, Rad. Prot. Dosimetry 76 (1998) 215.

[128] S. Agosteo, G. Fehrenbacher and M. Silari, Nucl. Instr. and Meth. B226 (2004) 231.

[129] K. Gunzert-Marx, "Nachweis leichter Fragmente aus Schwerionenreaktionen mit einem BaF2-Teleskop-Detektor", Ph.D Thesis, Technical University Darmstadt, Germany (2004).

[130] J.-J. Gaimard and K.-H. Schmidt, Nucl. Phys. A531 (2003) 709.

[131] E. Hanelt and K.-H. Schmidt, Nucl. Instr. and Meth. A321 (1992) 434.

[132] International Commission on Radiological Protection, "Conversion Coefficients for use in Radiological Protection against External Radiation", ICRP Publication 74, Pergamon Press (1996).

[133] J. Wei et al., "Beam-loss driven design optimization for the spallation neutron source (SNS) ring", in Proceedings of the 1999 Particle Accelerators Conference, New York, p.3185.

[134] E. Mustafin, I. Hofmann and H. Weick, Nucl. Instr. and Meth. A501 (2003) 553.